

**AFRL-ML-TY-TR-2006-4522**



**DEVELOPMENT OF COMPUTATIONAL MODELS AND  
INPUT SENSITIVITY STUDY OF POLYMER  
REINFORCED CONCRETE MASONRY WALLS  
SUBJECTED TO BLAST**

**James S. Davidson and Sushant Sudame  
University of Alabama at Birmingham  
Department of Civil and Environmental Engineering  
140 Hoehn Building, 1075 13th Street South  
Birmingham, AL 35294-4440**

**Robert J. Dinan  
Air Force Research Laboratory  
139 Barnes Drive, Suite 2  
Tyndall AFB, FL 32403-5323**

**Interim Report, Dec 2004**

**DISTRIBUTION STATEMENT A: Approved for public release;  
distribution unlimited.**

**Air Force Research Laboratory  
Materials and Manufacturing Directorate  
Airbase Technologies Division  
139 Barnes Drive, Suite 2  
Tyndall AFB, FL 32403-5323**

**REPORT DOCUMENTATION PAGE**

*Form Approved  
OMB No. 0704-0188*

The public reporting burden for this collection of information is estimated to average 1 hour per response, including the time for reviewing instructions, searching existing data sources, gathering and maintaining the data needed, and completing and reviewing the collection of information. Send comments regarding this burden estimate or any other aspect of this collection of information, including suggestions for reducing the burden, to the Department of Defense, Executive Services and Communications Directorate (0704-0188). Respondents should be aware that notwithstanding any other provision of law, no person shall be subject to any penalty for failing to comply with a collection of information if it does not display a currently valid OMB control number.

**PLEASE DO NOT RETURN YOUR FORM TO THE ABOVE ORGANIZATION.**

<b>1. REPORT DATE (DD-MM-YYYY)</b> 01-12-2004		<b>2. REPORT TYPE</b> Interim Technical Report		<b>3. DATES COVERED (From - To)</b> 01-12-2003 - 01-12-2004	
<b>4. TITLE AND SUBTITLE</b> Development of Computational Models and Input Sensitivity Study of Polymer Reinforced Concrete Masonry Walls Subjected to Blast				<b>5a. CONTRACT NUMBER</b> F08637-02-C-7027	
				<b>5b. GRANT NUMBER</b>	
				<b>5c. PROGRAM ELEMENT NUMBER</b> 63112F	
<b>6. AUTHOR(S)</b> Davidson, James S.; Sudame, Sushant; Dinan, Robert J.				<b>5d. PROJECT NUMBER</b> 4918	
				<b>5e. TASK NUMBER</b> C10B	
				<b>5f. WORK UNIT NUMBER</b> 4918C10B	
<b>7. PERFORMING ORGANIZATION NAME(S) AND ADDRESS(ES)</b> University of Alabama at Birmingham Department of Civil and Environmental Engineering 140 Hoehn Building, 1075 13th Street South Birmingham, AL 35294-4440				<b>8. PERFORMING ORGANIZATION REPORT NUMBER</b>	
<b>9. SPONSORING/MONITORING AGENCY NAME(S) AND ADDRESS(ES)</b> Air Force Research Laboratory, Materials and Manufacturing Directorate Airbase Technologies Division, Force Protection Branch 139 Barnes Drive, Suite 2 Tyndall AFB, FL 32403-5323				<b>10. SPONSOR/MONITOR'S ACRONYM(S)</b> AFRL/MLQF	
				<b>11. SPONSOR/MONITOR'S REPORT NUMBER(S)</b> AFRL-ML-TY-TR-2006-4522	
<b>12. DISTRIBUTION/AVAILABILITY STATEMENT</b> Distribution Statement A: Approved for public release; distribution unlimited.					
<b>13. SUPPLEMENTARY NOTES</b> Technical contact: Dr. Robert J. Dinan, AFRL/MLQF, 850-283-3605. Report contains color images.					
<b>14. ABSTRACT</b> Computational models were developed and used to simulate polymer reinforced masonry walls subjected to blast loading and the models were used to understand the response of the structure. LS-DYNA, a nonlinear finite element solver, was used. Model development challenges were considered, and appropriate input parameters were determined. With these pedestal values, a baseline model of one unit width of concrete masonry block was developed, and the response under two load conditions was studied. Dimensional and mechanical variants involved in the system were varied to study their effect on wall behavior. The effects of door and window openings on the performance of the polymer reinforcement were evaluated. This report also presents an analysis of strain rate that occurs in the polymer coating and results were compared to theory-based closed form solutions. Finally, the static nonlinear capabilities of LS-DYNA were used to describe the static resistance of the system, and a theoretical description of a simply supported membrane subjected to pressure load is provided and compared with nonlinear finite element results.					
<b>15. SUBJECT TERMS</b> computational model, finite element, polymer, masonry, blast, reinforcement					
<b>16. SECURITY CLASSIFICATION OF:</b>			<b>17. LIMITATION OF ABSTRACT</b> UU	<b>18. NUMBER OF PAGES</b> 170	<b>19a. NAME OF RESPONSIBLE PERSON</b> Elizabeth Trawinski
<b>a. REPORT</b> U	<b>b. ABSTRACT</b> U	<b>c. THIS PAGE</b> U			<b>19b. TELEPHONE NUMBER (Include area code)</b> 850-283-3605

## NOTICE

Using Government drawings, specifications, or other data included in this document for any purpose other than Government procurement does not in any way obligate the U.S. Government. The fact that the Government formulated or supplied the drawings, specifications, or other data does not license the holder or any other person or corporation; or convey any rights or permission to manufacture, use, or sell any patented invention that may relate to them.

This technical report was reviewed and cleared for public release by the Air Force Research Laboratory Tyndall Site (AFRL/MLQ) Public Affairs Office (PAO) and is releasable to the National Technical Information Service (NTIS). Reference PAO Case Number: 06-022

This report is releasable to the National Technical Information Service (NTIS) where it will be available to the general public, including foreign nationals.

5285 Port Royal Road

Springfield VA 22161

Telephone (703) 487-4650, (703) 487-4639 (TDD for the hearing impaired)

e-mail: [orders@ntis.fedworld.gov](mailto:orders@ntis.fedworld.gov)

<http://www.ntis.gov/index.html>

This technical report is approved for publication.



ELIZABETH TRAWINSKI, 1st Lt, USAF  
Work Unit Manager



AL D. NEASE  
Chief, Force Protection Branch



JIMMY L. POLLARD, Colonel, USAF  
Chief, Airbase Technologies Division

This report is published in the interest of scientific and technical information exchange and its publication does not constitute the Government's approval or disapproval of its ideas or findings.

# **DEVELOPMENT OF COMPUTATIONAL MODELS AND INPUT SENSITIVITY STUDY OF POLYMER REINFORCED CONCRETE MASONRY WALLS SUBJECTED TO BLAST**

## **ABSTRACT**

Public and government buildings have become the target of bomb attacks carried out by terrorists worldwide. Most casualties of blast attacks are due to fragmentation of walls and windows. New design and engineering techniques are needed to protect people and property in buildings at risk of bomb attacks.

The Air Force Research Laboratory at Tyndall Air Force Base, Florida, has demonstrated the effectiveness of an elastomeric polymer for blast reinforcement of concrete masonry walls. However, full-scale testing is expensive, and extraction of data during explosive tests is difficult due to the short duration and destructive nature of the structural response.

This document describes the development of computational models used to simulate polymer reinforced masonry walls subjected to blast loading and the use of the models to understand the response of the structure. LS-DYNA, a nonlinear finite element solver, was used. Model development challenges such as hourglass mode control, element formulation, gravity load application, and damping were considered, and appropriate input parameters were determined. With these pedestal values, a baseline model of one unit width of concrete masonry block was developed, and the response under two load conditions was studied. Dimensional and mechanical variants involved in the system, including polymer elongation, polymer thickness, elastic modulus, yield strength, etc., were varied to study their effect on wall behavior. The results are presented in the form of graphs and plots. The effects of door and window openings of various sizes and shapes on the performance of the polymer reinforcement were evaluated.

This report also presents an analysis of strain rate that occurs in the polymer coating. Several model approaches were used to analyze strain rate and to evaluate the stability of various material models that could be used to simulate the polymer coating. This included (1) a membrane-only model used to evaluate the stability of material models, (2) a rigid slab model used to analyze the polymer reinforcement in dynamic tension and shear environments, and (3) a one-way flexure model consisting of a single masonry unit width. The models were analyzed for two loading conditions. The results were compared to theory-based closed form solutions. The study resulted in conclusions about the strain rate when the polymer is used for concrete masonry wall reinforcement. Finally, the static nonlinear capabilities of LS-DYNA were used to describe the static resistance of the system, and a theoretical description of a simply supported membrane subjected to pressure load is provided and compared with nonlinear finite element results.

## TABLE OF CONTENTS

	<i>Page</i>
ABSTRACT.....	iii
LIST OF TABLES.....	vii
LIST OF FIGURES.....	viii
LIST OF ABBREVIATIONS.....	xvi
CHAPTER	
1. INTRODUCTION.....	1
1.1 Objectives.....	1
1.2 Scope and Methodology.....	1
1.3 Report Organization.....	2
2. LITERATURE REVIEW.....	3
2.1 Blast Load.....	3
2.2 Wall Reinforcement.....	5
2.3 Computer Modeling of Concrete Structures.....	5
2.4 Computer Modeling of Masonry Walls.....	6
2.5 Constitutive Relations for Concrete Material Models.....	8
3. DEVELOPMENT OF FINITE ELEMENT MODELS.....	11
3.1 Introduction.....	11
3.2 Unit System.....	11
3.3 Loads.....	11
3.4 Geometry and Materials.....	11
3.4.1 Wall.....	15
3.4.2 Concrete Masonry Unit (CMU).....	15
3.4.3 Polymer Reinforcement.....	15
3.5 Material Models.....	18
3.5.1 Concrete Masonry Units.....	18
3.5.2 Polymer.....	20
3.5.3 Roof and Floor Boundaries.....	24
3.6 Element Selection.....	24

TABLE OF CONTENTS (Continued)

CHAPTER	<i>Page</i>
3.7 Contact Surfaces .....	26
3.7.1 Selection of Contact Surface.....	26
3.7.2 Parameters Involved in Contact Definitions .....	27
3.8 Dynamic Relaxation.....	27
3.8.1 Interface Reaction Force Calculation.....	28
3.8.2 Effect of Variation in Preload .....	30
3.9 Damping .....	30
3.9.1 Eigenvalue Extraction .....	31
3.9.2 Calculation of Damping Coefficient.....	31
3.10 Hourglassing in Elements .....	32
3.10.1 Hourglassing in Shell Elements .....	33
3.10.2 Hourglassing in Solid Elements.....	34
3.10.3 Study of Hourglassing in the Single Unit Width Model With Two Elements Through the CMU Face Shells .....	35
3.10.4 Study of Hourglassing in the Hi-Fidelity Model .....	35
3.11 Energy Balance .....	35
3.12 Baseline Model .....	39
3.12.1 Description and Setup.....	39
3.12.2 General Behavior of Wall .....	41
3.12.3 Baseline Model Performance under Load I and Load III ..	41
3.13 Hi-Fidelity Model Development.....	50
3.13.1 Need .....	50
3.13.2 Model Description .....	50
3.13.3 Observations .....	50
3.14 Summary and Conclusions .....	50
4. INPUT SENSITIVITY STUDY .....	58
4.1 Introduction.....	58
4.2 Variants .....	58
4.2.1 Rupture Strain .....	58
4.2.2 Retrofit Thickness.....	59
4.2.3 Initial Modulus.....	70
4.2.4 Yield Strength .....	79
4.2.5 Top Clearance .....	79
4.2.6 Bond Strength between Mortar and Blocks .....	87
4.2.7 Bond Strength between Polymer and Blocks.....	90
4.3 Wall Openings .....	91
4.3.1 Model Setup.....	91
4.3.2 Results and Observations .....	100
4.4 Conclusions.....	100

TABLE OF CONTENTS (Continued)

CHAPTER	<i>Page</i>
5. STRAIN RATE ANALYSIS.....	104
5.1 Introduction.....	104
5.2 Model Development.....	104
5.3 Model #1: Membrane Only Model .....	105
5.3.1 Model Setup.....	105
5.3.2 Observations .....	105
5.3.3 Theoretical Approach.....	105
5.4 Model #2: Dynamic Opening of Rigid Slabs.....	107
5.4.1 Model Setup.....	107
5.4.2 Theoretical Solution.....	108
5.4.3 Factor Calculation.....	112
5.5 Model #3: Shear Test.....	113
5.6 Model #4: Hi-Fidelity Model.....	115
5.6.1 Model Setup.....	115
5.6.2 Results.....	115
5.7 Conclusions.....	116
6. MODELS FOR STATIC RESISTANCE FUNCTION .....	122
6.1 Definition of Static Resistance Using LS-DYNA .....	122
6.1.1 Model 1 Setup.....	122
6.1.2 Model 2 Setup.....	126
6.1.3 Model 3 Setup.....	129
6.2 Static Resistance of Membrane.....	131
6.2.1 Need.....	131
6.2.2 Equation.....	131
6.2.3 Results.....	132
6.3 Summary and Conclusions .....	133
7. CONCLUSIONS.....	136
7.1 Summary and Conclusions .....	136
7.2 Recommendations and Suggested Research.....	138
LIST OF REFERENCES.....	140
APPENDIX: LS-DYNA INPUT DECK FOR BASELINE MODEL.....	143

## LIST OF TABLES

<i>Table</i>		<i>Page</i>
1	Unit System Used .....	12
2	Properties of Polyurea.....	17
3	Shortlisted Constitutive Models for Retrofitted Polymers .....	22
4	Natural Frequencies for Single Unit Width Wall Model .....	31
5	Maximum Displacement and Velocity Due to Change in Rupture Strain of Polymer .....	59
6	Maximum Displacement and Velocity Due to Change in Polymer Thickness .....	63
7	Maximum Vertical Strain in Polymer Due to Change in Polymer Thickness .....	63
8	Maximum Displacement and Velocity Due to Change in Initial Modulus .....	71
9	Maximum Vertical Strain in Polymer Due to Change in Initial Modulus .....	71
10	Wall Openings .....	100
11	Strain Rate in Membrane Only Model.....	106
12	Model #2: Strain Rates for Polymer Reinforced Slab Model for 2 in. Gap.....	110
13	Comparison of Theoretical and Finite Element Strain Rate for Model #2.....	113
14	Shear Test: Strain Rates for Load I and Load II .....	115

## LIST OF FIGURES

<i>Figure</i>	<i>Page</i>
1 Load Time History for Load I.....	13
2 Load Time History for Load II .....	13
3 Load Time History for Load III.....	14
4 Test Wall Setup.....	14
5 Schematic of Wall Setup.....	16
6 Typical Concrete Masonry Block Meshing .....	17
7 Static Stress-Strain Curve for the Spray-On Polymer considered in Air Force Research Laboratory Explosive Tests.....	18
8 Mesh Fidelity for Concrete Masonry Unit.....	19
9 Displacement Time History at Mid-Height of Single Unit Width Model .....	19
10 Strain Energy in Polymer for Various Material Models for Concrete Masonry Unit .....	20
11 True Stress - True Strain Curve for Polyurea at Various Strain Rates .....	23
12 Reaction Time History for Interface #1 .....	29
13 Displacement Time History at Center of Wall for Varying Gravity Load .....	30
14 Variation in Mid-Height Displacement with Change in Critical Damping .....	33
15 Hourglassing in Shells with ELEFORM=16 .....	34
16 Internal and Hourglassing Energy in Solids without Hourglassing Control .....	36
17 Internal and Hourglassing Energy in Solids with Hourglassing Control.....	36
18 Single Unit Width Model with Hi-Fidelity Meshing in Lower Blocks .....	37

## LIST OF FIGURES (Continued)

<i>Figure</i>	<i>Page</i>
19 Internal and Hourglassing Energy in Finely Meshed Model with Single Point Integration Solid Elements .....	38
20 Internal and Hourglassing Energy in Coarsely Meshed Model with Fully Integrated Solid Elements .....	38
21 Energy Balance for Single Unit Width Wall Model .....	40
22 Baseline Model Setup .....	42
23 General Wall Behavior .....	44
24 Maximum Displacements for Baseline Model for Load I and Load III .....	45
25 Peak Velocity for Baseline Model for Load I and Load III .....	45
26 Relative Distance between Front and Back Walls of Block for Load III .....	46
27 Initial State of Block .....	47
28 Fractured State of Block under Load III .....	47
29 Interface Forces for Load I .....	49
30 Interface Forces for Load III.....	49
31 Vertical Strain in Polymer for Load I .....	52
32 Vertical Strain in Polymer for Load III.....	52
33 System Energy Distribution for Load I.....	53
34 System Energy Distribution for Load III.....	53
35 Concrete Masonry Unit with Hi-Fidelity Meshing.....	54
36 Mortar Layer with Hi-Fidelity Meshing .....	54
37 Stress Distribution in Finely and Coarsely Meshed Blocks.....	55
38 Effective Stress Concentration at Corners (Backside).....	55

LIST OF FIGURES (Continued)

<i>Figure</i>		<i>Page</i>
39	Effective Stress Concentration at Corners (Front side) .....	56
40	Crushing due to Block-Boundary Interaction .....	56
41	Shear Stress Distribution in Finely Meshed Blocks .....	57
42	Shear Failure at Mortar Interface in Finely Meshed Blocks.....	57
43	Effect of Rupture Strain on Maximum Displacement for Load I .....	60
44	Effect of Rupture Strain on Maximum Displacement for Load III .....	60
45	Effect of Rupture Strain on Maximum Velocity for Load I .....	61
46	Effect of Rupture Strain on Maximum Velocity for Load III.....	61
47	Effect of Rupture Strain on Internal Energy of the Polymer for Load I .....	62
48	Effect of Rupture Strain on Internal Energy of the Polymer for Load III .....	62
49	Effect of Polymer Thickness on Maximum Displacement for Load I .....	64
50	Effect of Polymer Thickness on Maximum Displacement for Load III.....	64
51	Effect of Polymer Thickness on Maximum Velocity for Load I .....	65
52	Effect of Polymer Thickness on Maximum Velocity for Load III .....	65
53	Vertical Strain in Polymer near Bottom Mortar Joint for Load I .....	66
54	Vertical Strain in Polymer near Center Mortar Joint for Load I .....	66
55	Vertical Strain in Polymer near Bottom Mortar Joint for Load III.....	67
56	Vertical Strain in Polymer near Center Mortar Joint for Load III .....	67
57	Variation of Internal Energy with Polymer Thickness for Load I.....	68
58	Variation of Kinetic Energy with Polymer Thickness for Load I .....	69
59	Variation of Internal Energy with Polymer Thickness for Load III .....	69

LIST OF FIGURES (Continued)

<i>Figure</i>	<i>Page</i>
60	Variation of Kinetic Energy with Polymer Thickness for Load III .....70
61	Effect of Initial Modulus on Maximum Displacement for Load I .....72
62	Effect of Initial Modulus on Maximum Displacement for Load III .....72
63	Effect of Initial Modulus on Maximum Velocity for Load I .....73
64	Effect of Initial Modulus on Maximum Velocity for Load III .....73
65	Vertical Strains in the Polymer near Bottom Mortar Joint for Load I .....74
66	Vertical Strains in the Polymer near Center Mortar Joint for Load I .....74
67	Vertical Strains in the Polymer near Bottom Mortar Joint for Load III .....75
68	Vertical Strains in the Polymer near Center Mortar Joint for Load III .....75
69	Variation of Internal Energy in Polymer with Initial Modulus for Load I .....77
70	Variation of Kinetic Energy in Polymer with Initial Modulus for Load I .....77
71	Variation of Internal Energy in the Polymer with Initial Modulus for Load III ....78
72	Variation of Kinetic Energy in the Polymer with Initial Modulus for Load III ....78
73	Effect of Variation in Polymer Yield Stress on Displacement of Wall for Load I .....80
74	Effect of Variation in Polymer Yield Stress on Displacement of Wall for Load III .....80
75	Effect of Variation in Polymer Yield Stress on Velocity of Wall for Load I .....81
76	Effect of Variation in Polymer Yield Stress on Velocity of Wall for Load III .....81
77	Vertical Strain in Polymer near Bottom Mortar Joint for Load I .....82
78	Vertical Strain in Polymer near Center Mortar Joint for Load I .....82
79	Vertical Strain in Polymer near Bottom Mortar Joint for Load III .....83

LIST OF FIGURES (Continued)

<i>Figure</i>	<i>Page</i>
80 Vertical Strain in Polymer near Center Mortar Joint for Load III .....	83
81 Variation of Internal Energy with Polymer Yield Stress for Load I.....	84
82 Variation of Kinetic Energy with Polymer Yield Stress for Load I .....	84
83 Variation of Internal Energy with Polymer Yield Stress for Load III .....	85
84 Variation of Kinetic Energy with Polymer Yield Stress for Load III.....	85
85 Plastic Strain in Polymer near Bottom Mortar Joint for Load I.....	86
86 Plastic Strain in Polymer near Bottom Mortar Joint for Load III.....	86
87 Top Block and Roof (Initial State).....	87
88 Deformation of Top Block .....	88
89 Vertical Displacement Time History of Top Block for Load I .....	89
90 Vertical Displacement Time History of Top Block for Load III .....	89
91 Variation in Vertical Strain in Polymer near Bottom Mortar Joint With Change in Mortar Bond Strength for Load I .....	92
92 Variation in Vertical Strain in Polymer near Center Mortar Joint With Change in Mortar Bond Strength for Load I .....	92
93 Variation in Vertical Strain in Polymer near Bottom Mortar Joint With Change in Mortar Bond Strength for Load III .....	93
94 Variation in Vertical Strain in Polymer near Center Mortar Joint With Change in Mortar Bond Strength for Load III.....	93
95 Variation in Displacement with Polymer Bonding for Load I.....	94
96 Variation in Displacement with Polymer Bonding for Load III.....	94
97 Variation in Velocity with Polymer Bonding for Load I.....	95
98 Variation in Velocity with Polymer Bonding for Load III .....	95

LIST OF FIGURES (Continued)

<i>Figure</i>	<i>Page</i>
99	Variation in Internal Energy with Polymer Bonding for Load I.....96
100	Variation in Kinetic Energy with Polymer Bonding for Load I .....96
101	Variation in Internal Energy with Polymer Bonding for Load III.....97
102	Variation in Kinetic Energy with Polymer Bonding for Load III.....97
103	Variation in Vertical Strain near Bottom Mortar Joint for Load I.....98
104	Variation in Vertical Strain near Center Mortar Joint for Load I .....98
105	Variation in Vertical Strain near Bottom Mortar Joint for Load III .....99
106	Variation in Vertical Strain near Center Mortar Joint for Load III.....99
107	Polymer Reinforced Wall without Opening .....101
108	Polymer Reinforced Wall with 40 in. X 40 in. Window Opening .....102
109	Polymer Reinforced Wall with 40 in. X 40 in. Window Opening and Polymer of Double Thickness near the Window .....102
110	Polymer Reinforced Wall with 40 in. X 80 in. Door Opening .....103
111	Center Displacements for Various Wall Openings under Load I .....103
112	Membrane Only Analytical Model .....106
113	Theoretical Approach to Membrane Equation .....107
114	Mesh Transition in Polymer near the Gap .....108
115	Comparison of Center Displacements for Load I .....109
116	Theoretical Solution for Model #2.....111
117	Model #2 Strain Rate Time History for Load I.....112
118	Model #2 Strain Rate Time History for Load II .....113
119	Model Setup for Shear Test .....114

LIST OF FIGURES (Continued)

<i>Figure</i>	<i>Page</i>
120 Baseline Model Setup Modified for Strain Rate Analysis.....	117
121 Strain in Polymer near Bottom Mortar Joint for Load I .....	118
122 Strain Rate in Polymer near Bottom Mortar Joint for Load I.....	118
123 Strain in Polymer near Center Mortar Joint for Load I.....	119
124 Strain Rate in Polymer near Center Mortar Joint for Load I .....	119
125 Strain in Polymer near Bottom Mortar Joint for Load II.....	120
126 Strain Rate in Polymer near Bottom Mortar Joint for Load II.....	120
127 Strain in Polymer near Center Mortar Joint for Load II .....	121
128 Strain Rate in Polymer near Center Mortar Joint for Load II.....	121
129 Model 1 Setup for Implicit Static Nonlinear Analysis .....	123
130 Load-Load Step Curve for Model 1 .....	124
131 Load-Displacement Curve for Model 1 .....	124
132 Strain in Mid-Height Mortar Interface.....	125
133 Strain in Mortar Joints near Mid-Height.....	125
134 Vertical Strain in Polymer near the Mid-Height Mortar Interface .....	126
135 Model 2 Setup for Implicit Static Nonlinear Analysis.....	127
136 Load-Load Step Curve for Model 2.....	128
137 Load-Displacement Curve for Model 2 .....	128
138 Mortar Joint Strain near Mid-Height .....	129
139 Load-Load Step Curve for Model 3.....	130
140 Load-Displacement Curve for Model 3 .....	130

LIST OF FIGURES (Continued)

<i>Figure</i>		<i>Page</i>
141	Strain in Polymer at Mid-Height.....	131
142	Membrane Static Analysis I.....	134
143	Membrane Static Analysis II .....	134
144	Membrane Static Analysis III.....	135
145	Membrane Static Analysis IV.....	135

## **LIST OF ABBREVIATIONS**

AFRL	Air Force Research Laboratory
CMU	Concrete Masonry Unit
LSTC	Livermore Software Technology Corporation
MPP	Massively Parallel Processing
TNT	Tri-Nitro Toluene
NFLS	Normal Failure Strain
SFLS	Shear Failure Strain

## **CHAPTER 1. INTRODUCTION**

The risk of attacks by fundamentalists, extremists, and terrorist organizations is escalating. Terrorist attacks are not restricted to government and military structures. Common and crowded public facilities such as office buildings and shopping complexes are also being targeted with intention to cause human injuries, death, and social unrest.

Much of the human injury and death occurring during an explosive attack is not caused directly by the blast but rather is due to the fragmentation of exterior walls, windows, and other structural components that are propelled at high velocity. Control of this fragmentation will reduce injuries and death.

Walls of high risk facilities must be reinforced to withstand blast load. Newly constructed walls can be designed for blast loads with the use of mass and ductility through steel reinforcement. However, strengthening existing walls for blast load remains challenging. Unreinforced concrete masonry walls are common and susceptible to fragmentation and collapse under blast pressure. Cost effective methods are being evaluated for improving blast resistance.

The Air Force Research Laboratory (AFRL) at Tyndall Air Force Base, Florida, is testing various polymer retrofit methods for protection against blast loads. Full-scale explosive tests are expensive and time consuming, and it is difficult to collect data during the few milliseconds of response time. Due to debris and dust resulting from the explosion, the response is difficult to record, even with the help of sophisticated high-speed cameras and gauges. Critical information such as deflections and strains is difficult to measure. Therefore, development of finite element models is imperative for understanding failure mechanisms and the distribution of stress and strains over time.

### **1.1 Objectives**

The objectives of the work in which this report is based were to (1) determine the best methodology for developing hi-fidelity finite element models for studying polymer reinforced concrete masonry walls subjected to blast loads, (2) use the models to understand failure mechanisms, and (3) perform an input sensitive study to determine the influence of major geometric and material properties.

### **1.2 Scope and Methodology**

The scope of this effort included an investigation of previous related work, investigation of modeling techniques, investigation of failure mechanisms, and the effects of dominant input parameters. Models were developed and analyzed using LS-DYNA v970 developed by Livermore Software Technology Corporation (LSTC). LS-DYNA is an advanced general-purpose nonlinear finite element program capable of simulating complex mechanics problems. It is based on an explicit solution, provides a wide range of constitutive material models, and has a built-in explosives load capability. Its usability on multiple processors made it suitable to solve computationally intensive problems. Finite

Element Model Builder (FEMB v28.0) was used as a preprocessor, whereas postprocessing was done using LS-PRE/POST v1.0. Large models were analyzed on a 128-processor supercomputer provided through the University of Alabama at Birmingham Enabling Technology Laboratory, Department of Mechanical Engineering. The MPP (Massively Parallel Processor) version of LS-DYNA was used. For lower fidelity models, a dual processor workstation was used. The following aspects of model development were evaluated: (1) hourglassing, (2) damping, (3) element formulation, (4) material model for CMU, (5) contact surface selection, (6) energy balance, (7) constitutive models for the polymer reinforcement, and (8) gravity preload through dynamic relaxation.

### **1.3 Report Organization**

This report is organized into seven chapters. Chapter 1 identifies the objectives, scope, methodology, and organization of the document. Chapter 2 provides a literature review that covers previous studies of blast load, wall reinforcement, computer modeling of concrete structures, computer modeling of masonry walls, and constitutive relations for material models for concrete. Chapter 3 discusses modeling components such as geometry and materials, material model selection, element formulation, system damping, hourglassing, and contact surfaces. Chapter 3 also discusses the development and behavior of a one-way flexure single masonry unit width model with several meshes. Chapter 4 discusses the behavior of a “baseline” model subjected to two loads and presents an input sensitive study using the baseline model. Chapter 4 also discusses an analysis of the wall with a highly refined mesh of the masonry blocks. Chapter 5 summarizes several analytical and theoretical models used to evaluate the stability of various LS-DYNA material models and presents an analysis of the strain rate in the polymer reinforcement under high shear and tension environments. Chapter 6 discusses the use of LS-DYNA for static nonlinear analysis of the wall and the development of nonlinear membrane resistance equations. Conclusions and research recommendations are made in Chapter 7. Finally, the Appendix provides LS-DYNA input files.

## CHAPTER 2. LITERATURE REVIEW

Concrete masonry walls can be designed as load bearing or non-load bearing and are comprised of hollow concrete block units. Concrete masonry walls may be unreinforced, lightly reinforced or strongly reinforced, depending on the purpose they serve. They are constructed in a concrete or steel frame. Masonry walls have high in-plane strength but perform poorly against lateral loading conditions such as wind or blast loading.

Masonry walls are not designed to resist blast loads. Concrete is brittle, has poor flexural resistance without ductile reinforcement, and cannot absorb significant strain energy. External reinforcement may be required to increase the ductility of masonry walls subjected to significant lateral loads. For hollow block masonry, flexural tensile strength parallel to bed joints is two to four times greater than the flexural tensile strength normal to the bed joint of the masonry. The tensile and compressive strength of blocks does not affect the flexural resistance of the masonry wall since the resistance to flexure is dominated by cracking at the mortar joints. The size of blocks plays an important role when tension is parallel to block joints (Hamid and Drysdale 1988). Support conditions determine fracture behavior of the wall parallel or perpendicular to the mortar joints, hence boundary conditions are key factors in determining the strength of the wall.

### 2.1 Blast Load

The load magnitude caused by blast is determined by many factors such as charge size, type of explosive, and standoff distance. Blast is broadly classified as air blast or subsurface blast. Air blast can be airburst or surface burst, depending on the distance of burst above the ground. Air blast generates a pressure sphere traveling radially at the speed of sound (Dharaneepathy et al. 1995). This pressure has a positive phase and negative phase. The positive phase has a peak side-on pressure, and the negative phase is characterized by suction. In many studies of blast effects on structures, this negative phase is ignored (Beshara 1994). Pressure intensity depends on location within the structure. Hence the impulse depends on standoff distance and angle of incidence. Parameters such as time of arrival, positive phase duration, wave decay coefficient, and side-on pressure depend on standoff distance. If the standoff equals the “critical blast distance,” the transient dynamic response is maximum (Dharaneepathy et al. 1995).

Explosive effects do not scale linearly. For example, a 2 lb charge does not produce the same effect as a 1 lb charge at half the distance. Scaling is generally done in terms of TNT equivalence. This equivalency is affected by charge size, confinement, nature of source, and pressure range under consideration. General important characteristics of the blast wave, such as energy release, are measured for standard TNT tests carried out with controlled explosions. These results are then used as a benchmark to calculate data for other explosions by using the cube root scaling law, which states that “when two charges of same explosive and geometry, but different sizes are detonated in

the same atmosphere, the shock waves produced are similar in nature of the same-scaled distances” (Beshara 1994).

The proximity factor is shown as

$$Z = \frac{R}{W^{\frac{1}{3}}} \quad (1)$$

where  $R$  = distance from center of explosion to given location, and  $W$  = weight of explosive. Using this law and the standard TNT explosion parameters available, parameters for other explosions can easily be calculated.

$$Z = \frac{R_r}{W_r^{\frac{1}{3}}} = \frac{R}{W^{\frac{1}{3}}} \quad (2)$$

where parameters with subscript ‘ $r$ ’ are reference parameters like TNT equivalence (Beshara 1994).

The point on the ground exactly below the explosion is referred to as ground zero. Pressure time history is composed of overpressure, dynamic pressure, and reflected pressure. Overpressure is a pressure that acts on the structure in the absence of obstacles such as the ground and is hydrostatic in nature. Dynamic pressure causes drag or wind type loads on the structure and exhibits sharper pressure decay over longer duration. Reflected pressure is generated when the shock front hits a rigid surface. The overpressure and dynamic pressure have longer duration than reflected pressure. For conventional high explosives, the magnitude of the peak reflected pressure is higher than the peak overpressure and peak dynamic pressure. Near the ground surface, the combined effect of incident pressure and reflected pressure is considered. However, while studying the effect of unconfined explosions such as nuclear explosions on multistoried structures, peak overpressure may be more important than the reflected pressure.

Krauthammer and Otani (1997) studied the behavior and design of reinforced concrete structures subjected to blast load and concluded that shock pressure has less effect on reinforced concrete structures than the lower overpressure that lasts for longer time duration. Therefore the function used for load application must consider both pressures. Since the maximum dynamic pressure is very small as compared to the other two, it can be neglected from load calculation. This load application depends on the angle of incidence, which is the angle between the line of wave propagation and the outer normal to the element.

The U.S. Army Engineer Waterways Experiment Station developed the Conventional Weapons Effect Program (CONWEP) that provides free-field spherical and hemispherical predictions (Randers-Pehrson and Bannister 1997). The calculations consider the blast wave angle of incidence. The BRODE model implemented in DYNA3D for modeling blast pressure excludes this feature. CONWEP, on the other hand, does not combine reflected pressure and incident pressure for calculation of angle of incidence. Randers-Pehrson and Bannister (1997) integrated a modified CONWEP model into DYNA2D and DYNA3D by incorporating the following equation:

$$P_L = P_R X \cos^2 \theta + P_I X (1 + \cos^2 \theta - 2 \cos \theta) \quad (3)$$

where  $P_L$  = pressure load,  $P_R$  = reflected pressure,  $P_I$  = incident pressure, and  $\theta$  = angle of incidence.

## 2.2 Wall Reinforcement

Blast resistant design philosophy allows structural elements to undergo large inelastic deformations in response to blast loading. Since blast loads act for a short period of time, the efficiency of the structural system depends on the energy absorption capacity of the system. Ductility, and therefore energy absorption capacity, can be added to the system through a technique referred to as retrofitting. The AFRL at Tyndall AFB, Florida, has tested the effectiveness of spray-on polymers for improving blast resistance of concrete masonry walls. The tests were successful, and potential retrofit methods were investigated (Thornburg 2004). The polymers were selected based upon ease of application, cost effectiveness, and flammability. Twenty one prospective polymers were classified on the basis of their application to wall surface: brush-on, spray-on, and extruded thermoplastic sheet. Laboratory tensile testing was conducted at AFRL at a loading rate of 0.33 in./sec. Tests indicated that the extruded thermoplastics were stiffer and stronger than other polymers considered, but its application on existing structures was difficult, eliminating it from consideration. The spray-on polyurea-based polymers were selected for further evaluation as a reinforcement material (Davidson et al. 2004).

Dinan et al. (2003) described the failure mechanisms involved in unreinforced concrete masonry walls reinforced with polymer coatings. AFRL conducted numerous explosive tests on one-way walls coated with polyurea to study composite behavior of wall and polymer. Flexural stiffness due to composite action is a “combination of increased flexural stiffness and the resistance provided by membrane action” (Dinan et al. 2003). For the completely bonded polymer, the bond in shear is much stronger than in tension. Therefore, high strains are experienced by the polymer at mortar joints when the wall opens at joints due to flexure. The front face of the wall fails due to the shear applied by the thrust line associated with the large displacement of wall. This is one of the reasons that the wall failure point is difficult to determine. Also, the polymer may not be uniformly sprayed over the entire surface of the wall. High strains in the polymer will develop due to mortar joint failure or due to polymer debonding. When the polymer is not bonded to the masonry, the strain will be more uniformly distributed over the membrane, and the problem becomes similar to the membrane subjected to uniform pressure (Dinan et al. 2003). “The displacement and strain calculations of such no bending stiffness members are difficult due to complex nature of boundary conditions” (Seide 1977). However an accurate numerical solution was given by Seide (1977) to determine displacement and strain at the center of the membrane when uniform lateral pressure is applied.

## 2.3 Computer Modeling of Concrete Structures

Concrete components such as building columns are vital parts of all structures. Their failure can lead to the complete collapse of the structure. Understanding the response of these structures to blast loads is necessary for improving design

methodology. Furthermore, strengthening these structures is necessary to increase resistance to blast loading.

Crawford et al. (1997b) reported a study on retrofitting reinforced concrete structures to resist blast loads. Buildings designed for gravity loads and blast loads were analyzed. The structural behavior was predicted using DYNA3D. Blast loads were developed using BLASTX (Britt and Lumsden 1994). A specially developed constitutive model was used to capture nonlinear behavior of concrete subjected to blast loading. The material model considered the variation of Poisson's ratio as function of load. Continuum elements were used for column perimeter, beam elements were used for steel reinforcement, and shell elements were used for floor joists and slabs. Fifteen hundred lb and three thousand lb TNT was simulated at 10 ft, 20 ft, and 40 ft standoff for bare columns, steel jacketed columns and fiber reinforced polymer jacketed columns for both cases. Five thousand psi concrete and American Society for Testing and Materials (ASTM) A615 grade steel was used with carbon wrap of 54 ksi strength and 7600 ksi stiffness. Failure of bare columns due to shear at supports was observed. The analyses clearly illustrated that jacketing prevented failure of the columns. Furthermore, increasing the number of wraps increased column stiffness.

Krauthammer and Otani (1997) reported a study of meshing, gravity, and load effects on finite element simulations of blast loaded reinforced concrete structures using DYNA3D. The near-cubical reinforced concrete structure was considered, and symmetry was used to reduce the structure to 1/8th of true size. The model consisted of a back wall, sidewall, and roof. Ten cases were analyzed with increasing reinforcement, load, and gravity effects. All of the cases were analyzed for coarse and fine mesh containing 4995 and 73211 elements, respectively. Reinforcement was modeled according to design drawings. The lumped mass approach was used for reinforcement in the coarse mesh model. A "soil and foam" material model with 8-node solid elements was used for the concrete material, whereas thin shell and beam elements were used to simulate steel reinforcement bars. 300 lb TNT was simulated for the loading. Roof and sidewalls were subjected to peak pressures of 1115 psi, and the back wall was subjected to 2470 psi. Maximum displacements were calculated for various cases. Deformations and stress distributions were analyzed for steel and concrete. Gravity loading affected the time of maximum displacement of the wall and roof and also increased the peak displacement.

Krauthammer and Otani (1997) pointed out that the fine mesh resulted in more displacement than the coarse mesh, but, as the reinforcement was increased, the difference decreased due to enhanced strength provided by the steel. Also, transverse stress showed significant differences in shear and radial reinforcements due to the lumped mass approach used in the coarse meshing. Gravity load initialization was found necessary before load application.

## **2.4 Computer Modeling of Masonry Walls**

General out-of-plane behavior of unreinforced masonry walls can be better understood by considering static loading. Martini (1996a) reported a study in which a finite element model was constructed for one-way out-of-plane failure of unreinforced masonry walls subjected to static loading. This study was conducted as an investigative approach for the two-way action walls. A discrete cracking material model involving 8-node elastic continuum elements were used to model masonry units, and 8-node surface

contact elements were used to model joints. Uniform pressure was applied until the equilibrium of the analysis became unstable. The system was solved using ABAQUS. Load-displacement plots were then compared with the literature to verify the suitability of the model.

In another study, Martini (1996b) developed a two-way unreinforced masonry wall panel supported at sides and bottom. Modified yield line theory was used for unreinforced masonry walls by considering post-cracking mechanisms of moment transfer for horizontal and vertical directions. ABAQUS models of the wall were analyzed. The modified theory predicted lower failure loads than finite element results but closely matched failure patterns.

Crawford et al. (1997a) evaluated the effects of explosive loads on masonry walls using an analytical model developed using DYNA3D. The aim was to estimate responses of lightly reinforced or unreinforced structures subjected to blast load. An analytical wall model having width of a single cell unit that includes two half cells and a web was studied. The analytical model was validated for pressure versus impulse diagrams by comparing with results obtained from field tests conducted in Sweden. Load was applied using blast curves generated by BLASTX. The analytical model was further used to validate and update the P-I curves typically associated with simplified assessment codes such as FACEDAP. Various retrofit techniques were assessed for increasing the strength of unreinforced or lightly reinforced masonry wall. It was found that “retrofit designs that uniformly reinforce a masonry wall, such as composite wrap and shotcrete, were shown to provide a better enhancement to blast protection than those that discretely reinforce a wall, such as pilasters.”

Dennis (1999) reported modeling of masonry walls subjected to blast loads using DYNA3D. Various uncertainties and complications such as strengthening of concrete due to high strain rates and boundary conditions were taken into consideration. A typical masonry unit of 8 in. X 8 in. X 16 in. hollow block that contained 3/8 in. mortar layers was used. A FORTRAN code accepting wall dimensions and expected block meshing was developed for generating the DYNA3D input file. Fidelity was limited to a maximum of five elements through the thickness of the face shell. Mortar joints were modeled using sliding surfaces defined in DYNA3D. Tied surfaces with and without failure criteria were used. Heuristic models were studied to verify the sliding-surface characteristics and material behavior. The “Drucker-Prager” material model was used for CMU blocks. Mortar was modeled with two constitutive conditions. The “Mohr-Coulomb” approach allowed mortar to fail in compression without restricting tension. Another approach, allowed the mortar to fail only in tension. Compressive strength of 2000 psi was assumed for the concrete blocks, and 1800 psi was assumed for mortar. To incorporate strain rate strengthening, a step function was defined, which could double the material strength at prescribed strain rate. To simulate one-way action, the wall was supported only at ends. The wall was gradually loaded with uniform pressure to study static response. Convergence was tested for various combinations of mesh fidelity for web and faces when the wall was subjected to lateral static pressure. However, these tests were carried out with “assumed” values of CMU mechanical properties. Mid-height velocity indicated the onset of instability and determined the static capacity of the wall. The results were then compared with “weak” (1800 psi) and “strong” (2800 psi) CMU. The strong wall failed due to mortar failure; the weak wall failed due to mortar failure

and CMU tensile failure at the supports. Hence it was concluded, “If the fundamental material properties aren’t more precisely known than that given in the published standards, the response is predictable only within a similarly wide uncertainty bound” Dennis (1999). It was concluded that the convergence of the static numerical solution requires at least three elemental divisions in the CMU face shells and webs due to local bending of face shells near the supports. DYNA3D slide surface 9 used in the analyses exhibited anomalous behavior of the mortar by failing only in tension without showing any compression failure. The tensile bond strength model for mortar that permits failure of the mortar only in tension by setting high shear failure criteria results in a more flexible response than the Mohr-Coulomb model, which can allow mortar to fail in tension or shear.

## 2.5 Constitutive Relations for Concrete Material Models

Reinforced and unreinforced concrete behaves differently under various loading conditions. The selection of a proper constitutive model is essential to accurate simulation of concrete under blast loading.

Govindjee et al. (1995) studied Anisotropic Modeling and Numerical Simulation of Brittle Damage in Concrete. The constitutive model formulated is implemented in the MAT\_BRITTLE\_DAMAGE (LS-DYNA material type 96). This three failure surface model covers brittle fracture behavior by introducing damage rules that address continuum and computational issues for anisotropic behavior for a given failure surface. Two fundamental assumptions were made to cover the limited information on micromechanics involved in damage evolution:

- (1) The elastic moduli depends on a set of internal damage variables.
- (2) The principle of maximum (damage) dissipation is applicable, which renders fully anisotropic damage evolution law for elastic moduli tensor that is free from any adjustable parameters once the failure surface is defined.

Based on these assumptions, Govindjee et al. postulated the design of continuum damage models. Computation issues such as numerical integration and strain-rate effects were considered, and alternative implementation of characteristic length is described. A continuum anisotropic damage model for tensile and shear crack development was formulated. Using a set of three different damage surfaces with damage evolution formula, a set of anisotropic evolution laws for the rank four stiffness tensor of the material and a set of softening variables was obtained. These laws were integrated using algorithmic formulations and incorporated in finite element code. Various numerical examples were analyzed and compared to experimental results to evaluate the validity of the model. Eight node brick elements with a standard Galerkin formulation were used in all examples. FEAP (University of California at Berkeley) and NIKE3D (Lawrence Livermore National Laboratory) were used in analyses. Four examples were studied under three-point bending tests. The first example examines the effect of shear surfaces  $\phi_2$  and  $\phi_3$  in plain concrete. The second example analyzed a notched plain concrete beam. The third and fourth example analyzed lightly and heavily reinforced beams.

Schwer (2001) illustrated the determination of parameters for MAT\_PSEUDO\_TENSOR (LS-DYNA material type 16) by the unconfined compression test (UCT) on

concrete cylinders. In a typical triaxial test, a 6 in. diameter and 12 in. height cylinder is subjected to lateral and axial loads, and corresponding displacements are measured. In the UCT, only axial stresses are induced, i.e.,  $\sigma_3 = 0$ . The load at which the specimen fails is called the unconfined compressive strength. Based on this knowledge parameter for a particular concrete, MAT\_PSEUDO\_TENSOR manipulates elastic strength, shear strength, compaction, and failure response. The model can be used in two modes. The first mode uses a pressure dependent yield surface, and the second mode uses two interconnectible yield-pressure functions. The second mode can define simple tensile failure, tensile failure plus plastic strain scaling, and tensile failure plus damage scaling. Strain rate multipliers can be used for concrete and reinforcement.

Linear elastic behavior occurs in cellular concrete subjected to small strain. When large deformations occur, a nonlinear stress-strain relationship occurs due to collapse of cells that consequently develops cohesive strength in concrete. This results in increased finite shear strength with increase in pressure. “*A Simple Constitutive Description of Cellular Concrete*” (Krieg 1972) discusses this concept. Concrete is presented as an elastic-plastic model with implementation details for computer code. The yield or loading surface is composed of a paraboloid-like surface of revolution capped by an ellipsoid of revolution. The stress state transforms from elastic to plastic during a time increment in spherical and deviatoric stresses. Thus, plasticity is contributed by volumetric and deviatoric stresses. The deviatoric plastic strain rate vector is assumed normal to hydrostatic stress in principle stress space. A detailed geometrical description of dependence of deviatoric stress rate on deviatoric strain rate and pressure rate is provided in the paper. Deformation theory is used for calculating pressure, and incremental theory is used for deviatoric stress. It was concluded that the large end of yield surface in cellular concrete is capped with a plane that is normal to hydrostat and moves outward only. MAT\_SOIL \_AND\_FOAM (LS-DYNA material type 5) uses this constitutive model.

MAT\_WINFRITH\_CONCRETE (LS-DYNA material type 84) was developed for finite element analysis of reinforced concrete subjected to impact loading. Broadhouse (1995) presented a report “*The Winfrith Concrete Model in LS-DYNA3D*” describing the execution of the model. The report describes the theory, input parameters, and an example. The Winfrith concrete model is a smeared crack, smeared rebar model applied to an 8-noded single integration point continuum element only. It calculates hydrostatic stresses from pressure-volumetric strain curves provided by the user. Deviatoric stresses are incremented elastically using a rate dependent elastic modulus. These stresses are limited by yield surfaces that expand with increasing hydrostatic stress; its radii are determined by locally rate sensitive compressive and tensile strengths. Tensile failure occurs when maximum principal stress at yield crosses half of the current tensile strength. After tensile failure, decay of tensile strength normal to the crack occurs as the crack propagates. The paper also reports the typical stress-deformation curves for tensile failure. Rate dependent local fracture energy defines the rate of stress decay. Decay in shear modulus results from softening of failed elements due to crack development.

The model also facilitates definition of reinforcement in three orthogonal directions. Rebars are assumed to be perfectly bonded to the surrounding concrete, resulting in complete transfer of strain between concrete and rebar elements. User-

defined stress-strain relationships with strain hardening and failure determine rebar stress. Full debonding between rebar and cracked elements is assumed. Reinforcement can be defined in a specific group of elements or as the ratio of steel to concrete. The report concludes with an example exhibiting finite element analysis of steel cylinder impact on concrete slab. The analysis shows similarity between the development of a 0.5 mm crack in predicted and observed cracks.

## CHAPTER 3. DEVELOPMENT OF FINITE ELEMENT MODELS

### 3.1 Introduction

The finite element model development process involves many steps before the model can be trusted for accurate simulation. A finite element model useable for complex problems is difficult to achieve because it involves many parameters, and a small change in any of the parameters may significantly change results.

Geometry and material property data must be gathered. The unit system is decided, and the geometry is built to represent the dimensions of the structure being simulated. Parameters such as shell thickness, rounded edges, and connections must be considered. Mesh fidelity must be carefully chosen, as there is a tradeoff between computational cost and desired accuracy of results. Proper choice of element formulation depends on integration scheme and expected behavior. Material models are selected and assigned to the elements. Mechanical and physical properties such as density, Poisson's ratio, strain rate effects, and stress-strain behavior, must be included in the material model. The choice of material model largely affects the behavior of the model and interaction between its components. Translation and rotational displacements are controlled by application of boundary conditions to the nodes. Loads must be applied in a desired manner. Development also consists of other issues such as damping, pre-tensioning, and gravity initialization. The interaction between two or more parts can be defined using contact surfaces. Contact surfaces and its parameters such as failure criterion are necessary to define interaction between model components. Control cards and database cards are then included to control the analysis and the results.

This chapter describes the development of finite element models for unreinforced masonry walls that are externally reinforced with a high-elongation polymer and subjected to blast loads. The LS-DYNA finite element solver was used to analyze the models. LS-DYNA is distributed by LSTC and is a commercial version of DYNA3D developed by Lawrence Livermore National Laboratory. LS-DYNA is an advanced general-purpose nonlinear finite element program capable of simulating complex real world problems. Though developed for explicit dynamic analysis, problems can be analyzed with implicit solutions within the single code environment. The single code environment enables the solution of multi-physics problems in one run. LS-DYNA supports network computing and MPP on Unix environments.

Finite Element Model Builder (FEMB) developed by Engineering Technology Associates, Inc. (ETA) was used as the preprocessor to develop models and generate input files for the LS-DYNA solver. LS-POST by LSTC was used for post-processing the results generated by the solver.

### 3.2 Unit System

The U.S. customary unit system was used for all analyses. Table 1 gives the measurement units used.

### 3.3 Loads

Three loads having various charge-standoff combinations were used. While charge size and standoff distances associated with Load I and Load II were used in field tests conducted by AFRL, Load III was not used in field tests but was chosen to represent a higher load condition. The time histories, peak pressures, and impulses of the three loads are given below.

(1) Load I: peak pressure = 66.3 psi, impulse = 214.8 psi-msec, load time history is shown in Fig. 1.

(2) Load II: peak pressure = 44.5 psi, impulse = 220.6 psi-msec, load time history is shown in Fig. 2.

(3) Load III: peak pressure = 129.9 psi, impulse = 356.8 psi-msec, load time history is shown in Fig. 3.

**TABLE 1. Unit System Used**

<b>Property</b>	<b>Measurement unit</b>
Mass	lbf-s <sup>2</sup> /in.
Length	in.
Time	sec
Velocity	in./sec
Force	lbf
Stress	psi
Energy	lbf-in.

### 3.4 Geometry and Materials

The masonry wall structures involved in the explosive tests conducted by AFRL had six key components that had to be accurately included in the model development: the CMU, mortar joint interfaces, polymer reinforcement (material behavior and interface with masonry), and roof and floor boundaries. A typical test wall is shown in Fig. 4. The system was subjected to impulse loading described in Section 3.3. There is a rapid variation of stresses and strains in the wall components. To effectively capture these phenomena, selection of appropriate material models is critical.

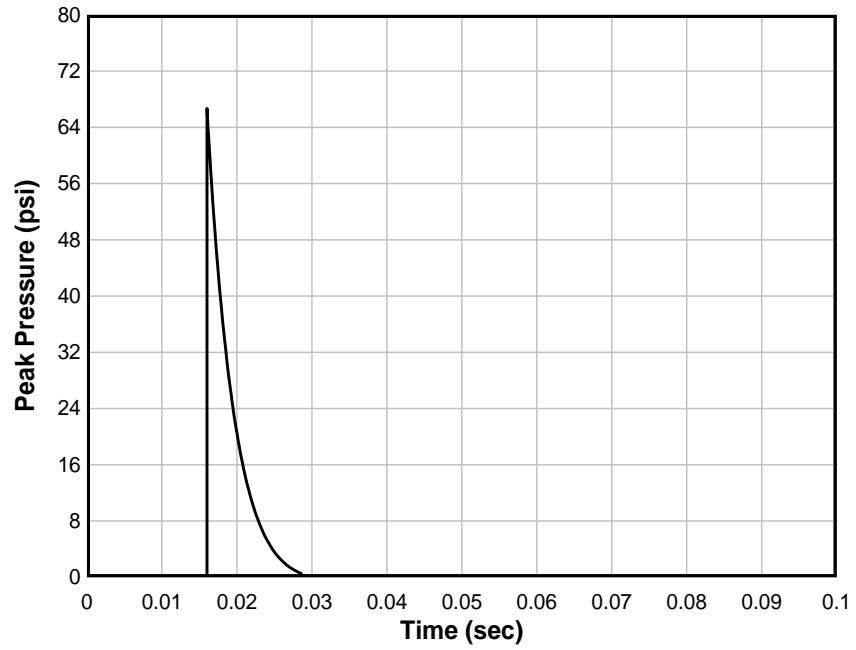


**FIG. 1. Load Time History for Load I**

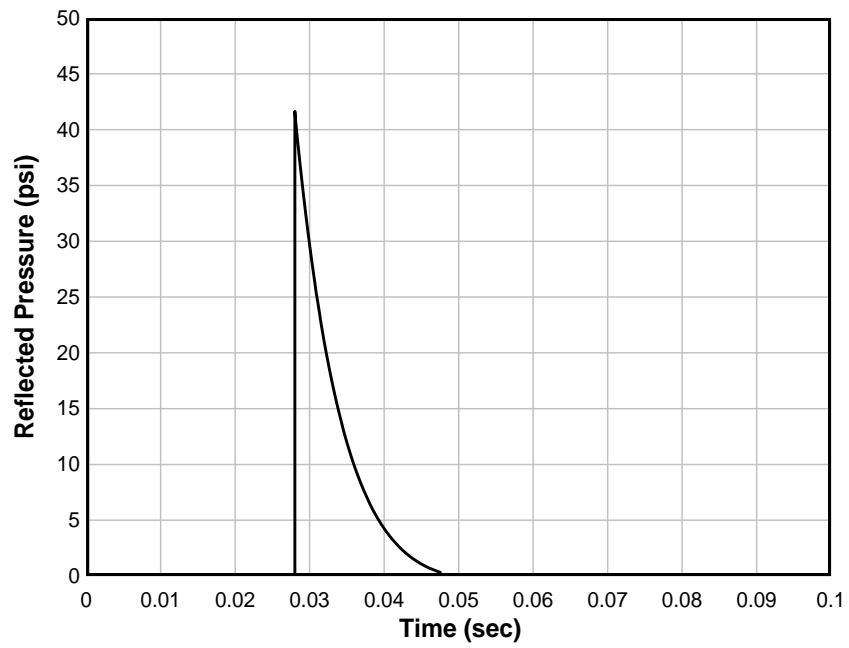


**FIG. 2. Load Time History for Load II**

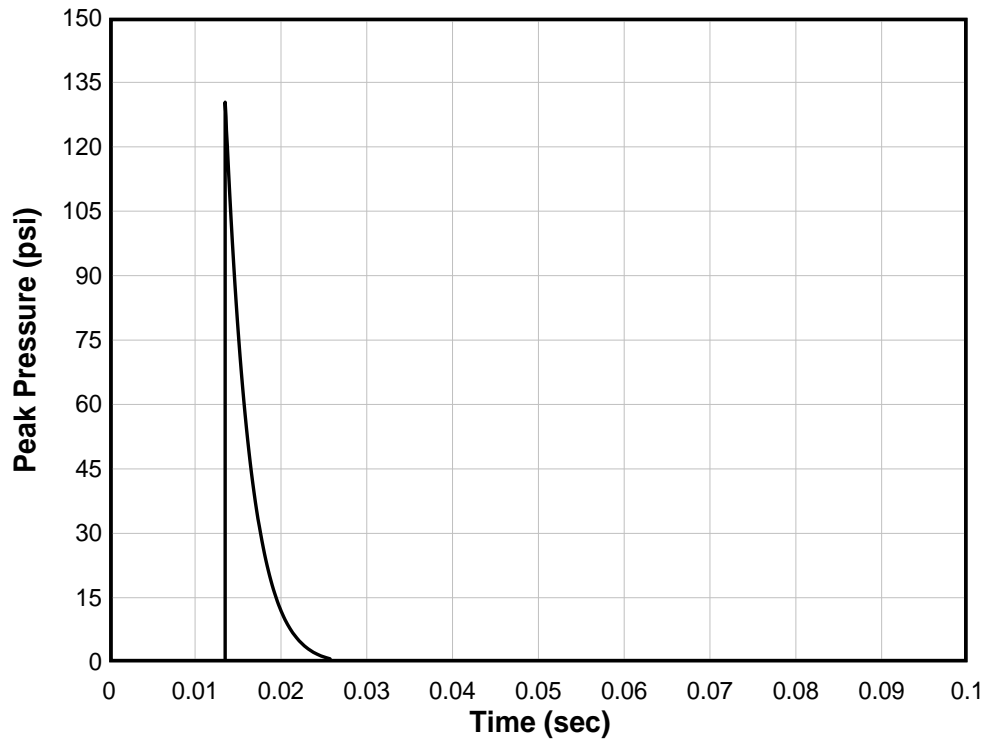


**FIG. 3. Load Time History for Load III**



**FIG. 4. Test Wall Setup**

### **3.4.1 Wall**

The wall setup is shown in Fig. 5. Unreinforced masonry walls measuring 7 ft 4 in. width and 12 ft height were simulated. The density of masonry concrete is approximately 0.07 lb/in.<sup>3</sup>, which results in a weight of each block of approximately 32 lb. The walls were constructed in reusable reaction structures. 3 in. X 4 in. X 0.25 in. steel angles were placed at top and bottom of the test wall to restrain lateral movement (Thornburg 2004).

### **3.4.2 Concrete Masonry Unit (CMU)**

The typical CMUs used in the tests were standard hollow concrete blocks weighing 32 lb. The dimensions of the block were 7.625 in. X 7.625 in. X 15.625 in. The outer edges of the block were 1.25 in. thick, and the center web was 1 in. thick. The blocks have a nominal compressive strength of 2000 psi. Mortar joints of approximately 3/8 in. thickness with type-N mortar separated the blocks (Connell 2002).

### **3.4.3 Polymer Reinforcement**

The spray-on polymer used for reinforcement was primarily comprised of polyurea. Table 2 provides key mechanical characteristics of the material considered (Davidson et. al 2004).

The stress-strain curve obtained from static uniaxial tension tests conducted by AFRL is shown in Fig. 7, where it can be noted that the material exhibited a discernable yield point and has an elongation capacity of approximately 80% (Knox et. al 2000).

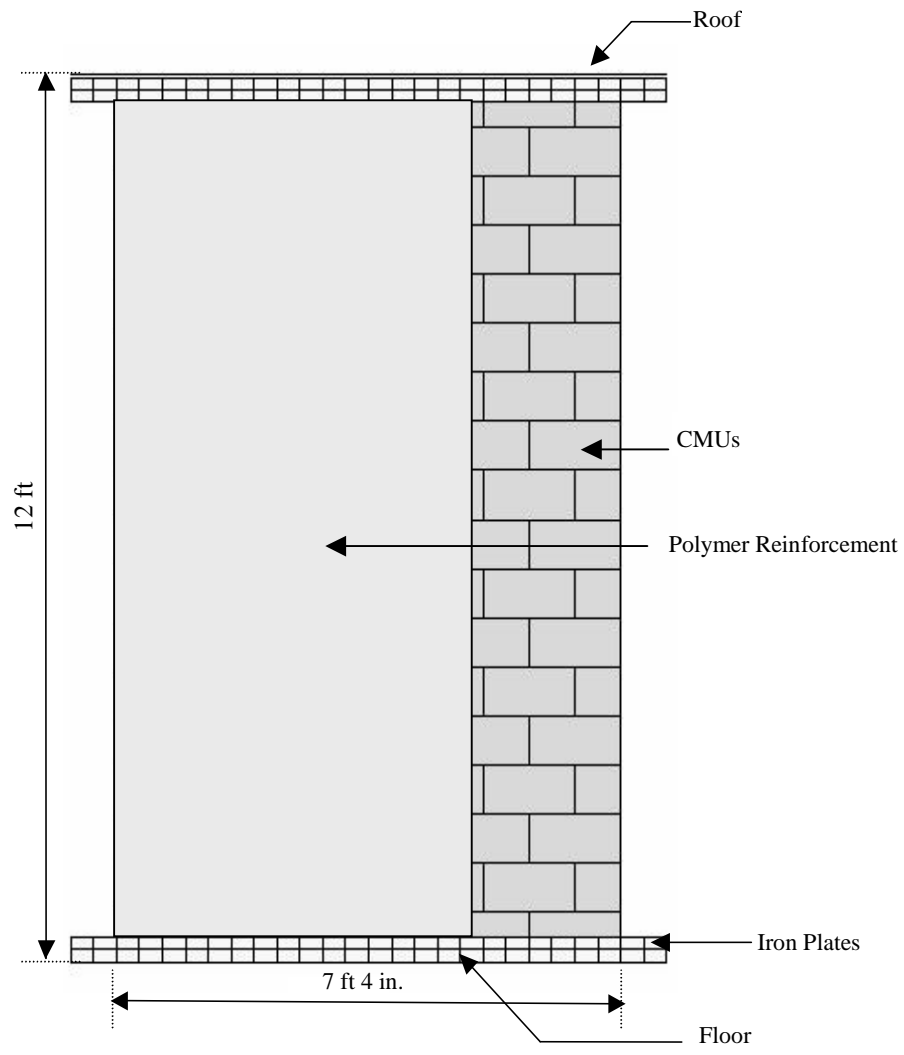


**FIG. 5. Schematic of Wall Setup**

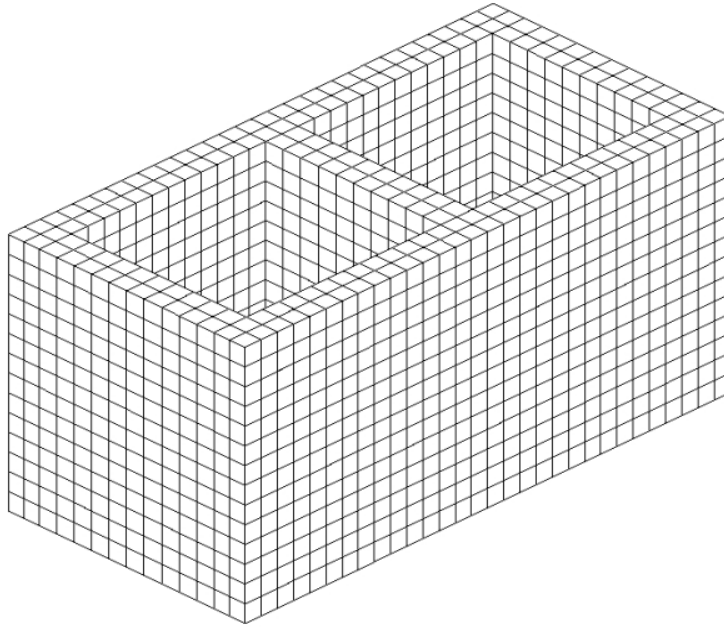


**FIG. 6. Typical Concrete Masonry Block Meshing**

**TABLE 2. Properties of Polyurea**

<b>Property</b>	<b>Value</b>
Modulus of Elasticity	34000 psi
Tangent Modulus	3400 psi
Elongation at Rupture	89%
Stress at Rupture	2011 psi
Maximum Tensile Strength	2039 psi
Density	90 lb/ft <sup>3</sup>
Poisson's Ratio	0.4
Shear Modulus	11620 psi

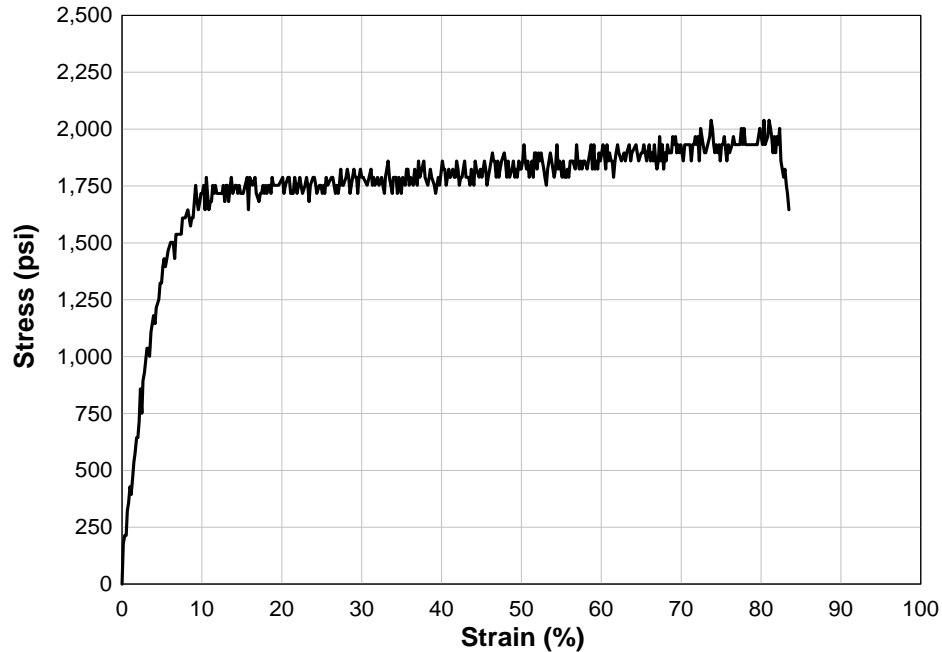


**FIG. 7. Static Stress-Strain Curve for the Spray-On Polymer considered in Air Force Research Laboratory Explosive Tests**

### 3.5 Material Models

#### 3.5.1 Concrete Masonry Units

Blast tests on individual CMU were conducted by AFRL for various standoffs. Fracture and modes of failure were studied, and a report comparing material models for CMU was presented by Moradi (2003). Moradi conducted finite element analyses on CMU subjected to blast loading and compared the results to field tests. The following material models were evaluated for simulating the CMU: (1) MAT\_SOIL\_AND\_FOAM (LS-DYNA material #5), (2) MAT\_BRITTLE\_DAMAGE (LS-DYNA material #96), (3) MAT\_PSEUDO\_TENSOR (LS-DYNA material #16), and (4) MAT\_WINFRITH\_CONCRETE (LS-DYNA material #83).

It was concluded that the MAT\_SOIL\_AND\_FOAM material best simulated the behavior of the CMUs under blast load and therefore was recommended for the analytical investigations of blast effects on CMU walls. Material failure is determined by pressure cutoff (PC) for tensile fracture. When the stresses in an element exceed PC, the pressure is set to the cutoff value, and stresses cease to increase. The following properties and parameters recommended by Moradi (2003) were used in the present work: (1) density = 0.00017972 lbm/in.<sup>3</sup> (120 lb/ft<sup>3</sup>), (2) Poisson's ratio = 0.15, (3) compressive strength = 2000 psi, (4) tensile strength = 200 psi, (5) shear limit = 100 psi, (6) fracture toughness = 0.8 lbs/in., (7) shear retention = 0.03, and (8) viscosity = 104 psi/sec.

A single masonry unit width wall model of 12 ft height was developed using 18 CMUs separated by mortar layers. The wall was reinforced by polymer on one side. Rigid boundaries restrained lateral wall translations at the top and bottom. The CMU

block had two elements through its thickness as shown in Fig. 8. Three-eighth inch thick mortar joints were simulated between the blocks. One mortar layer thickness separated the roof boundary from the top-most block. Load I was applied to the front face of the wall.

Fig. 9 shows the center displacement of the single unit width of wall using various material models for CMU along with displacement data from the gauge fixed at the center of a wall during one of the full-scale explosive tests conducted by AFRL at Tyndall Air Force Base (Thornburg 2004). The plot demonstrates that MAT\_SOIL\_AND\_FOAM best correlates with test data obtained from one of the field tests.

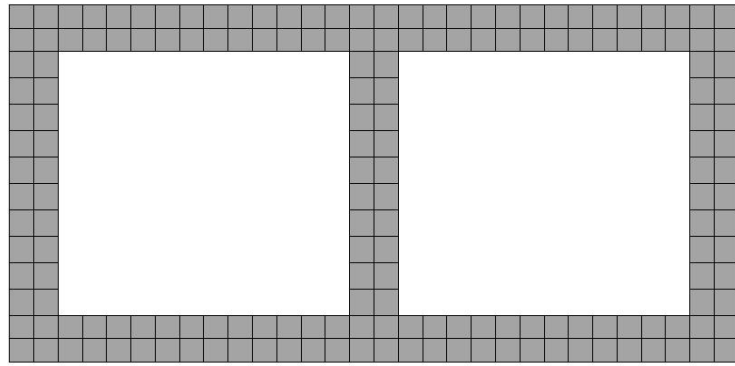


**FIG. 8. Mesh Fidelity for Concrete Masonry Unit**

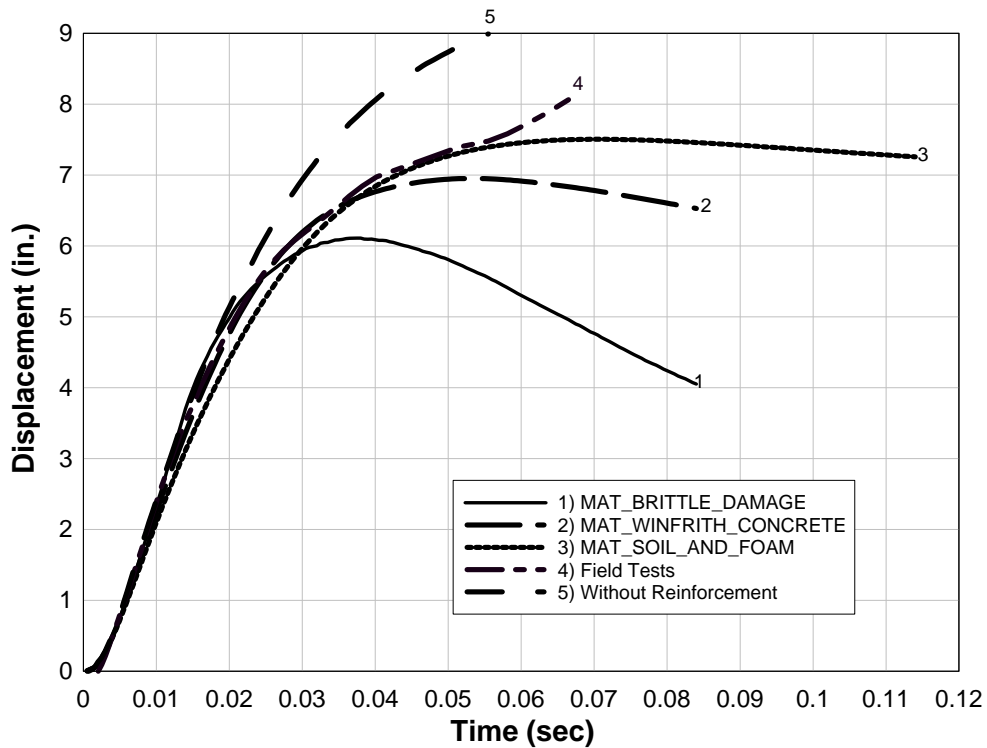


**FIG. 9. Displacement Time History at Mid-Height of Single Unit Width Model**

However, other observations were also made regarding strain energy in the polymer elements when various material models were used for concrete. Use of MAT\_BRITTLE\_DAMAGE for concrete elements resulted in lesser wall displacement, and 1580 lbf-in. strain energy was noted in the polymer. This indicated that more blast energy is transferred from the blocks to the polymer in contrast to MAT\_SOIL\_AND\_FOAM, which exhibited 625 lbf-in. strain energy. Use of MAT\_WINFRITH\_CONCRETE for CMUs developed 960 lbf-in. strain energy in the polymer. Fig. 10 shows strain energy in the polymer for various material models used for concrete blocks. This difference is significant and may reflect a need for additional investigation to determine the concrete material model for the CMU that results in an appropriate distribution of energy into the polymer reinforcement.

### 3.5.2 Polymer

LS-DYNA-970 has approximately 200 material models for simulating a wide range of material behaviors. The following criteria were used to determine the best material model for simulating the polymer reinforcement:

- (1) The model should have an appropriate failure criterion that will simulate rupture.
- (2) The model must be applicable to plastic and/or elastomer behavior.
- (3) The material model must have the ability to be modeled with shell elements.
- (4) Since high strain rates can occur in systems subjected to blast loading, the material model must have the ability to incorporate strain rate effects.

The constitutive model was selected for preliminary evaluation if it met two or more of the above conditions. Table 3 provides the list material models considered.

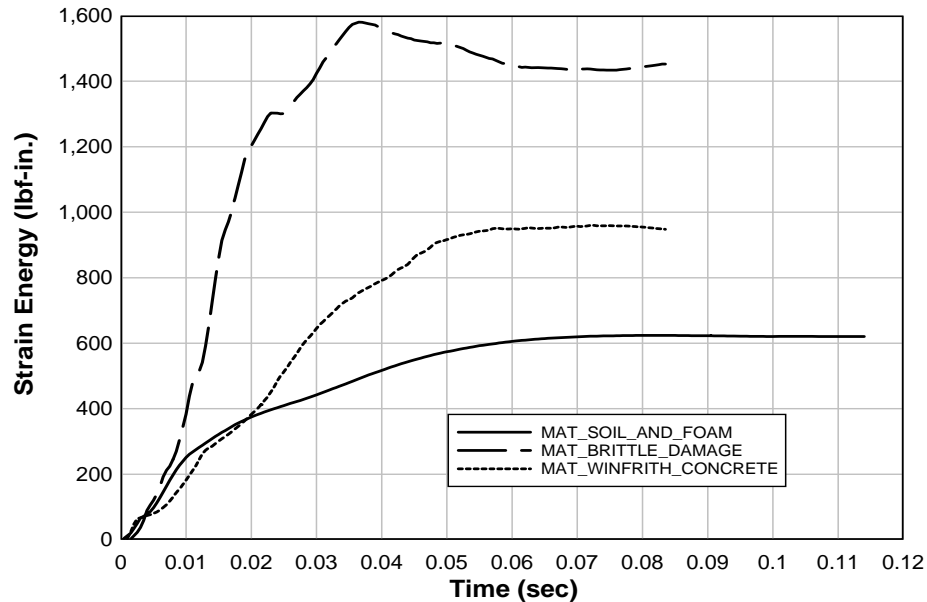


**FIG. 10. Strain Energy in Polymer for Various Material Models for Concrete Masonry Unit**

The following materials were accepted for further consideration:

(1) MAT\_PLASTIC\_KINEMATIC (Mat #3): This computationally cost effective model is available for shells and solids. It is used to model isotropic materials having kinematic hardening plasticity. Including plastic strain can provoke failure, whereas including viscoplastic formulation induces the strain rate effects by Cowper and Symonds constants (C and P).

(2) MAT\_BLAZ-KO\_RUBBER (Mat #7): This material is used to model incompressible rubber and has a fixed Poisson's ratio of 0.463. Density and shear modulus are the only parameters required for this card.

(3) MAT\_PIECEWISE\_LINEAR\_PLASTICITY (Mat #24): This model is used to simulate elasto-plastic behavior in which failure can be defined with a rupture strain. The stress-strain curve can be incorporated by defining yield point and tangent modulus or by defining eight plastic strain points and corresponding eight stress points. Strain rate effects can be included in one of following ways: by defining Cowper and Symonds constants (C and P) which scales the yield stress by factor of

$$I + \left( \frac{\zeta}{C} \right)^{\frac{1}{P}} \quad (4)$$

where  $\zeta$  = strain rate, by defining a load curve that includes a load factor scale (to scale yield stress) versus strain rate, or by defining a table of stress versus plastic strain curve for various strain rates.

(4) MAT\_OGDEN-RUBBER (Mat #77): This viscoelastic model is used to simulate rubber. Uniaxial or biaxial test data such as specimen gauge length, width, and thickness are required along with a load curve of force versus actual change in gauge length. Also, a stress relaxation function with respect to time is required for viscoelastic behavior.

(5) MAT\_PLASTICITY\_POLYMER (Mat #89): This is an elasto-plastic model used when elastic and plastic regions are not distinguishable. Stress-strain and strain-rate effect definitions are included in this model. Failure strains can be defined as a function of strain rate. This is particularly useful for materials that change state from ductile to leathery and from leathery to brittle with strain rate. This model can only be applied to shell elements.

(6) MAT\_FINITE\_ELASTIC\_STRAIN\_PLASTICITY (Mat #112): This elasto-plastic material model uses a finite strain formulation for the elastic region of the stress-strain curve. The finite strain formulation develops large elastic strains before yielding takes place. Also, strain-rate dependency can be defined using Cowper and Symonds constants (C and P) or by defining strain rate scaling effects on yield stress. However, this model can only be applied to solid elements.

(7) MAT\_RATE\_SENSITIVE\_POLYMER (Mat #141): This is a model for isotropic ductile polymer with strain rate effects and requires uniaxial test data. It takes into consideration initial hardness and maximum internal stress in the material to calculate elastic strain in the polymer.

**TABLE 3. Shortlisted Constitutive Models for Retrofitted Polymers**

<b>Mat #</b>	<b>Name</b>	<b>Accepted /rejected</b>	<b>Reason</b>
3	MAT_PLASTIC_KINEMATIC	Accepted	
6	MAT_LINEAR_VISCOELASTIC	Rejected	Long and short term shear modulus required
7	MAT_BLATZ-KO_RUBBER	Accepted	
17	MAT_ORIENTED_CRACK	Rejected	Equation of state required
18	MAT_POWER_LAW_PLASTICITY	Rejected	Unknown hardening exponent and strength coefficient
19	MAT_STRAIN_RATE_DEPENDENT_PLASTICITY	Rejected	Requires definition of yield stress as function of effective strain rate
24	MAT_PIECEWISE_LINEAR_PLASTICITY	Accepted	
38	MAT_BLATZ-KO_FOAM	Rejected	Poisson's ratio fixed at 0.25
77	MAT_OGDEN_RUBBER	Accepted	
81	MAT_PLASTICITY_WITH_DAMAGE	Accepted	
89	MAT_PLASTICITY_POLYMER	Accepted	
112	MAT_FINITE_ELASTIC_STRAIN_PLASTICITY	Accepted	
141	MAT_RATE_SENSITIVE_POLYMER	Accepted	

LS-DYNA material #24, MAT\_PIECEWISE\_LINEAR\_PLASTICITY, was selected for simulating the polymer reinforcement because rupture strain can be defined and the stress-strain relationships for various strain rates can be characterized. The strain rate dependent properties were obtained from the report submitted to AFRL by the Structural Test Group at University of Dayton Research Institute (Hill 2003). Fig. 11 shows strain rate dependent true stress versus true strain plots that were used in the models.

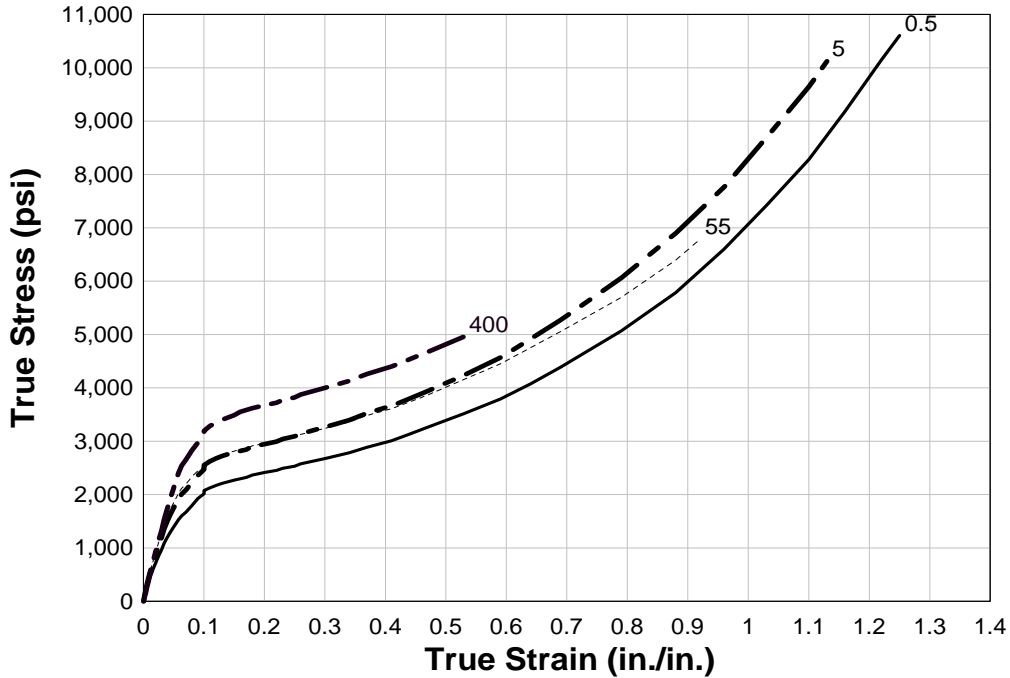


**FIG. 11. True Stress - True Strain Curve for Polyurea at Various Strain Rates**

Mat #24 requires true stress versus effective plastic strain at various strain rates. Effective plastic strain was calculated as follows (LS-DYNA Theoretical User's Manual 1998):

$$EPS = \varepsilon_{TT} - \frac{\sigma_T}{E} \quad (5)$$

where EPS = effective plastic strain,  $\varepsilon_{TT}$  = total true strain,  $\sigma_T$  = true stress, and  $E$  = elastic modulus.

The strain rate data were incorporated using the \*DEFINE\_TABLE card of LS-DYNA that facilitates definition of multiple curves. Failure was defined by 80% failure strain, and yield stress was used to scale strain rate effects. The Mat #24 card used in the analysis is given on following page.

### 3.5.3 Roof and Floor Boundaries

LS-DYNA Mat #5 MAT\_RIGID and properties of steel were used to simulate the rigid boundaries. The following card was used for the analysis.

```
*MAT_RIGID
$^M-20
$      MID      RO      E      PR      N      COUPLE      M      ALIAS
      2  0.000733  3.000E+07  0.30      0.0      0.0      0.0
$      CMO      CON1      CON2
      1.0      7.0      7.0
$LCO_OR_A1      A2      A3      V1      V2      V3
      0.0      0.0      0.0      0.0      0.0      0.0
```

### 3.6 Element Selection

LS-DYNA provides several element formulation options for shells and solids. Solid elements were used for the CMU blocks and are included in the \*SECTION\_SOLID card. Low fidelity heuristic models were used to analyze various element formulations. Initially, fully integrated elements (ELFORM=2) were used so that hourglassing would be eliminated. However, with this formulation, high computation costs resulted for hi-fidelity models. With the MAT\_SOIL\_AND\_FOAM model, negative volume errors occurred during large deformations. Also, full integration did not improve model correlation to experimental data. For most models, the constant stress solid elements (ELFORM=1) were used, which is the default formulation in LS-DYNA.

Since the polymer thickness is small (0.125 in.) compared to other dimensions, shell elements were used (\*SECTION\_SHELL). The Belytschko-Tsay element formulation (ELFORM = 2) was initially used. However, this formulation exhibited excessive hourglassing modes for large deflection. Therefore, fully integrated element formulation (ELFORM = 16) shells were used to ensure proper distribution of stresses, failure, and visualization.

```
*MAT_PIECEWISE_LINEAR_PLASTICITY
$      MID      RO      E      PR      SIGY      ETAN      FAIL      TDEL
      24  0.000135  34000.0  0.40  1400.0  3400.0  0.8  0.0
$      C      P      LCSS      LCSR      VP
      0.0      0.0      10001      0      0.0
$      EPS1      EPS2      EPS3      EPS4      EPS5      EPS6      EPS7      EPS8
      0.0      0.0      0.0      0.0      0.0      0.0      0.0      0.0
$      ES1      ES2      ES3      ES4      ES5      ES6      ES7      ES8
      0.0      0.0      0.0      0.0      0.0      0.0      0.0      0.0
$-----1-----2-----3-----4-----5-----6-----7-----8
$
$              TABLE FOR STRAIN RATE CURVES
$
$-----1-----2-----3-----4-----5-----6-----7-----8
*DEFINE_TABLE
$      TBID
      10001
$      VALUE
      0.5
$      VALUE
      5.0
$      VALUE
      55.0
$      VALUE
      400.0
*DEFINE_CURVE
$^FOR 0.5 /SEC (MEASURED STRESS-STRAIN)
$      LCID      SIDR      SFA      SFO      OFFA      OFFO      DAT TYP
```

```

1001      0      1.0      1.0      0.0      0.0      0
$          A1          O1
0.000,0
0.002,100
0.004,191
.
.
.
1.10,8280
1.16,9184
1.22,10146
1.25,10605
*DEFINE_CURVE
$^FOR 5.0 (MEASURED STRESS-STRAIN)
$  LCID      SIDR      SFA      SFO      OFFA      OFFO      DATYTP
   1002      0        1.0      1.0      0.0      0.0      0
$          A1          O1
0.000,0
0.002,124
0.004,235
.
.
.
1.10,9645
1.13,10122
*DEFINE_CURVE
$^FOR 55.0 (MEASURED STRESS-STRAIN)
$  LCID      SIDR      SFA      SFO      OFFA      OFFO      DATYTP
   1003      0        1.0      1.0      0.0      0.0      0
$          A1          O1
0.000,0
0.002,118
.
.
.
0.88,6396
0.92,6785
*DEFINE_CURVE
$^FOR 400.0 (MEASURED STRESS-STRAIN)
$  LCID      SIDR      SFA      SFO      OFFA      OFFO      DATYTP
   1004      0        1.0      1.0      0.0      0.0      0
$          A1          O1
0.000,0
0.002,90
0.004,183
.
.
.
0.47,4675
0.53,4962
$-----1-----2-----3-----4-----5-----6-----7-----8

```

Solid elements were also considered for the polymer. However, to provide for an appropriate aspect ratio, the mesh fidelity had to be substantially increased, which increased the computation time and storage requirements. Furthermore, the contact surface definitions became difficult with thin solid elements. Therefore solid elements were not used to simulate the polymer coating.

Solid elements modeled as rigid were used to define the roof and floor boundaries. Shell elements could also be used for these parts, but with increased complications in geometry construction and contact definitions.

### 3.7 Contact Surfaces

Contact surfaces are a vital part of simulations involving large displacements and fracture. Various interactions between parts, such as penetration, friction, and separation were simulated using contact surfaces. The choice of contact type depends on the interaction behavior between components.

LS-DYNA identifies contact by checking for potential penetration of slave set through a master set. Penetration algorithms perform this check at each time step. The contacts can be “offset” based or “non-offset” based. Offset based contacts involve the thickness of shells involved in contact definition. Geometry can be set up to include the thickness involved in contact definition. The inclusion of the shell thickness is controlled by the parameter SHLTHK in the \*CONTROL\_CONTACT card or in the \*CONTACT card. The \*CONTROL\_CONTACT card is used to define parameters applied globally for all contacts, and \*CONTACT defines parameters confined to a particular contact. The definition of parameters in the \*CONTACT card overwrites the parameters defined in \*CONTROL card. Contact thickness is also involved in the contact definition and can be specified directly by the user using optional parameters in the contact definition. Default contact thickness is equal to the shell thickness.

#### 3.7.1 Selection of Contact Surface

The polymer coating was modeled using shell elements. The parts representing the polymer contact the elements representing the masonry blocks. Therefore, shell thickness is included in the analysis by setting the THKOPT to 1. The elements representing the roof and floor boundaries are rigid. Therefore, SHLTHK was set to 2 in these contacts. When SHLTHK is set to 2, it is important to orient the contact segment normals toward the contacting surface based on right-hand-rule.

When the thickness of shell segments is considered in the geometry, SHLTHK can be set to zero. For such cases AUTOMATIC type of contacts should be used. These contact types consider shell thickness offsets. AUTOMATIC contacts do not have an orientation requirement, making them more robust than the corresponding non-automatic option. This is particularly useful when the master and slave segments have meshes of different densities. The adjacent segments do not follow the right hand rule in this case. Moreover, AUTOMATIC contact types detect penetration from both sides of shell elements. Considering these factors, CONTACT\_AUTOMATIC\_SURFACE\_TO\_SURFACE type contacts were used to define the contact between the roof and floor boundary elements.

Failure between the segments was based on forces or stresses along the normal and shear directions. \*CONTACT\_TIEBREAK\_SURFACE\_TO\_SURFACE was used for the tie-breaks. The orientations of the segments determine the tensile and compression direction. Considering these constraints, \*CONTACT\_TIEBREAK\_SURFACE\_TO\_SURFACE contacts were initially used for defining block-mortar layer contact and block-polymer contact. However, the MPP version of LS-DYNA does not support this contact type. \*CONTACT\_TIEBREAK\_NODES\_TO\_SURFACE contact was therefore used for the runs made on multiple processors. In this type of contact, one set is the node set and the other is the segment set. However, this failure criterion does not differentiate tension failure from compression failure (Dennis 1999).

### 3.7.2 Parameters Involved in Contact Definitions

Contacts with failure normal (tensile) failure force and shear failure force define failure by the following relationship:

$$\left(\frac{|f_n|}{NFLS}\right)^2 + \left(\frac{|f_s|}{SFLS}\right)^2 \geq 1 \quad (6)$$

Failure takes place when the left side of Equation 5 is larger than 1. Once failure has occurred, there is no normal or shear resistance at the interfaces, and the contact behaves as SURFACE\_TO\_SURFACE or NODES\_TO\_SURFACE contact.

Friction in LS-DYNA is defined by Coulomb's formulation. This formulation considers the relative velocity between the surfaces involved in the contact. Static (FS) and dynamic (FD) friction values are required. Coulomb's law defines the frictional coefficient as

$$\mu = FD + (FS - FD) e^{-DC} |V_{rel}| \quad (7)$$

where  $V_{rel}$  = relative velocity between surfaces,  $DC$  = decay coefficient,  $FS$  = static friction, and  $FD$  = dynamic friction.  $FS$  must be greater than  $FD$ , and the decay coefficient must be greater than zero to differentiate between two friction types (Bala 2001). However, for tiebreak type contacts, friction is not considered until the mortar joint interface fails by the criteria discussed above. After failure, the friction forces govern the contacts between surfaces. The value of decay coefficient was set to 1. The default values of the other parameters were used.

### 3.8 Dynamic Relaxation

Dynamic relaxation is a method of performing quasi-static analysis in an explicit integration based code. Dynamic relaxation increases damping by using a vector iteration method to minimize kinetic energy until it approaches zero. Geometric nonlinear problems are solved by equating it to a dynamic problem. Non-equilibrium (residual) forces exist in a dynamic behavior at each node.

Dynamic relaxation was used to incorporate gravity preload stresses prior to the application of the dynamic load simulating blast. A small amount of damping was included so that the velocities and hence kinetic energy approach zero before external load is applied on the structure. This is achieved by modifying velocities at the end of each timestep:

$$V_{new} = (Dynamic\ Relaxation\ Factor) \times V_{previous} \quad (8)$$

Nonlinear analyses require a lower dynamic relaxation factor (DRFCTR). When dynamic relaxation is used for damping, DRFCTR is calculated from the damping coefficient. The dynamic relaxation calculation involves the following steps:

$$Residual\ Force = Sum\ of\ Internal\ Forces - Applied\ Load\ at\ Each\ Node$$

$$R(i) = M \cdot \frac{d^2 y}{dt^2} + D \cdot \frac{dy}{dt} \quad (9)$$

To solve for equilibrium, (1) solve for member forces at each node using

$$F(i) = (dL \times A \times E)/L \quad (10)$$

(2) solve for residual forces geometrically and find velocity based on dynamic behavior, (3) find new position based on time increment (distance = velocity\*time), and (4) reiterate until residual forces approach zero.

DRFCTR must be less than one. A value of 1 for DRFCTR results in a completely undamped system. As this factor is decreased from one, damping increases and hence the kinetic energy decreases while the internal energy remains the same. DRFCTR determines the rate at which the system is stabilized. Runs were made from 0.9 to 1, but convergence was not reached. It was concluded that higher values of DRFCTR damp the system at slower rates and the analysis requires excessive computation and clock time to reach convergence. Therefore, to achieve faster convergence, a value of 0.10 was used for DRFCTR.

The gravity load was applied to the structure using \*LOAD\_BODY\_Z card. Two load curves induced the load. One gravity load curve was defined to load the structure for the entire life cycle, and another curve loaded the structure only during the dynamic relaxation phase. Twenty msec were allocated for convergence, so the blast time was delayed by setting time of blast (TBO) = 0.020 in the \*LOAD\_BLAZT card. The cards on the following were used for stress initialization.

### 3.8.1 Interface Reaction Force Calculation

The effect of dynamic relaxation was verified from the reaction forces produced at the interface layers. Reaction forces were included in the results by RCFORC database file of the LS-DYNA output. In a given contact surface, the forces at master and slave interfaces are counteractive. The vertical force at a particular interface is the weight of the blocks above that interface. For example, the vertical thrust at interface #1 between the second block from bottom and mortar layer below it can be calculated as follows. The effective size of block including one mortar joint is 16 in. X 8 in. X 8 in. Volume of block,  $V = 16 \times 8 \times 8 - 2 \times (6.4 \times 6 \times 8) = 409.6 \text{ in.}^3$ . Mass density of material used in the analysis = 0.0001797 lbm/in.<sup>3</sup>. Weight of 1 block = 0.0001797 x 409.6 x 386.1 = 28.41 lb. Weight of 17 blocks = 17 x 28.41 = 483 lb.

The reaction at interface #1 is shown in Fig. 12. It can be noted that the reaction force stabilized at approximately 480 lb before the impulse load was applied to the wall. However, the vertical stresses in the block elements showed dynamic oscillations during the gravity initialization period. Additional work may be required to achieve a better simulation of gravity preload.

```
*CONTROL_DYNAMIC_RELAXATION
$  NRCYCK      DRTOL      DRFCTR      DRTERM      TSSFDR      IRELAL      EDTTL      IDRFLG
      250      0.0001      0.1000      0.0          0.0          0          0.040      -1
*DEFINE_CURVE
$^GRAVITY
$  LCID      SIDR      SFA      SFO      OFFA      OFFO      DATTPP
```

```

100      0      1.0      1.0      0.0      0.0      0
$        A1      O1
          0.0      386.4
          0.150     386.4
*DEFINE_CURVE
$^DYNAMIC_RELAXATION
$      LCID      SIDR      SFA      SFO      OFFA      OFFO      DATTP
200      1      1.0      1.0      0.0      0.0      0
$        A1      O1
          0.0      0.0
          0.008     386.4
          0.150     386.4
*DATABASE_BINARY_D3DRLF
$ DT/CYCL
20
*LOAD_BODY_Z
$      LCID      SF      LCIDDR      XC      YC      ZC
100      1.0      200      0.0      0.0      0.0

```

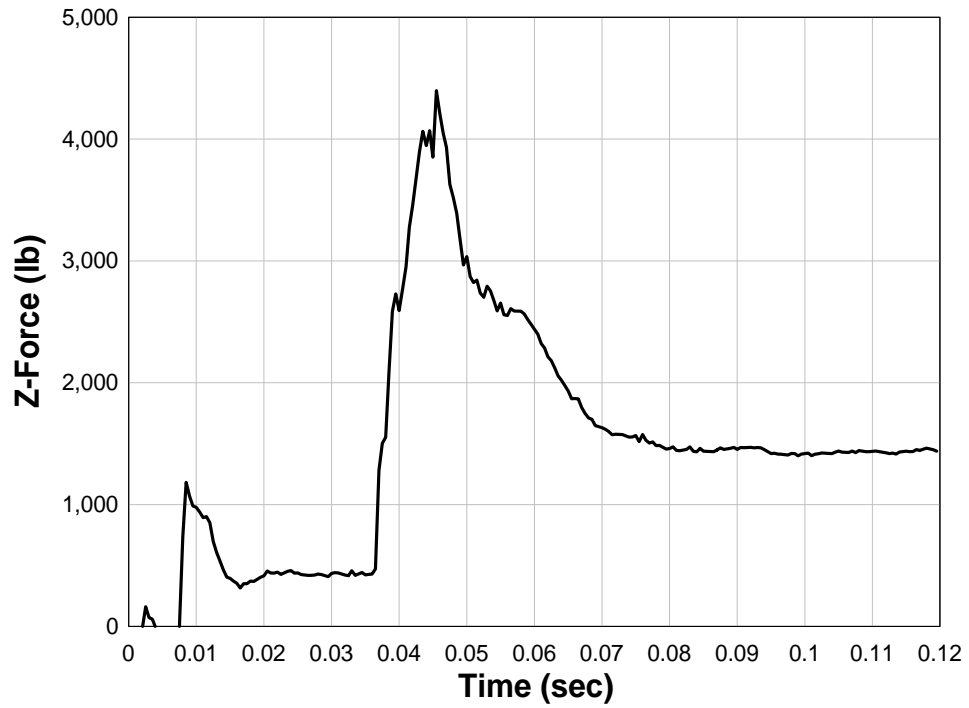


**FIG. 12. Reaction Time History for Interface #1**

### 3.8.2 Effect of Variation in Preload

Lateral displacements of two models, one with gravity load and the other without gravity load, are shown in Fig. 13. It can be noted that the gravity preload did not affect the lateral displacement of the wall. It is worth noting that the normal compressive stress in the height-wise direction at the bottom of the wall would vary from zero at the top to 9.7 psi at the bottom of the wall. Also, the relative timing is important. The wall reaches a maximum lateral deflection in approximately 30 msec, whereas a mass dropped from mid-height would take approximately 600 msec to reach a floor level (Equation 11).

$$T = \sqrt{\frac{2 \cdot h}{g}} = \sqrt{\frac{2 \cdot 72}{386.4}} = 0.61 \text{ sec} \quad (11)$$

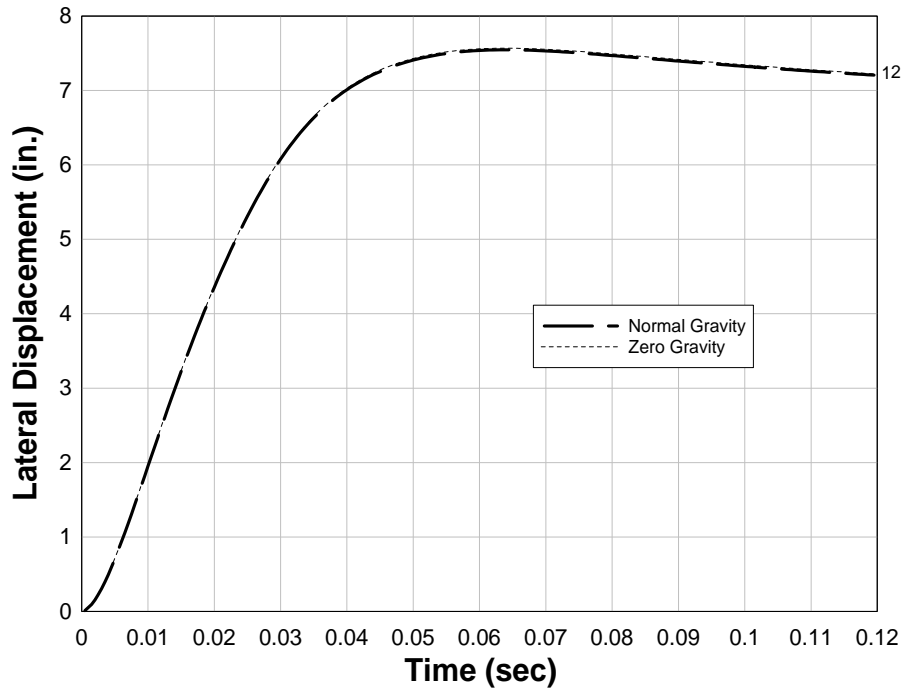


**FIG. 13. Displacement Time History at Center of Wall for Varying Gravity Load**

### 3.9 Damping

Damping is an important parameter for all structural systems subjected to dynamic loads. In LS-DYNA, damping can be applied locally to a specific part or globally to the entire structure.

### 3.9.1 Eigenvalue Extraction

Damping of the wall was calculated on a single unit width model by extracting the eigenvalues of the model and studying the mode shapes obtained. The contact surfaces were eliminated, and the nodes were merged for parts in contact to get an integrated system. Implicit eigenvalue analysis (\*CONTROL\_IMPLICIT\_EIGENVALUE card in LS-DYNA) of the single unit width model was carried out to determine the natural frequencies of the structure. The extracted 20 natural frequencies are listed in Table 4.

### 3.9.2 Calculation of Damping Coefficient

The seventh mode is a bending mode with frequency of 465.8 rad/sec. The damping ratio for this frequency is calculated as follows (LS-DYNA Theoretical User's Manual 1998):

$$C_{cr} = 2 \omega \quad (12)$$

Assuming 5% critical damping value (Melis 2002), damping ratio,  $\beta = C/C_{cr}$ ; Taking  $\beta = 5\%$ ,  $C = 46.58$ . Hence, a system damping value of 50 was used. The damping card used in the single unit width model is given on the following page. Fig. 14 shows the maximum displacement in the wall for 1% and 5% damping for Load I. No significant variation in the system was observed between these damping input parameters.

```
*DAMPING_GLOBAL
$      LCID      VALDMP      STX      STY      STZ      SRX      SRY      SRZ
          50.0          1.0          1.0          1.0          1.0          1.0          1.0
```

**TABLE 4. Natural Frequencies for Single Unit Width Wall Model**

Mode	Eigenvalue	Radian	Cycles	Period
1	-6.23E+01	7.90E+00	1.26E+00	7.96E-01
2	5.17E+01	7.19E+00	1.14E+00	8.73E-01
3	2.44E+02	1.56E+01	2.49E+00	4.02E-01
4	3.18E+02	1.78E+01	2.84E+00	3.52E-01
5	4.07E+02	2.02E+01	3.21E+00	3.12E-01
6	1.07E+05	3.26E+02	5.20E+01	1.92E-02
7	2.16E+05	4.65E+02	7.40E+01	1.35E-02
8	7.01E+05	8.37E+02	1.33E+02	7.51E-03
9	9.40E+05	9.69E+02	1.54E+02	6.48E-03
10	1.40E+06	1.18E+03	1.88E+02	5.31E-03
11	2.23E+06	1.49E+03	2.38E+02	4.20E-03
12	3.28E+06	1.81E+03	2.88E+02	3.47E-03
13	4.41E+06	2.10E+03	3.34E+02	2.99E-03
14	4.46E+06	2.11E+03	3.36E+02	2.98E-03
15	4.94E+06	2.22E+03	3.54E+02	2.83E-03
16	5.68E+06	2.38E+03	3.79E+02	2.64E-03

17	7.68E+06	2.77E+03	4.41E+02	2.27E-03
18	8.84E+06	2.97E+03	4.73E+02	2.11E-03
19	9.91E+06	3.15E+03	5.01E+02	2.00E-03
20	11.06E+06	3.43E+03	5.68E+02	1.87E-03

### 3.10 Hourglassing in Elements

Hourglassing is the deformation of elements that produces non-physical modes. It occurs with single-point integration elements that are used for large analyses. Non-physical modes result from rank deficiency in the element stiffness matrix caused by insufficient integration points. A portion of internal and kinetic energy is utilized for hourglassing of elements, thereby affecting accuracy. Excessive bending and warping of elements indicates hourglassing. In general, the hourglassing energy should be less than 10% of the internal energy (Du Bois 2004).

Displacements and velocities in the single unit width model agreed with experimental data but exhibited significant hourglassing energy in solid and shell elements. The default LS-DYNA hourglassing algorithm is computationally economical. Various element formulations and hourglass viscosity types were evaluated with the goal of minimizing hourglassing without affecting other crucial results. One or more of the methods listed below can control hourglassing:

(1) Refining the existing mesh without altering parameters may be a good option. However, this option is computationally expensive, and remeshing the entire model may be complicated and time consuming. Also, refining the mesh may not adequately eliminate hourglassing.

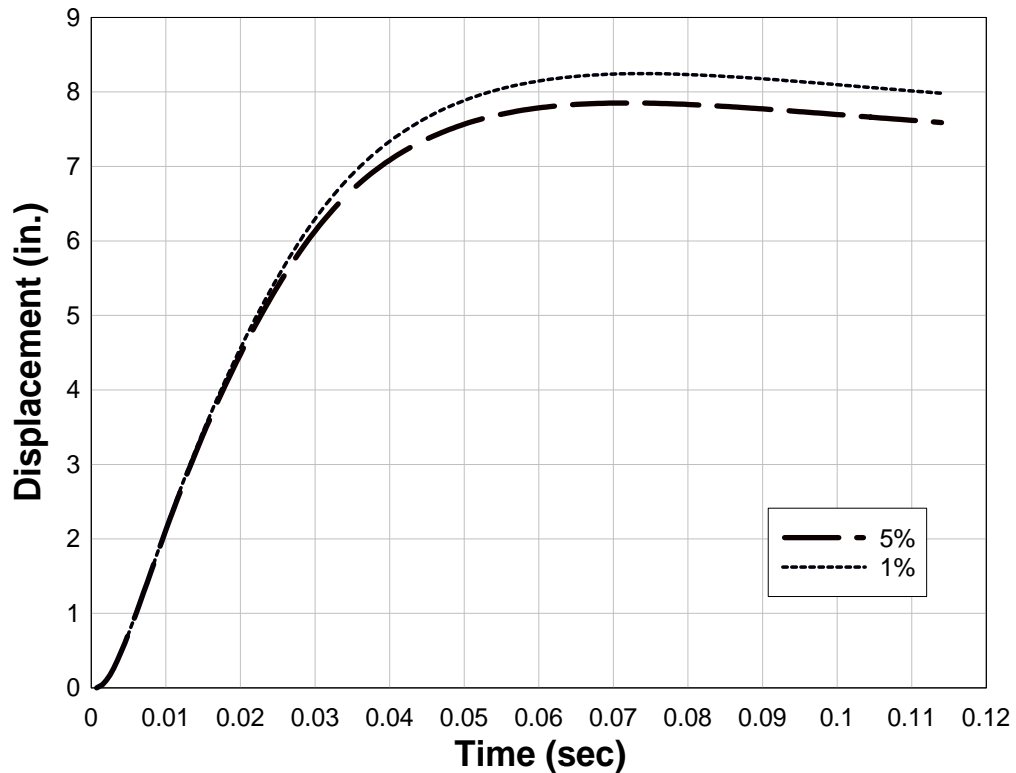


**FIG. 14. Variation in Mid-Height Displacement with Change in Critical Damping**

(2) Rank deficiency in element stiffness reduces with increase in number of integration points and thus decreases hourglassing. Use of fully integrated elements eliminates hourglassing. However, fully integrated elements may result in stiffer results for some material models. Also, full integration coupled with the use of foam materials and large deformations resulted in negative volume errors.

(3) Hourglassing is resisted by bulk viscosity of the structure, which is calculated automatically at the beginning of a DYNA-3D analysis. Increasing the bulk viscosity increases viscous damping in elements. Bulk viscosity is controlled by adjusting linear and quadratic coefficients (Q1 and Q2 in the \*HOURLASS card). Also, bending and warping stiffness can be controlled by parameters QB and QW in the \*HOURLASSING card. However, default values recommended by LS-DYNA were used since large changes in bulk viscosities affect the global behavior of the structure.

### 3.10.1 Hourglassing in Shell Elements

The default element formulation for shell elements is the Belytschko-Tsay (type 2). The hourglassing of polymer elements was controlled by using the fully integrated shell element formulation (ELEFORM=16). This element formulation activates warping in elements. Hourglassing energy was observed to be very low for the fully integrated

element formulation. Fig. 15 compares internal and hourglassing energy using ELEFORM = 16.

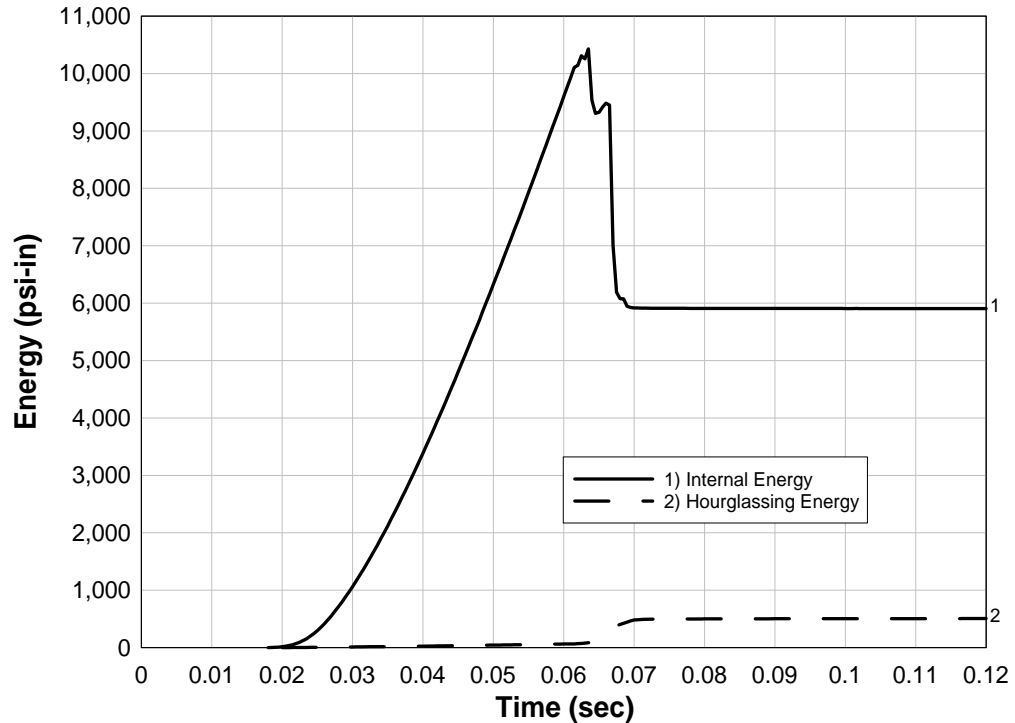


**FIG. 15. Hourglassing in Shells with ELEFORM=16**

### 3.10.2 Hourglassing in Solid Elements

The default solid element formulation is a constant stress solid element. The stiffness-based hourglass control was adopted for reducing hourglassing. In this approach the hourglass control type 4 and 5 was studied with fully integrated solid elements (type 2) and for 8-node solid elements with single point integration. To avoid nonphysical stiffening, the default hourglassing coefficient of 0.1 was reduced to 0.05.

When fully integrated solid elements were used with the Flanagan-Belytschko stiffness form (type 4), the finite element results significantly diverged from the test data. The maximum displacement of the model reduced from 7.2 in. to 5.12 in. Furthermore, the reduction in hourglass coefficient (QH) produced computational errors during the analysis (memory location error). Hourglass control type 5 (Flanagan-Belytschko stiffness form with exact volume integration) further reduced the maximum displacement in the wall model. However, in both cases, the hourglassing energy was observed to be practically zero.

The Flanagan-Belytschko stiffness form (type 4) proved effective at reducing hourglassing in 8-node continuum elements with single point integration without much nonphysical stiffening. Moreover, the shell elements showed zero hourglassing with this approach. Hence, the Flanagan-Belytschko approach was chosen for underintegrated

elements. However, this approach increases computation requirements. An 8-node solid with 1-point integration requires 12 msec per element cycle, whereas the same element type with Flanagan-Belytschko hourglass control requires 15 msec per element cycle.

### **3.10.3 Study of Hourglassing in the Single Unit Width Model with Two Elements through the CMU Face Shells**

The single unit width model consists of 18 hollow blocks separated by mortar joints. The blocks were meshed with two elements through the face shell and web wall thickness. Load I was applied. An analysis was carried out without hourglassing control. In this analysis, the largest hourglassing to internal energy ratio was 16% (Fig. 16). In the other analysis, hourglassing in solid elements was controlled by the Flanagan-Belytschko stiffness form (hourglassing type #4) with hourglassing coefficient equaling 0.05. In this analysis the largest hourglassing to internal energy ratio was 3.6% (Fig. 17).

### **3.10.4 Study of Hourglassing in the Hi-Fidelity Model**

Two CMU meshes were used as shown in Fig. 18.

(1) The bottom two blocks were meshed with five elements through the block face wall. Hourglassing was controlled by the Flanagan-Belytschko stiffness form (type #4) and hourglassing coefficient of 0.05, and default element formulation was used for solid elements. Fig. 19 illustrates low hourglassing energy with fine meshing. However, hourglassing was not completely eliminated. This indicated that refining the mesh reduces hourglassing but does not eliminate it.

(2) The remaining blocks were meshed with 1 element through face shell of the block. Hourglassing was controlled by standard LS-DYNA viscous hourglassing control, hourglassing coefficient equaling 0.01, and fully integrated solid elements (type 2). Fig. 20 illustrates the elimination of hourglass energy in solid elements by using fully integrated elements.

The use of higher order integration increased computation cost and analysis time without improving correlation to experimental data. Moreover, higher integration sections coupled with the foam material model and large displacements caused negative volume errors.

## **3.11 Energy Balance**

The energy associated with the system must be conserved. In LS-DYNA, global energy is reported in the GLSTAT file, and energies associated with system components are reported in the MATSUM file. MATSUM contains energies associated with each element. Nodes merged with rigid bodies will have kinetic energies included as total rigid-body energy. Also, rotational kinetic energy is included in GLSTAT and not in MATSUM. Therefore, the GLSTAT kinetic energies may be slightly different than MATSUM kinetic energies. The \*CONTROL\_ENERGY card provides an energy dissipation option. The GLSTAT option includes the following energy types: internal energy, kinetic energy, contact sliding energy, hourglass energy, system damping energy, rigidwall energy, and damping energy.

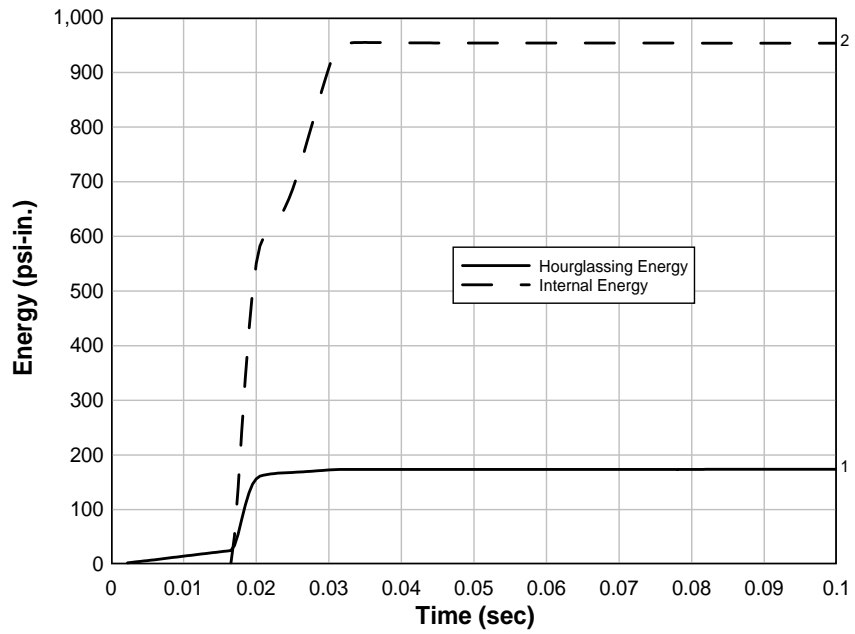


**FIG. 16. Internal and Hourglassing Energy in Solids without Hourglassing Control**

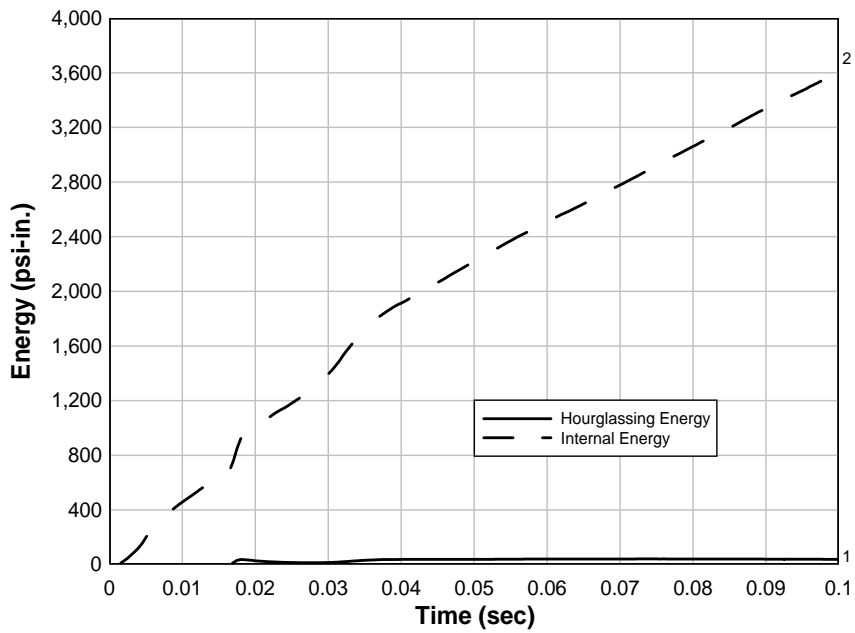


**FIG. 17. Internal and Hourglassing Energy in Solids with Hourglassing Control**

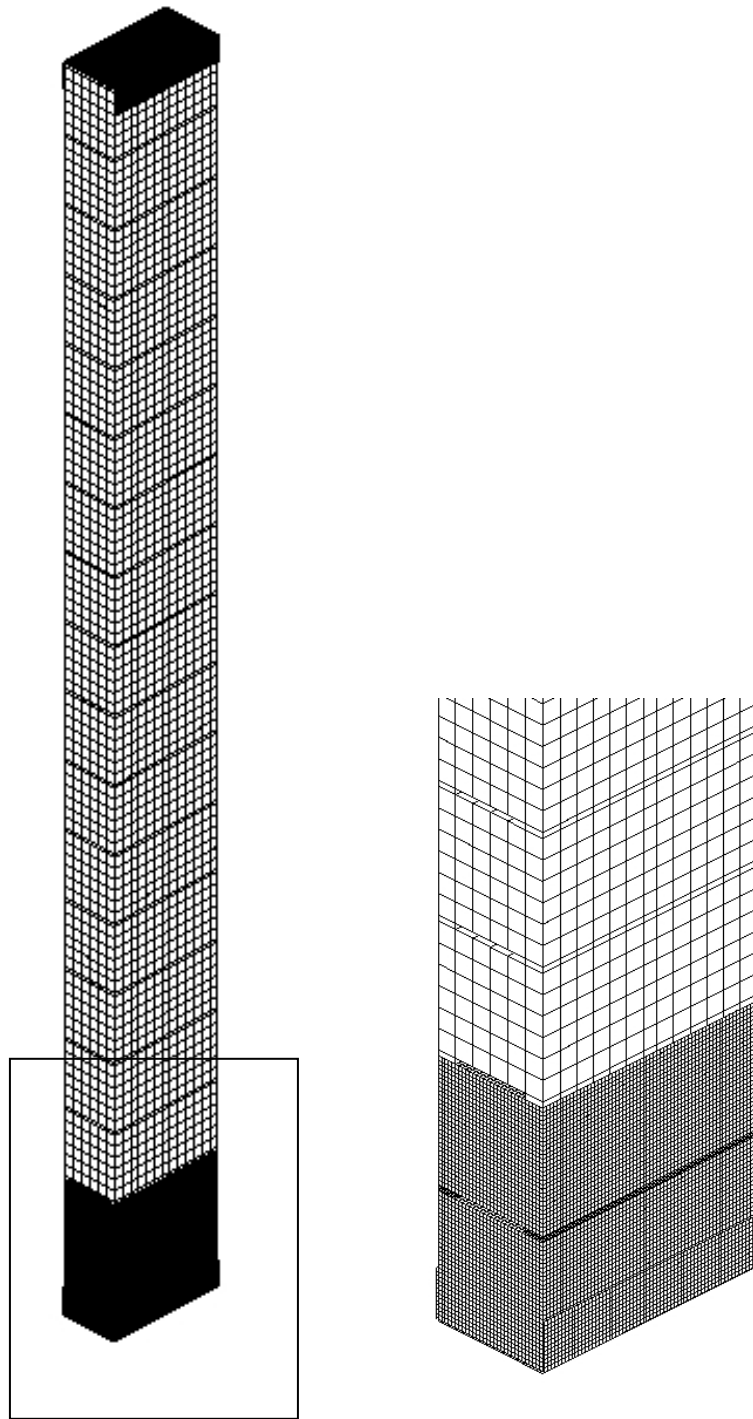


**FIG. 18. Single Unit Width Model with Hi-Fidelity Meshing in Lower Blocks**

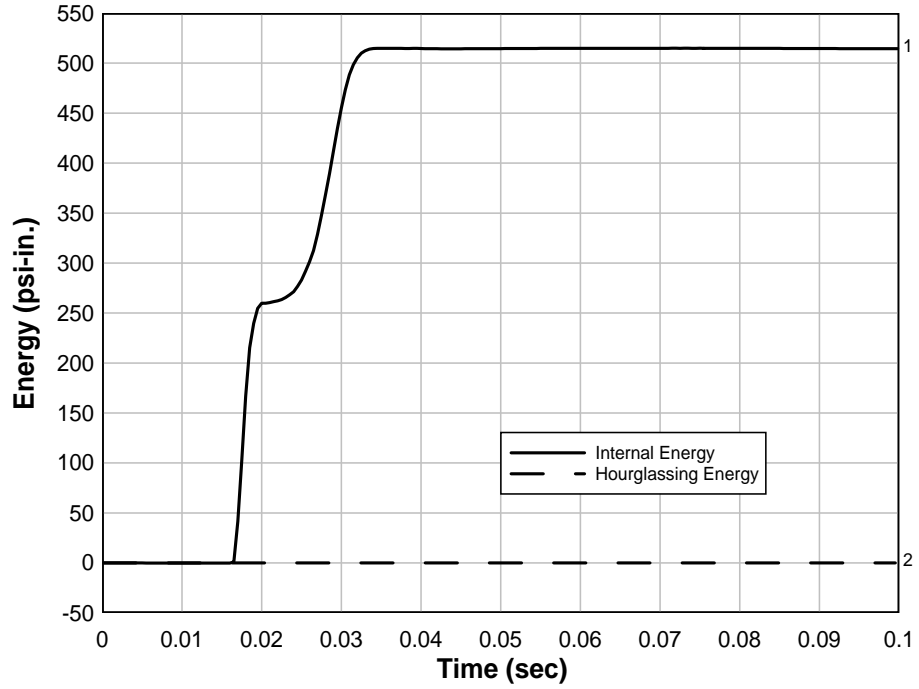


**FIG. 19. Internal and Hourglassing Energy in Finely Meshed Model with Single Point Integration Solid Elements**

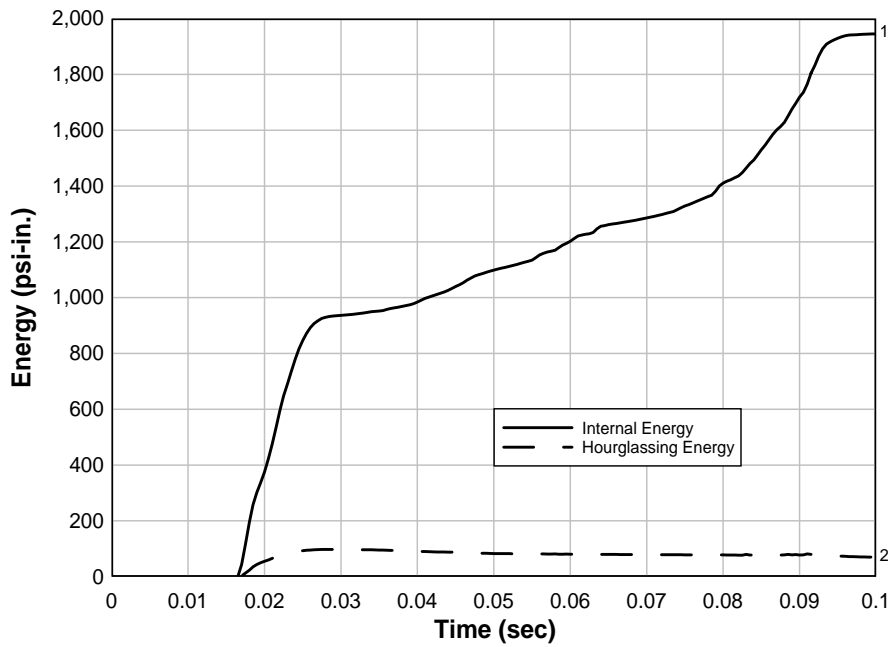


**FIG. 20. Internal and Hourglassing Energy in Coarsely Meshed Model with Fully Integrated Solid Elements**

Internal energy includes “spring and damper energy” and the strain energy of all elements unless there is no internal energy generation. When spring and damper energy is zero, internal energy is the strain energy. Since springs and dampers were not used in any of the models described in this report, internal energy refers to the strain energy. Sources at LSTC cited the following equation for energy conservation (LSTC 2003):

$$E_T = E_I + E_K + E_S + E_H + E_D + E_R = E_{TI} + W_E \quad (13)$$

where  $E_T$  = total energy,  $E_I$  = internal energy,  $E_K$  = kinetic energy,  $E_S$  = sliding energy,  $E_H$  = hourglassing energy,  $E_D$  = damping energy,  $E_R$  = rigidwall energy,  $E_{TI}$  = total initial energy, and  $W_E$  = external work. Since total initial energy = 0,

$$E_I + E_K + E_S + E_H + E_D = W_E \quad (14)$$

Fig. 21 shows overlapping of summed energies and external energy for one-way action single unit width wall model.

Alternatively, the energy balance can be verified in terms of energy ratio:

$$\text{Energy Ratio} = (E_T) / (E_I + W_E) \quad (15)$$

Energy balance exists when this ratio equals one.

## 3.12 Baseline Model

### 3.12.1 Description and Setup

This section describes the construction and features of the baseline model used for the input sensitivity study discussed in Chapter 4. Baseline refers to a moderate mesh fidelity model. The model contained 48760 solid elements and 8070 shell elements. This baseline model was then subjected to Load I and Load III.

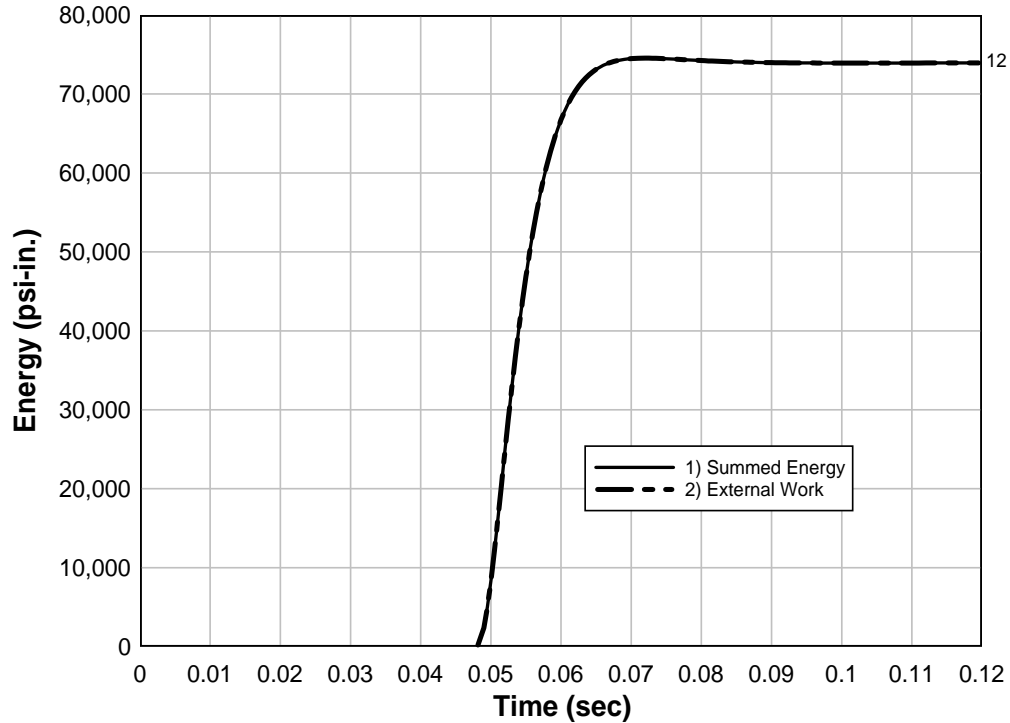


**FIG. 21. Energy Balance for a Single Unit Width Wall Model**

The baseline model consisted of 18 hollow concrete blocks connected by mortar interface. Mortar was simulated only over the flanges of the concrete blocks. CMUs were supported by the rigid floor boundaries. A gap between the topmost block and the roof boundary was kept equivalent to the thickness of one mortar layer. This provided room for the rotation of the top block. A boundary 1 in. wide extending throughout the width of one block on the backside at the top and bottom provided a restraint against lateral movement of the wall. (The side subjected to the blast load is termed as “front”). A 0.125 in. polymer coating was simulated only on the rear side of the block. The distance between the boundaries and the block was equal to the thickness of the polymer. Fig. 22 illustrates the overall model setup. Various contact definitions and parameters were selected as follows.

(1) The MPP version of LS-DYNA does not support the CONTACT\_TIEBREAK\_SURFACE\_TO\_SURFACE contact type. Interfaces between blocks and mortar layers were modeled using the TIEBREAK\_NODE\_TO\_SURFACE contact type. Node sets were made slaves, and the segment sets were made as master in each block-mortar interface contact. Failure criteria was dictated by NFLS equal to 100 psi and shear SFLS equaling 250 psi (Drysdale et al. 1994).

(2) The TIEBREAK\_NODE\_TO\_SURFACE contact definition was used for contact between the polymer and the blocks. Polymer nodes were made to act as slaves and the block segment sets as master. The spray-on polymer approach results in a very strong

bond between the concrete and the polymer (Thornburg 2004). Hence, a value of 1 was used for the static coefficient of friction. The value of dynamic friction was chosen equal to 0.8, which is the friction between concrete and rubber (Avallone and Baumeister 1987). Pull tests on polymer reinforced concrete block resulted in concrete spalling without separation of polymer from concrete (Dinan et. al 2003). Therefore, a 150 psi tensile limit was used as normal failure force for the bond between polymer and concrete, and shear failure force of 1000 psi was used for contact definition.

### **3.12.2 General Behavior of Wall**

The rigid top and bottom boundaries resist the lateral translation of the wall, which results in high shear forces at the top-most and bottom-most mortar joint interfaces. Relative motion occurs between the lowermost block and the block above it due to less freedom for rotation. A similar phenomenon is observed near the upper block (Fig. 23b). However, the space between the top block and roof boundary allows the upper block to rotate. Therefore, less shear is observed at the top mortar joint as compared to the shear at the bottom mortar joint. The amount of rotation that occurs depends on the presence of rigid boundaries on the front side and their width. Absence of the boundaries results in more rotation and less shear.

A noticeable flexural response then occurs. The blocks near the mid-height separate in tension, and wall continues to deflect until its movement is resisted by the polymer reinforcement (Fig. 23c). At this point, the polymer is subjected to tension. If the polymer has low rupture strain, it fails in tension, allowing further movement of the wall. If the polymer does not undergo failure, it rebounds slightly.

### **3.12.3 Baseline Model Performance under Load I and Load III**

The behavior of the baseline model is described in terms of fracture, mid-height center displacement, mid-height center velocities, interface reactions, vertical strain in the polymer, and kinetic and internal strain energy of the polymer.

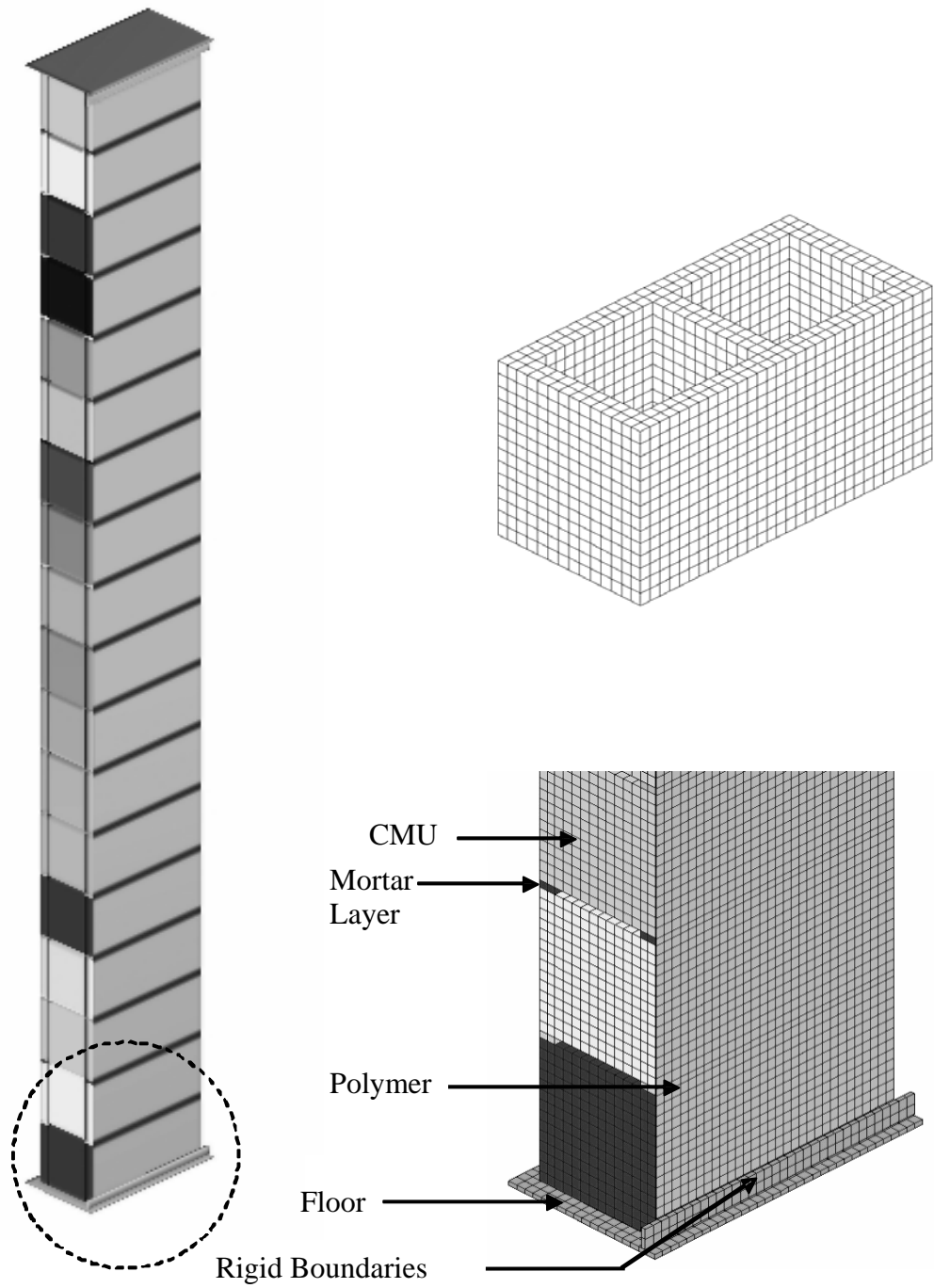


**FIG. 22. Baseline Model Setup**

### **3.12.3.1 Mid-Height Displacement**

Fig. 24 shows the maximum displacement attained by the wall for the two loading cases. The maximum displacement is 7.5 in. and 12.7 in. for Load I and Load III, respectively.

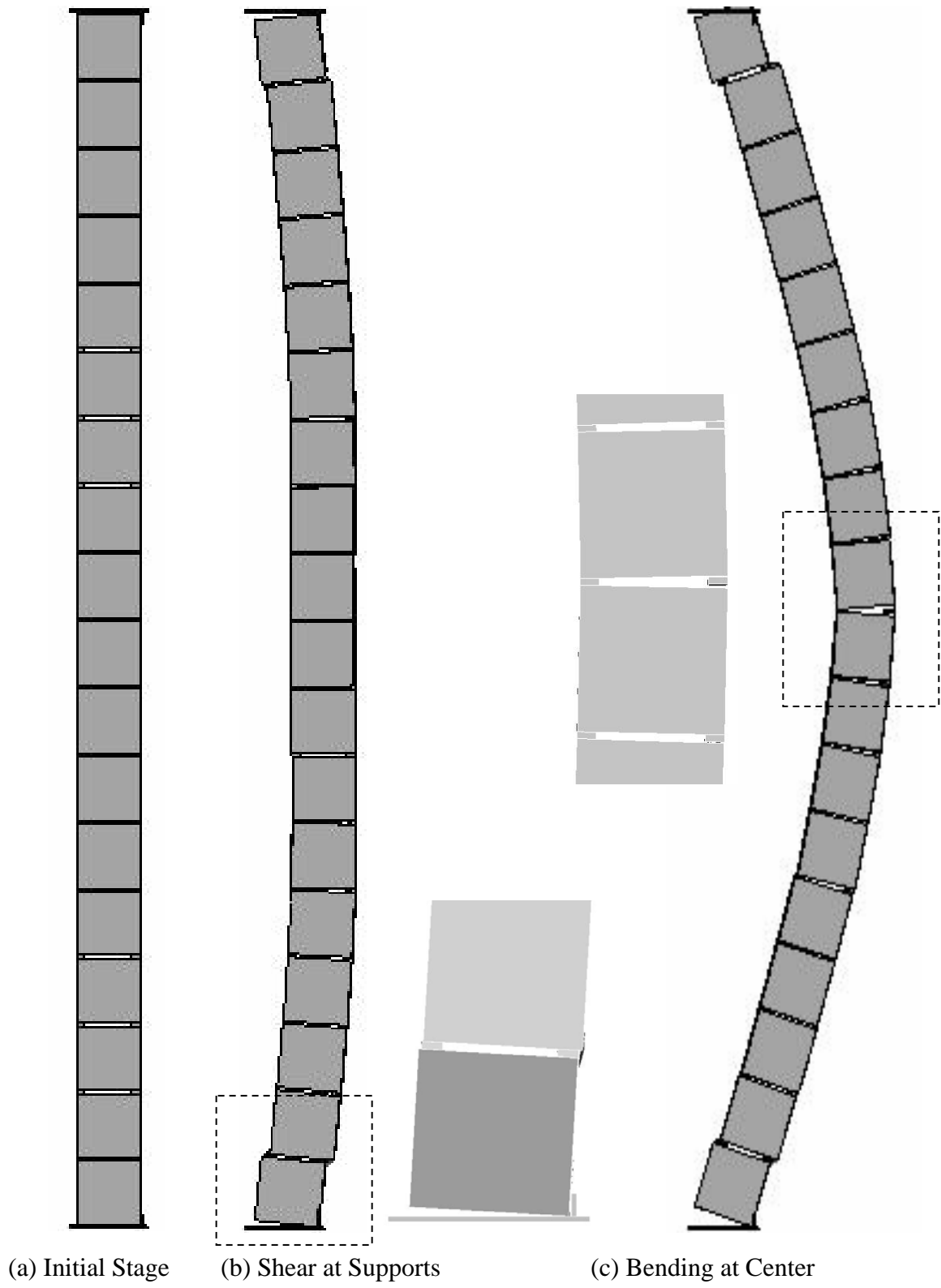
### **3.12.3.2 Mid-Height Velocity**

Fig. 25 shows mid-height velocity for the two load cases. Negative velocity reflects wall movement back toward the load. A maximum velocity of 270 in./sec and 485 in./sec resulted from Load I and Load III, respectively

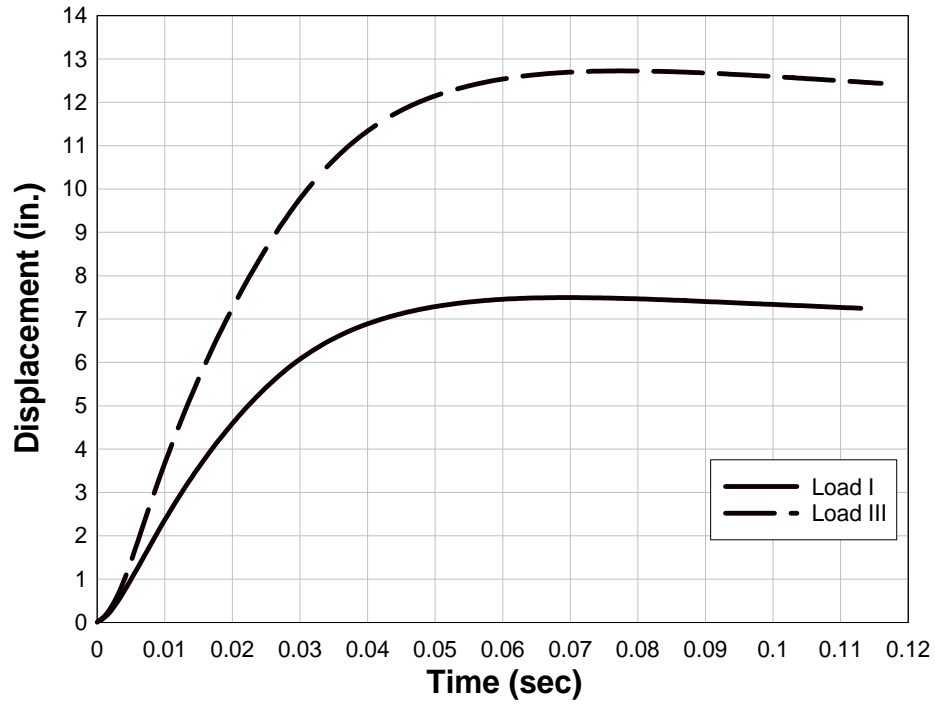
### **3.12.3.3 Fracture**

Fig. 26 shows the plot of relative distance between front and back face of a block situated at wall mid-height versus time. The Load I peak pressure and impulse are much lower than Load III. Hence, a lesser amount of front face displacement of the CMUs under Load I occurred.

Due to the higher peak pressure and impulse of Load III, the front face shells of the blocks fracture. When the blast load reaches the wall, a rapid decrease in the distance is observed, followed by unvarying relative distance (Fig. 26). This indicates failure of the front face of wall within 5 msec -7 msec of loading. Fig. 27 and Fig. 28 illustrate the initial and fractured states of the blocks.



**FIG. 23. General Wall Behavior**



**FIG. 24. Maximum Displacements for Baseline Model for Load I and Load III**

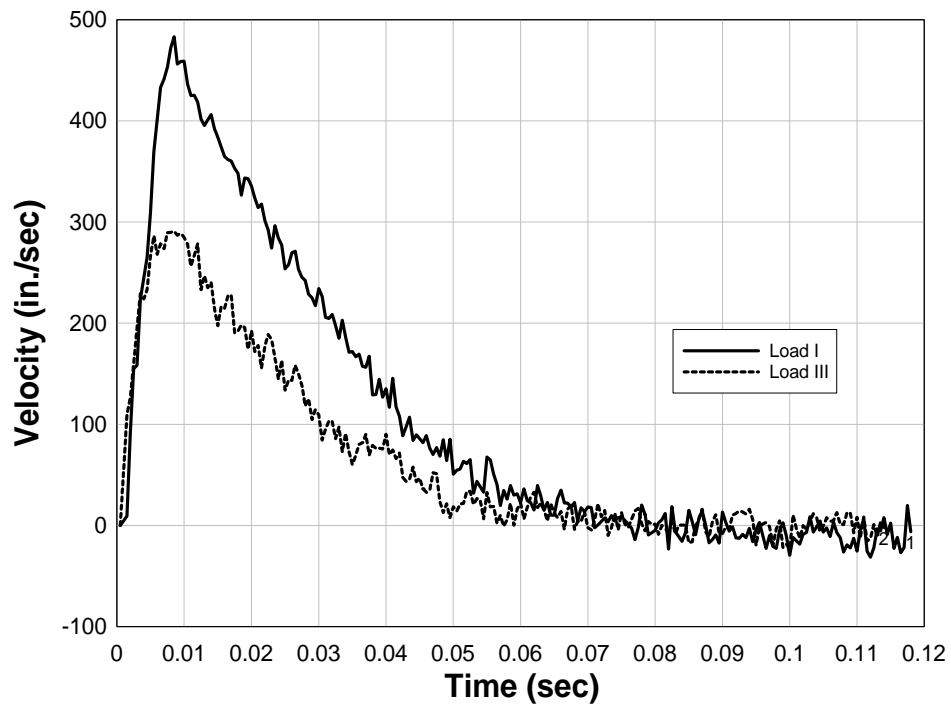


**FIG. 25. Peak Velocity for Baseline Model for Load I and Load III**

### 3.12.3.4 Stress Distribution in CMUs

In solid mechanics, failure is predicted by comparing stress and strain parameters to limits of performance in uniaxial tension testing of a material. The von Mises stress at a point is the sum of the squares of difference in the principal stresses at a point. It is a reflection of distortional stress and is given by

$$\sigma_{vm} = \frac{1}{\sqrt{2}} \left[ (\sigma_1 - \sigma_2)^2 + (\sigma_1 - \sigma_3)^2 + (\sigma_2 - \sigma_3)^2 \right]^{\frac{1}{2}} \quad (16)$$

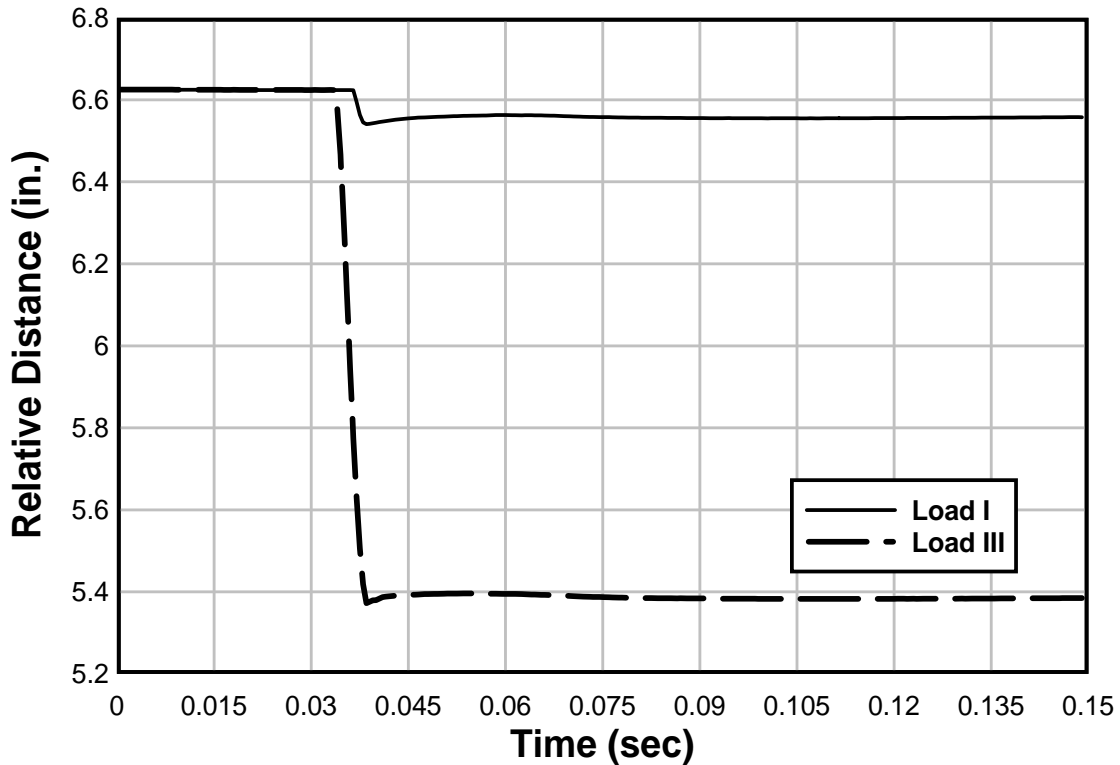


**FIG. 26. Relative Distance Between Front and Back Walls of Block for Load III**

Von Mises stress considers the three principal stresses at a point and therefore is also known as effective stress. Although fracture of concrete is not based upon a Von Mises criterion, Von Mises stress is used herein since the locations of high von Mises are the locations of probable failure.

The stress distribution under Load I varied over the entire analysis time cycle. Just after the load is applied, the end blocks exhibited high stresses due to the rigidity of the boundaries. The tensile limit was 200 psi in the MAT\_SOIL\_AND\_FOAM concrete model used. When the value exceeded 200 psi, the deviatoric stress tensor is made null (LS-DYNA Theoretical User's Manual 1998). These high stresses then propagated

toward the center from both ends. As the stresses progressed, the flexural compression crushed the end mortar interfaces. The crushing occurred in the form of high first principal stress of 295 psi. Effective (von Mises) strain rates in the block elements varied up to  $150 \text{ sec}^{-1}$ . These strain rates occurred in mortar interfaces and the backside of the wall. On the backside, the strain rates concentrated at edges and corners. This indicated the deformation of edge elements at faster rates than the elements away from the edge. Maximum shear stresses varied up to 115.5 psi and occurred at mortar joints.

In early phases of the response to Load I, the polymer experienced a maximum tensile stress of 1400 psi and effective stress of 1600 psi near the top and bottom mortar joints. The stresses then advanced toward the center of the wall but concentrated at the mortar interfaces with a tensile stress magnitude in range of 1000 psi to 1200 psi and effective stress magnitude in the range of 1000 psi to 1500 psi. The maximum polymer strain was 2.4%.

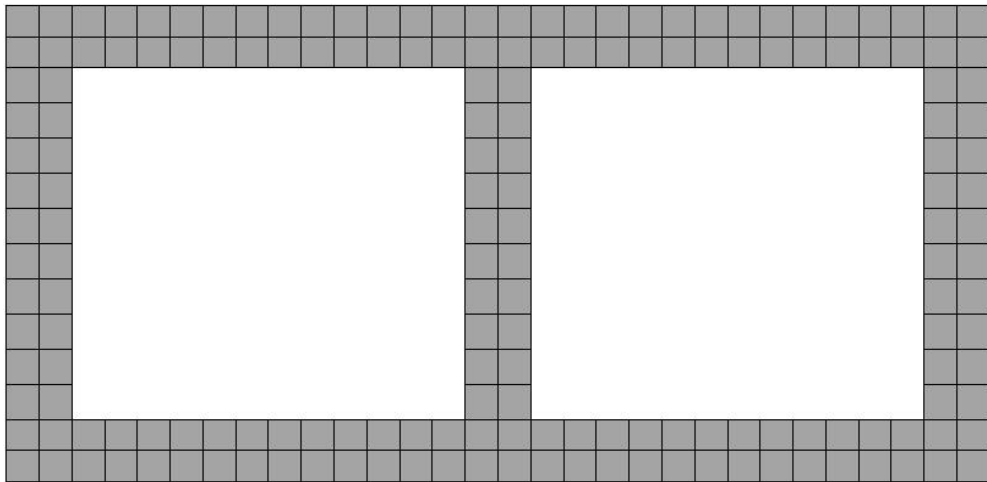


**FIG. 27. Initial State of Block**

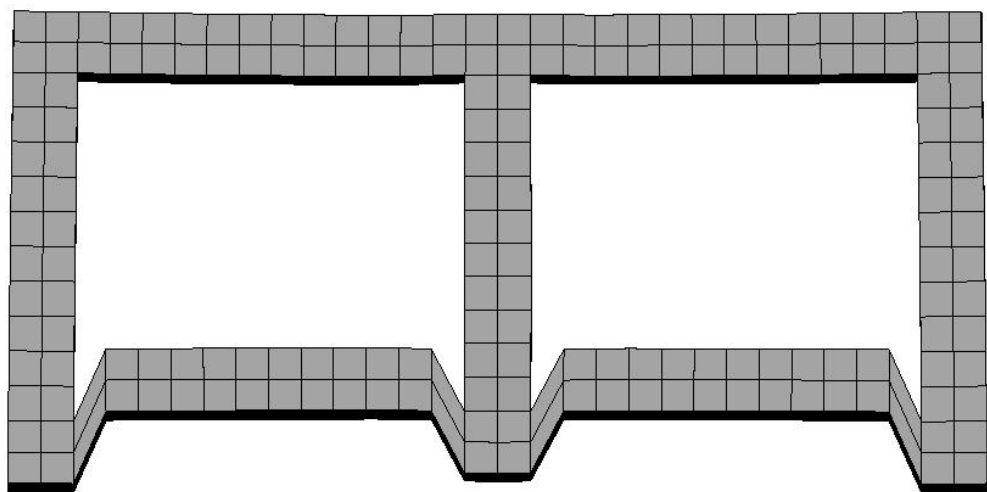


**FIG. 28. Fractured State of Block under Load III**

The stress distribution under Load III is different from that caused by Load I due to higher magnitude of the loading. The stresses did not propagate from supports to central portion gradually. Instead, the entire wall displayed high stress at the same time, indicating crushing of the front face of wall. The blocks at mid-height were partially crushed. The maximum first principal stress was 330.4 psi. The maximum stresses were concentrated at the mortar joint elements, indicating high compression. The highest strain rates were observed on the front face of the blocks. The maximum strain rate in the blocks varied between  $100 \text{ sec}^{-1}$  and  $200 \text{ sec}^{-1}$ . Maximum shear stress of 115 psi was noted as in the previous load case and occurred at mortar joints.

Under Load III, the polymer experienced a maximum tensile stress of 2100 psi and effective stress of 2150 psi near top and bottom mortar joints in early phases of the response. The stresses then advanced toward the center of the wall but concentrated at the mortar interfaces with tensile and effective stress magnitudes in the range of 1500 psi to 2000 psi. The maximum polymer strain was 3.4%.

### **3.12.3.5 Interface Forces**

Fig. 29 and Fig. 30 show the reactions at the bottom and mid-height mortar joint for Load I and Load III, respectively. The values calculated for the bottom and mid-height interfaces were 512 lb and 256 lb, respectively, whereas the model exhibited 480 lb and 236 lb, respectively.

### **3.12.3.6 Vertical Strain in the Polymer**

Since the polymer is primarily subjected to tension normal strains, study of vertical strains in the polymer is critical, especially at the mortar joints. Figs. 31 and 32 illustrate the vertical strain in the polymer at the top, bottom, and mid-height mortar joint for two loading cases. The strains in the plots are at the elements chosen at mid-width of the polymer.

For Load I, 2.9% strain occurred at the lower shear mortar joint 8 msec after loading initiated. A 2.7% - 2.8% strain occurred at the interfaces near the mid-height between 50 msec and 75 msec, respectively. For Load III, 4.5% strain occurred in the polymer near the bottom and top mortar joints 7 msec after the blast reached the wall. The maximum 5.8% strain was noted at quarter height 21 msec into the loading. The strain in the polymer near the mid-height did not exceed 5%.

### **3.12.3.7 Energy Distribution**

The hourglassing energy, internal energy, kinetic energy, sliding interface energy, and total energy were plotted for Load I and Load III (Fig. 33 and Fig. 34). It can be observed that hourglassing energy is less than 10% of the internal energy for both of the loads. The internal and sliding interface energies continue to increase as the system responds. The maximum total energy for Load III is 3.75 times that of Load I, whereas the kinetic energy in the system for Load III is thrice that for Load I. The internal energy doubles for Load III.

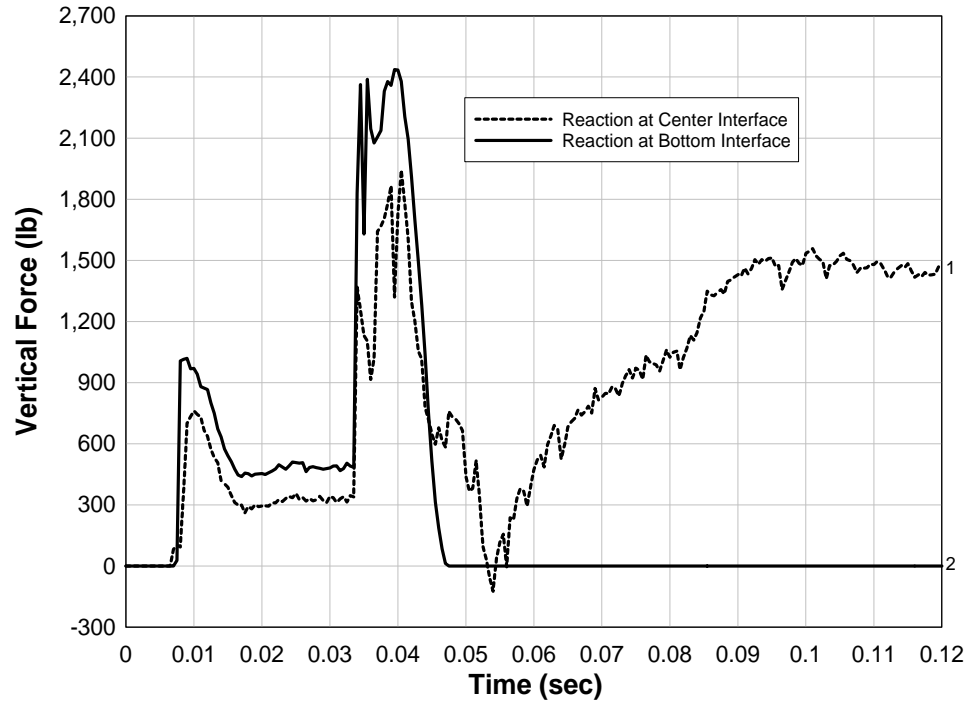


**FIG. 29. Interface Forces for Load I**

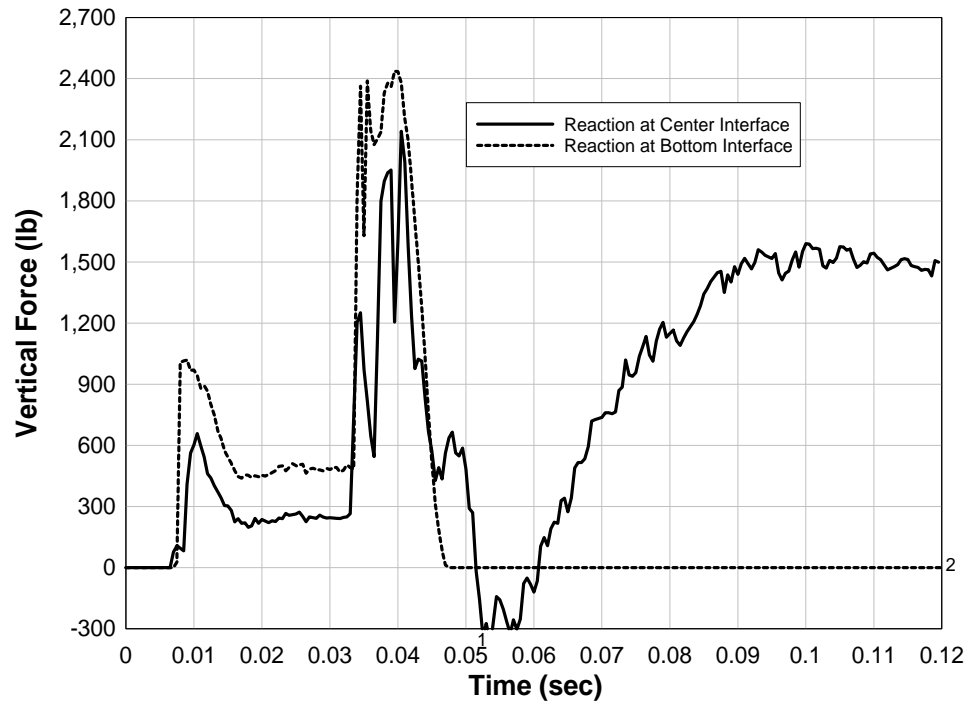


**FIG. 30. Interface Forces for Load III**

### **3.13 Hi Fidelity Model Development**

#### **3.13.1 Need**

A finer mesh is required to capture a more-detailed distribution of stresses in the wall. The coarse mesh does not accurately reveal stress and strains at localized points of failure. However, limited computational power and computational costs precludes fine meshing of the entire model. Therefore, some components of the system were meshed at a greater fidelity than other components to study local effects.

#### **3.13.2 Model Description**

An investigative model was built to study the lowermost mortar joint and stress distribution due to plate-block interaction. The lower two blocks were meshed to have five elemental divisions through the face shells and four through the webs. These two blocks were composed of 27000 elements. The mortar layer between these blocks was also meshed with four element layers through its thickness, resulting in 480 elements total for each interface. The block and mortar meshing is shown in Fig. 35 and Fig. 36. The other blocks were meshed with a single element through the thickness of the block face shell. Rigid boundaries were placed on both sides of the top and bottom. \*CONTACT\_TIEBREAK\_SEGMENT\_TO\_SEGMENT was used to define all interfaces. Load I was applied to the system.

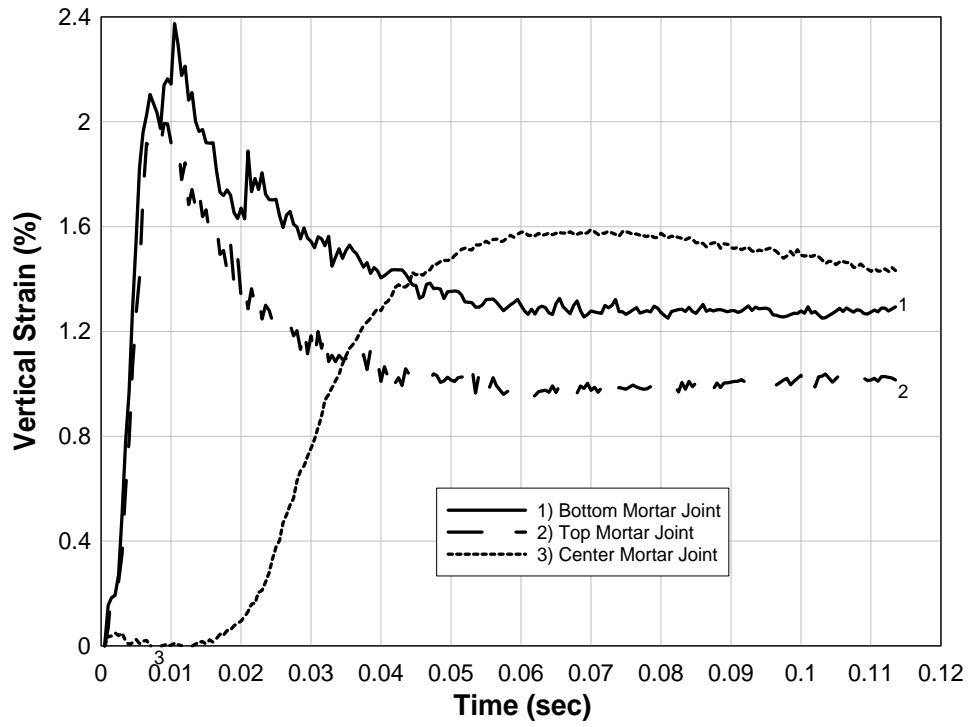
#### **3.13.3 Observations**

Fig. 37 shows shear stress distribution in the blocks. The plots indicate the areas of stress localization in the finely meshed blocks and coarsely meshed blocks, especially at corners and edges (Fig. 38 and Fig. 39). High stresses were observed at the block and plate interface indicating crushing of concrete at these areas (Fig. 40). Fig. 41 shows shear stress concentration at the mortar interface with a peak value of 115 psi. This indicates failure of the contact interfaces with relative movement (Fig. 42).

### **3.14 Summary and Conclusions**

Chapter 3 focused on finite element modeling approaches for simulating polymer reinforced concrete masonry walls subjected to blast. It was concluded that the MAT\_SOIL\_AND\_FOAM material model is the most appropriate material model for simulating blast loaded concrete masonry. The MAT\_PIECEWISELINEAR\_PLASTICITY was used for the polymer reinforcement to incorporate the full nonlinear stress-strain relationship and strain rate effects. Eight-node elements were used for the masonry blocks and mortar interfaces with the Flanagan-Belytschko stiffness hourglassing control. Fully integrated shell elements were determined to be best suitable for the polymer reinforcement. For the hollow masonry units, one element through the block face shells and webs resulted in inaccurate results, whereas multiple elements increased the computational and storage cost per model run. Therefore, it was concluded that two elemental divisions through the face shell of the block are required. The MAT\_RIGID material model was used for the floor and roof boundaries. Gravity preload was incorporated using dynamic relaxation. Contact surfaces were used to define mortar bond interfaces of the blocks and polymer-block interfaces using the \*CONTACT\_

TIEBREAK\_SURFACE\_TO\_SURFACE type contact. The interface between boundaries and block were simulated using the \*CONTACT\_AUTOMATIC\_SURFACE\_TO\_SURFACE. A damping coefficient of 50 was used for the system to represent 5.3% global damping. Energy conservation in the system was confirmed. The behavior of the baseline model was discussed for Load I and Load III. Its performance was then studied for displacements, velocities, CMU fracture, stress distribution in CMUs, interface forces, strain in the polymer, and internal and kinetic energy in polymer. A hi-fidelity model was developed by refining the mesh for the lower two CMUs and mortar layer between them. Shear and von Mises stresses in these blocks were then compared to coarsely meshed blocks.



**FIG. 31. Vertical Strain in Polymer for Load I**

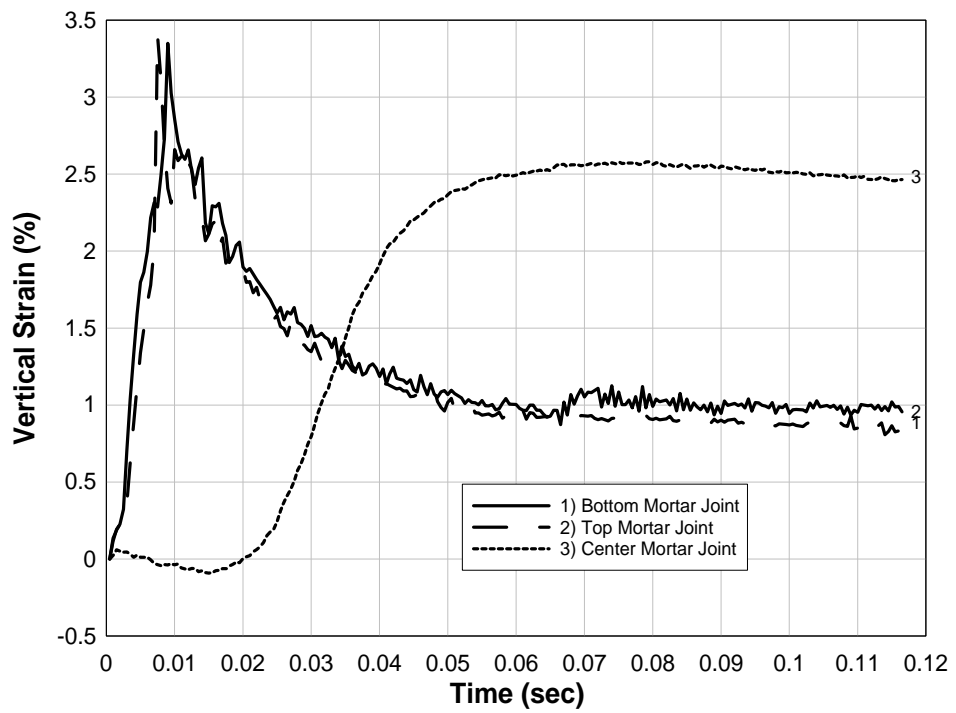


**FIG. 32. Vertical Strain in Polymer for Load III**

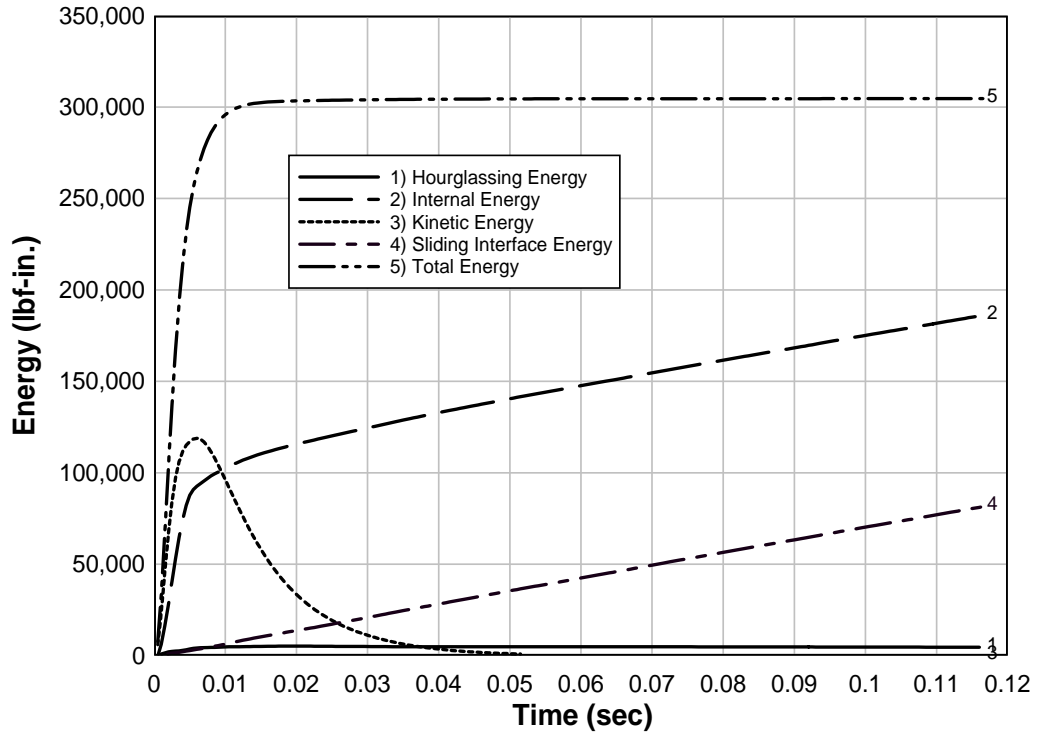


FIG. 33. System Energy Distribution for Load I

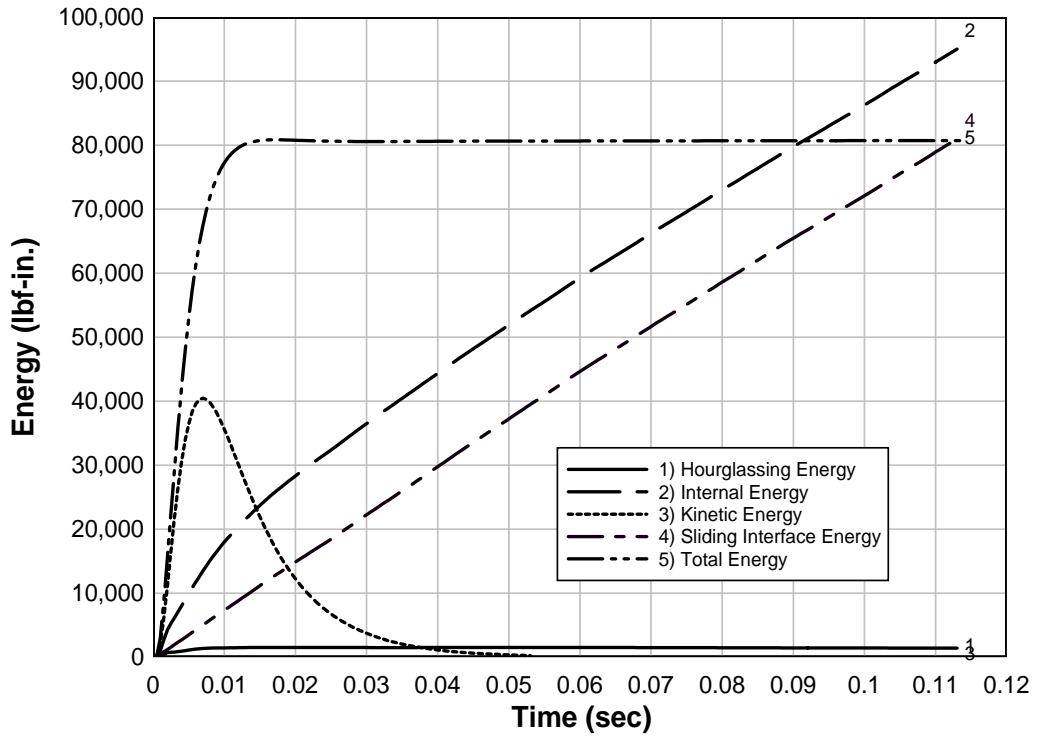
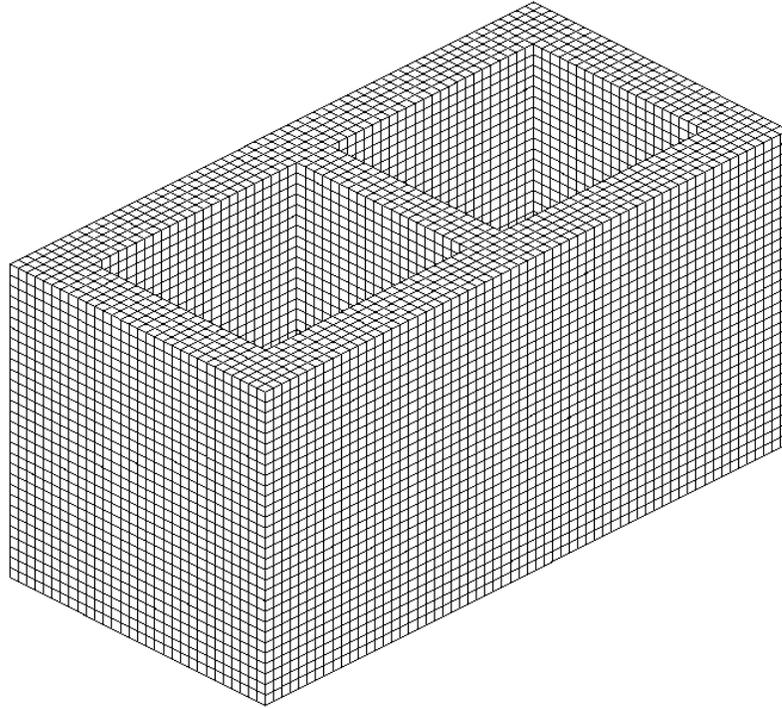
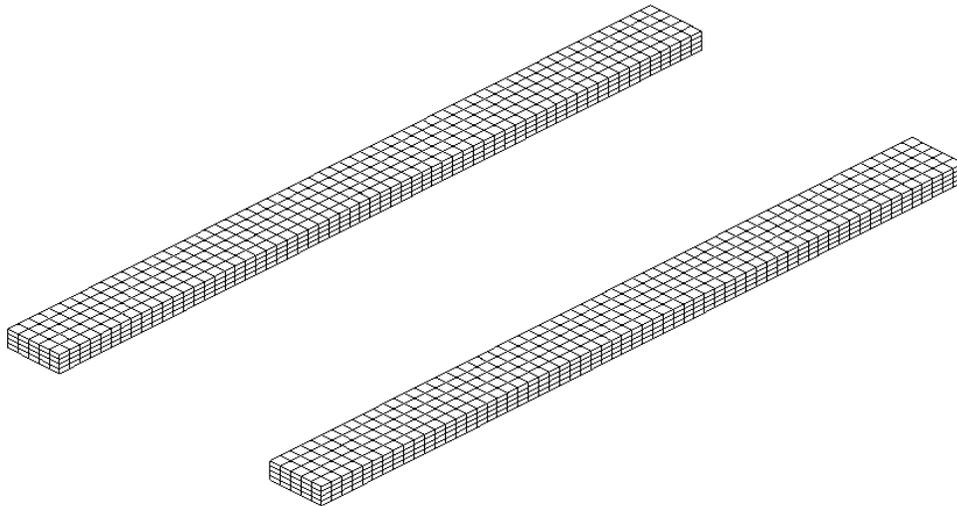


FIG. 34. System Energy Distribution for Load III



**FIG. 35. Concrete Masonry Unit with Hi-Fidelity Meshing**



**FIG. 36. Mortar Layer with Hi-Fidelity Meshing**

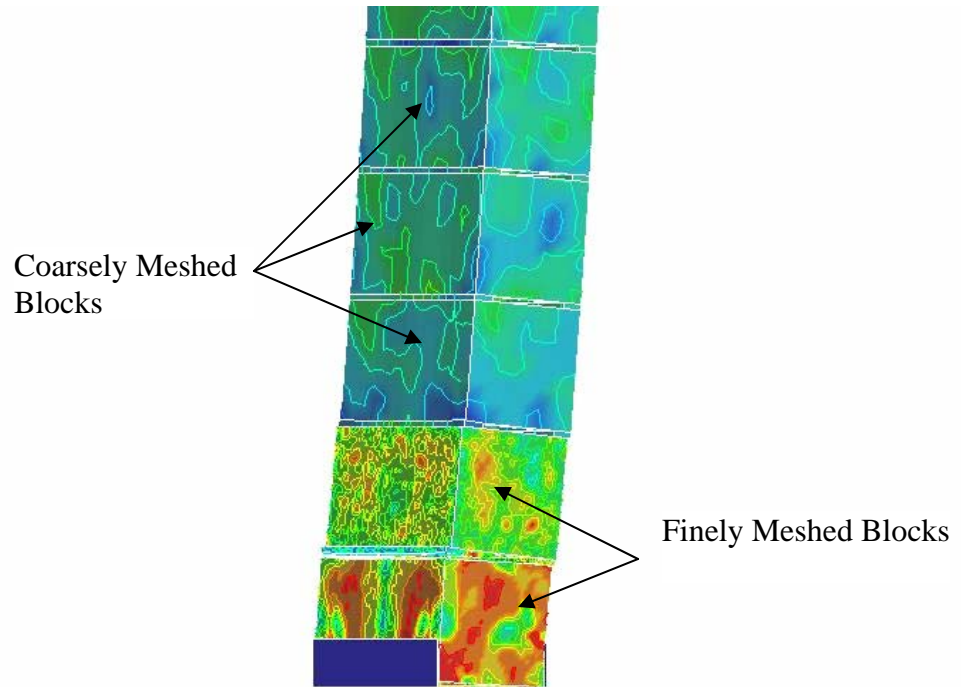


**FIG. 37. Stress Distribution in Finely and Coarsely Meshed Blocks**

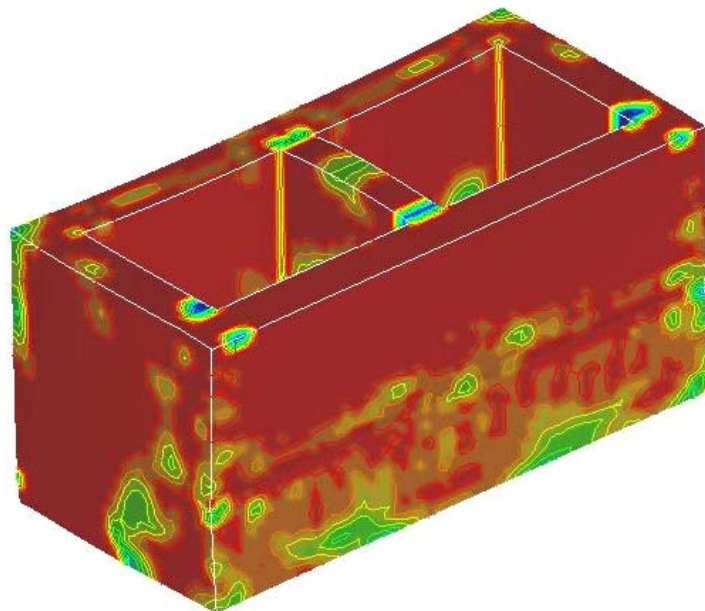


**FIG. 38. Effective Stress Concentration at Corners (Backside)**

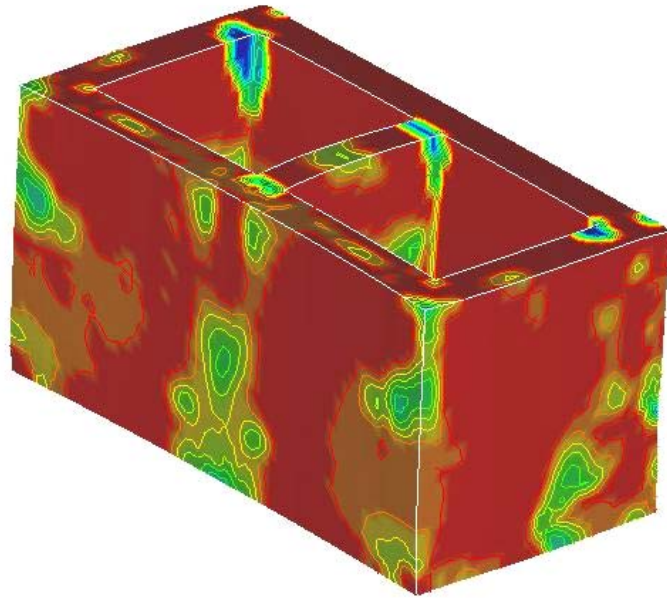


**FIG. 39. Effective Stress Concentration at Corners (Front Side)**

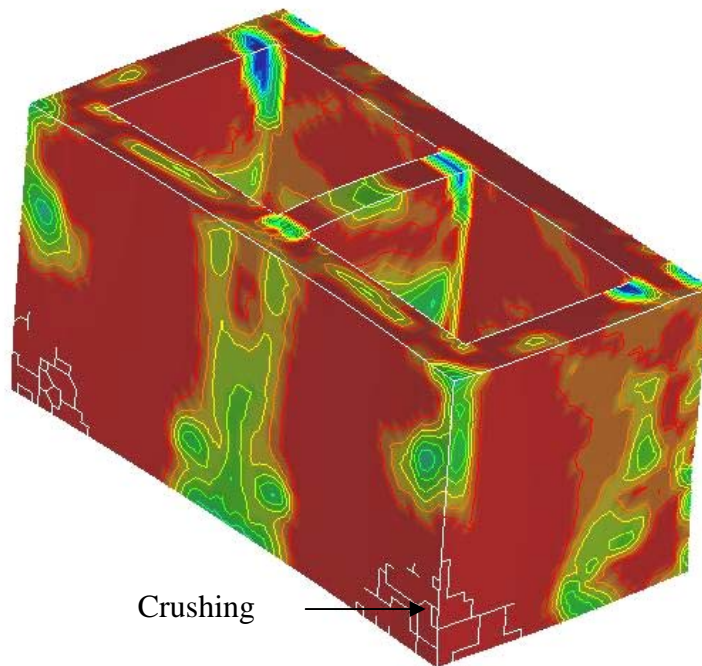


**FIG. 40. Crushing Due to Block-Boundary Interaction**

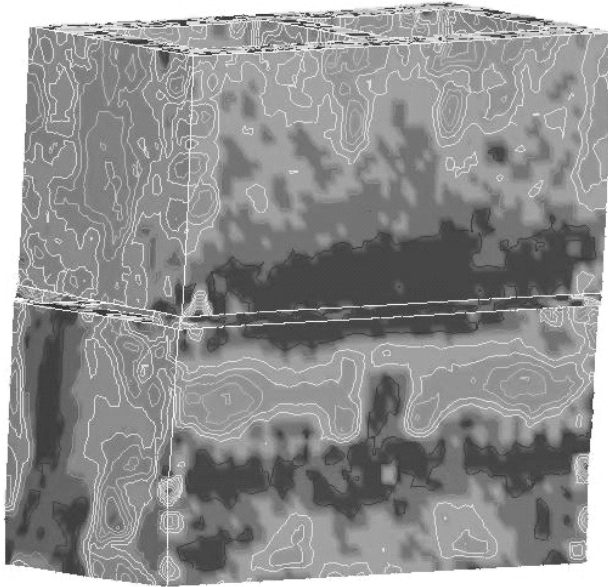


**FIG. 41. Shear Stress Distribution in Finely Meshed Blocks**

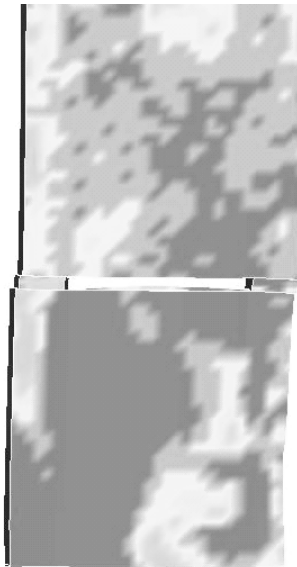


**FIG. 42. Shear Failure at Mortar Interface in Finely Meshed Blocks**

## CHAPTER 4. INPUT SENSITIVITY STUDY

### 4.1 Introduction

The input sensitivity study includes effects of variation in polymer properties on the behavior of the wall and polymer. The following aspects of wall behavior were used to study the parameter variation effects:

- (1) Mid-height deflection and velocity time histories were analyzed to study effects of property variance on maximum wall displacement.
- (2) Vertical strains in the polymer were plotted for polymer elements near the bottom mortar joints and at the center mortar joint. The shear at the bottom-most mortar joint is greater than the shear at the top-most mortar joint due to the space between the top block and the roof boundary. This space facilitates rotation of the top block that results in a comparatively lower shear at the top-most mortar joint. Hence, strain in the polymer near the top-most mortar joint is less than near the bottom mortar joint. Therefore the polymer strain near the bottom mortar joint and center mortar joint was considered. Elements midway along the width of the polymer reinforcement were chosen.
- (3) Blast energy is transferred from the CMUs to the polymer. The effectiveness of the polymer depends on its strain energy absorption capacity. Therefore, the kinetic energy of the system and strain energy absorbed by the polymer was studied.

### 4.2 Variants

#### 4.2.1 Rupture Strain

The energy absorption capacity of the polymer reinforcement is a function of the elongation ability of the material. The polymer used in the blast tests had a rupture strain of approximately 80%. Maximum vertical strain in the polymer indicated by baseline model was 2.4% and 3.5% for Load I and Load III, respectively (Section 3.12.3). However, to study the effect on wall for varying polymer rupture strain, the baseline finite element model was analyzed for 2%, 5%, and 10% rupture strain for Load I and Load III. Table 5 illustrates the peak values. Fig. 43 through Fig. 46 shows the displacement and velocity time histories. Fig. 47 and Fig. 48 show internal energy in the polymer for Load I and Load III, respectively.

**TABLE 5. Maximum Displacement and Velocity Due to Change in Rupture Strain of Polymer**

<b>Elongation (%)</b>	<b>Maximum displacement (in.)</b>	<b>Time (msec)</b>	<b>Maximum velocity (in./sec)</b>	<b>Time (msec)</b>
<b>(a) Load I</b>				
2	9.0	55.5	345.5	10.0
5	7.5	70.5	282.5	8.0
10	7.5	70.5	282.5	8.0
<b>(b) Load III</b>				
2	15.0	64.5	573.1	10.3
5	12.7	78.0	469.4	6.8
10	12.7	78.0	472.0	7.3

**4.2.1.1 Conclusions**

Polymer with 2% rupture strain failed near top and bottom mortar joints due to shear after which the wall continues to deflect. Displacement and velocity in models for polymer with 5% and 10% rupture strain are equal. In general, it can be concluded that polymers with lower failure strains have less energy absorption capacity but can be used for reinforcing masonry walls against blast. The difference in internal energy in polymer with 5% and 10% rupture strain is negligible. However, internal energy in polymer with rupture strain 2% initially increases with rupture strain 5% and 10% until rupture occurs at 8 msec, after which it follows a different path resulting in lower internal energy.

**4.2.2 Retrofit Thickness**

The thickness of the polymer was varied as 1/16 in., 2/16 in., 3/16 in., and 4/16 in. Table 6 presents the change in mid-height displacement and velocity for Load I and Load III with variation in polymer thickness. Displacement and velocity time histories for Load I and Load III are indicated in Fig. 49 through Fig. 52.

**4.2.2.1 Vertical Strains in the Polymer**

Fig. 53 through Fig. 56 indicate the vertical strains in the polymer near the bottom and center mortar joints with change in polymer thickness for Load I and Load III. The maximum strains are presented in Table 7.

#### 4.2.2.2 Internal and Kinetic Energy in the Polymer

Fig. 57 through Fig. 60 show internal and kinetic energy in the polymer under Load I and Load III, respectively.

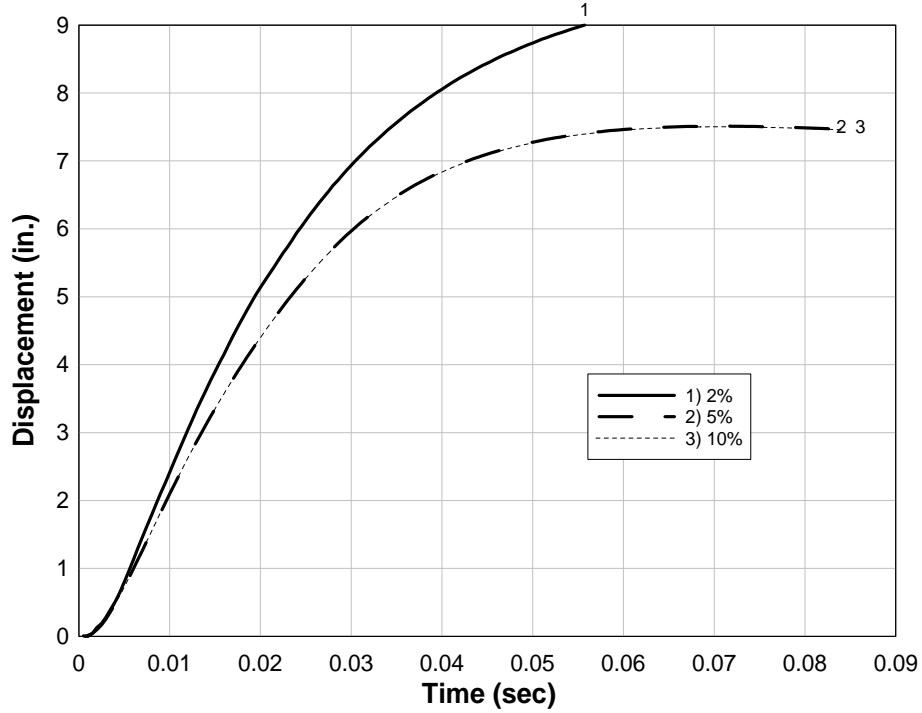


FIG. 43. Effect of Rupture Strain on Maximum Displacement for Load I

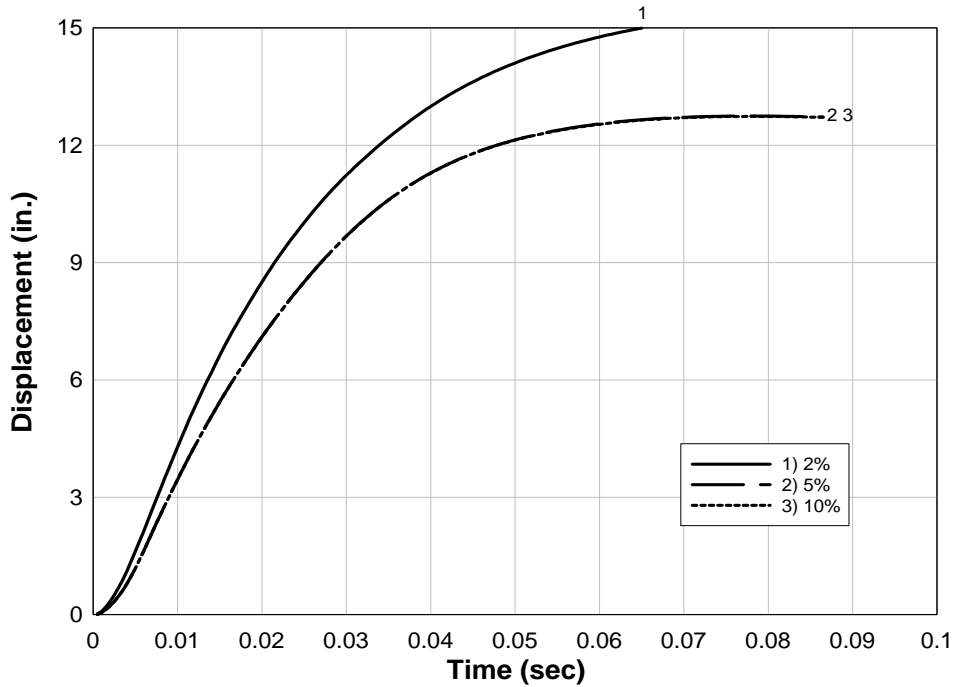
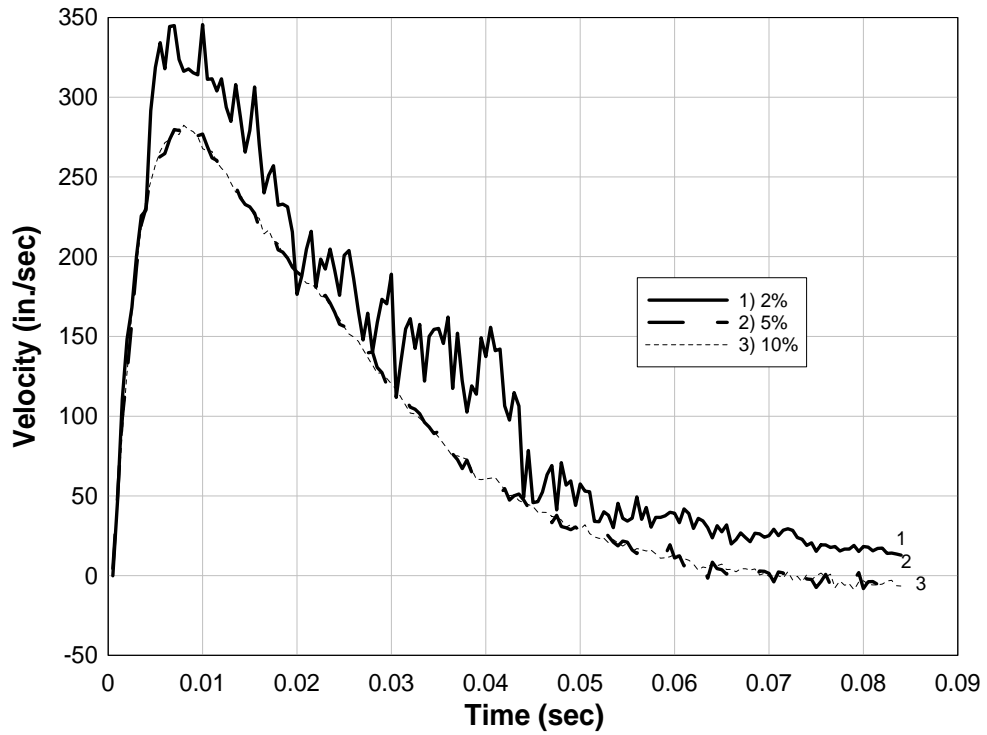
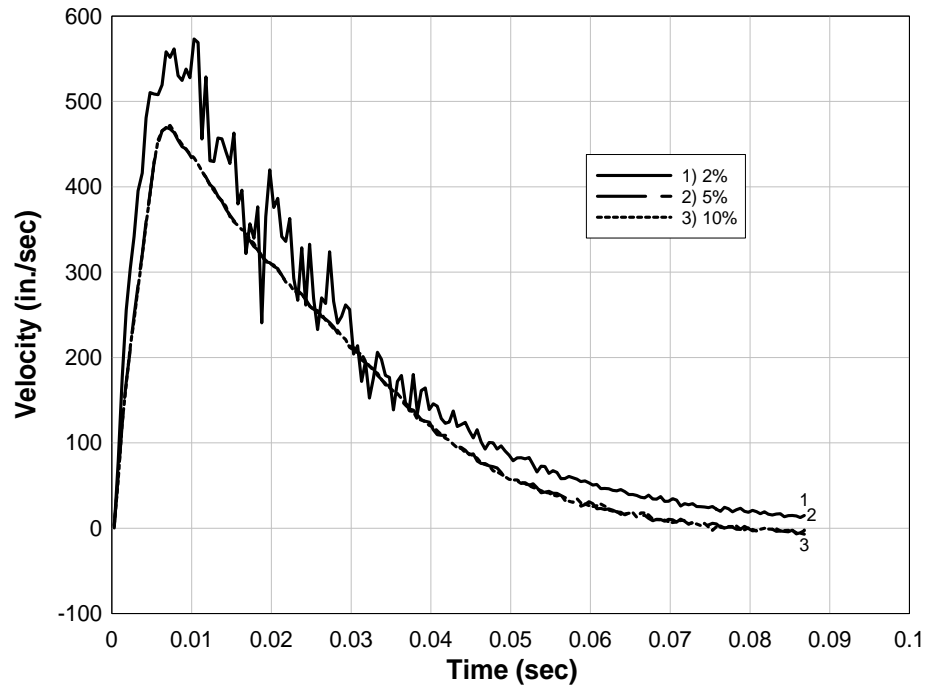


FIG. 44. Effect of Rupture Strain on Maximum Displacement for Load III



**FIG. 45. Effect of Rupture Strain on Maximum Velocity for Load I**



**FIG. 46. Effect of Rupture Strain on Maximum Velocity for Load III**

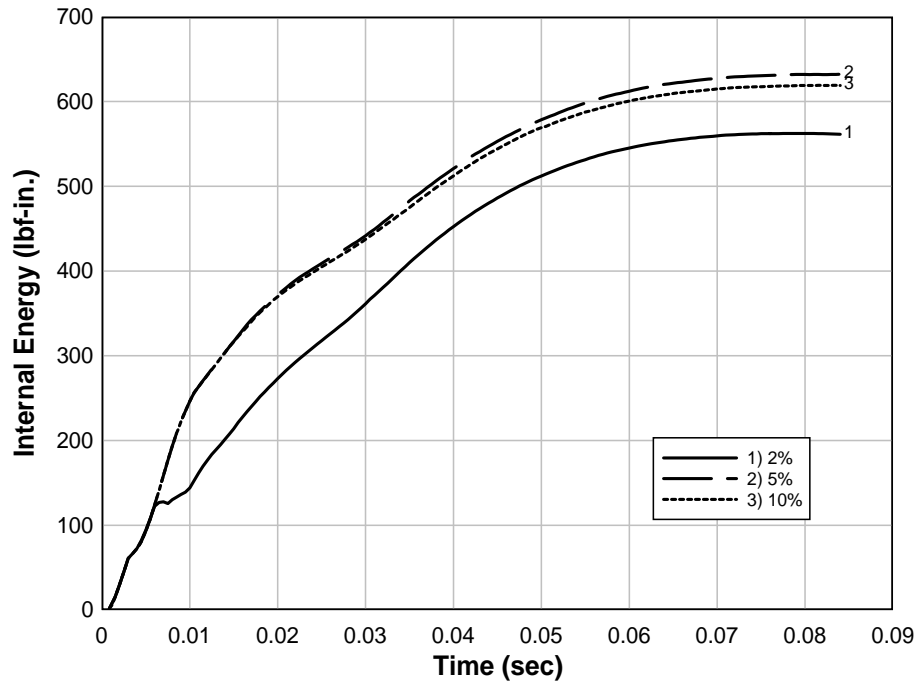


**FIG. 47. Effect of Rupture Strain on Internal Energy of the Polymer for Load I**

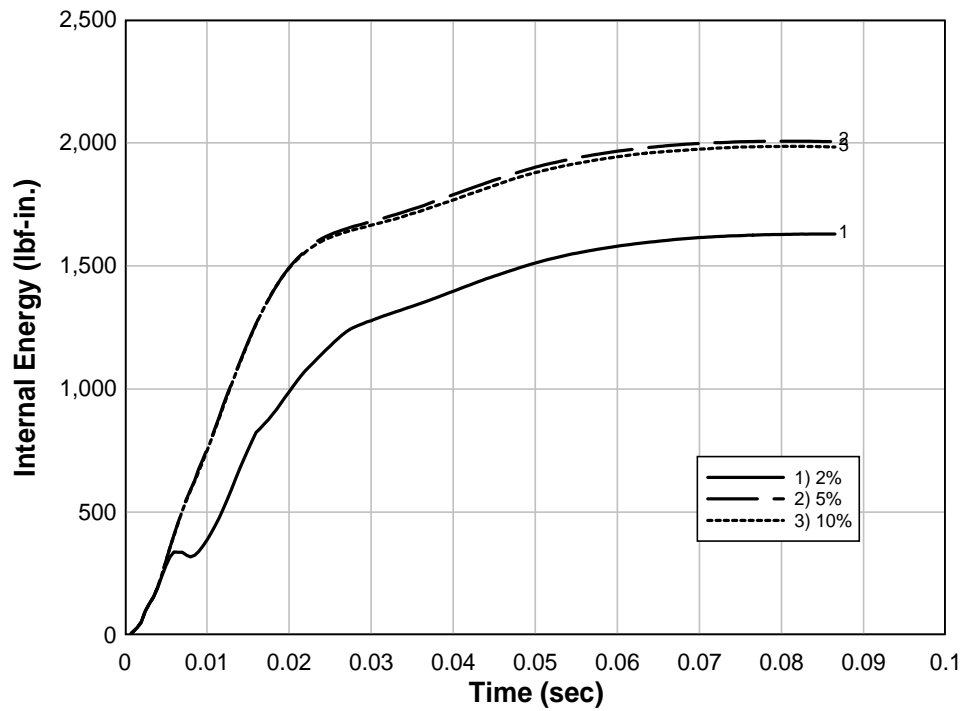


**FIG. 48. Effect of Rupture Strain on Internal Energy of the Polymer for Load III**

**TABLE 6. Maximum Displacement and Velocity Due to Change in Polymer Thickness**

<b>Polymer thickness (in.)</b>	<b>Maximum displacement (in.)</b>	<b>Time (msec)</b>	<b>Maximum velocity (in./sec)</b>	<b>Time (msec)</b>
<b>(a) Load I</b>				
0.0625	7.3	65.0	289.8	7.5
0.125	7.4	69.5	280.8	7.0
0.1875	7.3	70.0	277.0	6.5
0.25	7.2	69.0	271.4	7.0
<b>(b) Load III</b>				
0.0625	12.5	75.5	475.2	7.2
0.125	12.5	78.0	470.9	7.2
0.1875	12.4	77.0	465.3	7.7
0.25	12.2	74.5	456.7	7.7

**TABLE 7. Maximum Vertical Strain in Polymer Due to Change in Polymer Thickness**

<b>Polymer thickness (in.)</b>	<b>Maximum strain (%)</b>	<b>Location</b>	<b>Time (msec)</b>
<b>(a) Load I</b>			
0.0625	3.7	Near Boundaries	17.5
0.125	3.0	Bottom Mortar Joint	20.0
0.1875	2.7	Quarter Height	15.5
0.25	2.2	Quarter Height	23.5
<b>(b) Load III</b>			
0.0625	8.0	Quarter Height	17.5
0.125	5.8	Quarter Height	20.0
0.1875	4.9	Quarter Height	15.5
0.25	4.2	Quarter Height	23.5

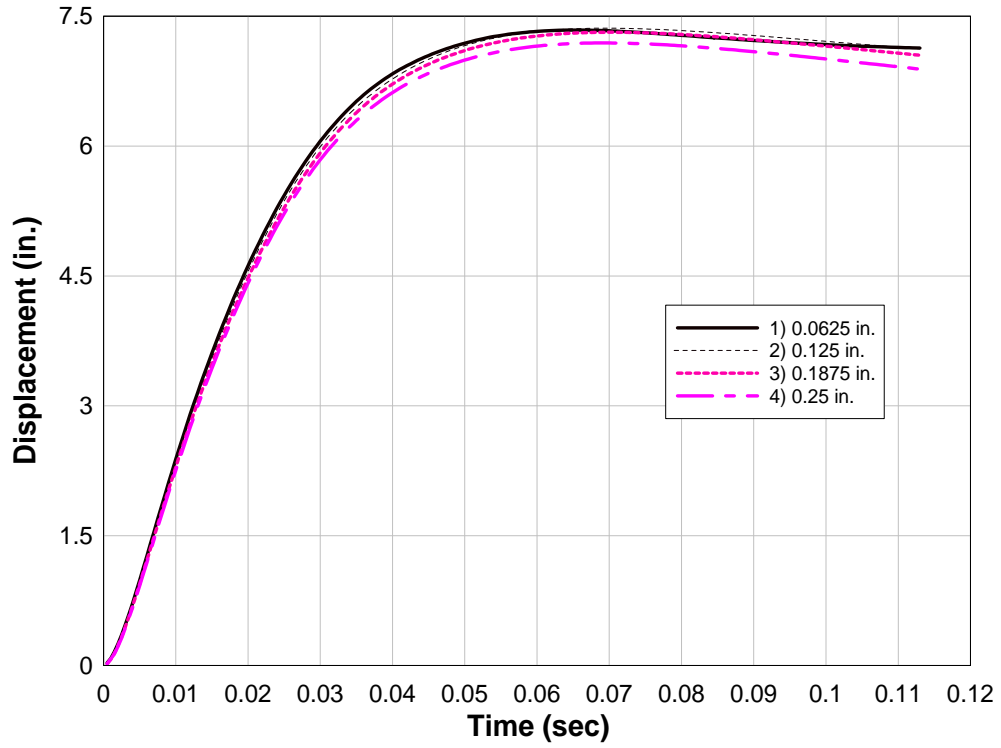


**FIG. 49. Effect of Polymer Thickness on Maximum Displacement for Load I**

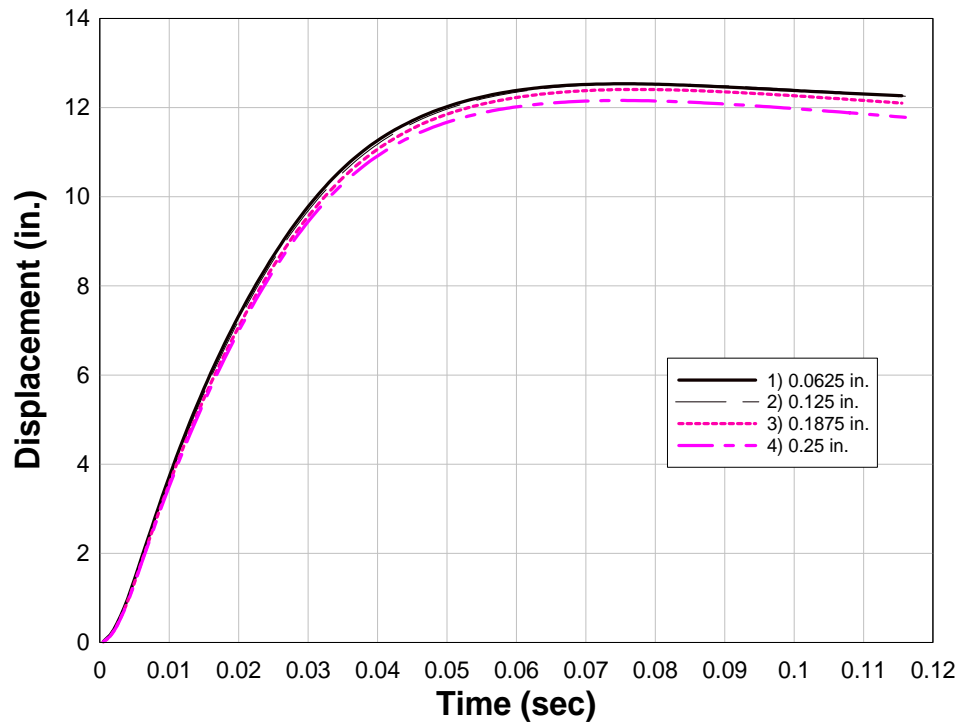


**FIG. 50. Effect of Polymer Thickness on Maximum Displacement for Load III**

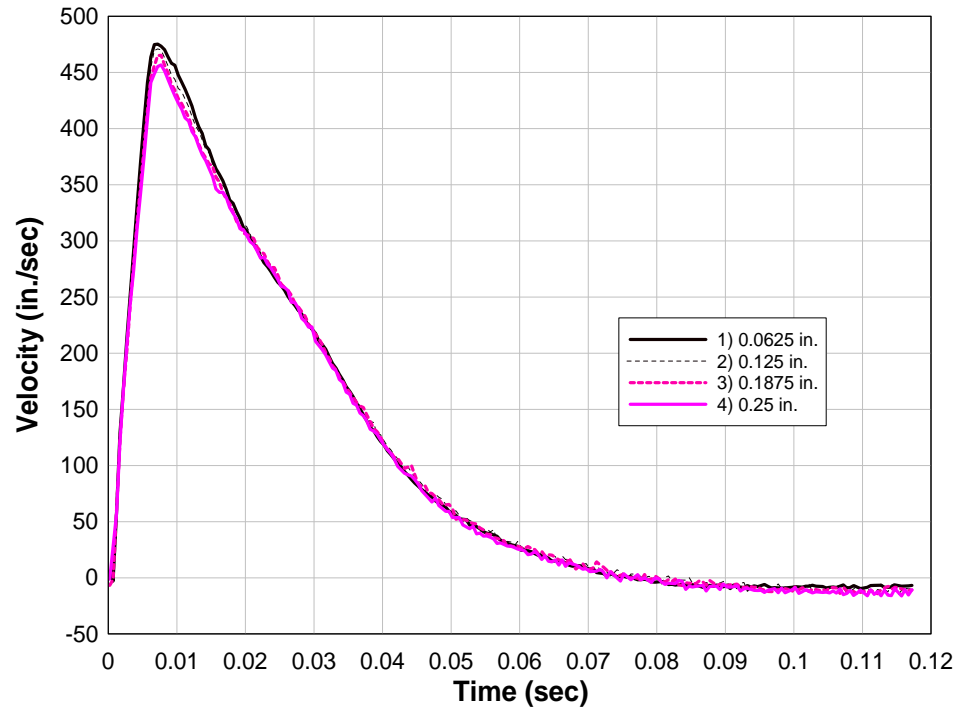


**FIG. 51. Effect of Polymer Thickness on Maximum Velocity for Load I**

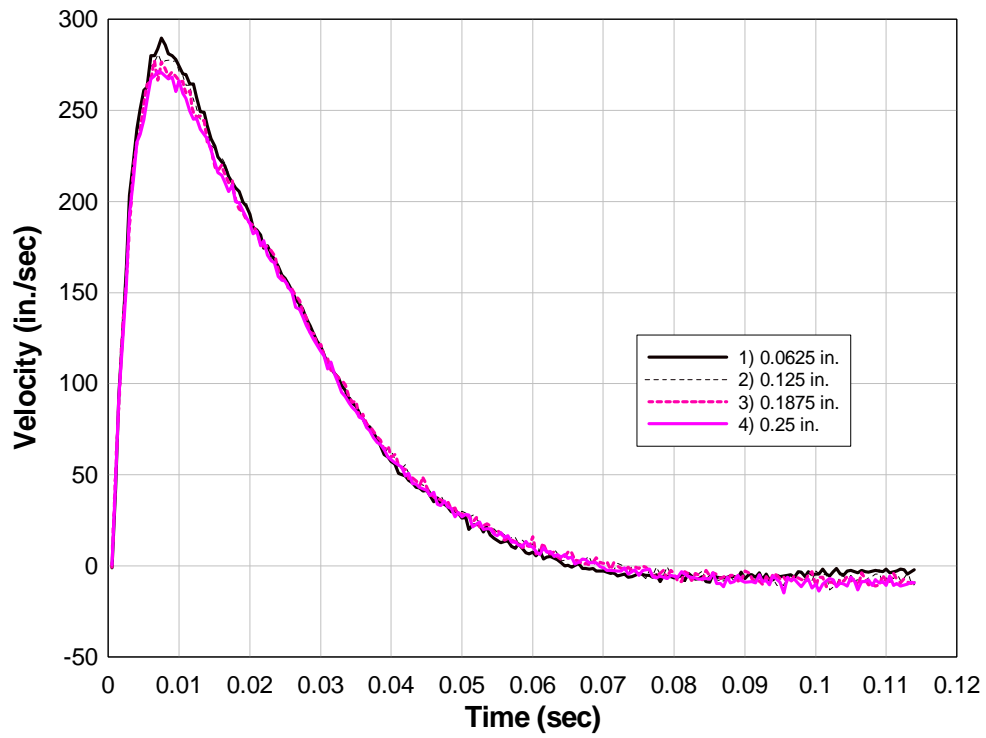


**FIG. 52. Effect of Polymer Thickness on Maximum Velocity for Load III**

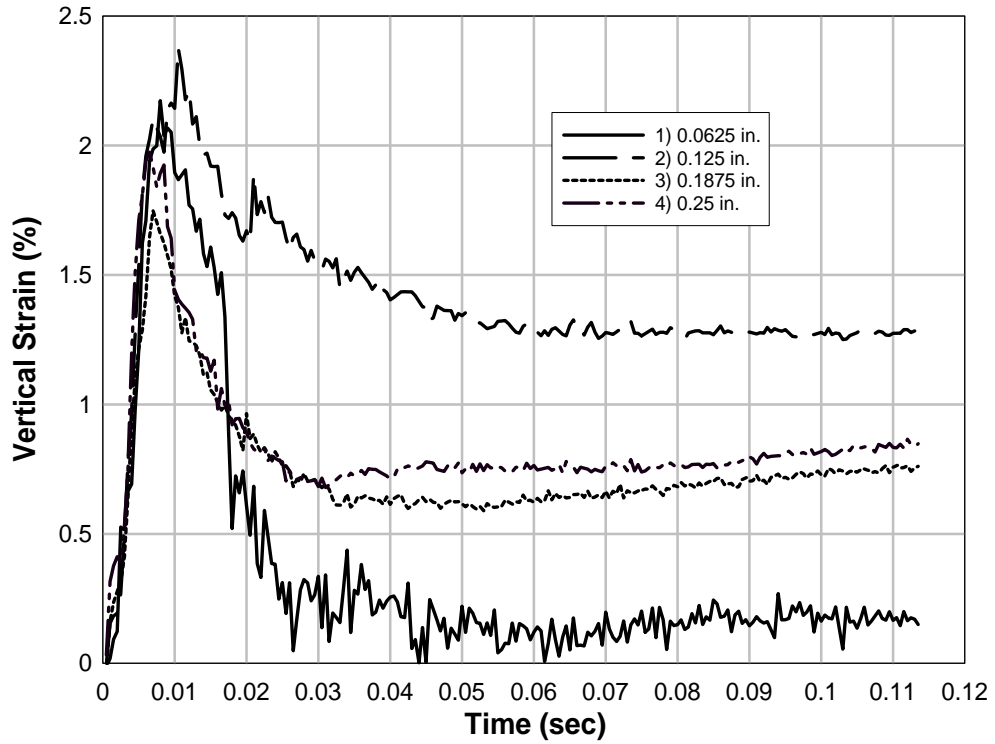


**FIG. 53. Vertical Strain in Polymer near Bottom Mortar Joint for Load I**

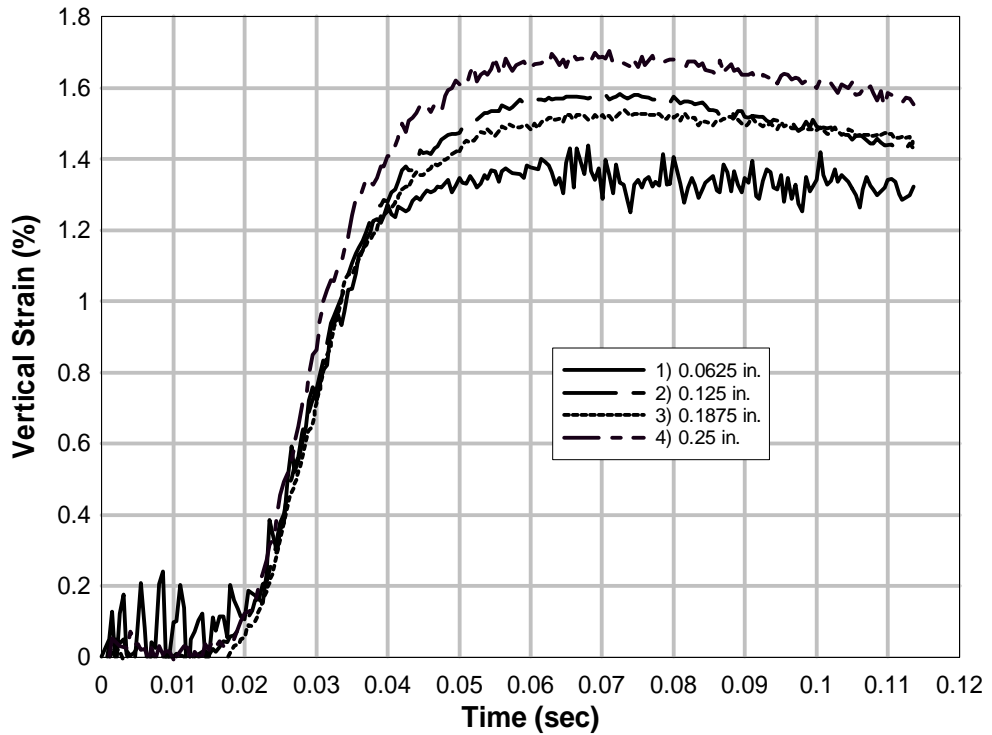


**FIG. 54. Vertical Strain in Polymer near Center Mortar Joint for Load I**

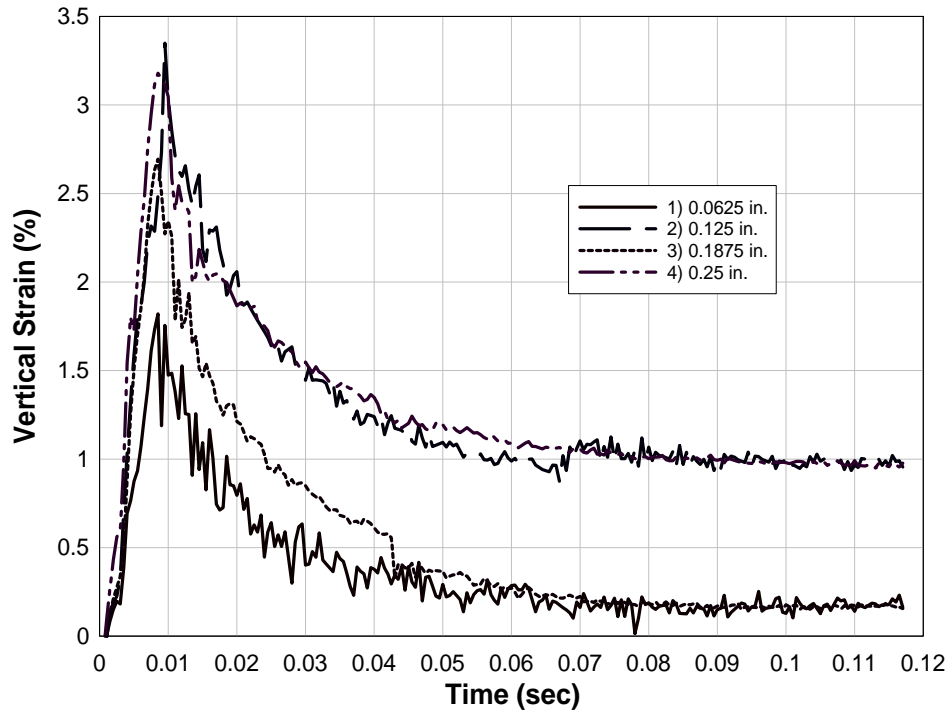


**FIG. 55. Vertical Strain in Polymer near Bottom Mortar Joint for Load III**

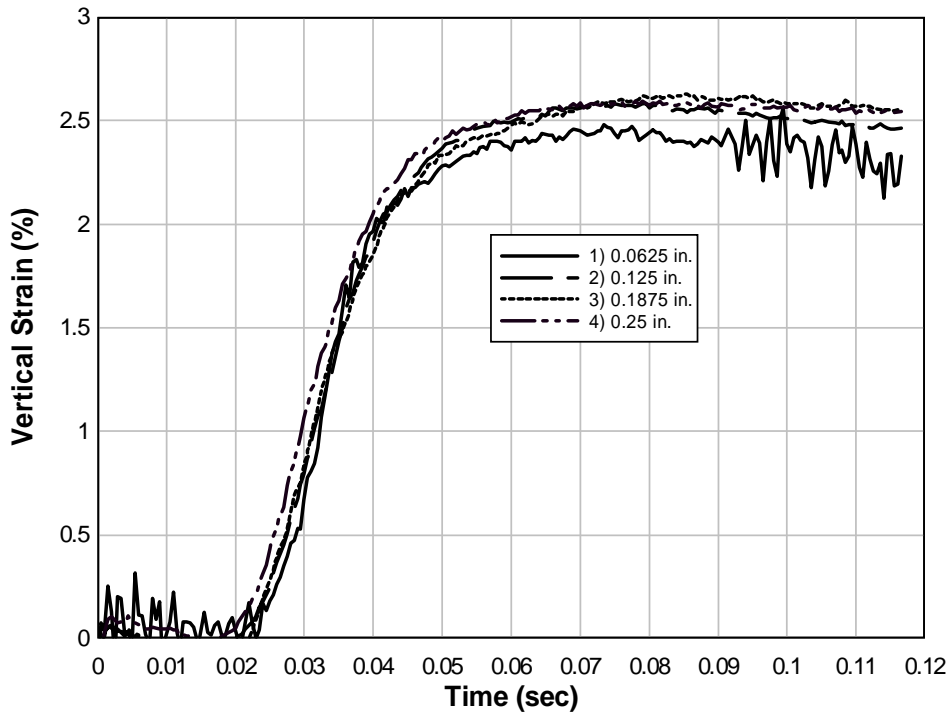


**FIG. 56. Vertical Strain in Polymer near Center Mortar Joint for Load III**

### 4.2.2.3 Conclusions

An increase in retrofit thickness increases the energy absorption capacity of the structure. For Load I, 2% decrease in displacement occurred between 0.0625 in. and 0.25 in., and the velocity decreased by 6.5%. Even for Load III, the displacement decreased by 3% and velocity decreased by 4.1% when the retrofit thickness was quadrupled. No significant difference in displacements for 0.0625 in., 0.125 in., and 0.1875 in. was observed for either load cases.

Vertical strain in the polymer near the bottom mortar joint of 1.6% to 2.4% was observed with change in polymer thickness. However, the 0.125 in. thick polymer resulted in 1.3% vertical strain. Near the mid-height, the strain varied from 1.4% to 1.7%. Under Load III, the strain in the 0.0625 in. thick polymer exhibited 1.8% strain near the bottom mortar joint. Near the center mortar joint, the strain remained close to 2.5% for all thicknesses.

The internal and kinetic energy of the polymer increases proportionately with polymer thickness. Increase in kinetic energy is due to increase in mass of the polymer, whereas increase in internal energy is due to increase in strain. Increase in polymer thickness increased energy absorption capacity and hence the internal energy of the polymer. Moreover, kinetic energy in the polymer for Load III is thrice that for Load I for equal polymer thickness because the lateral velocity of wall for Load III is higher than that for Load I.

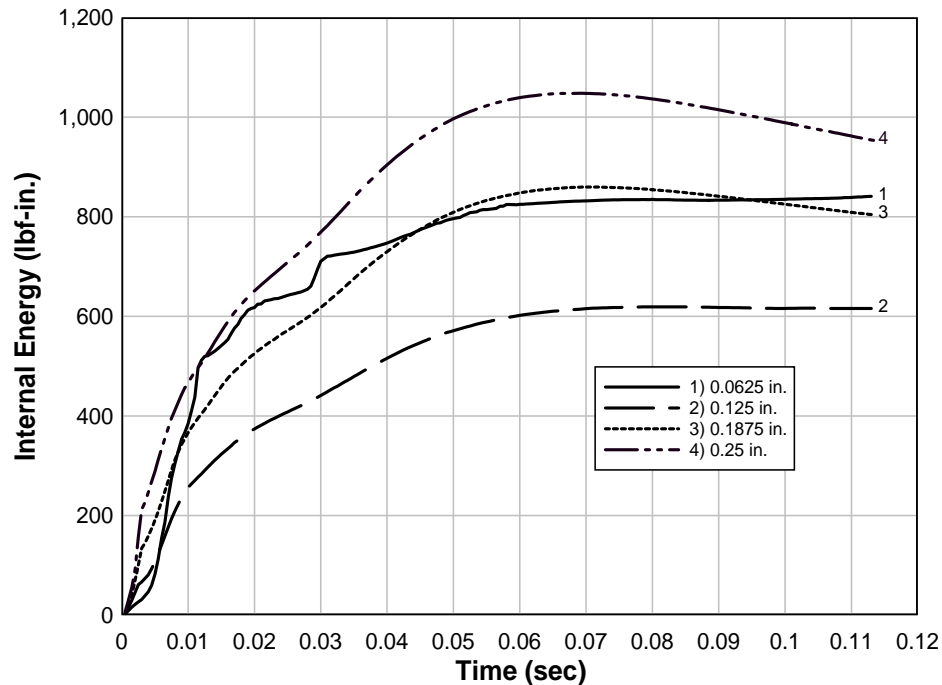
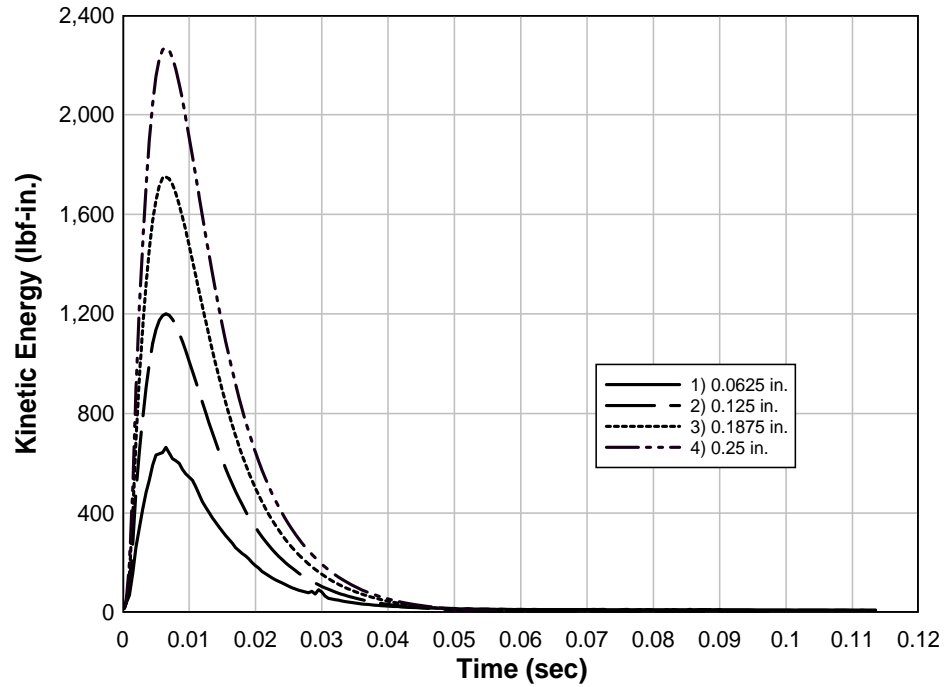
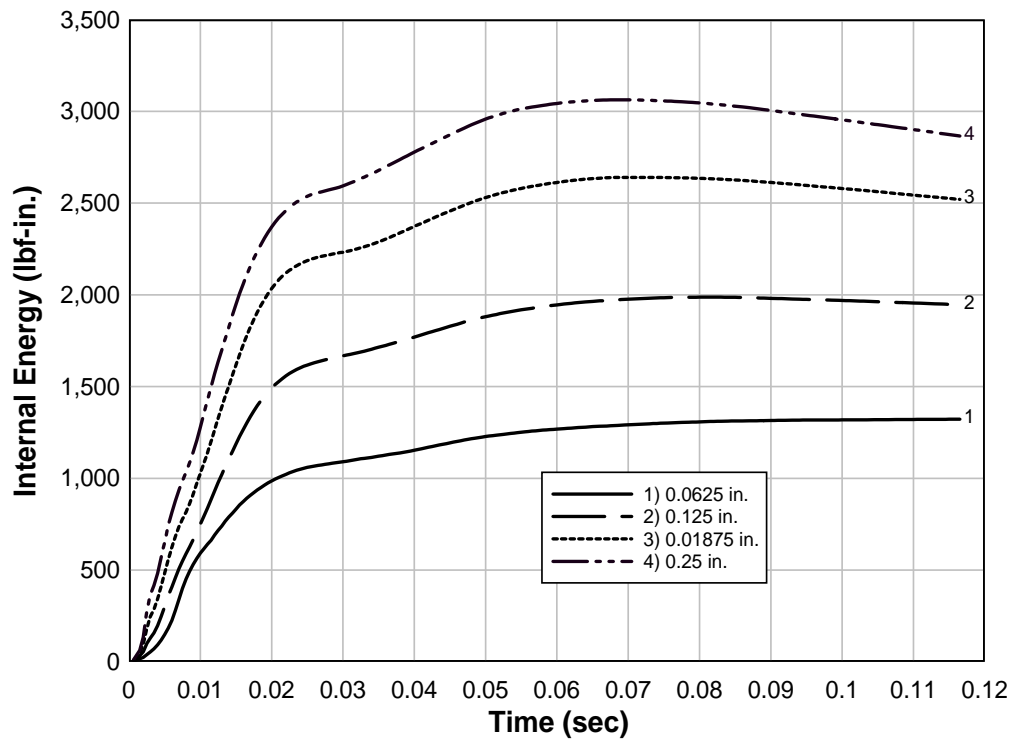


FIG. 57. Variation of Internal Energy with Polymer Thickness for Load I



**FIG. 58. Variation of Kinetic Energy with Polymer Thickness for Load I**



**FIG. 59. Variation of Internal Energy with Polymer Thickness for Load III**

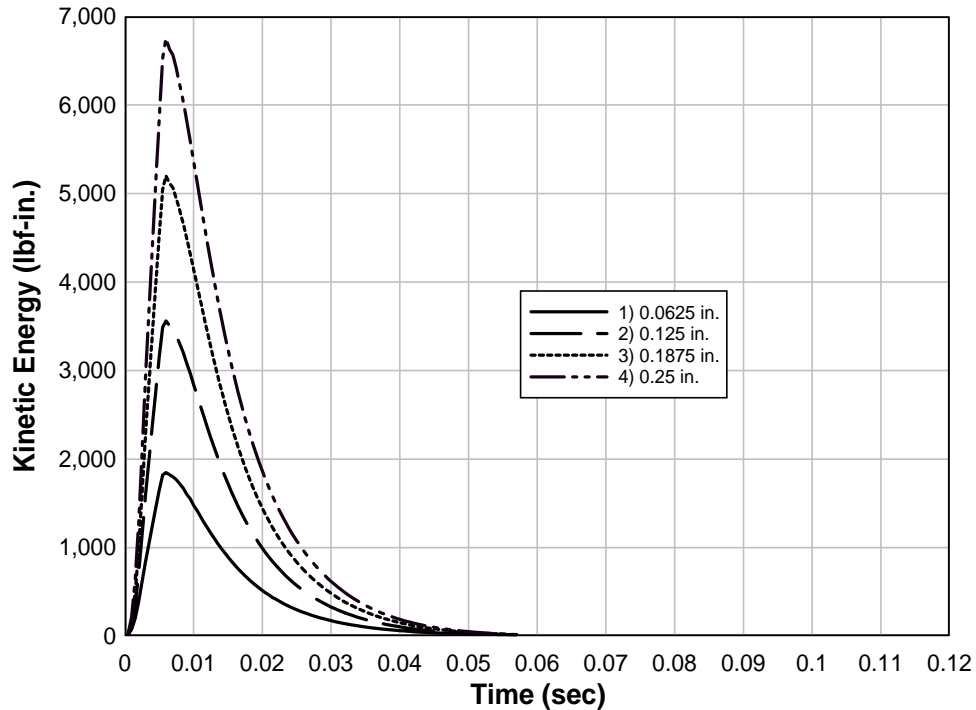


**FIG. 60. Variation of Kinetic Energy with Polymer Thickness for Load III**

### 4.2.3 Initial Modulus

The effect of initial stiffness of the polymer on the behavior of the wall was studied. Initial stiffness of the polymer was increased by multiples of 10. However, the yield stress and rupture strain input parameters were not altered. Therefore, with increase in stiffness, higher stresses were attained at lower strains. For a given yield stress, a stiffer material has less area under the stress-strain curve and hence less energy absorption capacity.

#### 4.2.3.1 Displacement and Velocity

Table 8 summarizes the maximum displacements and velocities for various values of initial modulus and the decrease in peak displacement and velocity with increase in initial elastic modulus of the polymer. Fig. 61 through Fig. 64 shows displacements and velocities for various initial moduli.

#### 4.2.3.2 Polymer Strain

Fig. 65 through Fig. 68 indicate the strains in the polymer at the bottom and center mortar joints with change in initial modulus for Load I and Load III. The maximum strains and their locations are provided in Table 9.

It should be noted that the reason why the 340000 psi case illustrated in Fig. 65 does not follow the trend of the other cases is because the strain is plotted for the same element for all of the initial modulus parameter runs and does not reflect the strain in entire polymer.

**TABLE 8. Maximum Displacement and Velocity Due to Change in Initial Modulus**

<b>Initial modulus (psi)</b>	<b>Maximum displacement (in.)</b>	<b>Time (msec)</b>	<b>Maximum velocity (in./sec)</b>	<b>Time (msec)</b>
<b>(a) Load I</b>				
34000	7.5	70.5	279.3	7.5
340000	7.4	65.5	279.0	7.0
3400000	7.3	93.0	277.8	7.5
34000000	7.3	65.0	276.4	8.0
<b>(b) Load III</b>				
34000	12.8	77.9	471.1	7.5
340000	12.5	72.4	468.1	7.0
3400000	12.3	72.4	467.9	7.0
34000000	12.5	77.9	465.9	7.0

**TABLE 9. Maximum Vertical Strain in Polymer Due to Change in Initial Modulus**

<b>Initial modulus (psi)</b>	<b>Maximum strain (%)</b>	<b>Location</b>	<b>Time (msec)</b>
<b>(a) Load I</b>			
34,000	3.1	Bottom Mortar Joint	6.5
340,000	2.1	Bottom Mortar Joint	7.0
3,400,000	1.6	Bottom Mortar Joint	7.5
34,000,000	1.7	Top Mortar Joint	12.5
<b>(b) Load III</b>			
34,000	5.8	Quarter Height	20.0
340,000	4.2	Quarter Height	15.0
3,400,000	3.0	Quarter Height	26.5
34,000,000	3.2	Quarter Height	58.0

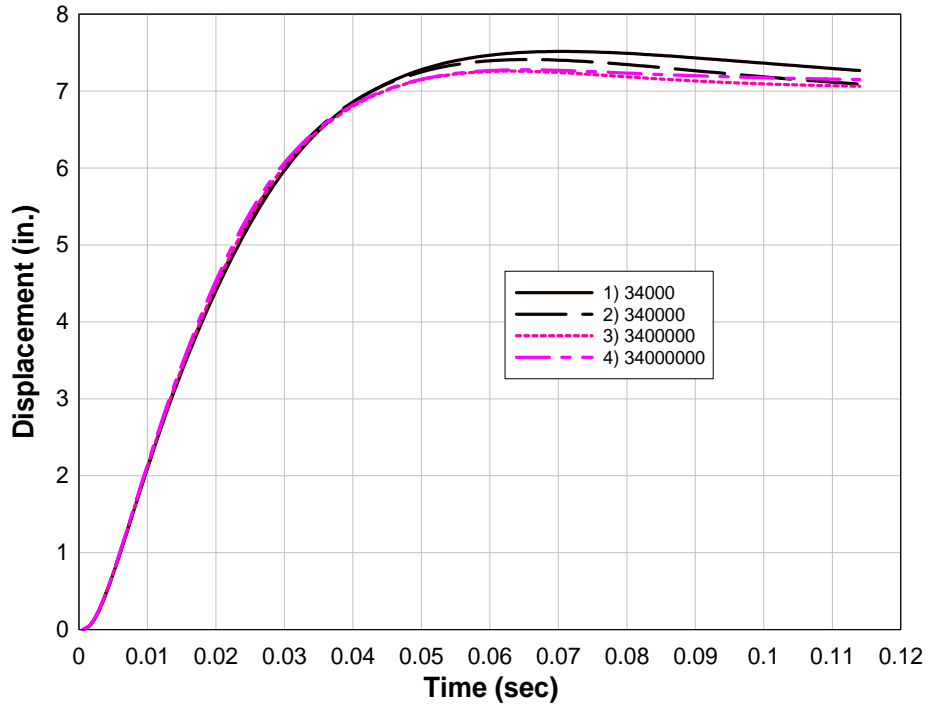


**FIG. 61. Effect of Initial Modulus on Maximum Displacement for Load I**

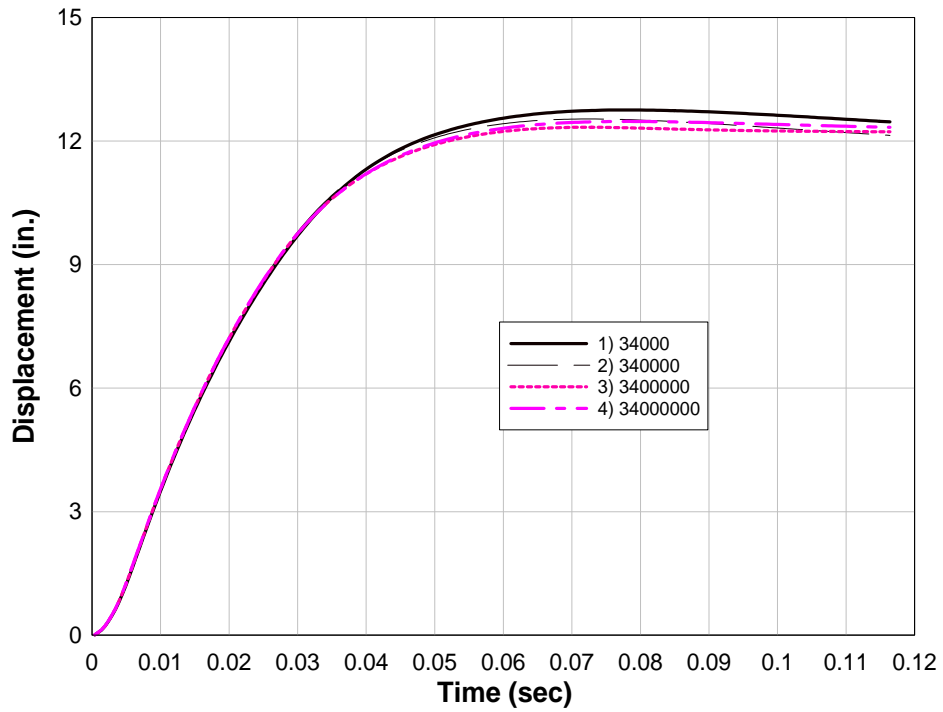


**FIG. 62. Effect of Initial Modulus on Maximum Displacement for Load III**

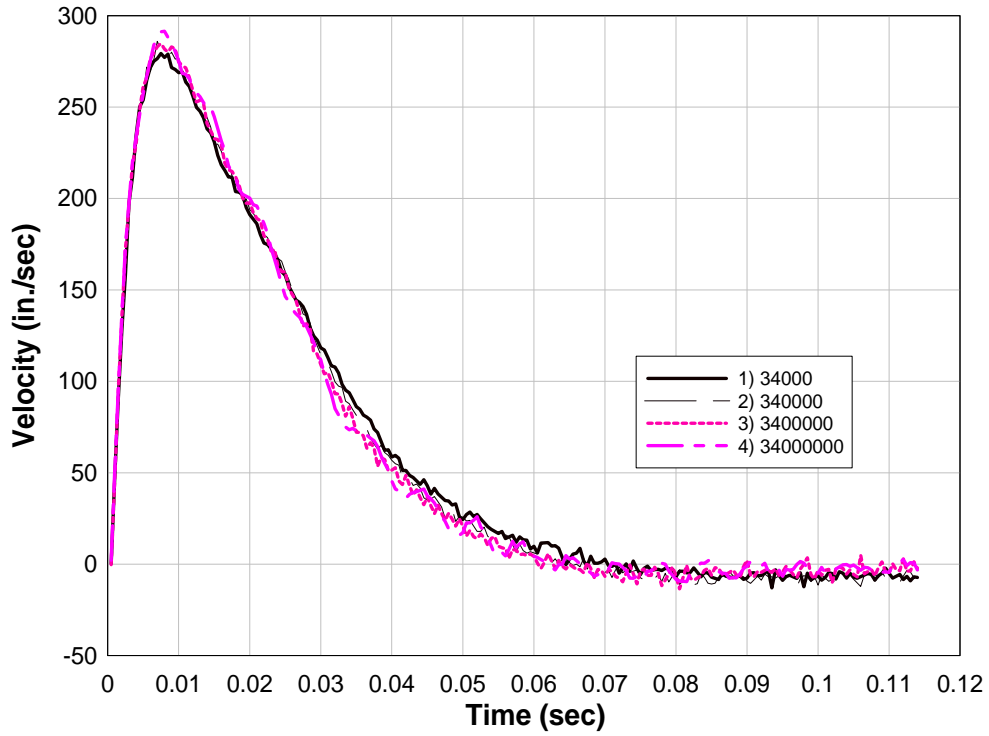


**FIG. 63. Effect of Initial Modulus on Maximum Velocity for Load I**

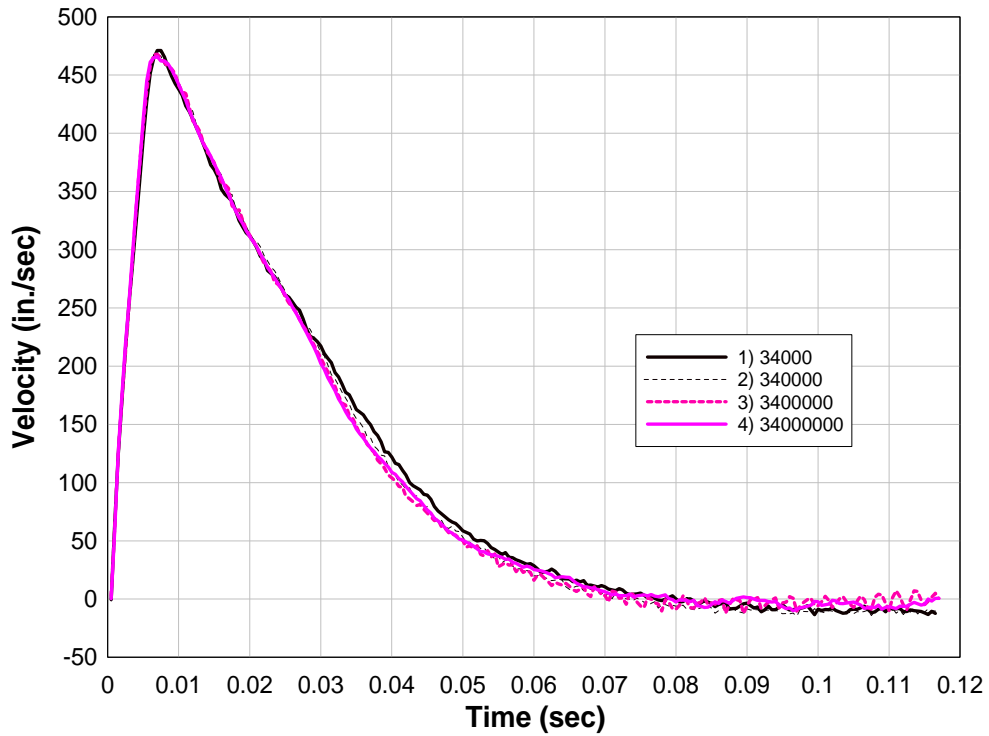


**FIG. 64. Effect of Initial Modulus on Maximum Velocity for Load III**

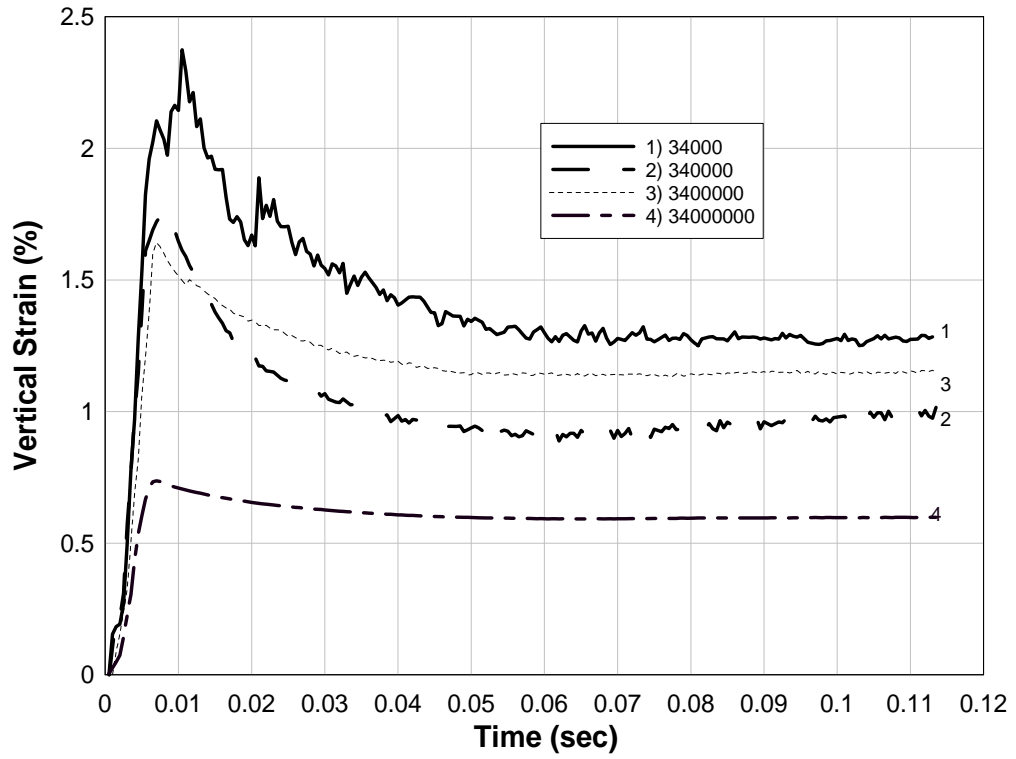


FIG. 65. Vertical Strains in the Polymer near Bottom Mortar Joint for Load I

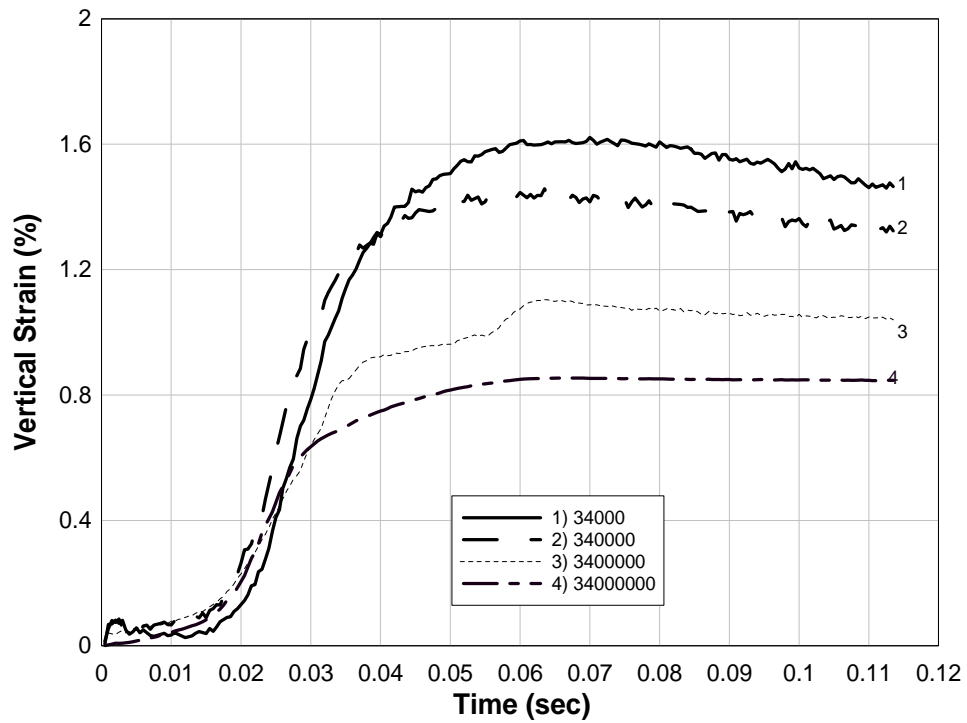


FIG. 66. Vertical Strains in the Polymer near Center Mortar Joint for Load I

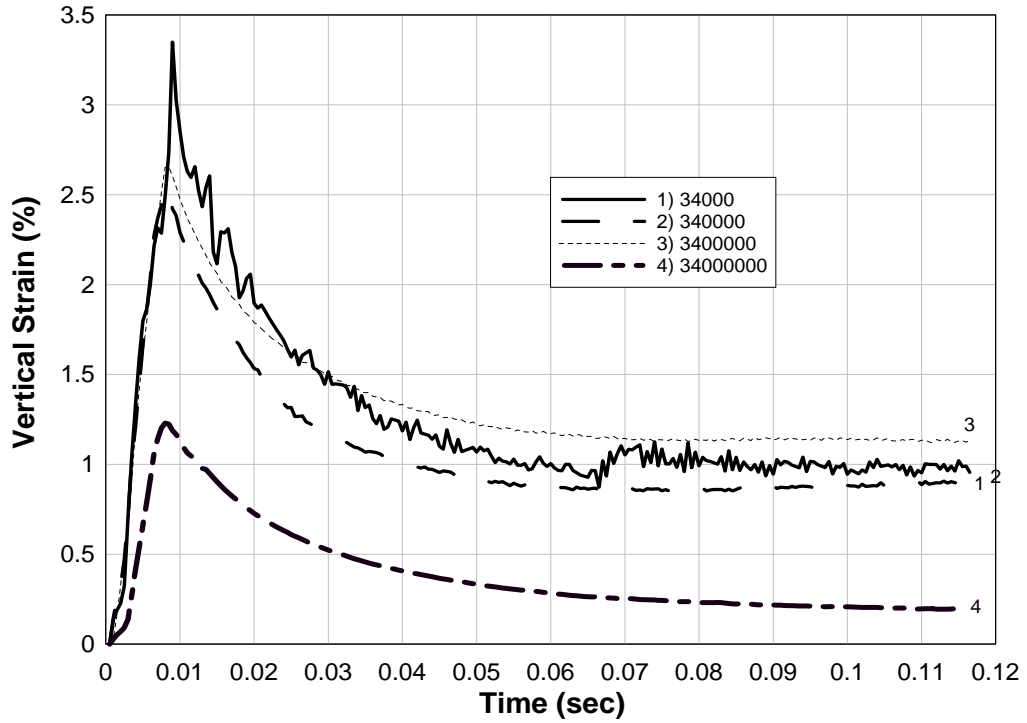


FIG. 67. Vertical Strains in the Polymer near Bottom Mortar Joint for Load III

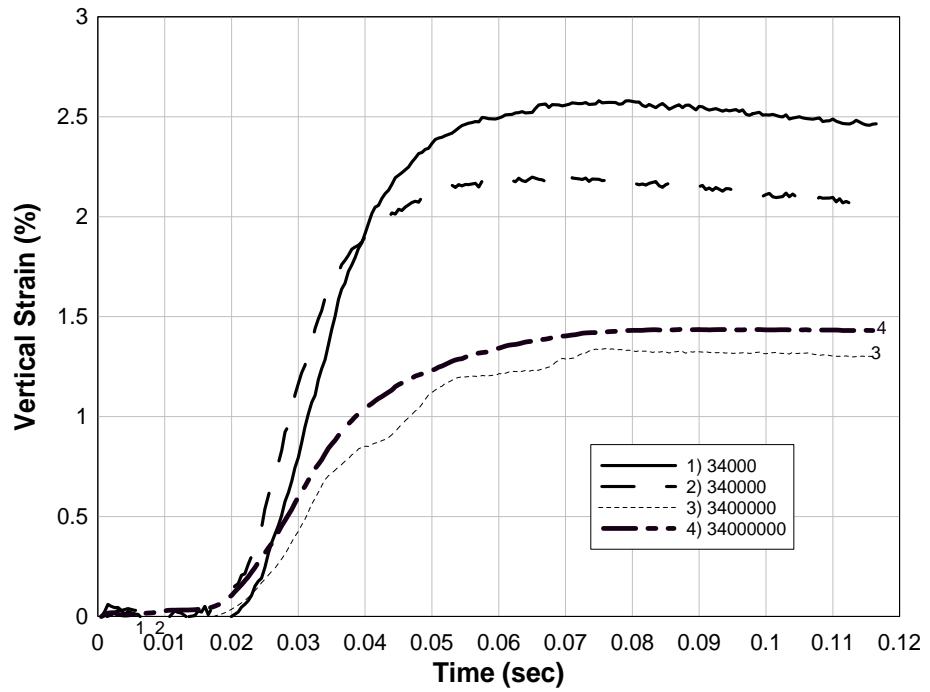


FIG. 68. Vertical Strains in the Polymer near Center Mortar Joint for Load III

#### **4.2.3.3 Internal Energy and Kinetic Energy in the Polymer**

Fig. 69 through Fig. 72 demonstrates the variation in internal energy and kinetic energy with change in initial modulus for Load I and Load III.

#### **4.2.3.4 Conclusions**

The change in initial modulus has little effect on maximum velocity and displacement due to dominance of wall mass on the global displacement behavior of the system. Polymer near the bottom mortar joint incurs the highest vertical strain at early phases of the response. In contrast, the polymer near the center mortar joint does not significantly strain until flexural displacements occur. As the initial stiffness of the polymer is increased by one order of magnitude, the strain in the polymer near the bottom mortar joint and center mortar joint decreases by 20% to 25% and 10% to 15%, respectively. Kinetic energy does not vary with increase in polymer stiffness since the mass and lateral velocities do not change significantly. However, the increase in internal strain energy with stiffness indicates an increase in energy absorbed by the polymer with increase in initial modulus. As the polymer stiffness is increased by one order of magnitude, the internal energy absorbed by the polymer increases by a multiple of 2.5 to 3 for Load I and 1.5 to 2.5 for Load III.

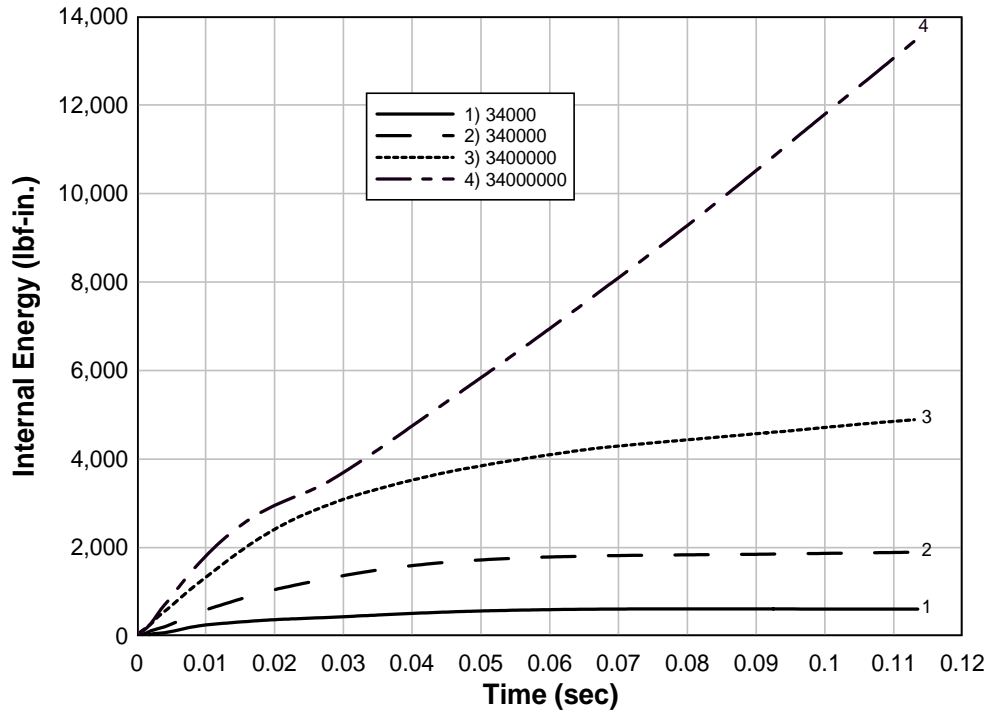


**FIG. 69. Variation of Internal Energy in Polymer with Initial Modulus for Load I**

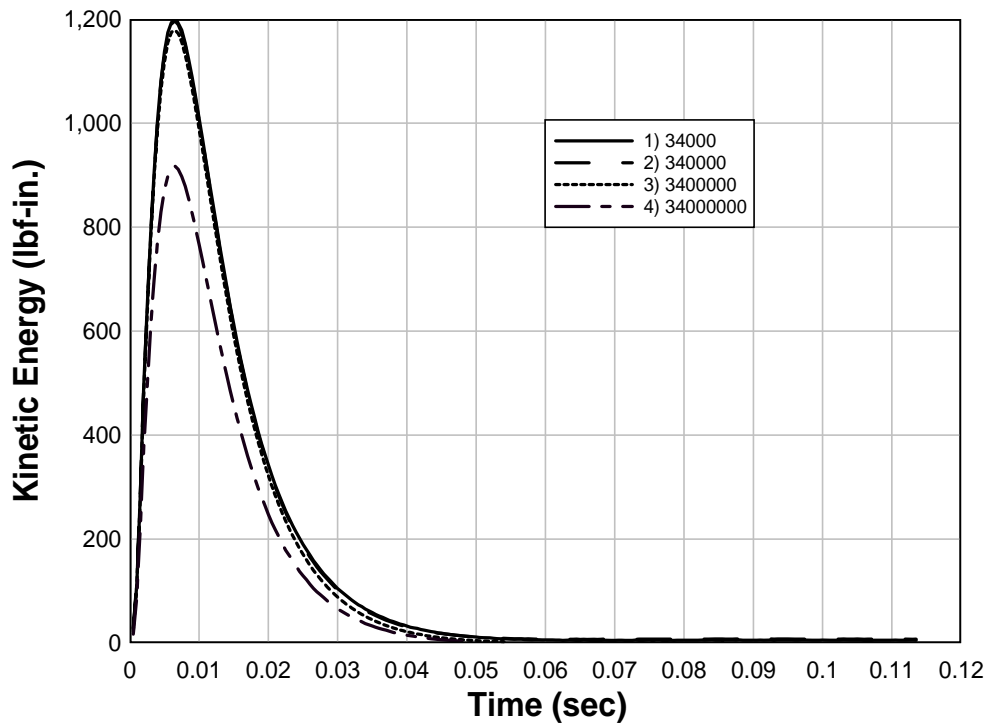


**FIG. 70. Variation of Kinetic Energy in Polymer with Initial Modulus for Load I**

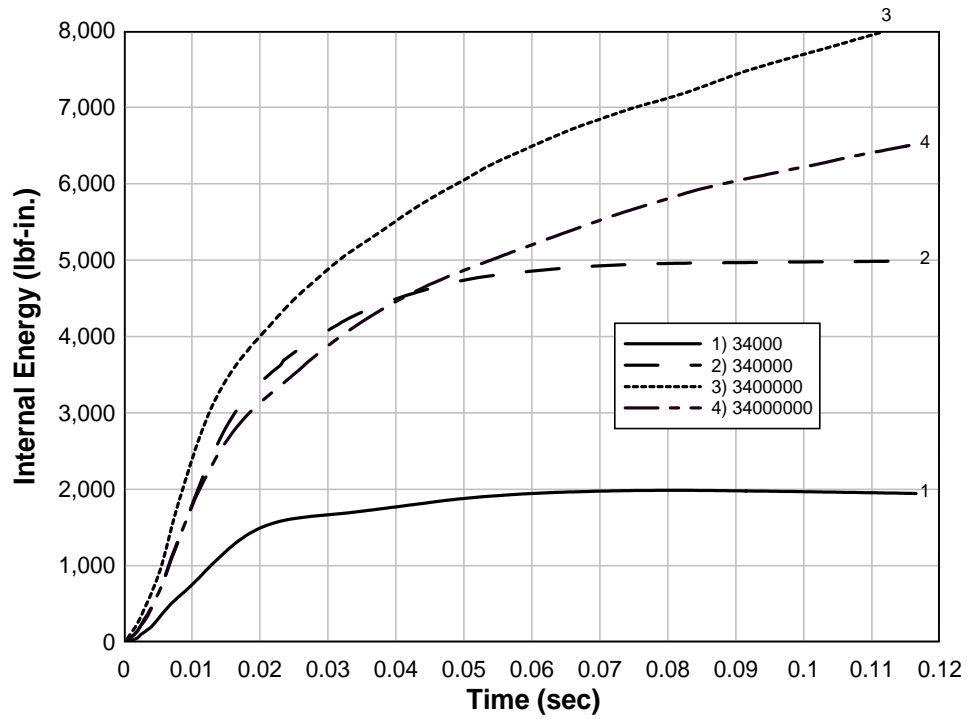


**FIG. 71. Variation of Internal Energy in the Polymer with Initial Modulus for Load III**

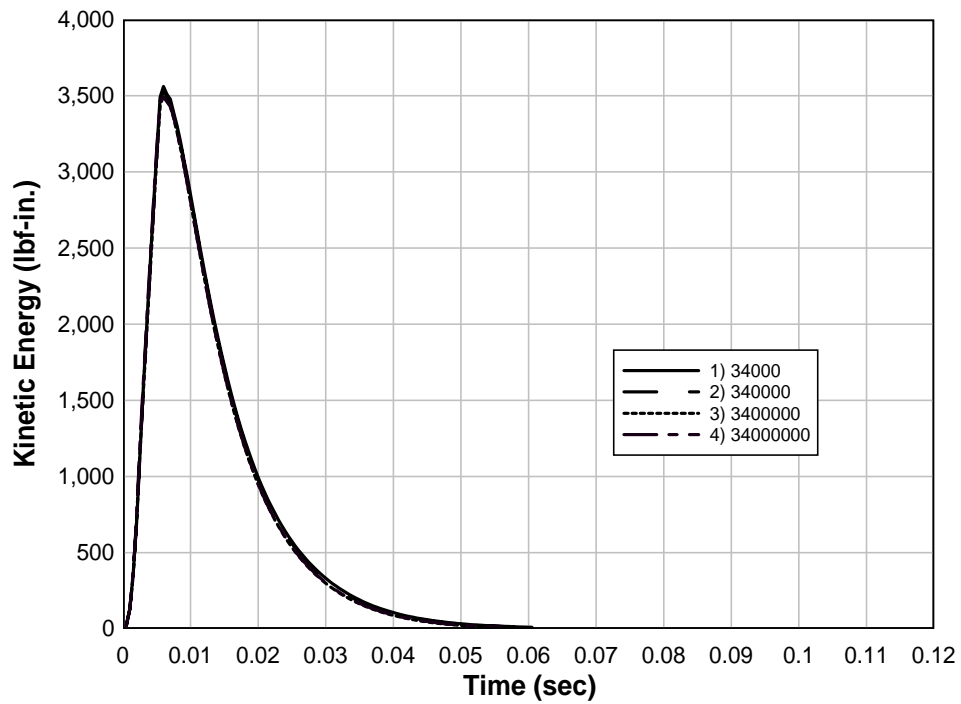


**FIG. 72. Variation of Kinetic Energy in the Polymer with Initial Modulus for Load III**

#### **4.2.4 Yield Strength**

The effect of yield strength of the polymer is important for strain rate dependent polymers since the yield stress of polymeric materials is a function of strain rate. The polymer used in the baseline model had a yield stress of 1400 psi. The stresses of the baseline analyses did not exceed this yield stress for Load I and Load III. Therefore for the input sensitive study, 800 psi and 1000 psi yield stress were used for Load I and Load III. A simple definition of the polymer stress-strain curve involving only the initial modulus, yield stress, tangent modulus, and rupture strain was used for the yield strength parameter investigation.

##### **4.2.4.1 Displacement and Velocity**

Fig. 73 through Fig. 76 show that a change in yield strain did not affect the lateral displacement and velocity of the wall.

##### **4.2.4.2 Vertical Strain**

Fig. 77 through Fig. 80 show the variation in vertical strain in polymer near mid-height and near bottom mortar joint for Load III and Load I.

##### **4.2.4.3 Internal and Kinetic Energy**

Fig. 81 through Fig. 84 show the variation of internal energy and kinetic energy of polymer Load I and Load III with change in yield stress of the polymer.

##### **4.2.4.4 Plastic Strain**

Plastic strains were observed in the polymer near the bottom mortar joint. This again indicated that strain in the polymer near the bottom mortar joint is higher than that near the mid-height. Fig. 85 and Fig. 88 show plastic strain time histories in the polymer near bottom mortar joint for Load I and Load II, respectively. The baseline model did not show any plastic strain in polymer with the decrease in yield stress. While the kinetic energy of the polymer remained unchanged, there was increase in internal (strain) energy of the polymer with the decrease in yield stress. In case of Load I, 3.7% and 5.2% plastic strain was noted in the polymer near the bottom interface for 1000 psi and 800 psi yield stress, respectively. While for Load III, the polymer exhibited plastic strain of 4.8% and 6.7% for 1000 psi and 800 psi yield stress, respectively.

#### **4.2.5 Top Clearance**

The top clearance refers to the space between the top-most block and the roof boundary. Top clearance affects the compressive forces in the vertical direction exerted by the roof on the blocks by restricting the vertical movement of blocks. This may result in crushing of blocks and formation of interlocked arch of the wall, called arching. The amount of arching depends on the space between the top block and the roof boundary. The baseline model did not result in upward movement of the top block (Fig. 88). This was attributed to (1) the shear displacement at the mortar joints, and (2) the strain of some of the front face shell elements exceeded the concrete fracture strain, allowing the front side of the wall to move downward. Therefore, the space between the top block and

the rigid boundary did not affect model behavior. Fig. 89 and Fig. 90 show the vertical displacement time histories of front and back of the block under Load I and Load III, respectively.

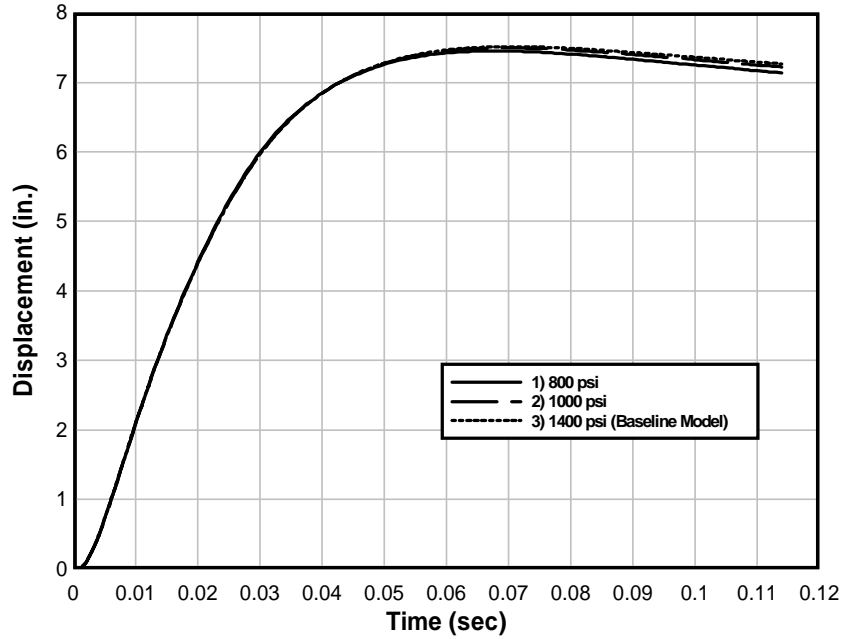


**FIG. 73. Effect of Variation in Polymer Yield Stress on Displacement of Wall for Load I**

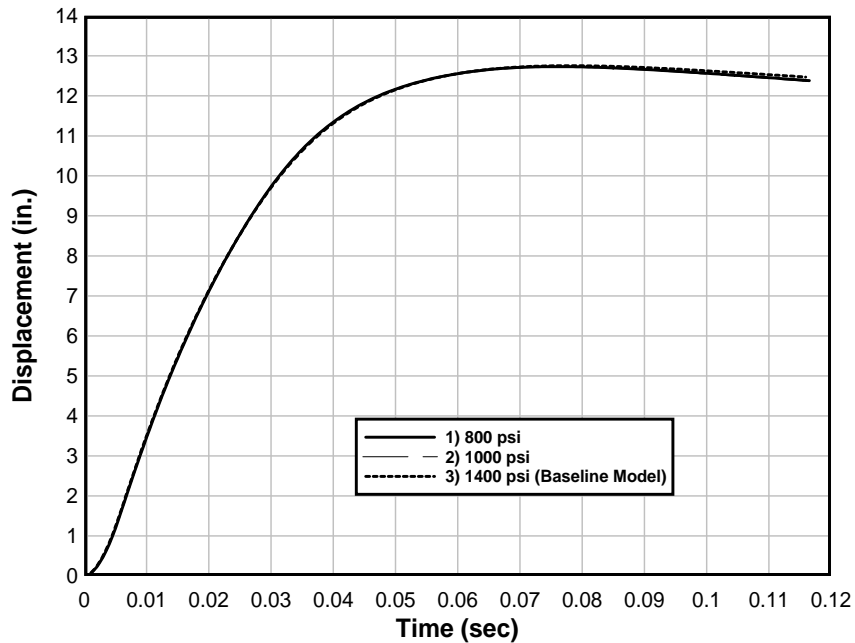


**FIG. 74. Effect of Variation in Polymer Yield Stress on Displacement of Wall for Load III**

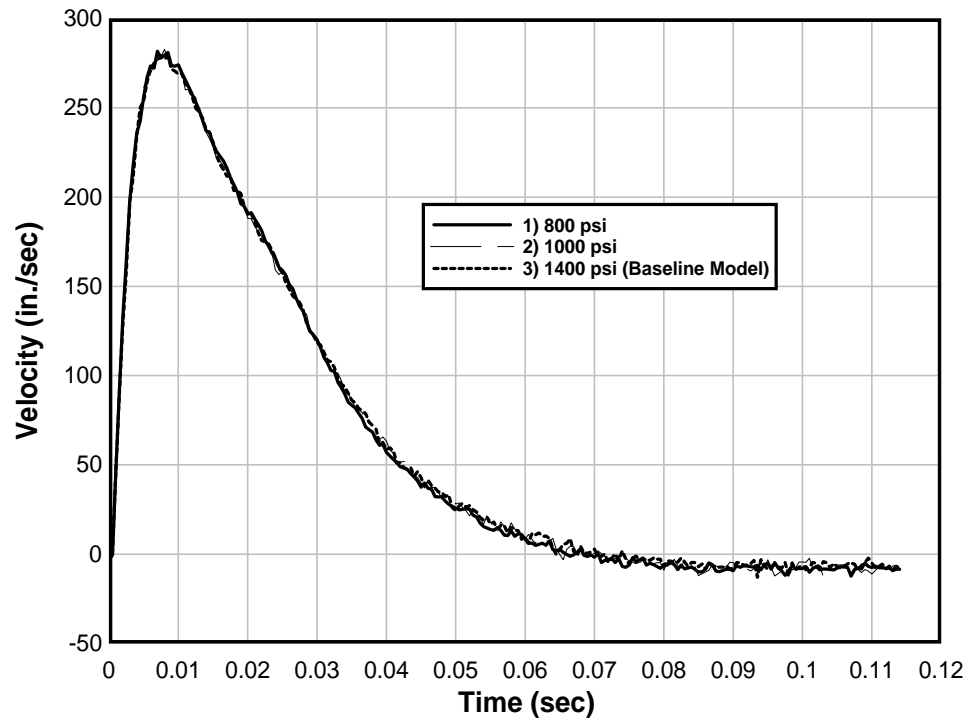


**FIG. 75. Effect of Variation in Polymer Yield Stress on Velocity of Wall for Load I**

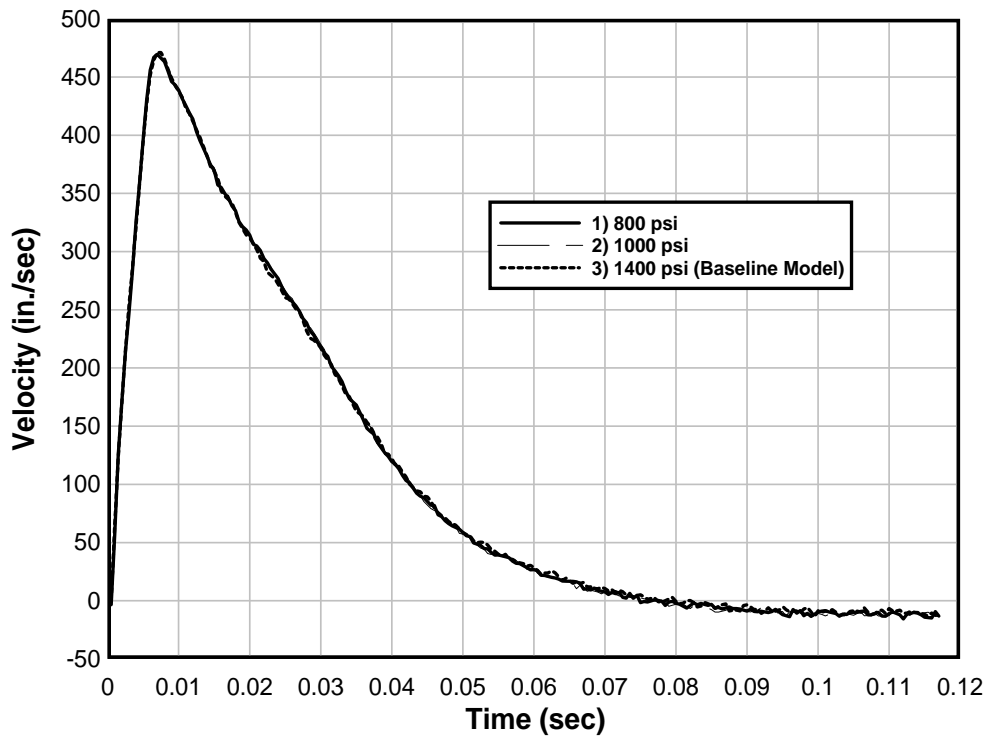


**FIG. 76. Effect of Variation in Polymer Yield Stress on Velocity of Wall for Load III**

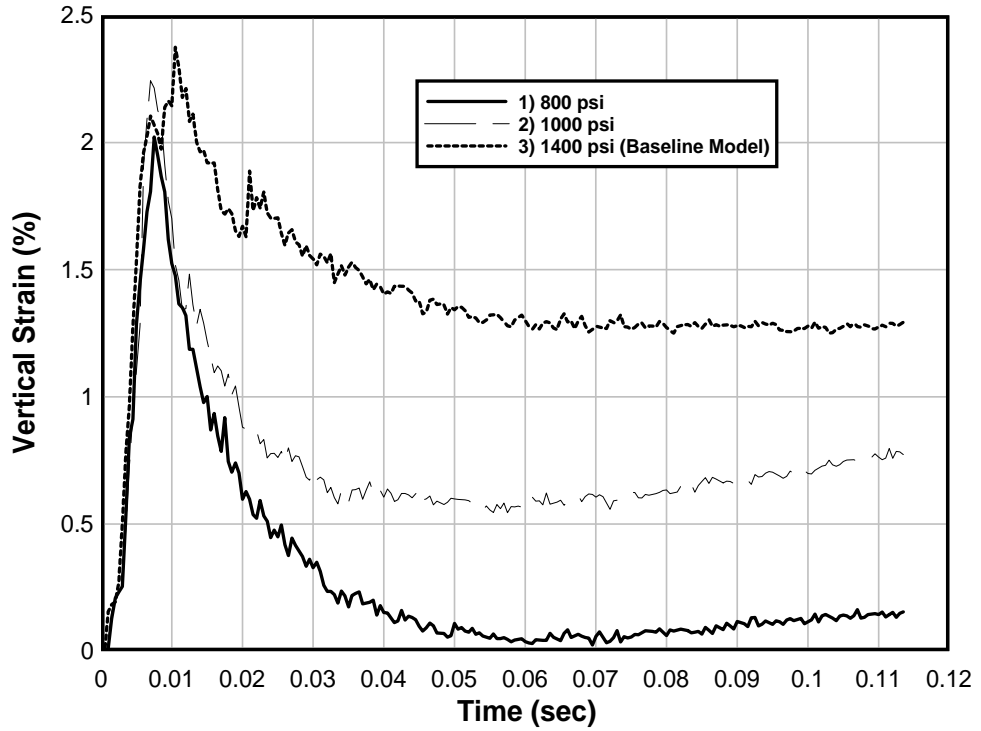


**FIG. 77. Vertical Strain in Polymer near Bottom Mortar Joint for Load I**

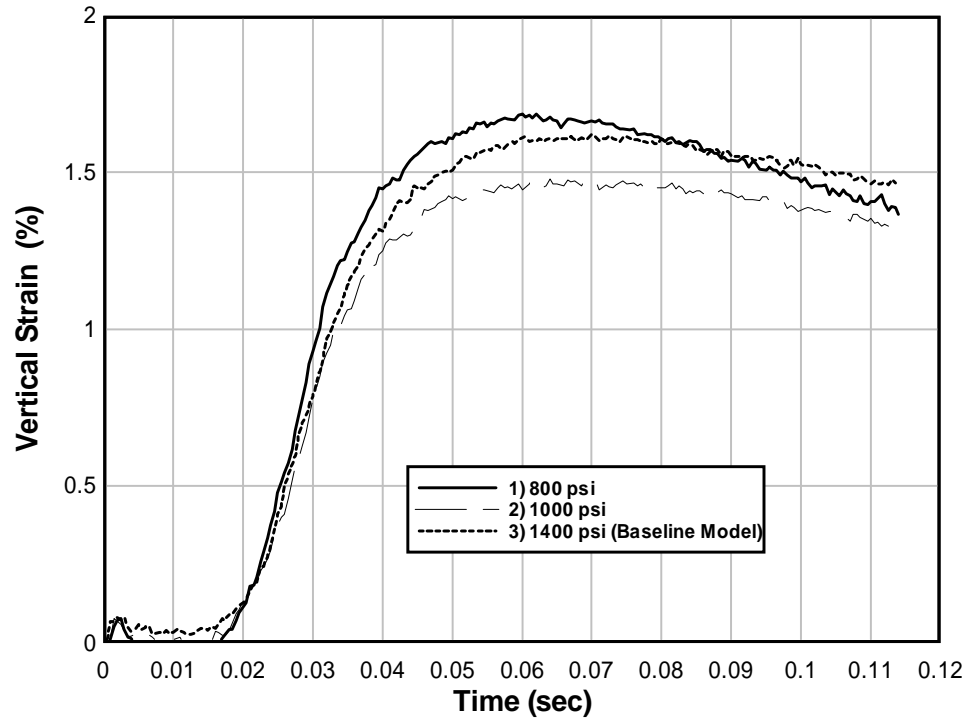


**FIG. 78. Vertical Strain in Polymer near Center Mortar Joint for Load I**

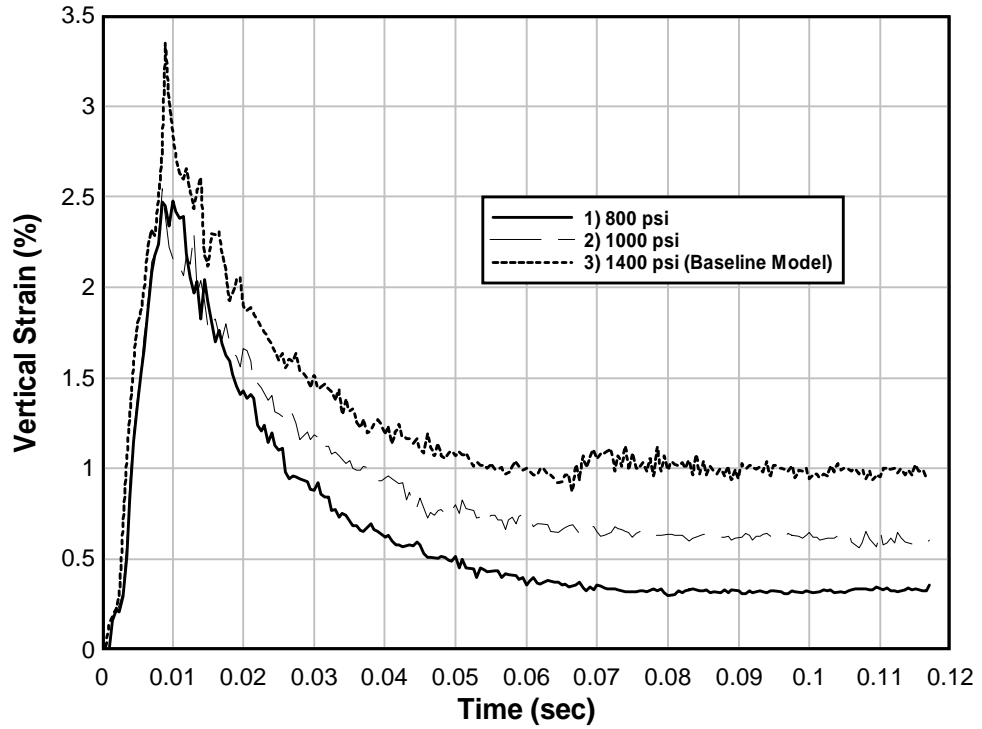


FIG. 79. Vertical Strain in Polymer near Bottom Mortar Joint for Load III

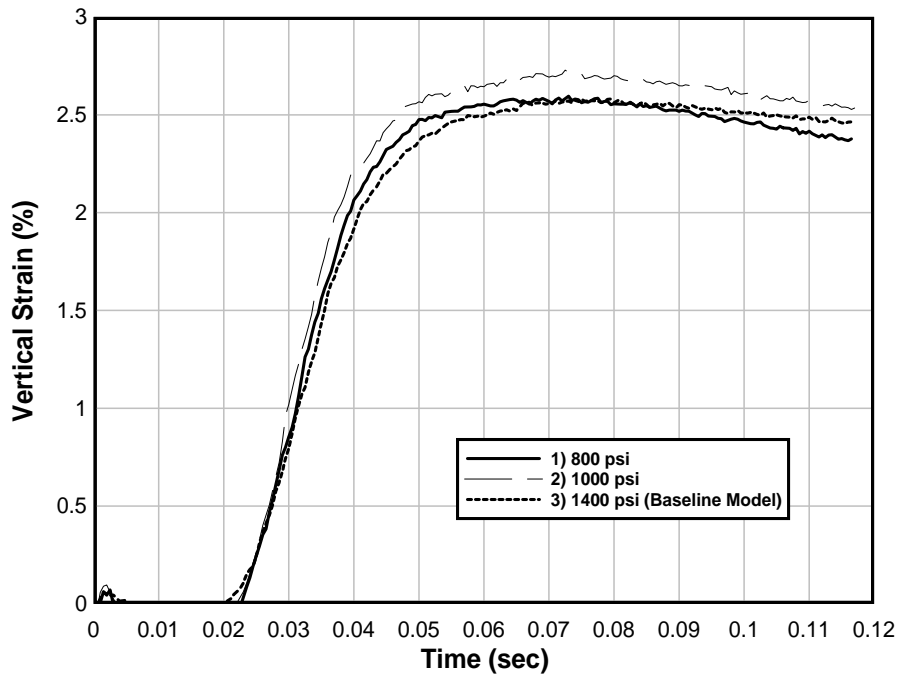
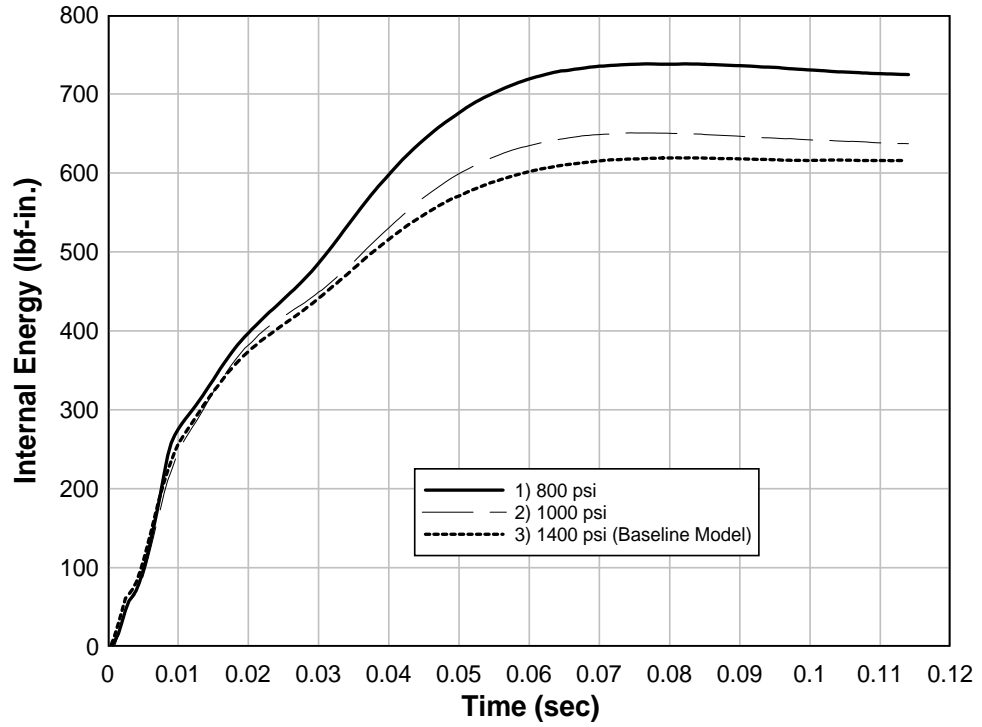
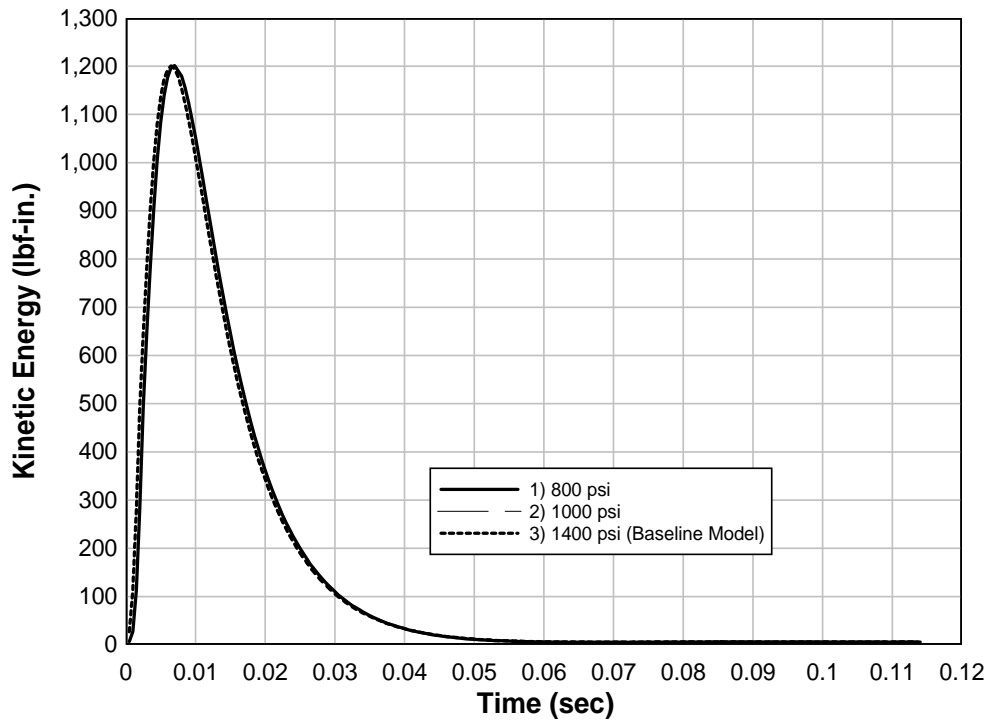


FIG. 80. Vertical Strain in Polymer near Center Mortar Joint for Load III



**FIG. 81. Variation of Internal Energy with Polymer Yield Stress for Load I**



**FIG. 82. Variation of Kinetic Energy with Polymer Yield Stress for Load I**

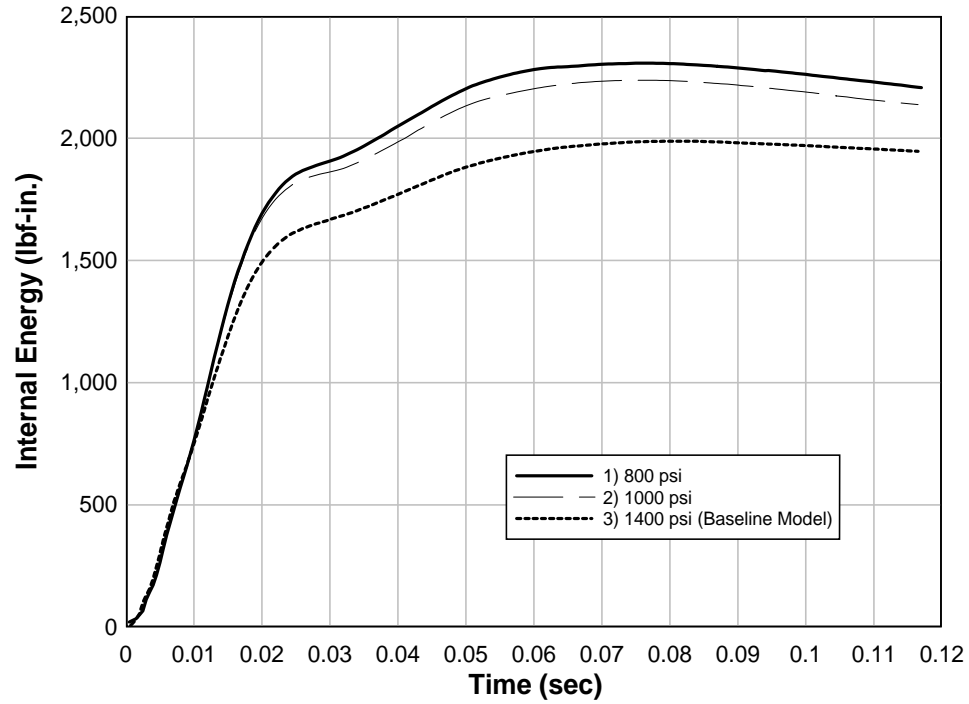


**FIG. 83. Variation of Internal Energy with Polymer Yield Stress for Load III**

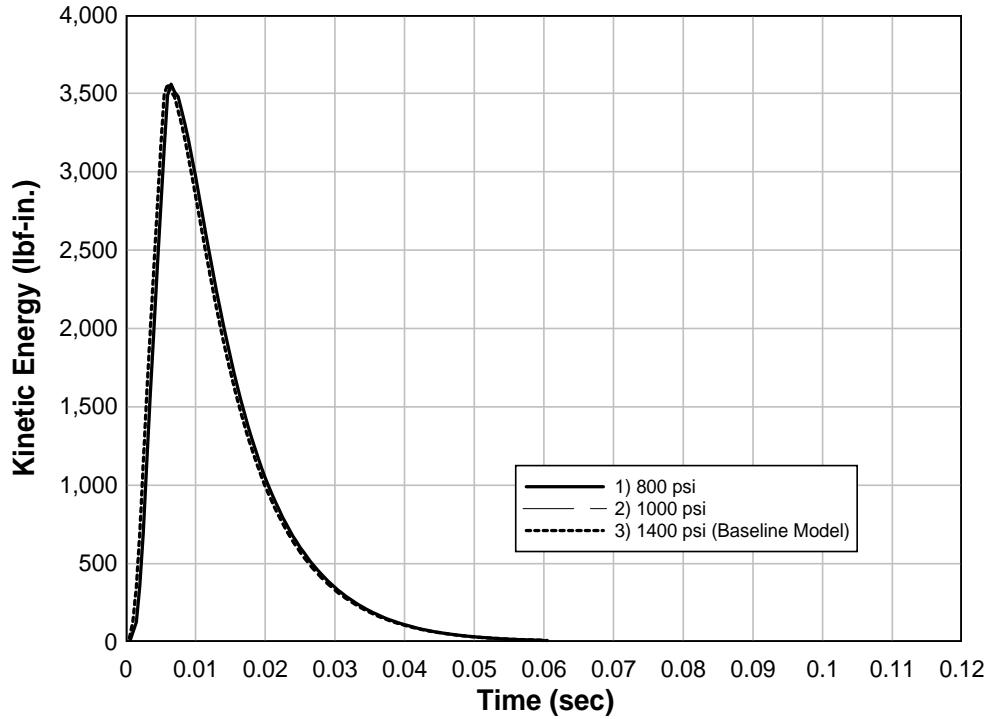


**FIG. 84. Variation of Kinetic Energy with Polymer Yield Stress for Load III**

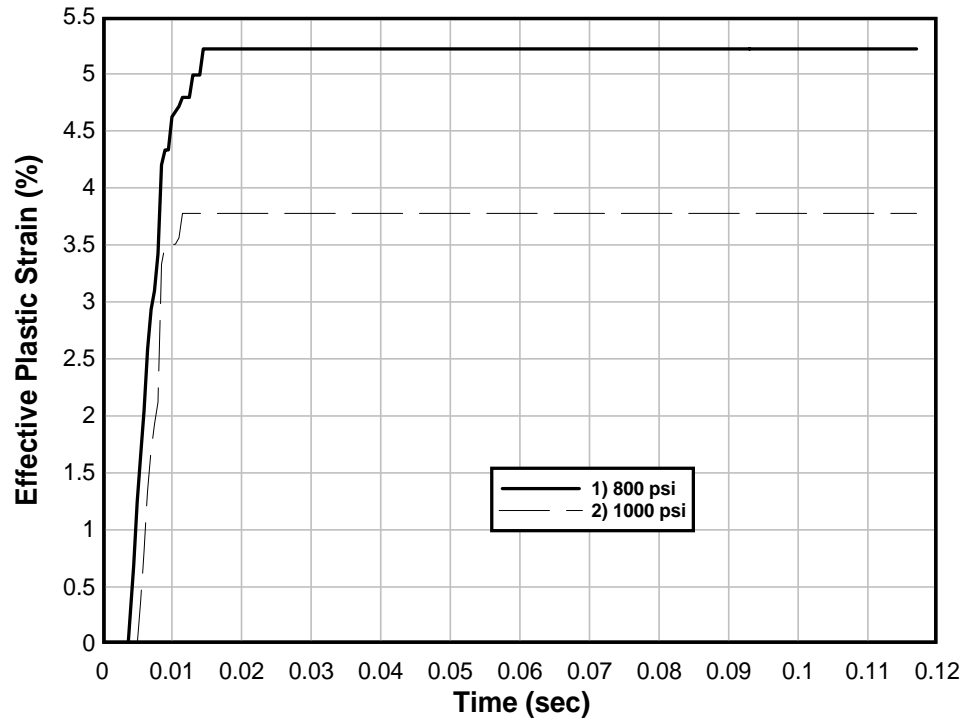


**FIG. 85. Plastic Strain in Polymer near Bottom Mortar Joint for Load I**

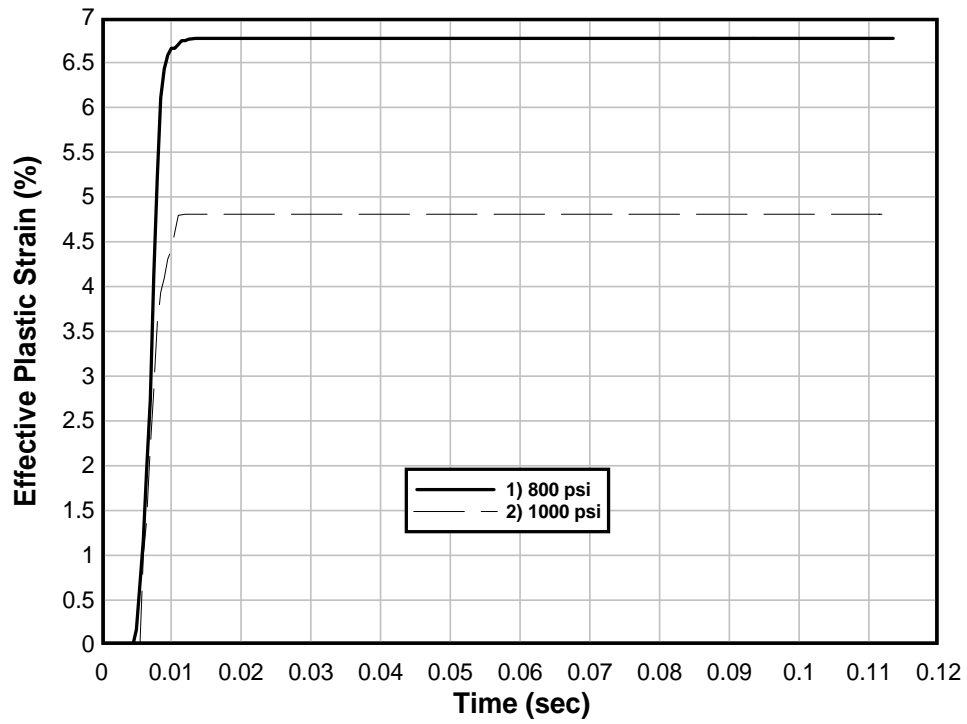


**FIG. 86. Plastic Strain in Polymer near Bottom Mortar Joint for Load III**

#### 4.2.6 Bond Strength between Mortar and Blocks

The effect of change in mortar joint bond strength on the wall behavior was evaluated. The bond strength input parameters for the mortar joint includes normal and shear stress limits. A mortar joint fails when the stresses between two surfaces exceed normal or shear stress criteria. As discussed in Section 3.12.2, the type of failure at the mortar layer depends on its location in the wall. The center layer separates under tension, whereas the end mortar joints separate in shear. The baseline model has a NFLS and SFLS of 100 psi and 250 psi, respectively. Other than the baseline model, the following two cases were analyzed for Load I and Load III by varying values of normal and shear failure. One case had stronger mortar bond than the baseline model, and the other had zero mortar bond.

##### 4.2.6.1 Normal Failure Stress = 175 psi; Shear Failure Stress = 475 psi

This case has stronger failure criteria than the baseline model. A lower tension failure criteria results in separation of the interfaces in tension prior to separation in shear. For this case, very little shear was observed at the bottom mortar joint. Instead, these blocks failed in tension. The center blocks opened up to 1.03 in. This resulted in high stresses in the polymer elements. Since tensile separation was dominant over shear, all of the layers experienced normal failure.

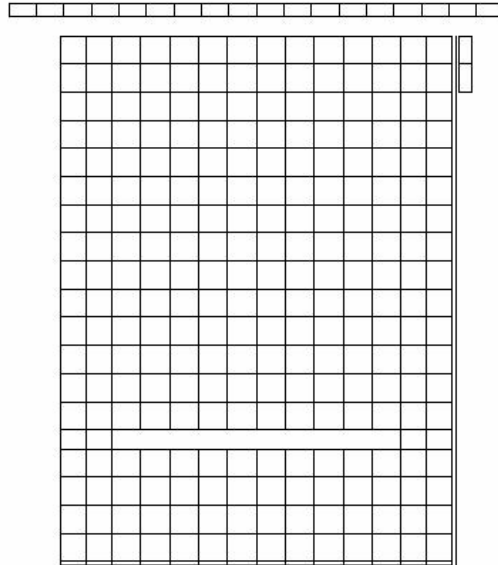


**FIG. 87. Top Block and Roof (Initial State)**

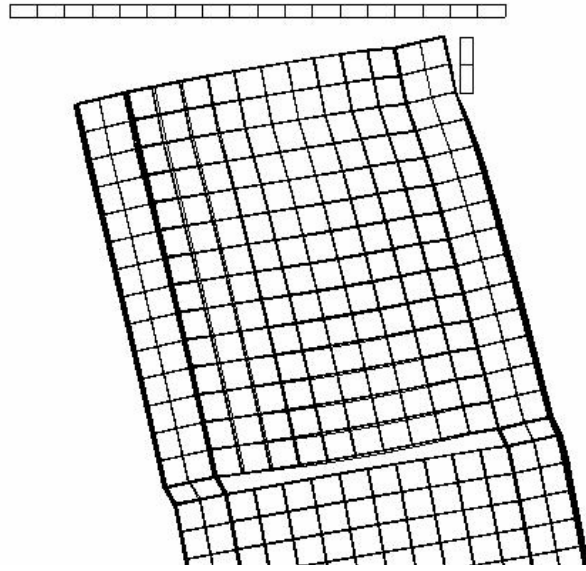


**FIG. 88. Deformation of Top Block**

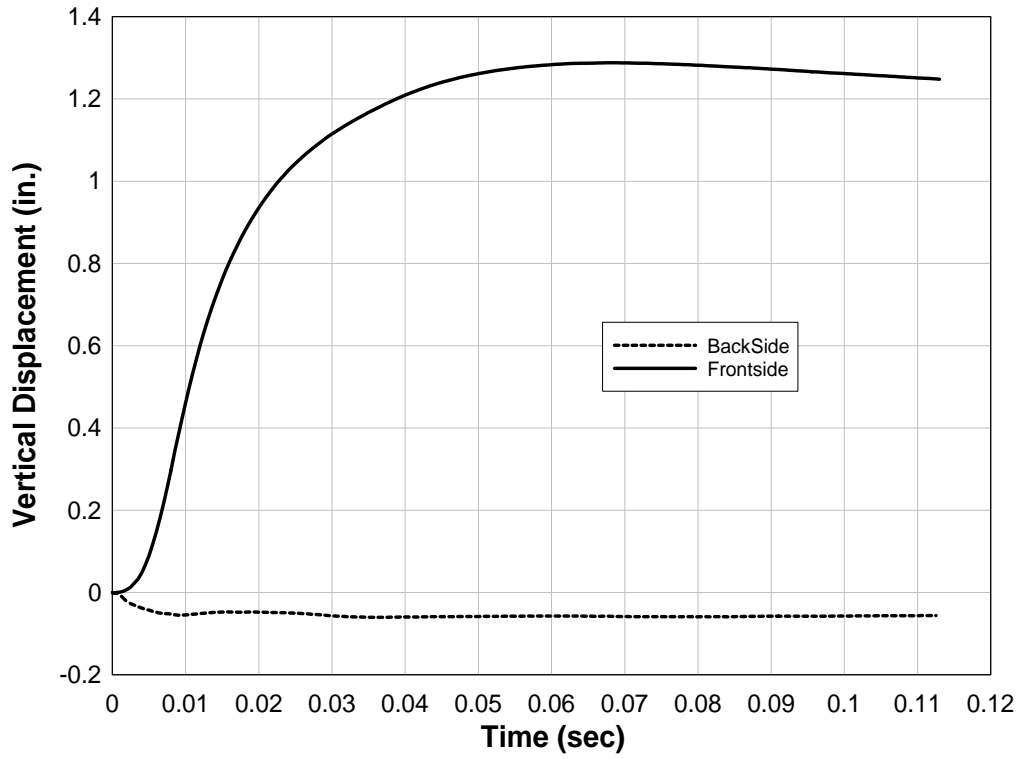


**FIG. 89. Vertical Displacement Time History of Top Block for Load I**

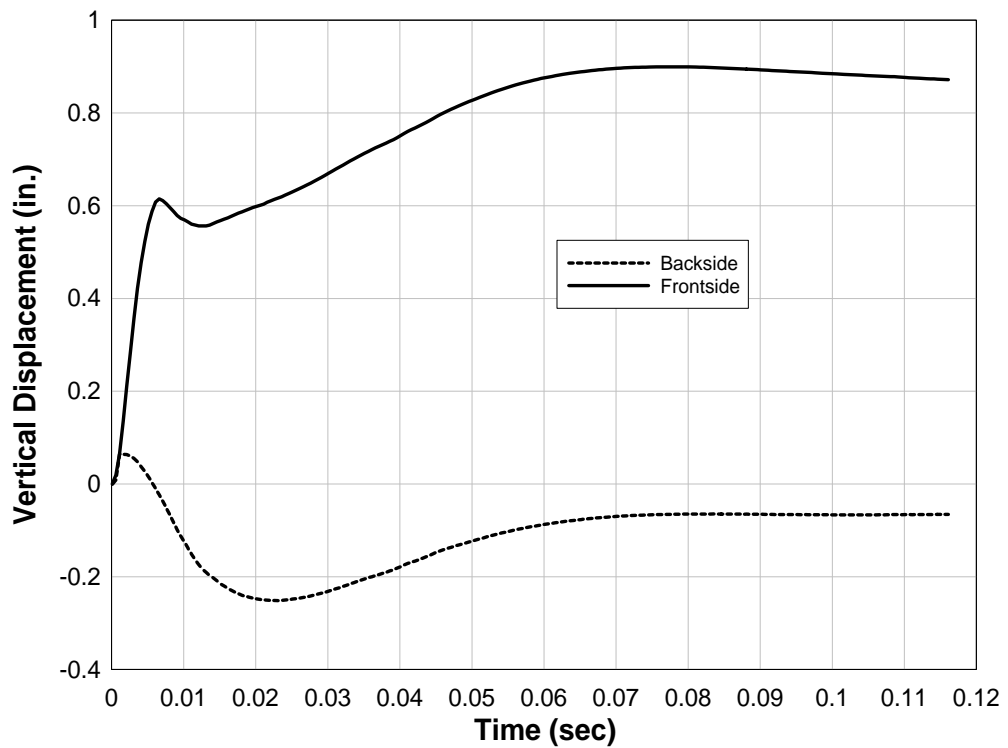


**FIG. 90. Vertical Displacement Time History of Top Block for Load III**

#### **4.2.6.2 Normal Failure Stress = 0.5 psi; Shear Failure Stress = 0.5 psi**

This case simulated virtually no bonding forces between the mortar joints and the blocks. The stresses in the wall are transferred to the polymer and are then further propagated to the supports. No energy is lost in overcoming the resistance of mortar joints in this case, and the blocks move laterally. Thus strain energy is more uniform over the height of the polymer reinforcement. Polymer near the boundaries showed high effective stresses. Localized stress action in the polymer near mid-height mortar joints was eliminated in this system. Only static and dynamic friction resisted the relative displacement at interfaces. Higher effective stresses than the previous two cases were observed in the polymer, as no energy was dissipated in mortar bond rupture. The opening at the center mortar joint was low (0.75 in.).

The effect of mortar bond strength on the vertical strain in the polymer near the bottom mortar joint and mid-height mortar joint for Load I and Load III is shown in Fig. 91 through Fig. 94. Absence of mortar bonds resulted in maximum strain of 6.1% at mid-height for Load I and 13.1% near bottom-most mortar joint for Load III. Stronger mortar bond resulted in maximum strain of 1.9% and 2.7% at mid-height for Load I and Load III, respectively.

#### **4.2.7 Bond Strength between Polymer and Blocks**

For this study, the bond between the masonry and polymer was eliminated. The polymer was fixed against translation at the top and bottom boundaries. The polymer therefore acted like a “catcher” for the wall. \*CONTACT\_NODES\_TO\_SURFACE contact card was used to prescribe the resistance between the polymer and blocks. Only friction provides resistance between the surfaces since the surfaces are not tied together.

##### **4.2.7.1 Displacement and Velocity**

Fig. 95 through Fig. 98 shows the variation in displacement and velocity for Load I and Load III for a catcher system.

##### **4.2.7.2 Internal and Kinetic Energy**

Fig. 99 through Fig. 102 shows the variation of internal and kinetic energy in the polymer for Load I and Load III.

##### **4.2.7.3 Vertical Strain in the Polymer**

Fig. 103 through Fig. 106 shows the strain in polymer near bottom and center mortar interface for Load I and Load III.

##### **4.2.7.4 Conclusions**

Since the polymer was not bonded to the wall, stresses were uniformly distributed over the height of the polymer. The catcher system eliminated stress concentrations at mortar interfaces, and polymer strains near mid-height and bottom mortar joints decreased by 50% and 66%, respectively. Even though the maximum displacement of the wall did not change significantly, the residual displacement in wall was reduced by 1 in. for both loading conditions. No change in lateral velocity was observed. The kinetic

energy increased by 10% to 15%. The internal energy decreased by 10% due to lesser straining of the polymer.

The catcher system proved effective at reducing the polymer strains. Even though stress concentration in the polymer near mortar joints was eliminated, the stresses near the top and bottom edges of the polymer where the polymer is attached to roof and floor increase substantially.

### **4.3 Wall Openings**

The wall behavior is affected by door and window openings. Window and door sizes considered in this investigation are expressed as a percentage of overall wall area. Openings decrease the internal resistance of wall due to loss of mass. This internal resistance in turn depends on support conditions, size, and location of openings. Moreover, blast resistant doors and windows result in concentrated loads on surrounding frame panels. The corners of openings result in weak points in the walls.

#### **4.3.1 Model Setup**

A wall measuring 144 in. X 88 in. was modeled. The CMUs were modeled as solid block with the equivalent mass as the hollow concrete blocks. The blocks were resized to include mortar layers in the block dimensions that scaled 16 in. X 8 in. X 8 in. The CMUs were arranged to form running bond type of block arrangement. In this, each vertical mortar joint was positioned halfway over the unit below. Rigid boundaries at top and bottom imparted one-way action of the wall. The vertical movements were restricted by the floor and roof boundaries. A one-mortar layer thick gap was left between the top layer and roof. A crude mesh was used since computation capacity would be exceeded if the full wall width was modeled at the same resolution as the single block width models. Each block was meshed with eight 8-noded solid elements with single point integration between two elements. Block to block interaction was defined by contact surfaces.

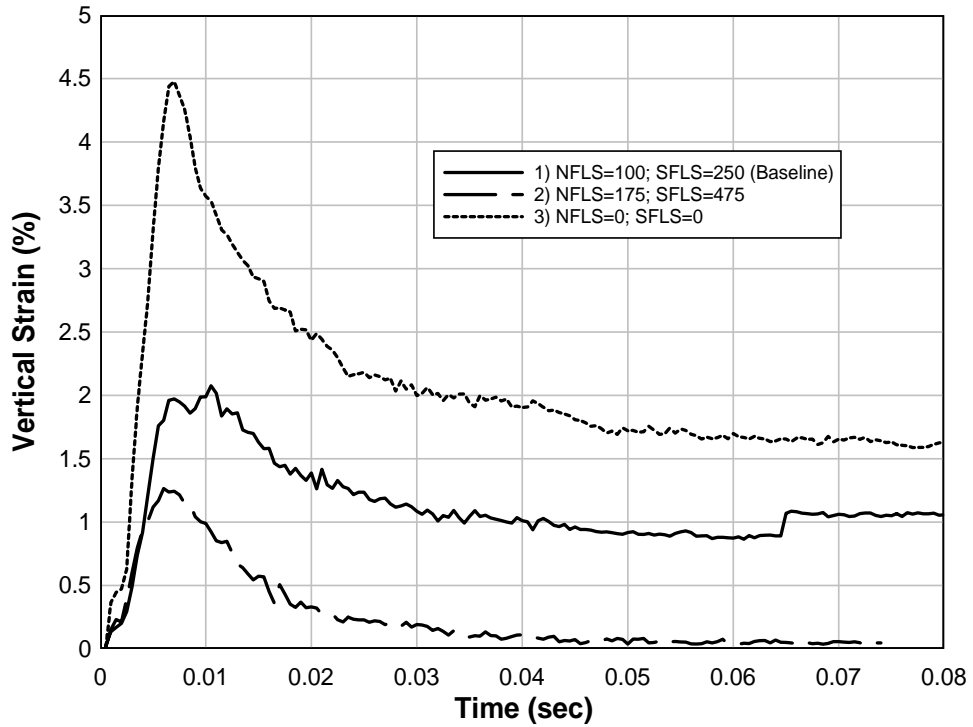


**FIG. 91. Variation in Vertical Strain in Polymer near Bottom Mortar Joint with Change in Mortar Bond Strength for Load I**

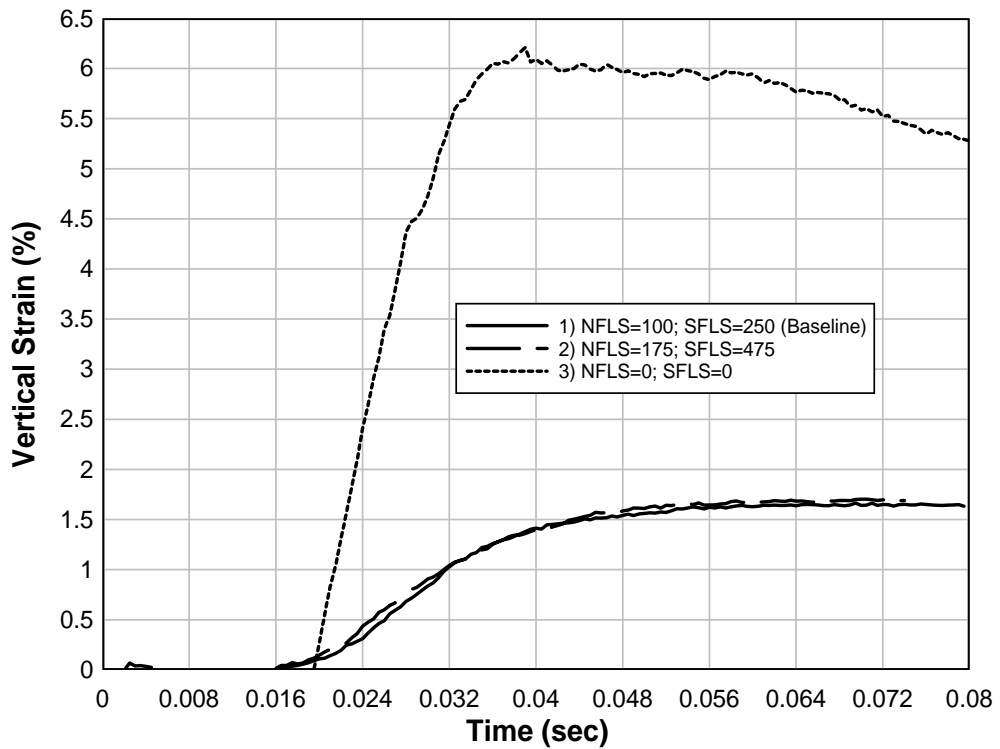


**FIG. 92. Variation in Vertical Strain in Polymer near Center Mortar Joint with Change in Mortar Bond Strength for Load I**

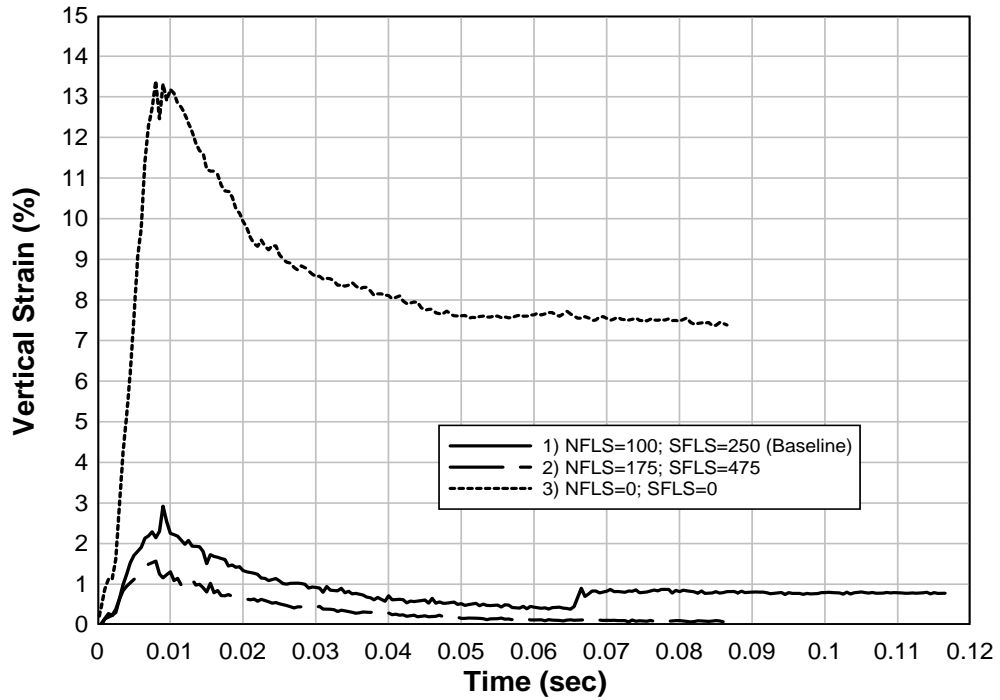


**FIG. 93. Variation in Vertical Strain in Polymer near Bottom Mortar Joint with Change in Mortar Bond Strength for Load III**

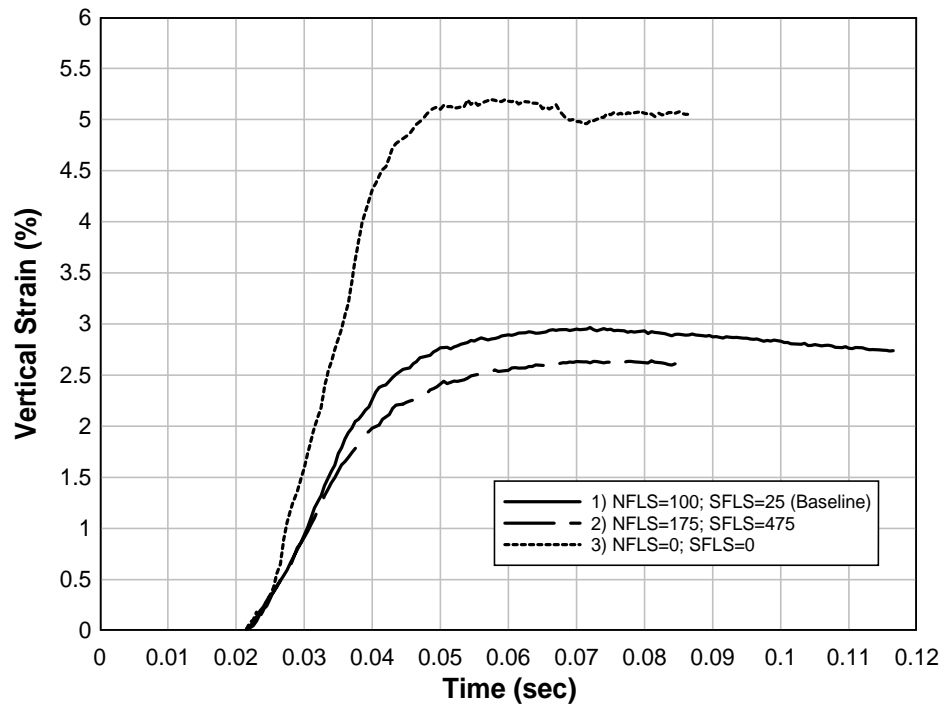


**FIG. 94. Variation in Vertical Strain in Polymer near Center Mortar Joint with Change in Mortar Bond Strength for Load III**

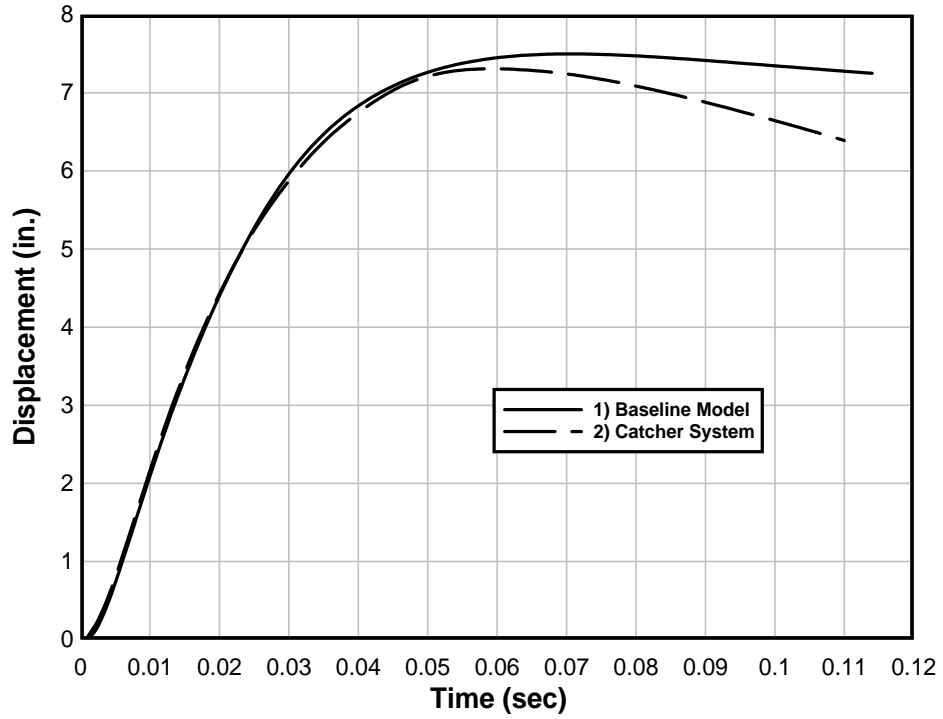


**FIG. 95. Variation in Displacement with Polymer Bonding for Load I**

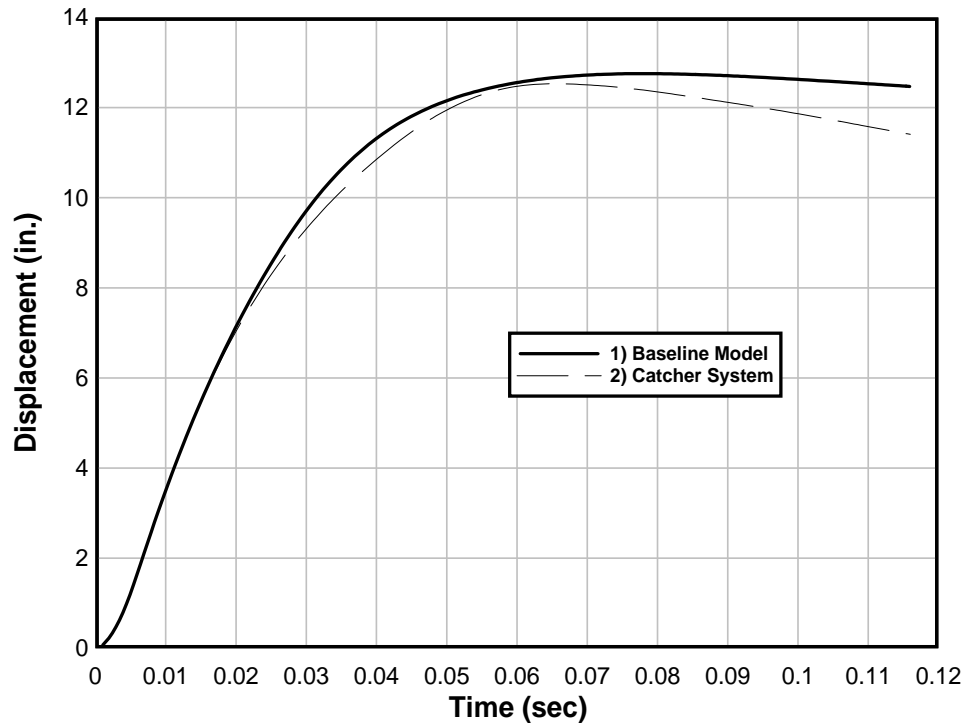


**FIG. 96. Variation in Displacement with Polymer Bonding for Load III**

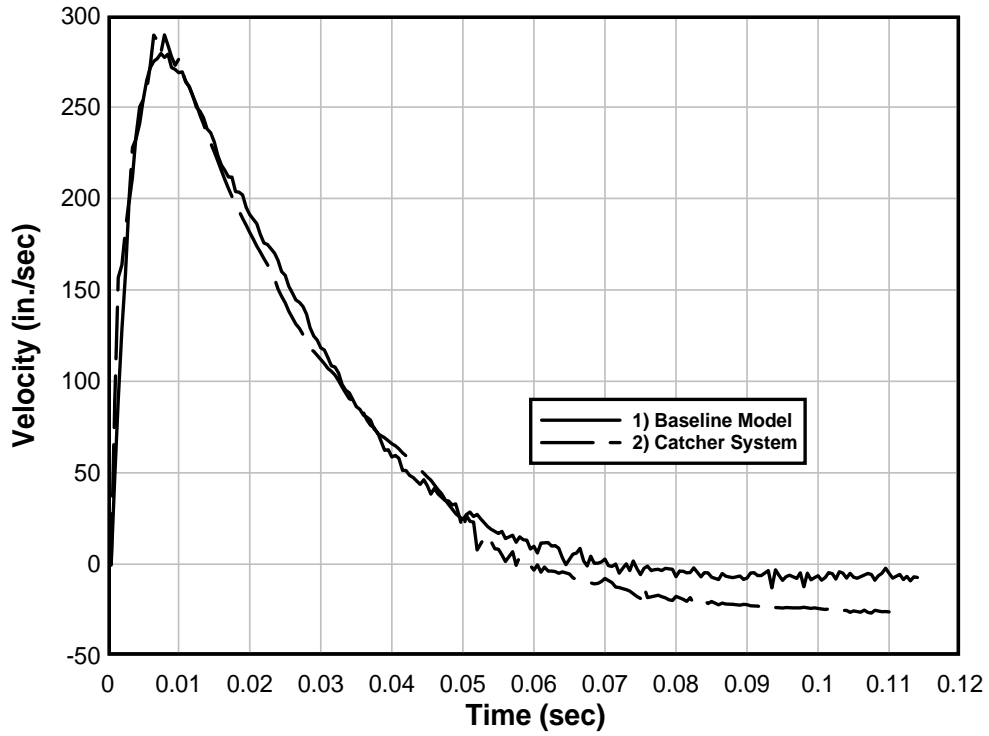


**FIG. 97. Variation in Velocity with Polymer Bonding for Load I**

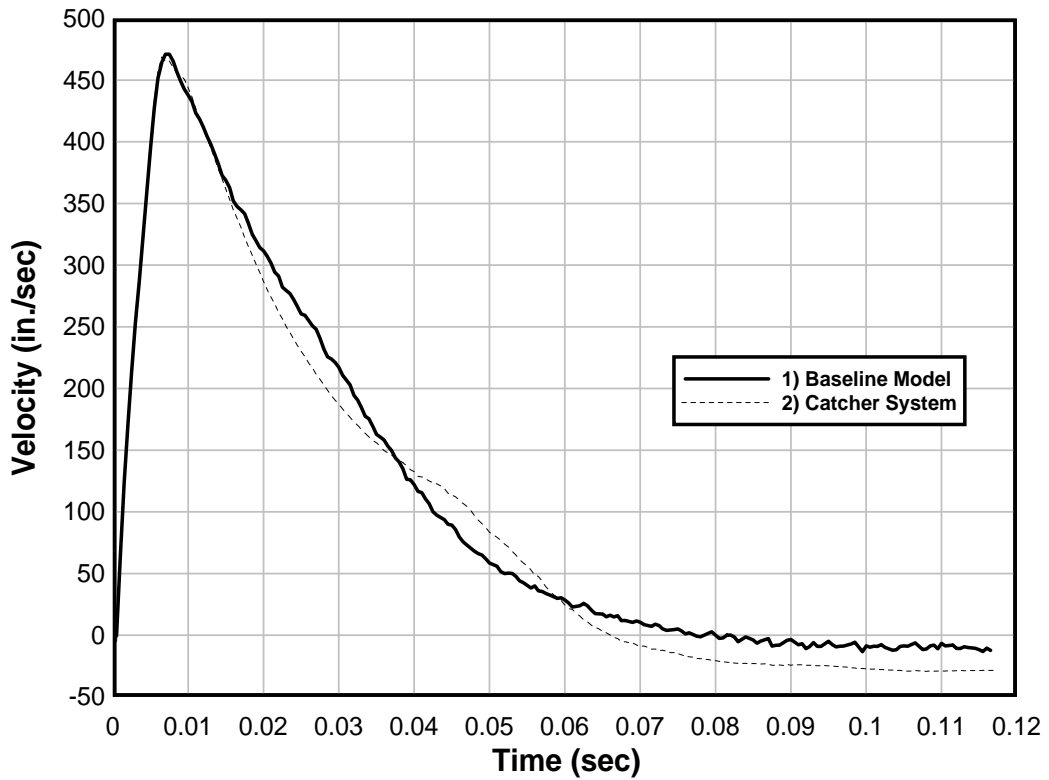


**FIG. 98. Variation in Velocity with Polymer Bonding for Load III**

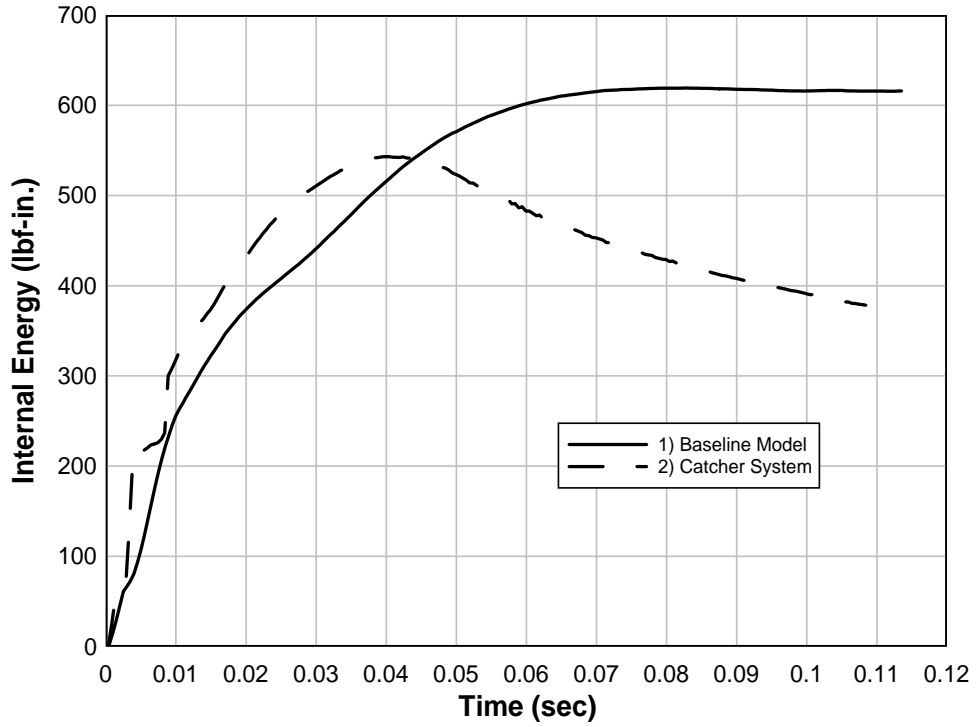


**FIG. 99. Variation in Internal Energy with Polymer Bonding for Load I**

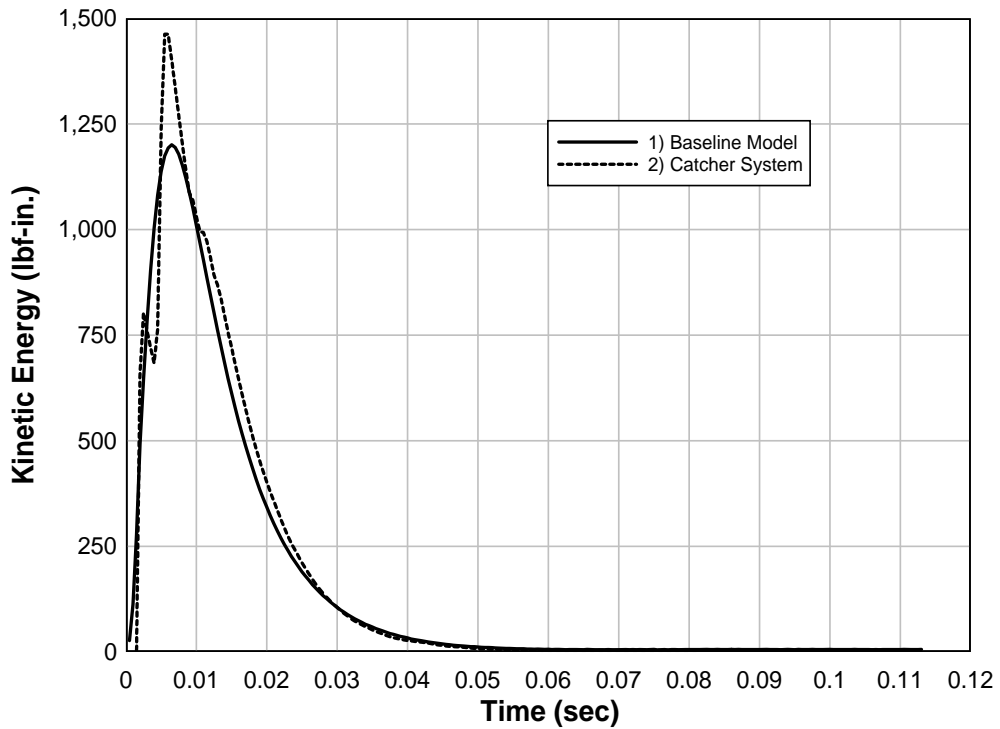


**FIG. 100. Variation in Kinetic Energy with Polymer Bonding for Load I**

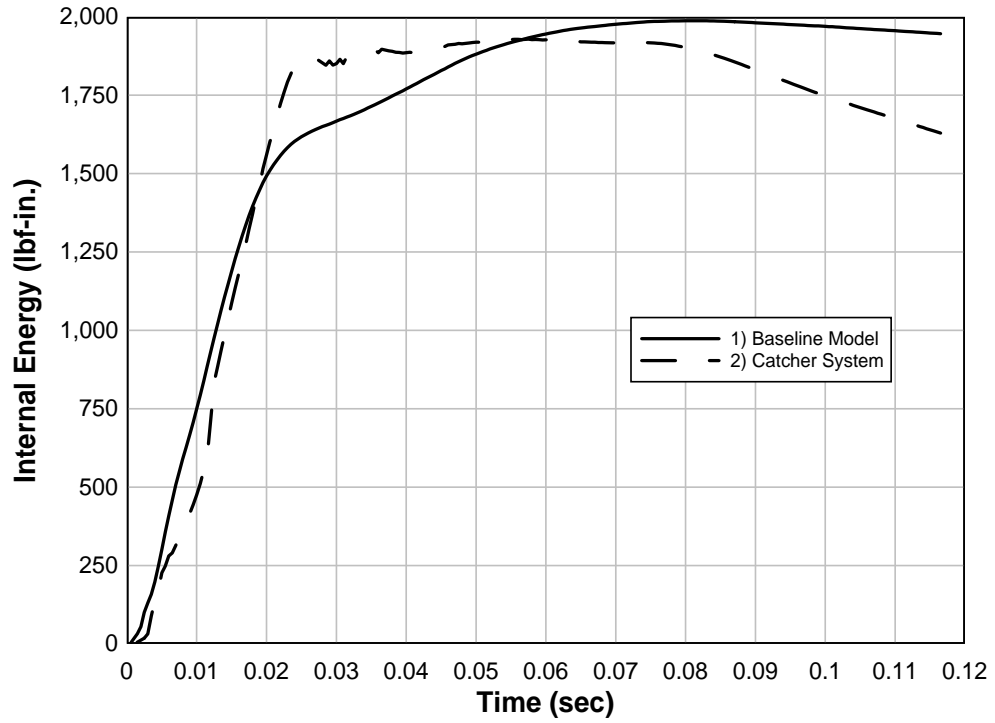


**FIG. 101. Variation in Internal Energy with Polymer Bonding for Load III**

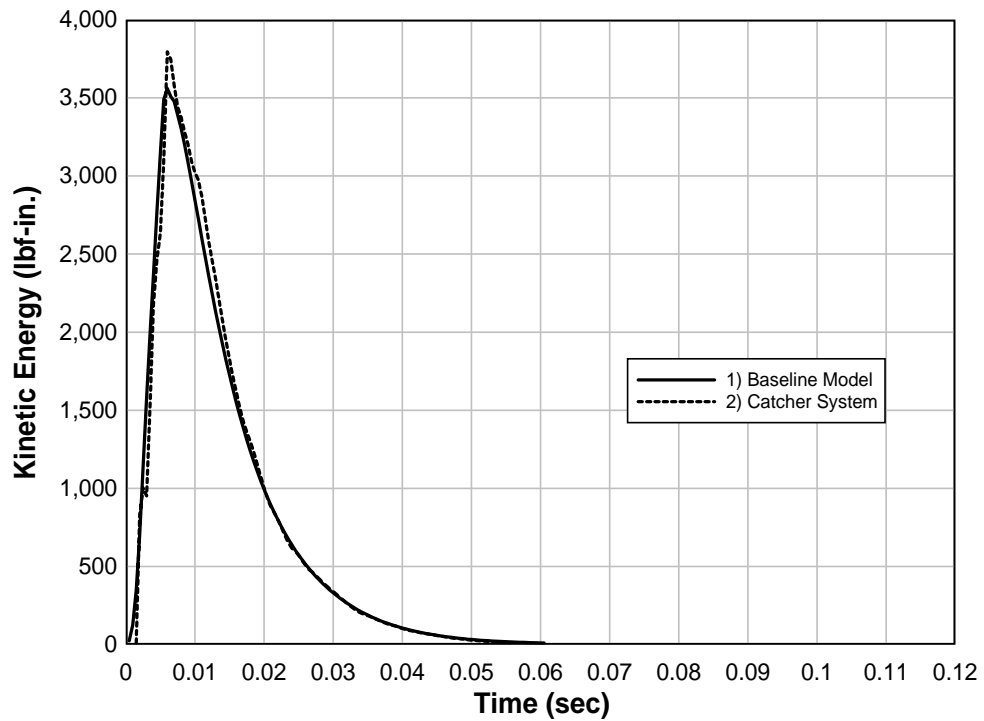


**FIG. 102. Variation in Kinetic Energy with Polymer Bonding for Load III**

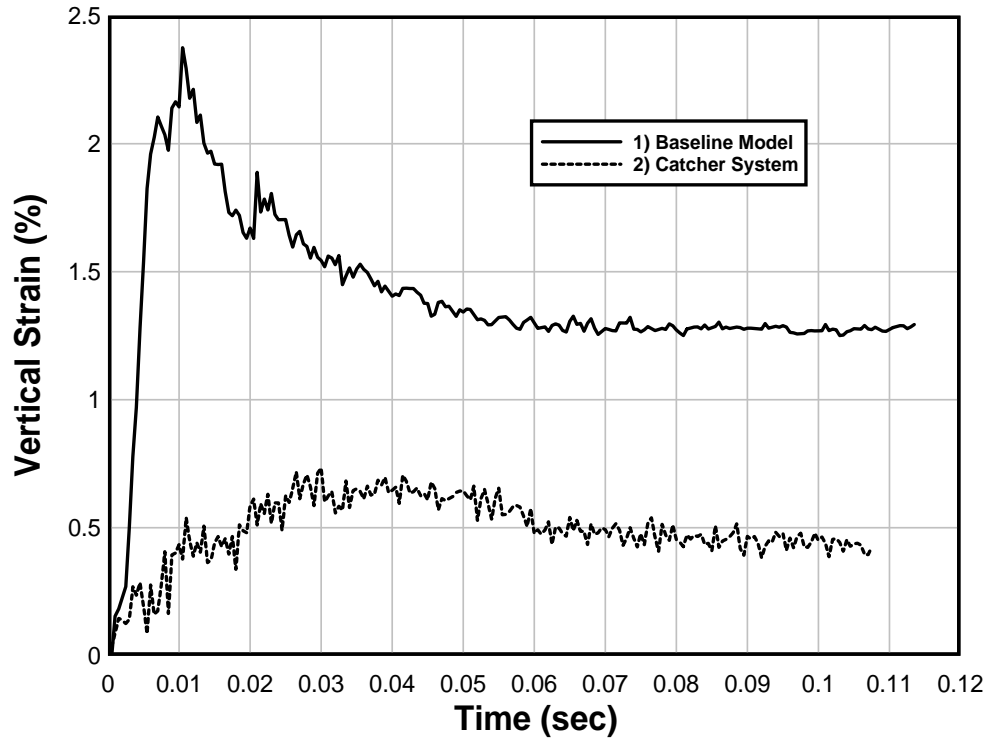


**FIG. 103. Variation in Vertical Strain near Bottom Mortar Joint for Load I**

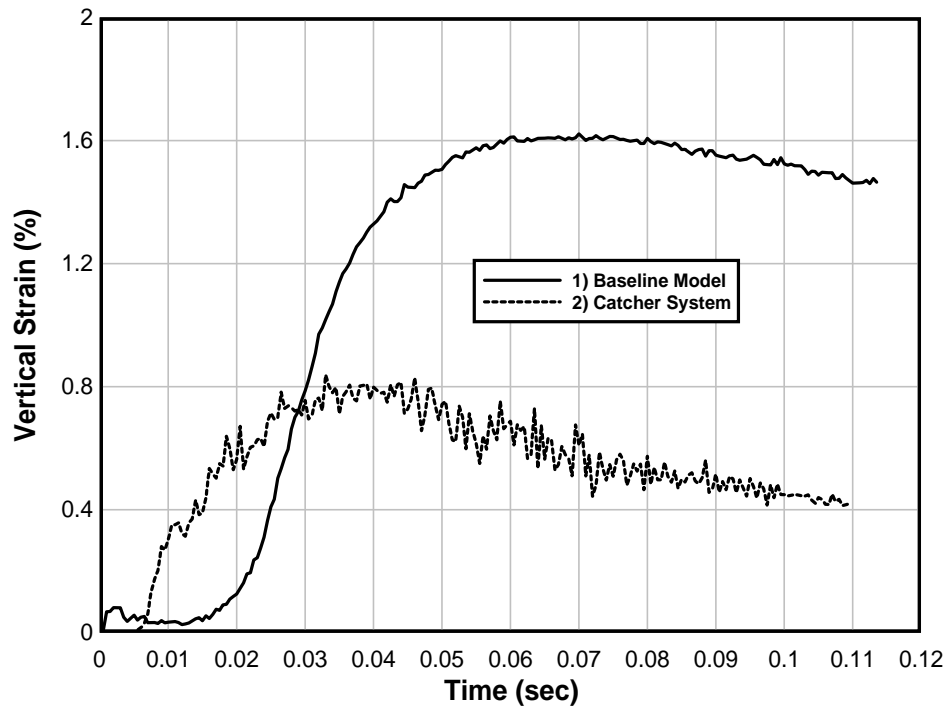


**FIG. 104. Variation in Vertical Strain near Center Mortar Joint for Load I**

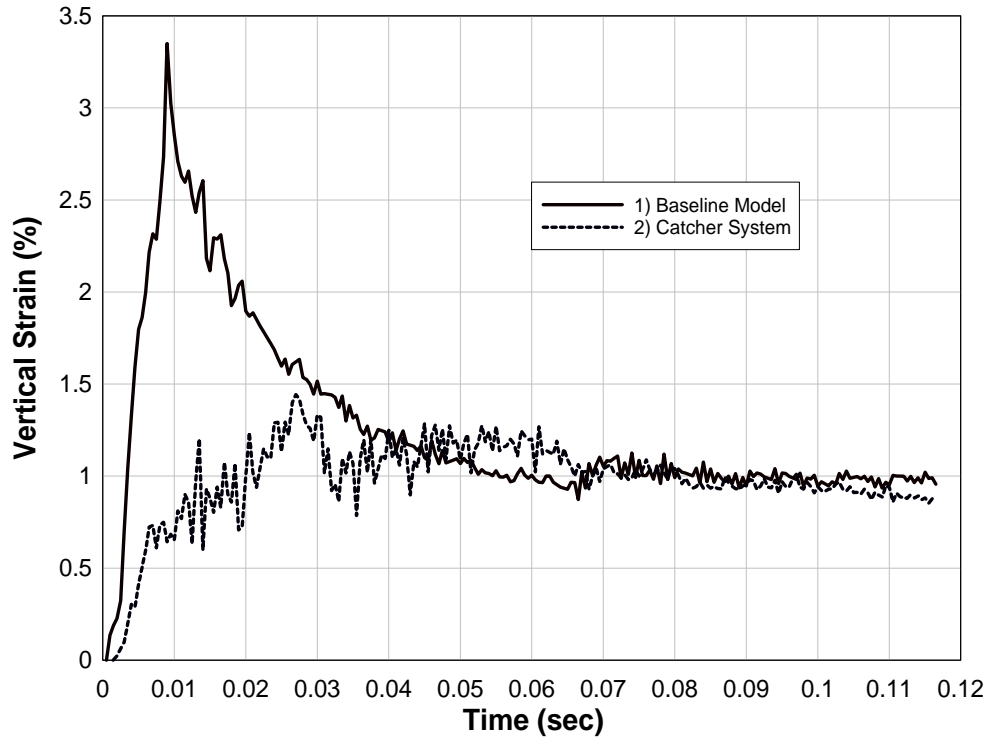


**FIG. 105. Variation in Vertical Strain near Bottom Mortar Joint for Load III**

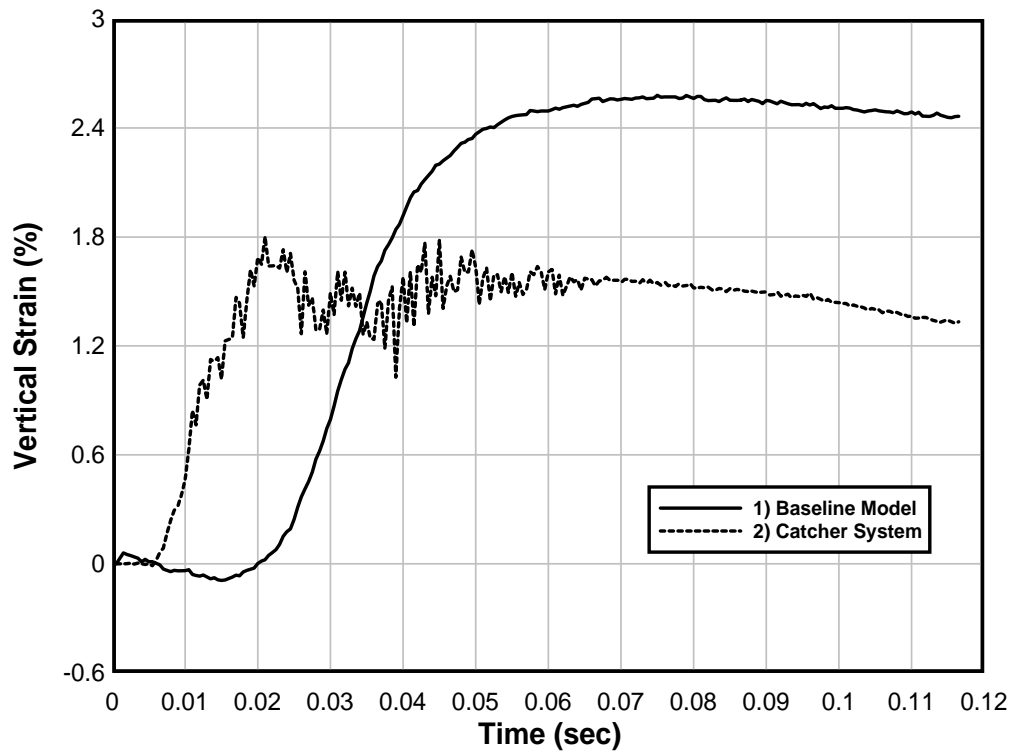


**FIG. 106. Variation in Vertical Strain near Center Mortar Joint for Load III**

The door and window frames were not simulated. A typical wall setup is shown in Fig. 107. Table 10 summarizes the openings. Fig. 108 through Fig. 110 shows the setup of various wall openings.

**TABLE 10. Wall Openings**

<b>Analysis</b>	<b>Description</b>	<b>Opening size</b>	<b>Percent opening</b>
1	Polymer Reinforced Wall	No opening	-
2	Window placed at center of panel	40 in. X 16 in.	5.1%
3	Window placed at center of panel	40 in. X 40 in.	12.6%
4	Door	40 in. X 80 in	25.2%
5	Window with double polymer thickness near the opening	40 in. X 40 in.	12.6%

Only Load I was applied on the wall since Load III gave computational discrepancies for large displacements in low-fidelity meshing. Mid-height displacement time history for Load I is shown in Fig. 111.

#### **4.3.2 Results and Observations**

Fig. 111 compares centerline displacement of walls with openings with the baseline model. Walls without openings act as a cohesive unit without any planes of weaknesses. However, when openings are introduced, bending occurs at the planes of weaknesses near these openings. Also, openings provide more edges and corners in the wall that result in stress concentrations. It can be seen from Fig. 111 that increasing polymer thickness around the opening can control overall displacement. This arrests the yield lines by absorbing more energy.

#### **4.4 Conclusions**

The baseline model showed displacements of 7.5 in. and 12.7 in. for Load I and Load III, respectively. Load III fractured the front face of the wall. Maximum 5% and 10% strain in the polymer was observed for Load I and Load III, respectively, from the baseline models. From the input parameter study, insignificant changes in displacement were observed due to changes in initial modulus, thickness, yield, and tensile capacity of the polymer. An increase in polymer thickness increased the strain energy absorption capacity. An increase in polymer stiffness increased stresses at boundaries and therefore increased the potential of the polymer to fail near boundaries.

Mortar joint bond strength affected the tensile failure between the blocks. When blocks were not bonded, the flexural opening at the center blocks of the wall increased to almost 1 in. High effective stresses occurred near the supports instead of at the central

region making the polymer near the supports susceptible to failure. The space between the roof and top-block had no effect on wall behavior.

The window and door openings increased the overall displacement at the center of the wall by 10% to 15%. However the increase in displacement depends on the percent of opening and its location.

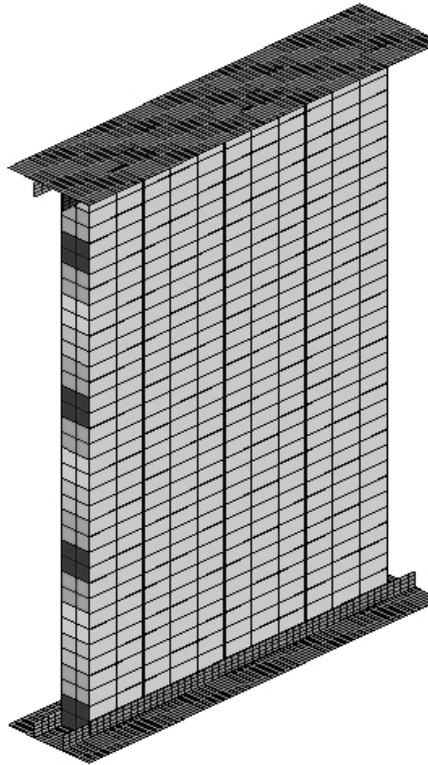


**FIG. 107. Polymer Reinforced Wall without Opening**

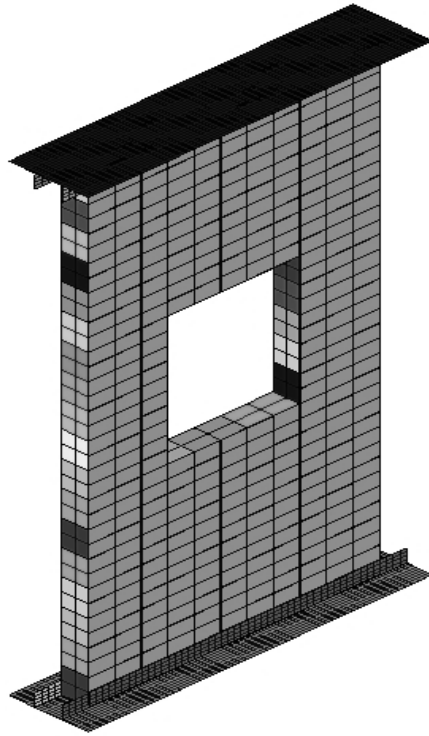


**FIG. 108. Polymer Reinforced Wall with 40 in. X 40 in. Window Opening**

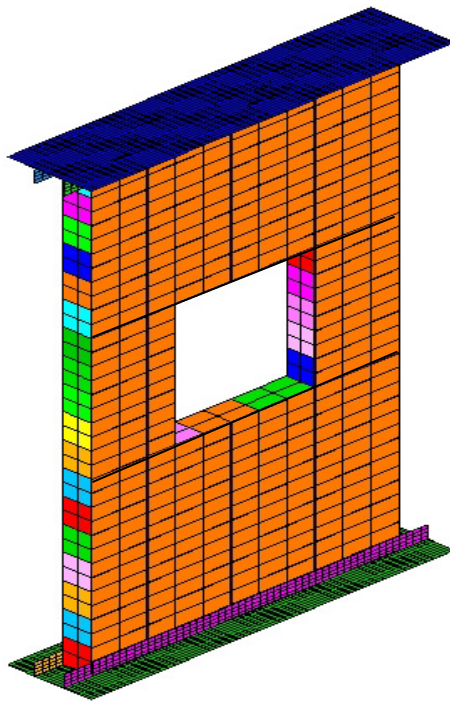


**FIG. 109. Polymer Reinforced Wall with 40 in. X 40 in. Window Opening and Polymer of Double Thickness near the Window**

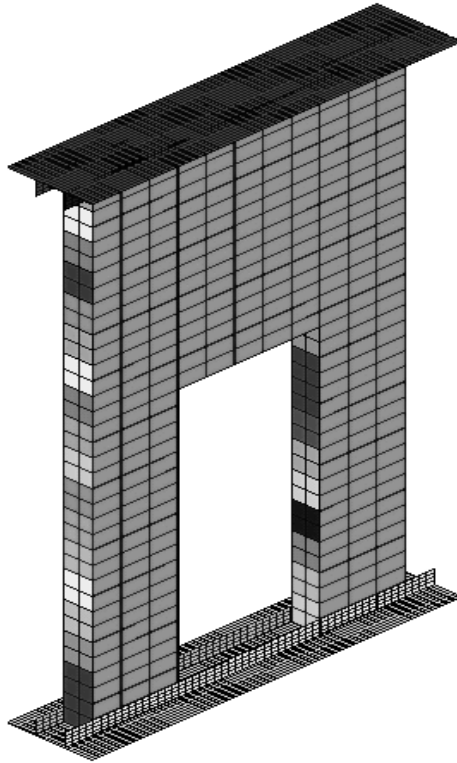


**FIG. 110. Polymer Reinforced Wall with 40 in. X 80 in. Door Opening**

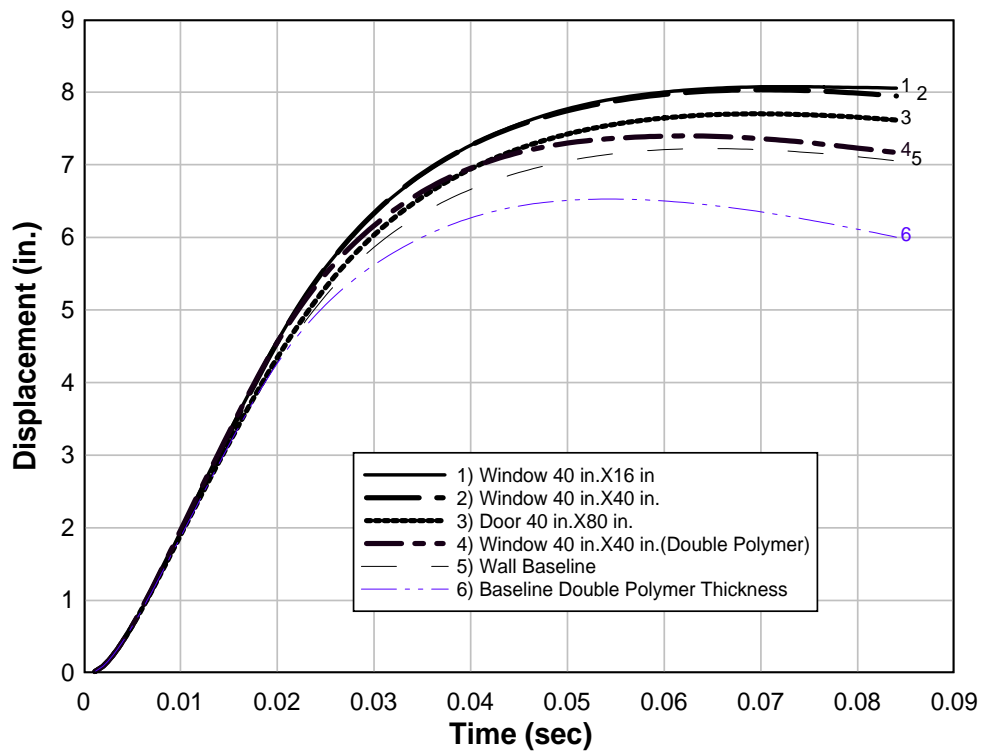


**FIG. 111. Center Displacements for Various Wall Openings under Load I**

## CHAPTER 5. STRAIN RATE ANALYSIS

### 5.1 Introduction

Strain rate dependent behavior plays an important role in the effectiveness of polymer for blast reinforcement. The polymer coating prevents the scattering of fragments resulting from blast. The loading and response of the masonry wall system lasts only a few milliseconds, and energy is transferred from the CMUs to the polymer at high rates. A stress wave travels through the block in less than 2 msec (Connell 2002).

The mechanical properties of the polymer reinforcement depend upon the rate of strain encountered. Strain rate is the change of strain with respect to time [ $\dot{\epsilon} = \frac{d\epsilon}{dt}$ ] and is expressed as  $\text{sec}^{-1}$ . Stress concentrations arise in the polymer at connections and at the mortar joints, which results in localized strains and the potential for rupture of the polymer coating. The distribution and variation of stresses and strains is not uniform over the area of the coating. Hence, it is necessary to understand the magnitude and distribution of maximum strains and the rates of strain encountered by the polymer reinforcement system.

Strain rate behavior is an important consideration for materials that may be used as blast reinforcement. It is impossible to measure strain rates of highly elongated material during explosive field-testing. Also, the baseline model described in Chapter 3 had one element over the mortar joint, making it difficult to extract an accurate representation of the strain rate. Therefore, various catechistic finite element models were developed to investigate the distribution, magnitudes, and rates of strains in the polymer reinforcement, as well as to evaluate the stability of various material models that could be used.

### 5.2 Model Development

Several analytical models were developed to form a broad understanding of strain rates that are encountered by the polymer reinforcement. LS-DYNA offers an extensive database of material models. Therefore, the various finite element models described below were also used to evaluate the behavior of potential material models in both tensile-membrane and high shear environments. Polymer properties described in Section 3.4.3 were used.

Evaluating the advantages and disadvantages of the element form type (shell vs. solid) combined with the complicated set of input parameters for each of the material models is a difficult task. For example, some choices (element type, material model, input parameters) are stable and simulate the polymer coating in tension well but do not perform well in a high shear environment. Some material models do not have an appropriate failure criteria input. Some choices do not appropriately reflect debonding between the masonry and the polymer. There is significant disparity in strain rate results

between various material models. To be selected, material models should (1) follow an appropriate failure criterion, (2) exhibit elastomer and/or plastic behavior, and (3) include strain rate effects. Material models for which shell elements were used include (1) MAT\_BLATZ-KO\_RUBBER, (2) MAT\_PIECEWISE\_LINEAR\_PLASTICITY, (3) MAT\_PLASTICITY\_WITH\_DAMAGE, and (4) MAT\_PLASTIC\_KINEMATIC. Material models for which solid elements were used include (1) MAT\_FINITE\_ELASTIC\_STRAIN\_PLASTICITY, (2) MAT\_OGDEN\_RUBBER, and (3) RATE\_SENSITIVE\_POLYMER.

### 5.3 MODEL #1: Membrane Only Model

Model #1 is simply a membrane subjected to an impulse load. This model is not directly applicable to the masonry wall problem but is useful for evaluating differences in tension failure behavior between the various material types. When subjected to an impulse simulating blast, the velocity of the membrane is greater than that of the masonry wall due to lesser mass associated with the membrane.

#### 5.3.1 Model Setup

Model #1 consists of a 72 in. X 144 in. membrane. Nodes along the short edges were fixed against translation and rotation. The model was meshed with an aspect ratio of 1 with 10368 elements. Fully integrated shell elements and plane stress 3-D solid elements were used to ensure least loss of energy due to hourglassing. Load I and Load II impulse loads were applied using the CONWEP blast function in LS-DYNA. The analytical model is shown in Fig. 112.

#### 5.3.2 Observations

The strain was not uniform under impulse pressure; the maximum strain propagates from the supported edges toward the center. Failure and high strain rates occurred at approximately quarter height of the membrane. Table 11 provides maximum strain rate for several of the material models. The strain rate depended on mechanical properties and stress-strain dependency on strain rate considered by the constitutive model. The maximum strain rate occurs near the supports within 5 msec. Solid elements resulted in computational errors under large displacements.

#### 5.3.3 Theoretical Approach

A closed form solution for the large displacement of a thin membrane can be derived (Seide 1977):

$$\varepsilon = \frac{8 \cdot t \cdot \Delta^2}{3 \cdot (1 - \nu^2) \cdot a^3} \quad (17)$$

where  $\Delta$  = deflection normal to plane of the membrane,  $a$  = unsupported length (Fig. 112),  $t$  = membrane thickness,  $E$  = elastic modulus, and  $\nu$  = Poisson's ratio.

Equation 17 was developed for static loading. The theoretical solution of a membrane subjected to lateral pressure was associated with the dynamic deflection of the

masonry wall subjected to blast and solved for the strain and strain rate. This solution provides a lower bound because it (1) uses the real velocity of the masonry wall subjected to blast and (2) assumes uniform distribution of strain. Furthermore, this solution may be useful for estimating strains and strain rates in single degree of freedom models where only a weak block/retrofit bond is assumed. Fig. 113 illustrates the strain rate prediction at mid-height from Equation 17 using the displacement data obtained from the baseline model subjected to Load I and Load II.

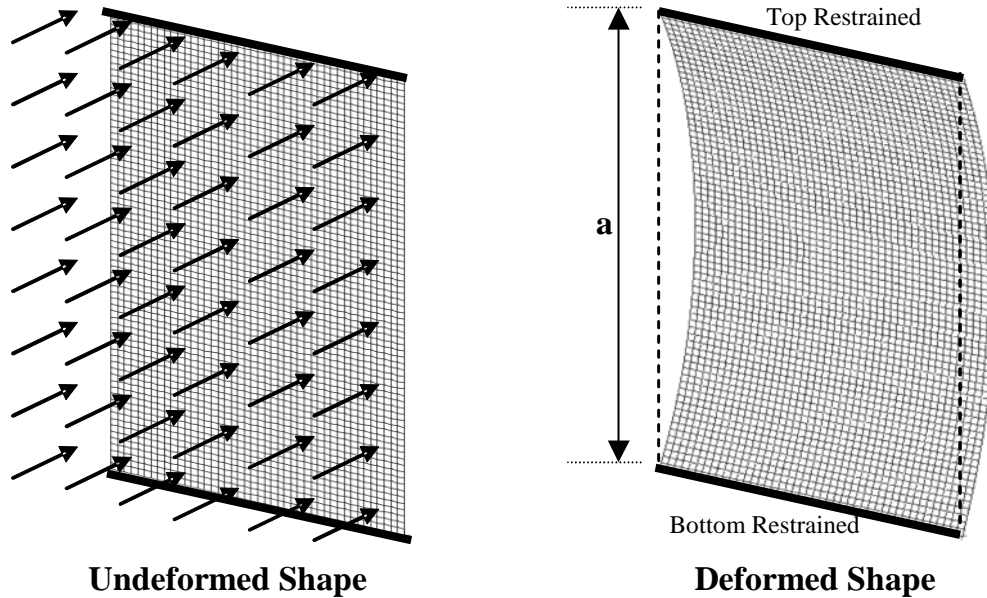


**FIG. 112. Membrane Only Analytical Model**

**TABLE 11. Strain Rate in Membrane Only Model**

Material	Element type	Max strain rate (sec <sup>-1</sup> )	
		Load I	Load II
MAT_BLASTZ-KO_RUBBER	Shell	747	247
MAT_PIECEWISE_LINEAR_PLASTICITY	Shell	261	175
MAT_PLASTICITY_WITH_DAMAGE	Shell	478	175
MAT_PLASTIC_KINEMATIC	Shell	463	310
MAT_FINITE_ELASTIC_STRAIN_PLASTICITY	Solid	856	309
MAT_OGDEN_RUBBER	Solid	811	429
MAT_RATE_SENSITIVE_POLYMER	Solid	132	241

These strain rates were seen within 3 msec – 5 msec after the blast load reached membrane.

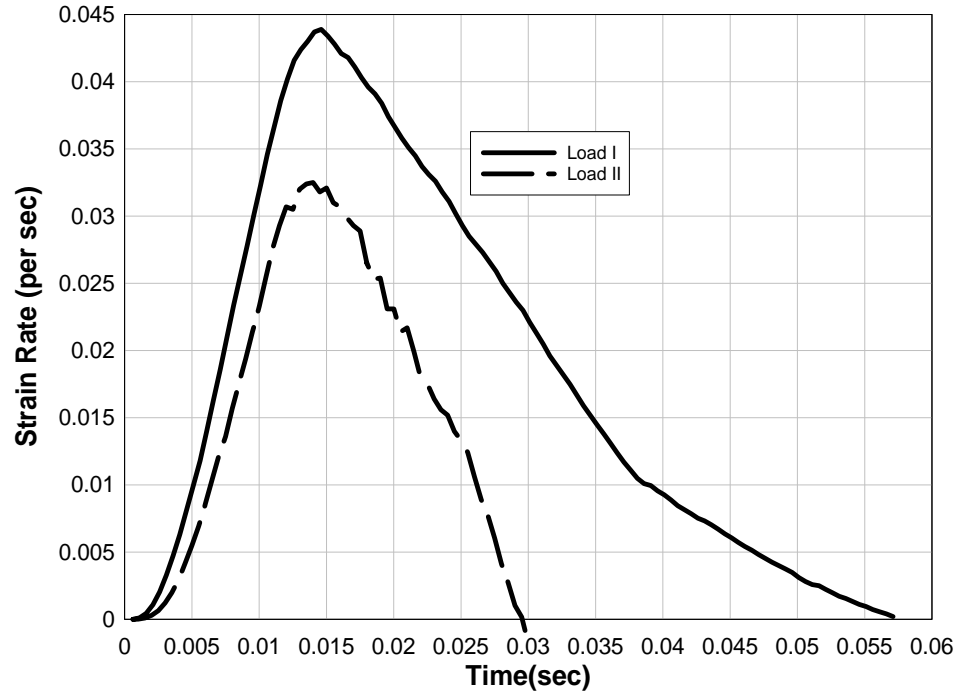


**FIG. 113. Theoretical Approach to Membrane Equation**

## 5.4 Model #2: Dynamic Opening of Rigid Slabs

### 5.4.1 Model Setup

Model #2 simulates the dynamic opening at the center of the masonry wall. Setup of this model is shown in Fig. 114. The upper and lower halves of the system are rigid with pinned boundary conditions at the front (loaded side) top/bottom edges. Fully integrated solid elements are utilized for the slabs, and the rigid material model is assigned. The total mass of the slabs was made equal to that of the single unit width model. Impulse pressures simulating Load I and Load II were applied using the \*LOAD\_BLAST card in LS-DYNA. The polymer was meshed with eight elements with an aspect ratio of one (1 element per inch) along the width except at the gap. In the vicinity of the gap, this mesh density was increased to three or four elements with an aspect ratio of one using the transition mesh as shown in Fig. 114. This facilitated a better simulation of stress gradient over the area of interest in the polymer. The \*CONTACT\_TIEBREAK\_SURFACE\_TO\_SURFACE contact type was used for the slab-polymer interface. Fully integrated elements were used to prevent hourglassing modes in the polymer. Since the momentum of the masonry wall system is dominated by mass, the velocity and displacement at the center of this system is very close to that observed in explosive tests and higher fidelity finite element models (Fig. 115).

This model provides an efficient means of evaluating the various DYNA-3D material models in the dynamic membrane stress environment and the block-polymer shear debonding behavior of material and element types. Strain rate in the polymer was analyzed for a 2 in. gap using the two load cases to evaluate various material models. The maximum strain rate for chosen material models simulating Load I and Load II is summarized in Table 12.

### 5.4.2 Theoretical Solution

An approximation for the strains and strain rates occurring with Model #2 can be solved by associating the lateral displacement at the wall center with geometric parameters and the geometry of deformation and assuming linear elastic material behavior. Fig. 116 illustrates the solution.

Consider a wall of thickness  $w$  and height  $h$ . The wall is comprised of two rigid slabs separated by a gap of width  $a$ . One face of the wall is covered with a polymer while the blast load acts on the other side of the wall. The wall is hinged at edges on the backside. The impulse load opens the wall and stretches the polymer as shown in Fig. 116.  $\Delta$  is the deflection at the center of the wall and,  $\alpha$  is the angle of deflection. Consider the lower half of the wall as shown in Fig. 116.

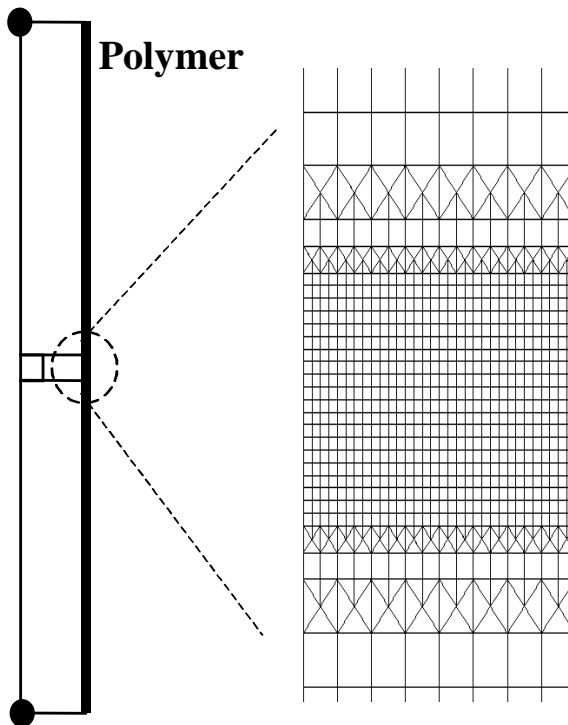
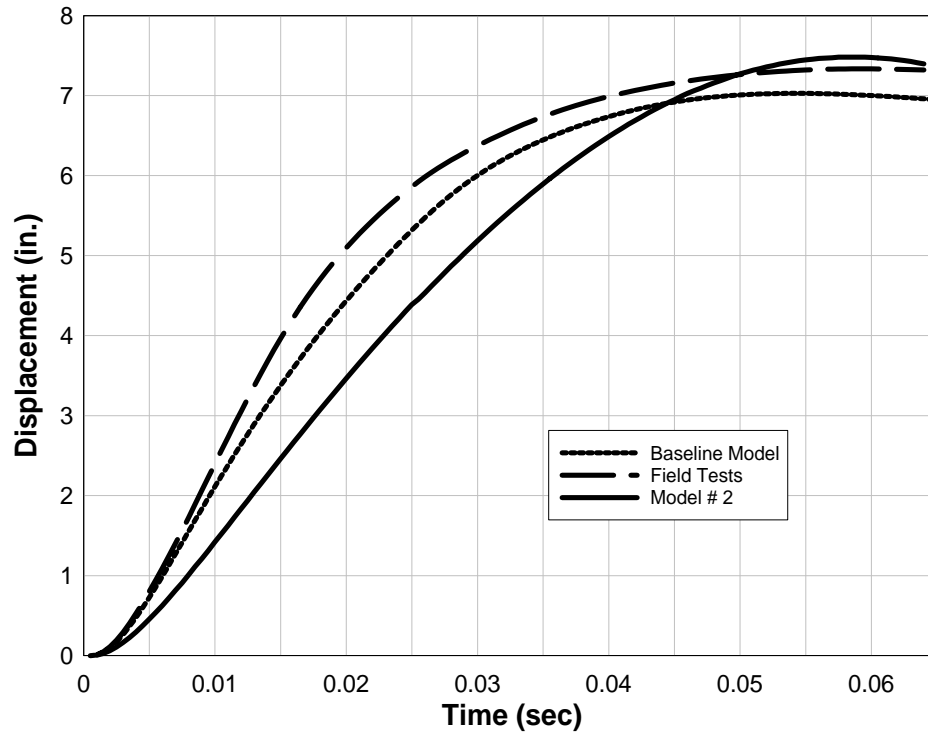


FIG. 114. Mesh Transition in Polymer near the Gap



**FIG. 115. Comparison of Center Displacements for Load I**

**TABLE 12. Model #2: Strain Rates for Polymer Reinforced Slab Model for 2 in. Gap**

Material model	Element type	Load I		Load II	
		Lateral velocity (in./sec)	Maximum strain rate (sec <sup>-1</sup> )	Lateral velocity (in./sec)	Maximum strain rate (sec <sup>-1</sup> )
MAT_PLASTIC_KINEMATIC	Shell	240	25	210	15
	Solid	240	25	200	20
MAT_BLATZ-KO_RUBBER	Shell	225	20	200	15
	Solid	260	18	200	15
MAT_PIECEWISE_LINEAR_PLASTICITY	Shell	230	25	200	12
	Solid	240	20	200	18
MAT_PLASTICITY_WITH_DAMAGE	Shell	240	30	190	10
MAT_FINITE_ELASTIC_STRAIN_PLASTICITY	Solid	230	18-20	200	15
MAT_OGDEN_RUBBER	Solid	240	16	200	18
MAT_RATE_SENSITVE_POLYMER	Solid	260	80	200	22
MAT_PLASTICITY_POLYMER	Shells	This material gave errors during analysis			

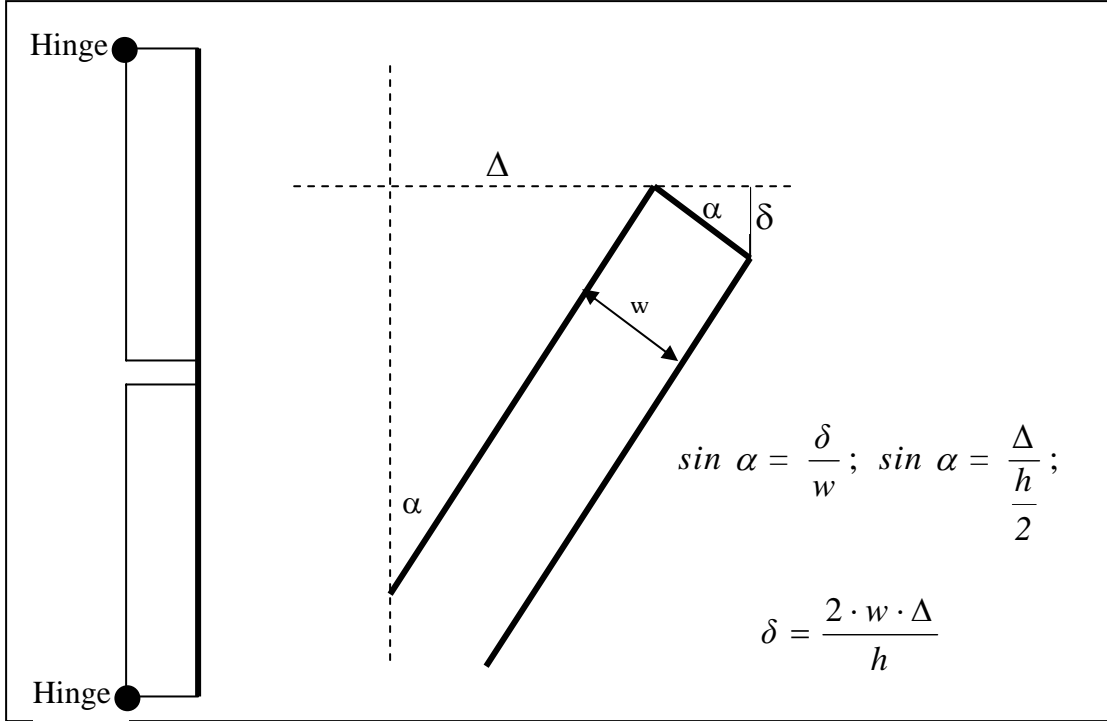


**FIG. 116. Theoretical Solution for Model #2**

The total width of gap (the elongated length of polymer) is shown as

$$W_G = a + \delta + \delta = a + 2\delta \quad (18a)$$

Engineering strain in the gap portion in vertical direction is given by

$$\varepsilon = \frac{2\delta}{a} \quad (18b)$$

$$\varepsilon = \frac{4w\Delta}{ha} \quad (18c)$$

Strain Rate is given by

$$\zeta = \frac{d\varepsilon}{dt} \quad (18d)$$

$$\zeta = \frac{4wv}{ha} \quad (19)$$

where 'v' is the lateral velocity at the gap.

It can be seen from Equation (18c) that the strain is inversely proportional to the initial space between the two slabs. The strain rate can be obtained for a particular value of ‘a’ using the displacement data provided from analytical or test data. However, this is a purely geometric derivation. Furthermore, lateral velocities at mid-height of Model #2 for Load I and Load II were obtained from finite element analysis. These velocities were associated with Equation (18e), and strain rate was calculated. Fig. 117 and Fig. 118 show the plots of strain rate versus time for various values of ‘a’ for Load I and Load II, respectively.

This solution may be useful for estimating strains and strain rates in SDOF models where a strong block/retrofit bond is assumed. Usually, the thickness of the mortar layer is 0.375 in. For  $a = 0.375$  in., the maximum strain rate achieved using this approach for Load I is about  $190 \text{ sec}^{-1}$ , and Load II is  $175 \text{ sec}^{-1}$ . Table 13 presents rates at a particular element in the polymer over the gap, whereas the values from the theoretical analysis consider the entire gap. This results in a large difference between these two analyses.

### 5.4.3 Factor Calculation

To link the analytical and theoretical models, heuristics models were constructed with gap widths of 0.375 in., 0.5 in., 1 in. and, 2 in. For each model, the mesh was changed to have multiple (3-4) elements across the gap. MAT\_PLASTIC\_KINEMATIC (LS-DYNA material #3) without failure criteria was used for the polymer. The models were studied only for Load II. For each model, the velocity of the rigid slab at the gap was extracted. This velocity was then substituted into Equation 19 to get theoretical strain rate.

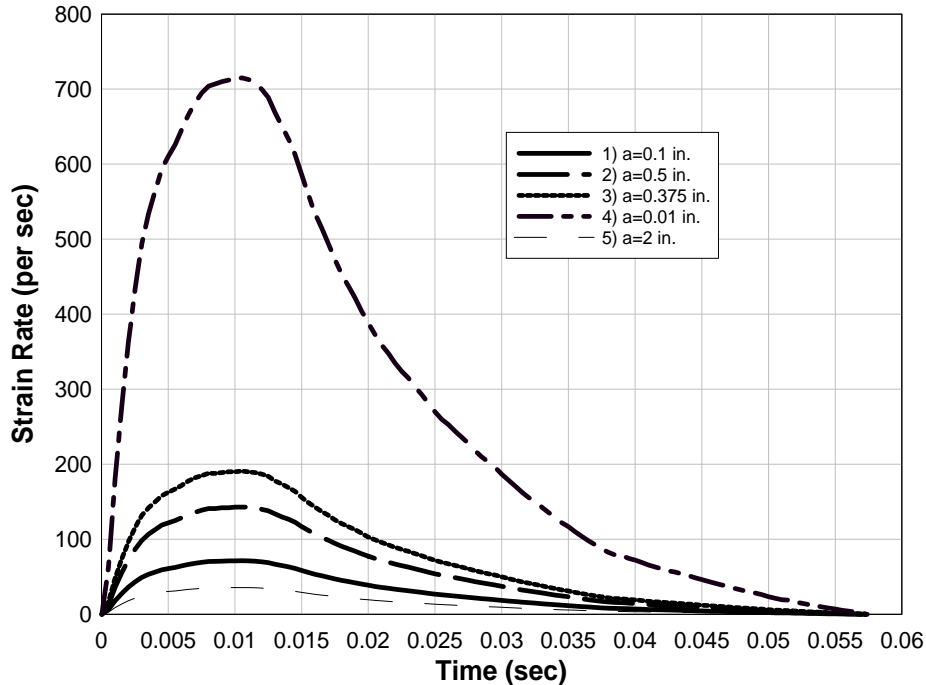


**FIG. 117. Model #2 Strain Rate Time History for Load I**

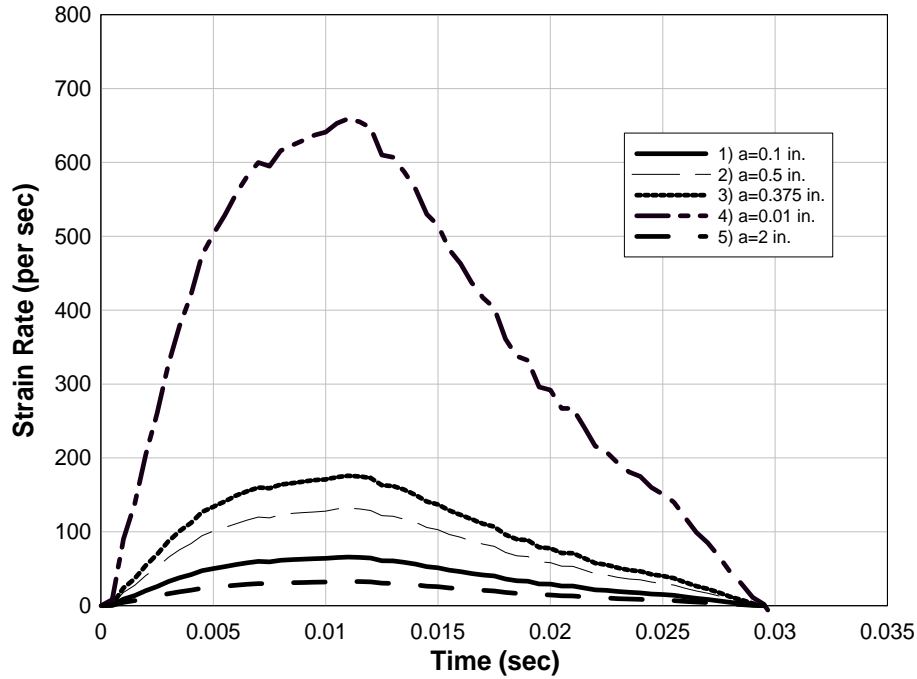


**FIG. 118. Model #2 Strain Rate Time History for Load II**

**TABLE 13. Comparison of Theoretical and Finite Element Strain Rate for Model #2**

Gap width (in.)	Theoretical strain rate (sec <sup>-1</sup> ) (1)	Finite element strain rate (sec <sup>-1</sup> ) (2)	Factor (1)/(2)
0.375	122.67	61.80	1.98
0.5	88.88	69.54	1.28
1.0	42.82	38.50	1.11
2.0	14.83	23.33	1.57

### 5.5 Model #3: Shear Test

Model #3 is the same as Model #2 except that one side of the wall panel is forced to translate relative to the other side to simulate a dynamic high shear environment (Fig. 119). The upper and lower halves of the system are rigid with pinned boundary conditions used at the front (loaded side) top edge. The bottom slab was restrained against translation and rotation. A high-density mesh having 32 elements along the width and an aspect ratio of 1 was used to model the polymer. Impulse pressures simulating Load I and Load II were applied. Since the momentum of the masonry wall system is dominated by mass, the velocity and displacement at the center of this system is very

close to that observed in tests and higher-fidelity finite element models. This model provides an efficient means of evaluating the various DYNA-3D material models in the dynamic shear environment and the block/polymer tension debonding behavior of material and element types. The maximum strain rate for several of the material models simulating Load I and Load II is summarized in Table 14.

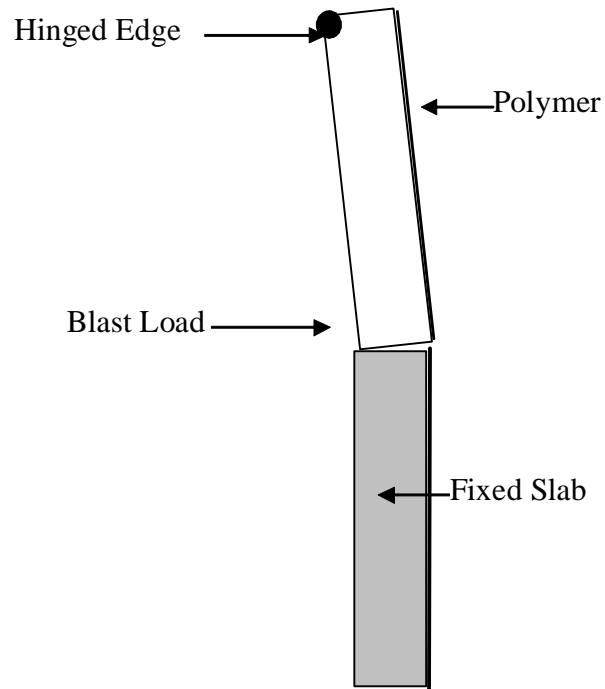


**FIG. 119. Model Setup for Shear Test**

**TABLE 14. Shear Test: Strain Rates for Load I and Load II**

Material	Element type	Max. strain rate (sec <sup>-1</sup> )	
		Load I	Load II
MAT_BLATZ-KO_RUBBER	Shell	83	52
MAT_PIECEWISE_LINEAR_PLASTICITY	Shell	110	58
MAT_PLASTICITY_WITH_DAMAGE	Shell	89	55
MAT_PLASTIC_KINEMATIC	Shell	25 (failure)	60
MAT_FINITE_ELASTIC_STRAIN_PLASTICITY	Solid	150 (Complete debonding)	97 (Complete debonding)
MAT_OGDEN_RUBBER	Solid	25	22
MAT_RATE_SENSITIVE_POLYMER	Solid	12	14

## 5.6 Model #4: Hi-Fidelity Model

### 5.6.1 Model Setup

Model #4 is the high-fidelity finite element model of one-way flexure unreinforced concrete masonry blocks as described in Section 3.12.1. The polymer strain distribution over time was examined for Load I and Load II. The polymer meshing contains four elements through the thickness of the mortar joints (Fig. 120) to gain a better distribution of stress concentrations in these regions.

The maximum strain rate occurs at the mortar joints. Since the top and bottom blocks are restrained against translation, relative displacement occurs at top-most and bottom-most mortar joints. This results in high shear in the polymer near these interfaces, causing large strains in the polymer during early phases of the loading. This case is similar to Model #3 described in Section 5.5. As the blast energy is transformed into momentum, the blocks at mid-height open at the mortar layer due to flexure and the polymer stretches. The polymer elongation is maximum at the centermost mortar interface. Thus, high strain rate is observed at the centermost mortar interface in later phases of the analysis. This case is analogous to Model #2 described in Section 5.4.

### 5.6.2 Results

Elements equidistant from the edges were chosen for strain analysis to avoid the stress concentrations due to edge effects. Strain and strain rate time history in the polymer near the top-most, bottom-most, and center mortar joint interface is shown in Fig. 121 through Fig. 128 for Load I and Load II. From Fig. 121 it can be observed that the strain in the polymer near the bottom-most mortar joint interface for Load I surges early in the response. The strain rate reaches 9.71 sec<sup>-1</sup>. Similarly, for the center mortar

joint, strain variation is maximum between 0.012 sec and 0.048 sec, and the maximum strain rate is  $2.3 \text{ sec}^{-1}$ . Furthermore, for Load II, the peak strain rate in the polymer near the bottom-most mortar joint is  $7.3 \text{ sec}^{-1}$  and near center mortar joint is  $1.6 \text{ sec}^{-1}$ .

## 5.7 Conclusions

Of the material models considered, MAT\_PLASTIC\_KINEMATIC and MAT\_PIECEWISE\_LINEAR\_PLASTICITY models result in appropriate material fracture without computational problems. The strain rates in these material models were observed to be less than other material models due to the early failure of the polymer. Although these models can be applied to solids, the use of shell elements is recommended, as it is difficult to achieve a good aspect ratio in solids. The MAT\_PIECEWISE\_LINEAR\_PLASTICITY model considers dependency of stress-strain relationship on strain rate. When these data are not available, material can be defined using initial modulus, yield stress, tangent modulus, and rupture strain of the polymer. Four models were developed to study the strain rate in the polymer reinforcement material. Model #1 does not represent a structural reinforcement scenario, but was used to evaluate membrane behavior of various material models when subjected to blast load. Model #2 and Model #3 give the strain rates in tension and shear environments, respectively. Model #2 predicts strain rate near the mortar layers in the polymer under tension. Model #3 provides strain rates when the polymer is subjected to shear. This is beneficial in predicting the rate attained at the early stages of loading when the shear in polymer is high near the supports.

Model #4 was used to study strain rate in the polymer reinforcement for the one-way action single unit width wall model. Peak strain rates in polymer for Load I near bottom-most and center mortar joint interface were observed to be  $10 \text{ sec}^{-1}$  and  $2 \text{ sec}^{-1}$ , respectively. For Load II, the maximum strain rates in the polymer near the bottom-most and center mortar joint were  $7 \text{ sec}^{-1}$  and  $1.5 \text{ sec}^{-1}$ , respectively. The maximum strain rate in the center portion of the wall was observed to be less than the maximum strain rate in shear for both loading types. In this model, the strain rate in the polymer is not directly proportional to the velocity because the blocks absorb most of the energy from the blast before being transferred to the polymer. Moreover, the strain rates in this model are much lower than in the other two models because rigid material was used for concrete slabs in Model #2 and Model #3. Also, the blast energy in Model #4 is absorbed by CMU deformation and overcoming bonding and friction at mortar interfaces. The opening of the two blocks assumed in Model #2 does not occur in Model #4, resulting in lower strains in Model #4 than in Model #2. The strain rate in the polymer reinforcement remains below  $10 \text{ sec}^{-1}$ .

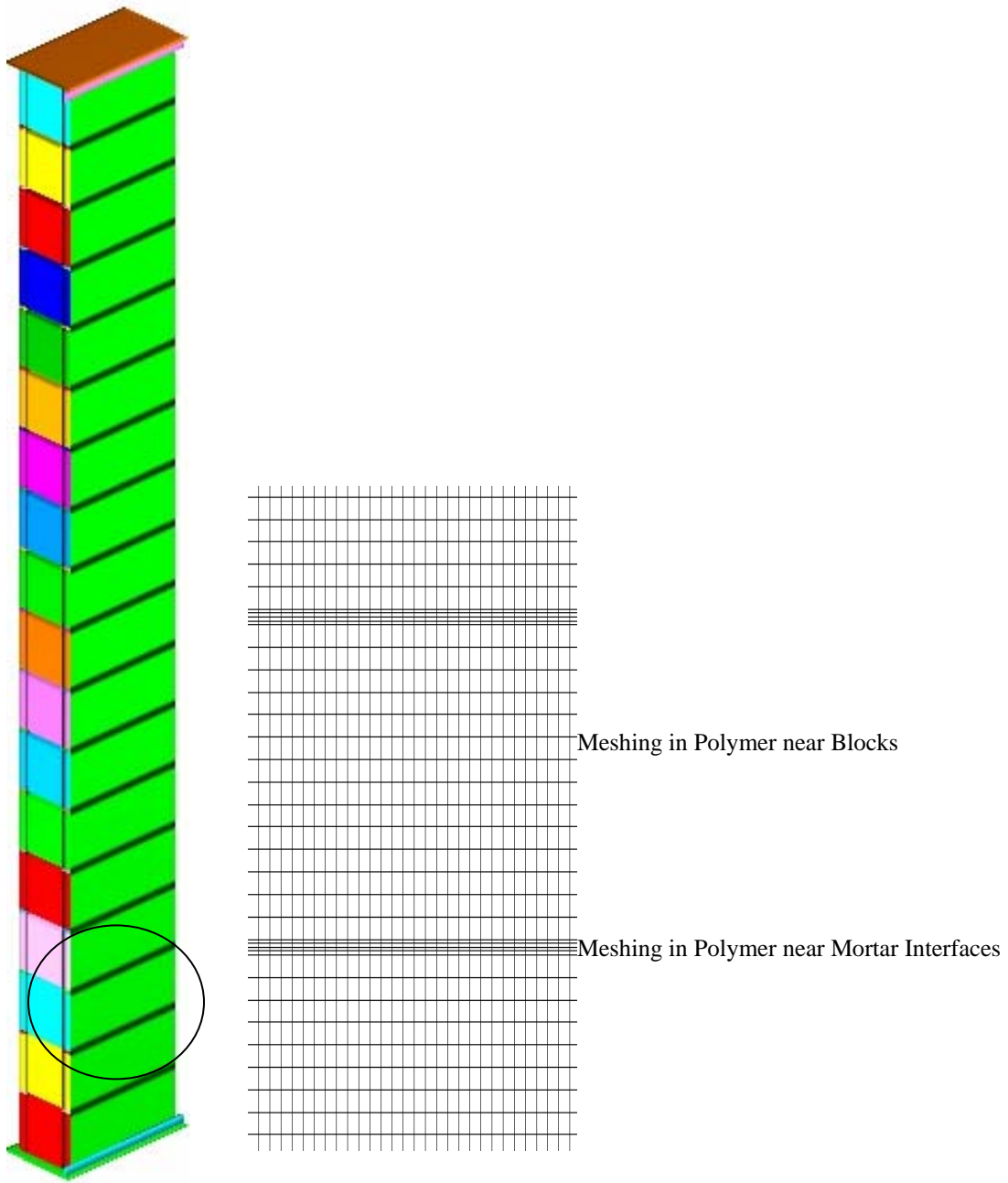


**FIG. 120. Baseline Model Setup Modified for Strain Rate Analysis**

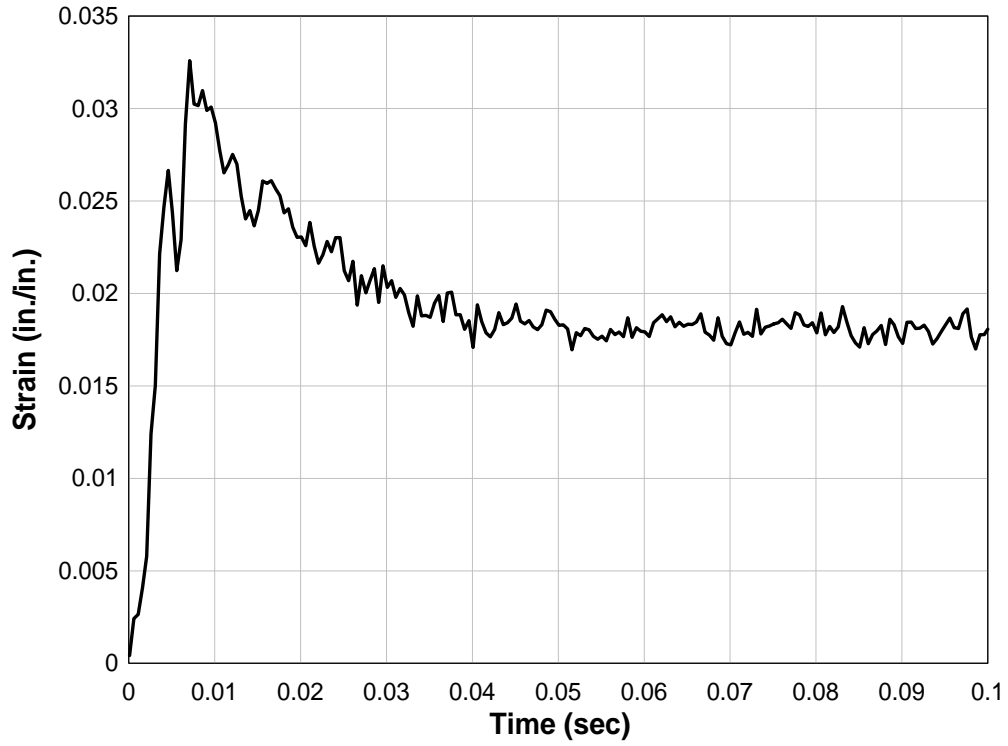


**FIG. 121. Strain in Polymer near Bottom Mortar Joint for Load I**

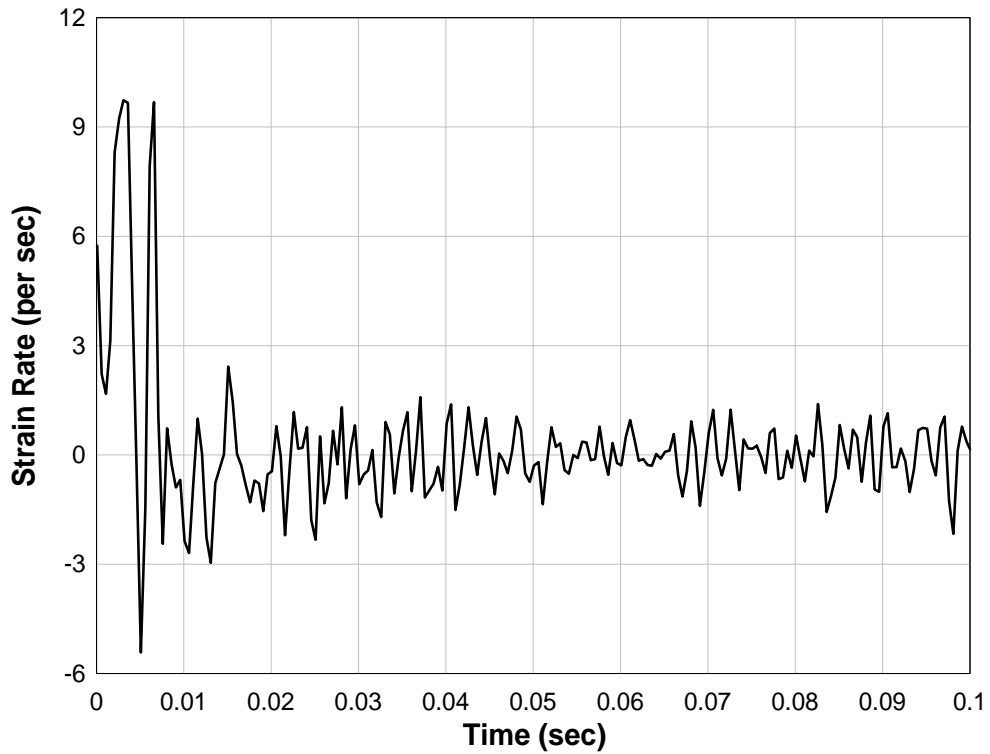


**FIG. 122. Strain Rate in Polymer near Bottom Mortar Joint for Load I**

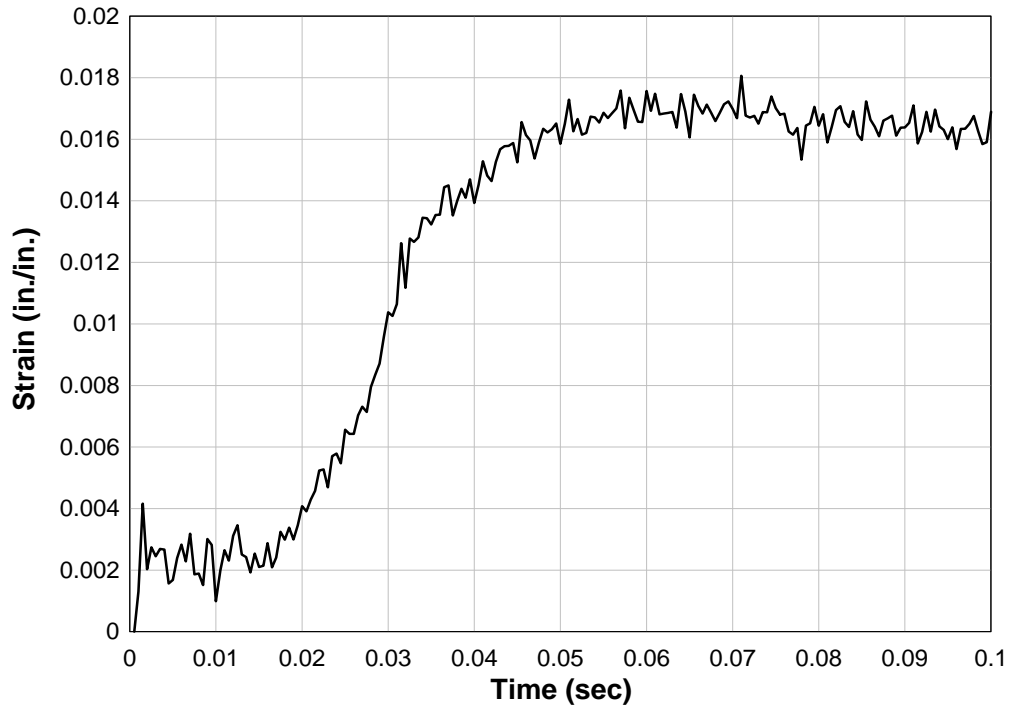


**FIG. 123. Strain in Polymer near Center Mortar Joint for Load I**

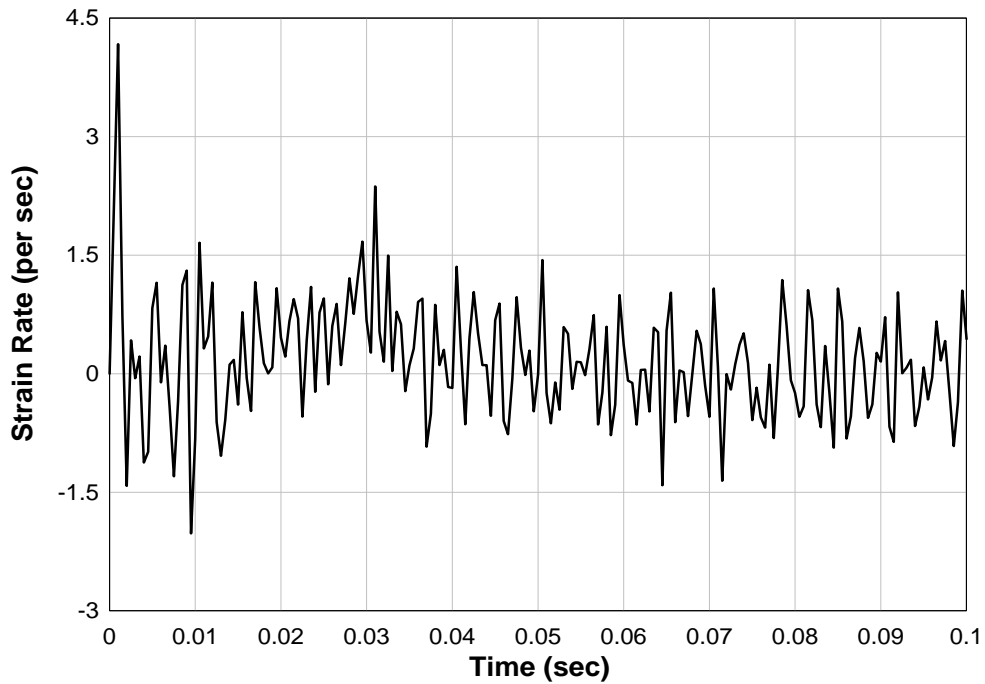


**FIG. 124. Strain Rate in Polymer near Center Mortar Joint for Load I**

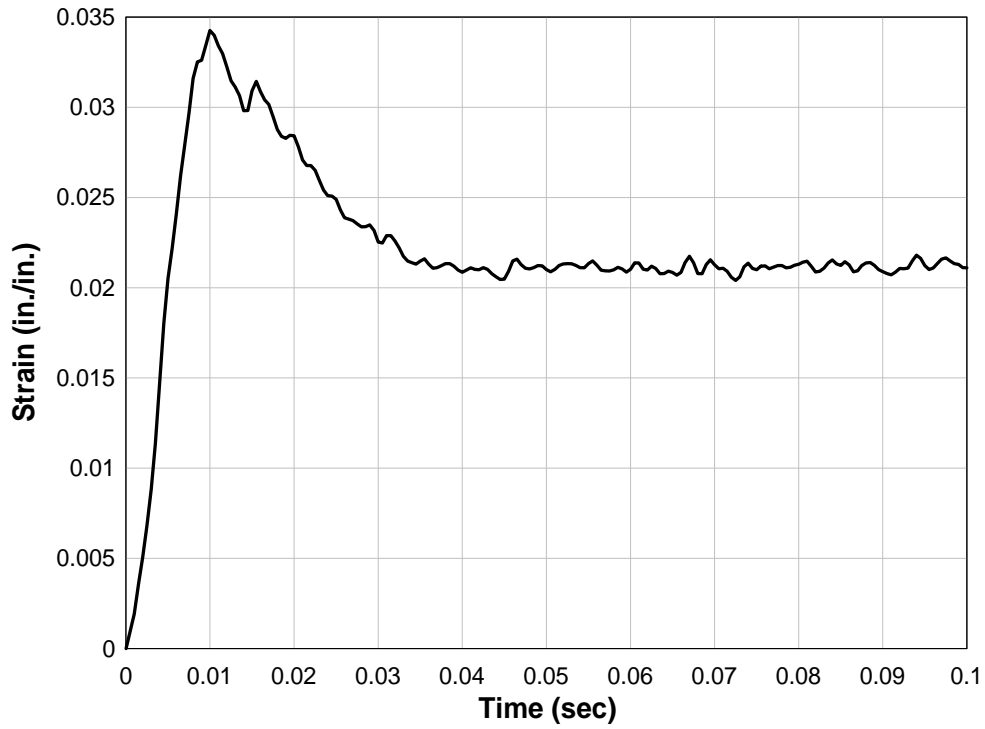


**FIG. 125. Strain in Polymer near Bottom Mortar Joint for Load II**

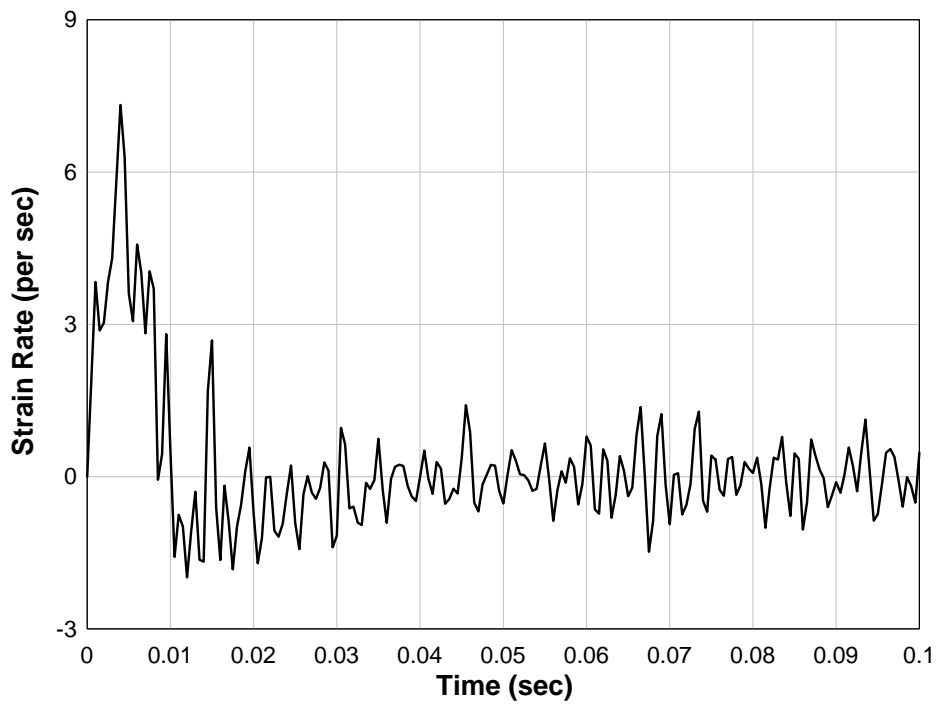


**FIG. 126. Strain Rate in Polymer near Bottom Mortar Joint for Load II**

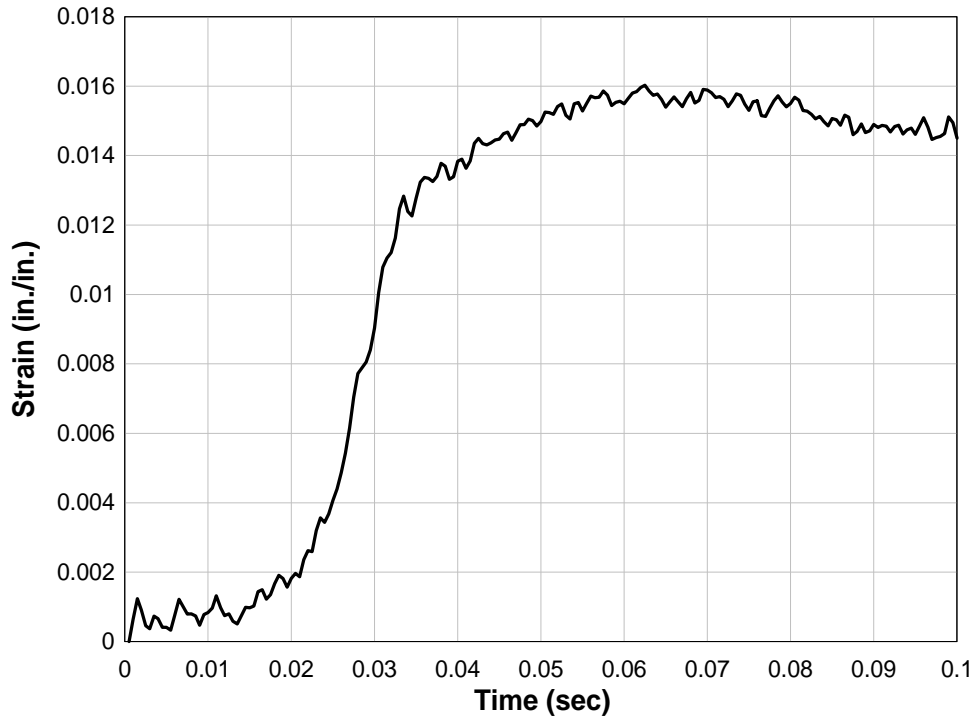


**FIG. 127. Strain in Polymer near Center Mortar Joint for Load II**

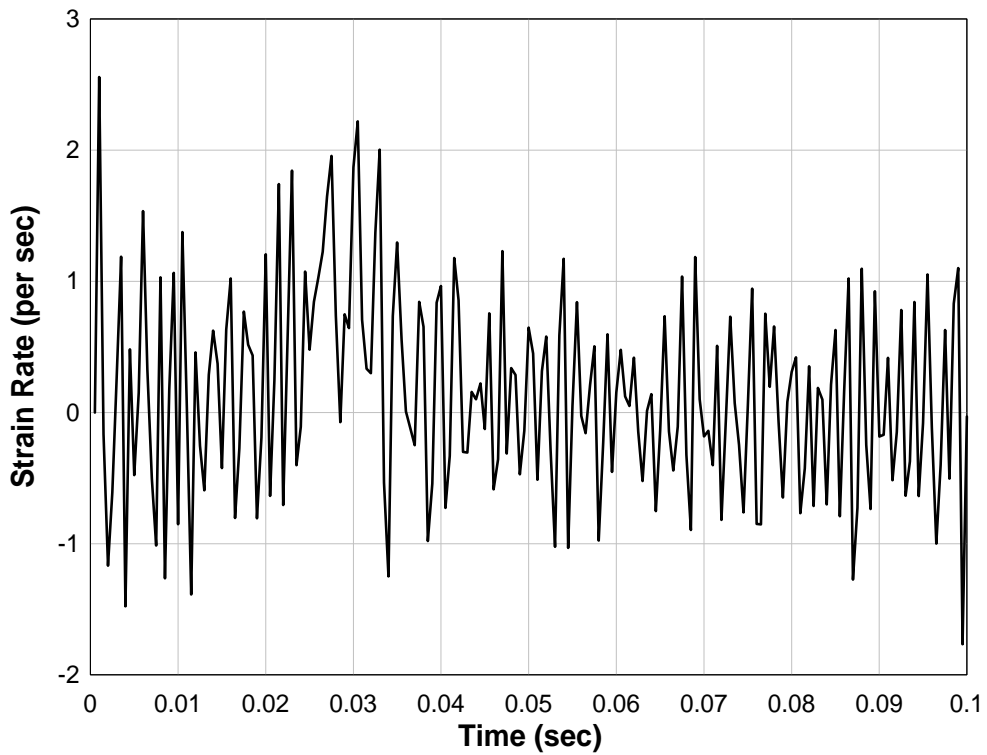


**FIG. 128. Strain Rate in Polymer near Center Mortar Joint for Load II**

## CHAPTER 6. MODELS FOR STATIC RESISTANCE FUNCTION

### 6.1 Definition of Static Resistance Using LS-DYNA

Static nonlinear analysis using a modified version of the baseline model was carried out using LS-DYNA. Since contact surfaces are problematic in static analyses, the contact surfaces used in the dynamic analyses were eliminated, and the nodes of corresponding interfaces were merged. The MAT\_BRITTLE\_DAMAGE material model was used for concrete elements. The tensile limit (TLIMIT) in the \*MAT\_BRITTLE\_DAMAGE was set to 50 psi. The static implicit analysis was conducted by introducing the following cards in the input deck. \*CONTROL\_IMPLICIT\_GENERAL card was used to activate the implicit analysis. The IMFLAG parameter was set to 1, and the initial load step (DTO) of 0.01 was used. Default values of remaining parameters were used. The implicit card used for the analysis is shown. Three models, varying in boundary conditions, were studied.

#### 6.1.1 Model 1 Setup

Polymer nodes were merged with block nodes on the back face of the blocks except in a region surrounding the mortar joints. This ensured a stable resistance provided by the polymer after failure of the mortar joint. The top and bottom edges on the backside of the wall model were restrained against translation so that the model behaves like a simply supported beam (Fig. 129). To start with, 1 psi load was uniformly applied on the front face of the wall.

```
*CONTROL_IMPLICIT_GENERAL
$  IMFLAG      DTO      IMFORM      NSBS      IGS      CNSTN      FORM
   1          0.01
```

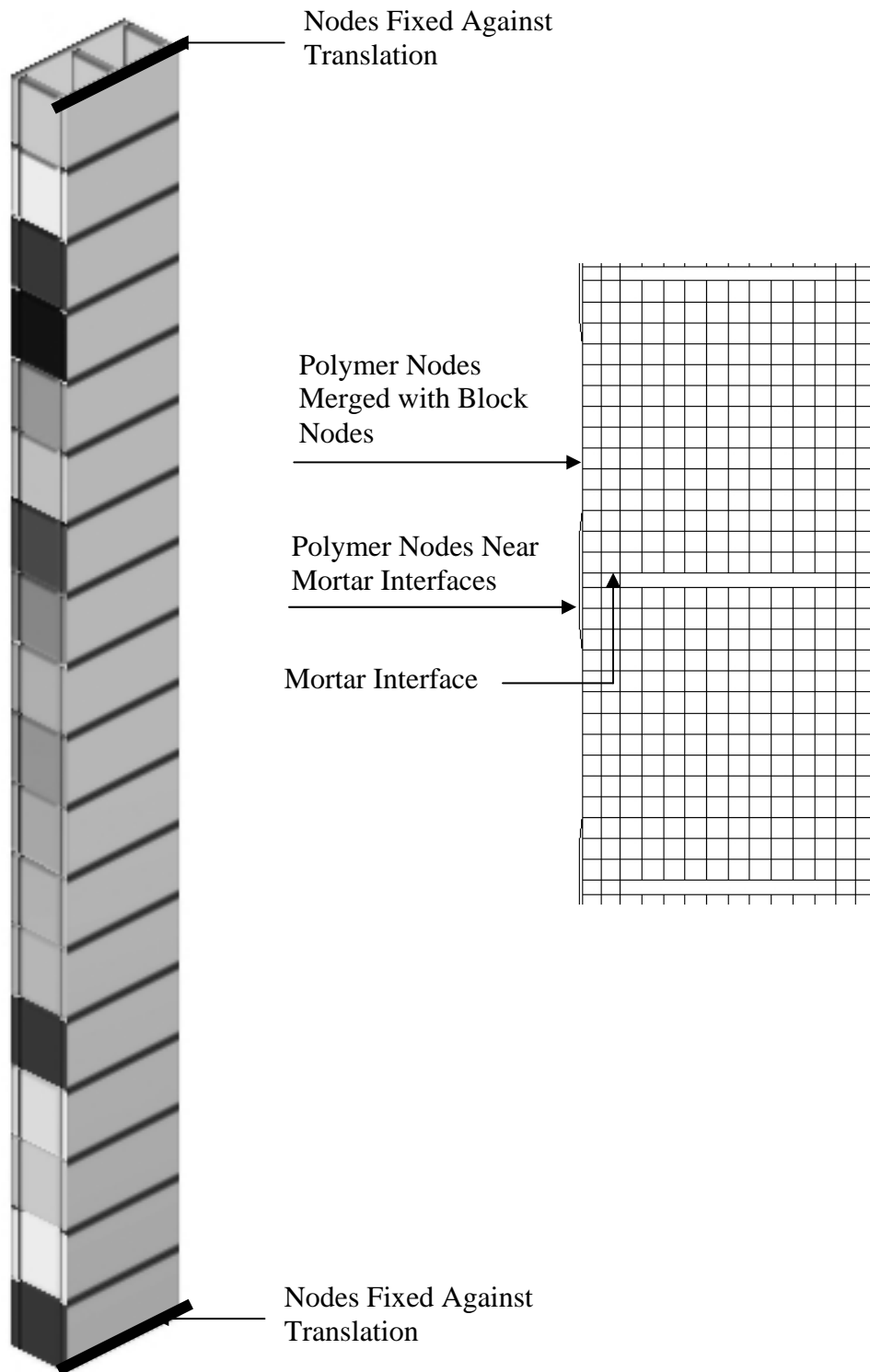
##### 6.1.1.1 Results

The load curve illustrated in Fig. 130 was applied, and the load-displacement curve shown in Fig. 131 resulted. The elements in the mortar interface reached their tensile limit at 0.42 psi of lateral pressure (Fig. 129). Brittle failure of the center mortar interface was indicated by a jump corresponding to 0.42 psi load. Fig. 132 shows the strain in the center mortar joint elements. Arching stiffness in the system occurred after failure in the concrete.

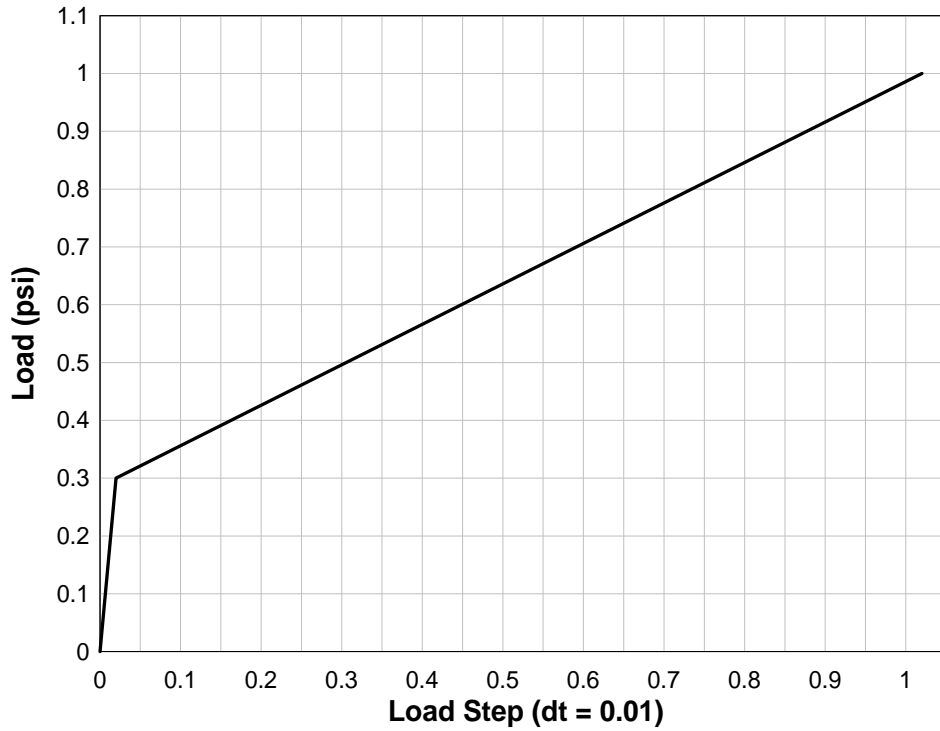
Strains in two mortar joints above mid-height mortar joint are shown in Fig. 133. Although the strain in the center mortar interfaces increases even after 0.42 psi (failure load), the strain in the other mortar interfaces reduces after 0.42 psi. This indicates failure of center mortar interface only.

Fig. 134 shows strain in the polymer near the mid-height mortar interface. It can be seen that, before failure of the concrete (0.42 psi load), stress at the polymer mid

height is only 1.2 psi, whereas after concrete rupture stresses increase rapidly as the load is taken by the polymer.



**FIG. 129. Model 1 Setup for Static Nonlinear Analysis**



**FIG. 130. Load-Load Step Curve for Model 1**

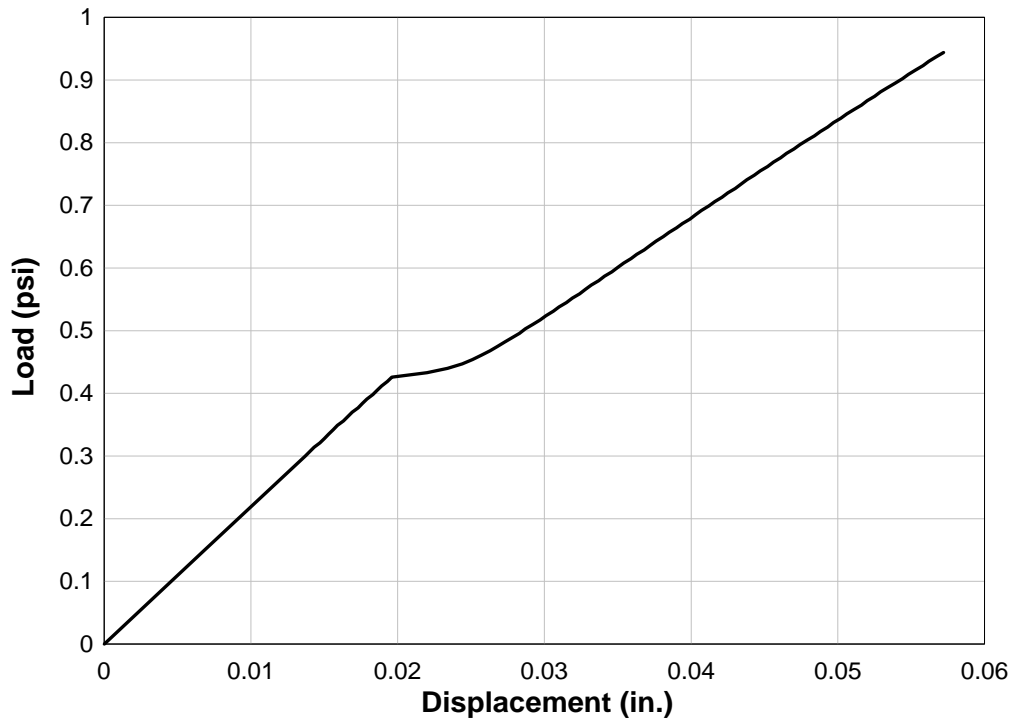


**FIG. 131. Load-Displacement Curve for Model 1**

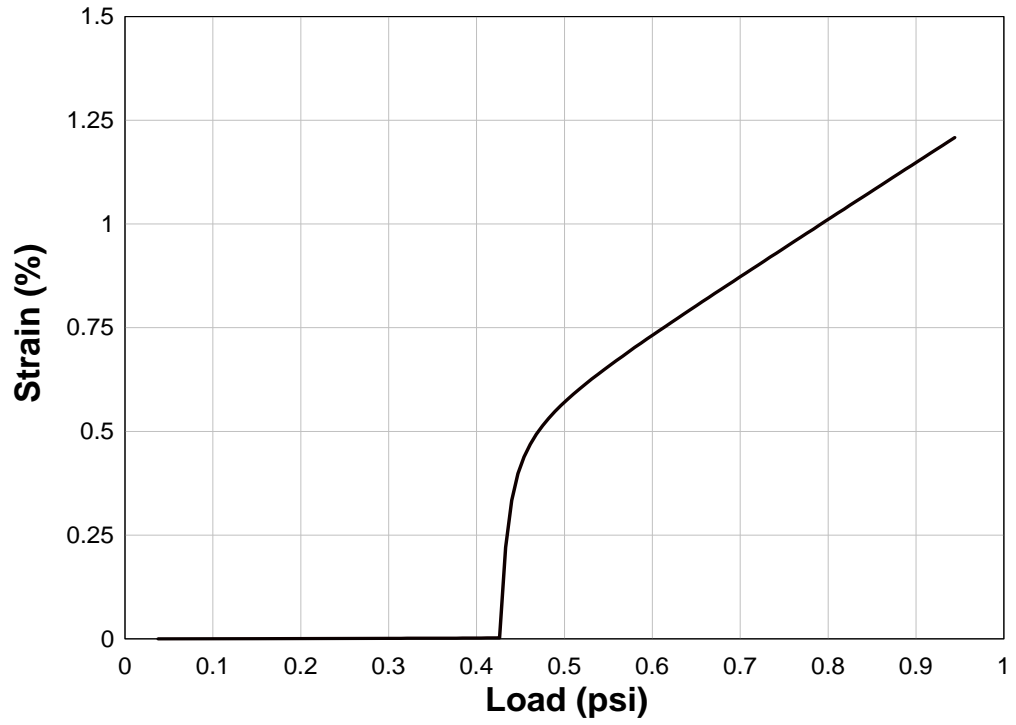


**FIG. 132. Strain in Mid-Height Mortar Interface**

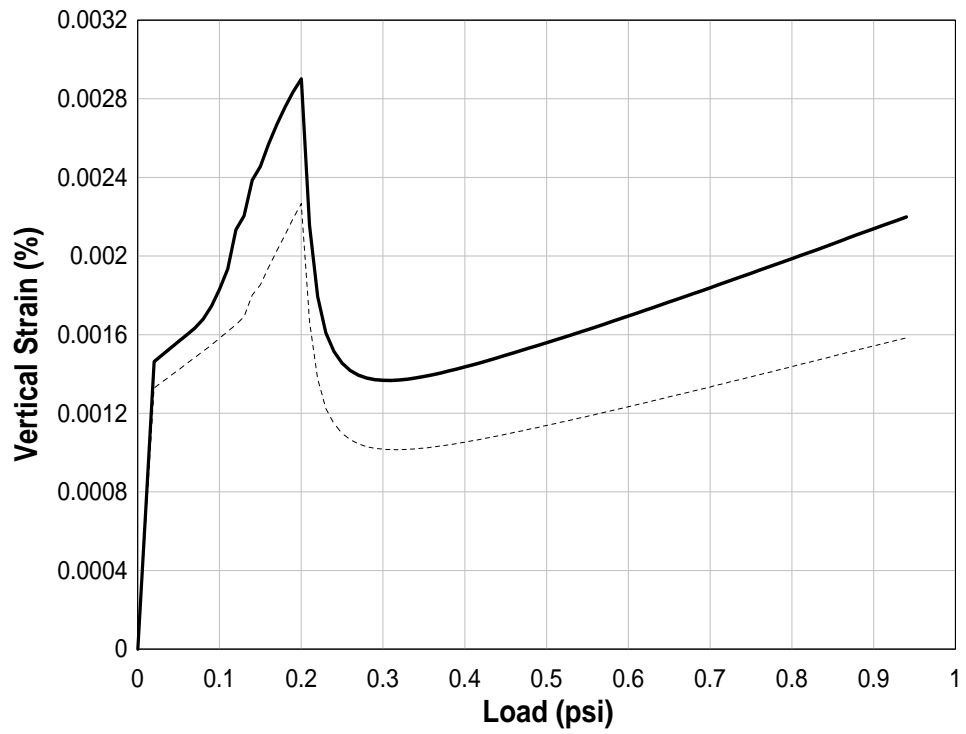


**FIG. 133. Strain in Mortar Joints near Mid-Height**

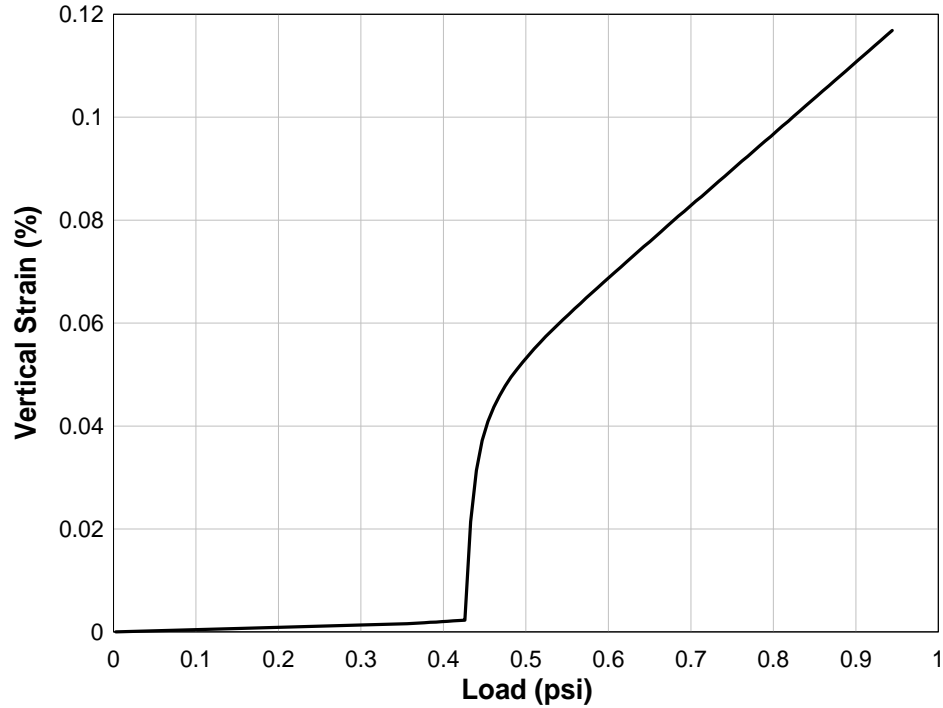


**FIG. 134. Vertical Strain in Polymer near the Mid-Height Mortar Interface**

### 6.1.2 Model 2 Setup

This model is similar to Model 1 except that all the polymer nodes were merged to the concrete nodes (Fig. 135). A maximum load of 0.133 psi was applied to capture concrete failure in load-displacement curve.

#### 6.1.2.1 Results

Resistance function as seen in Fig. 137 was obtained when 1 psi load was obtained, as shown in Fig. 136. Fig. 137 and Fig. 138 present the load-displacement curve and strain in the concrete for Model 2. As seen from Fig. 138, the concrete ruptures at 0.35 psi load. Since there is not much difference in post-failure stiffness of the system with and without polymer, it was concluded that arching resists further deflection of the wall.

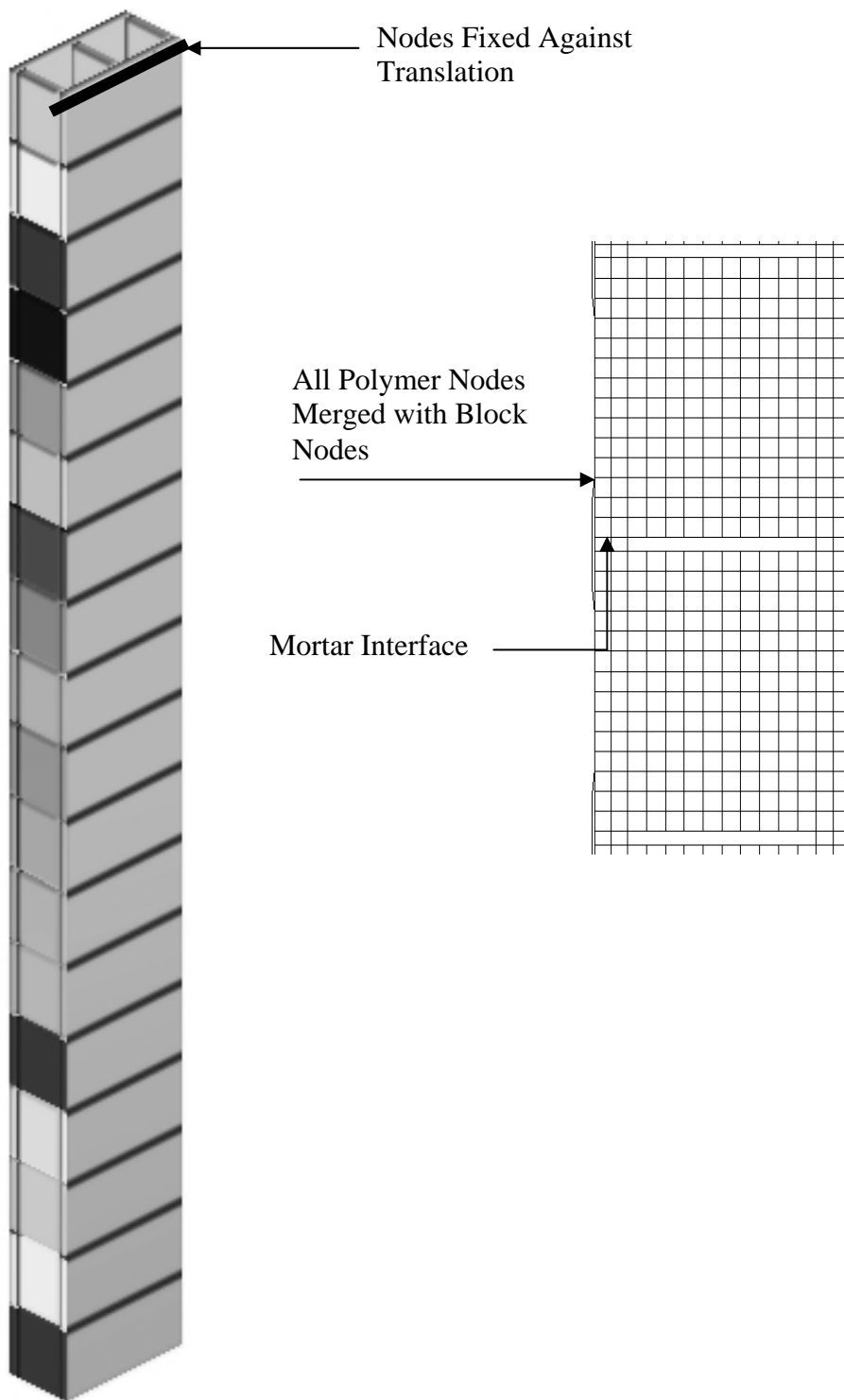


**FIG. 135. Model 2 Setup for Implicit Static Nonlinear Analysis**

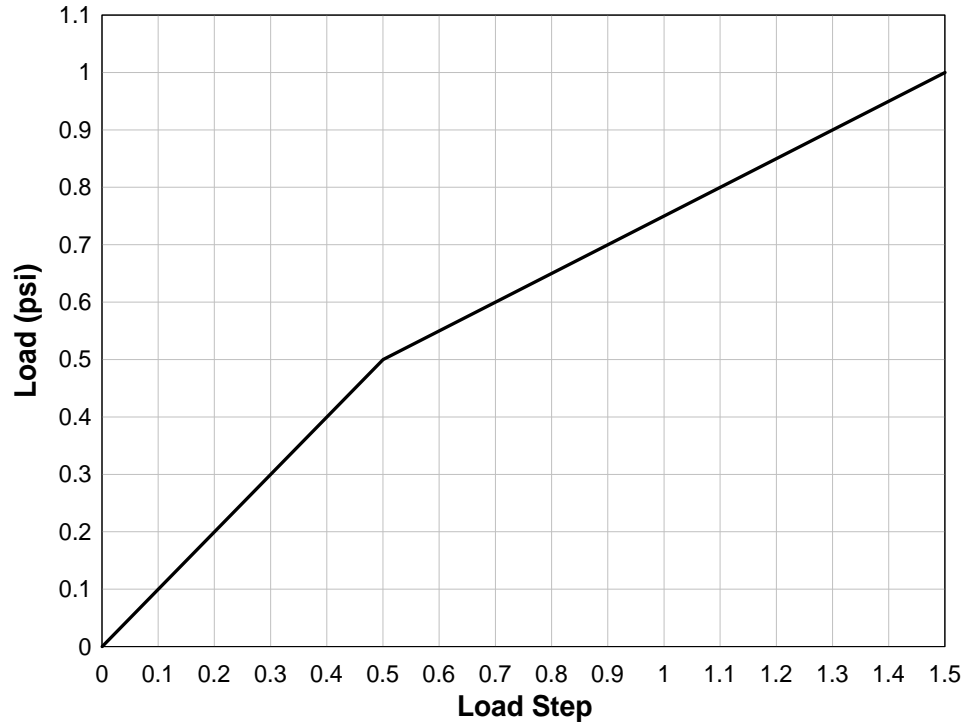


**FIG. 136 Load-Load Step Curve for Model 2**

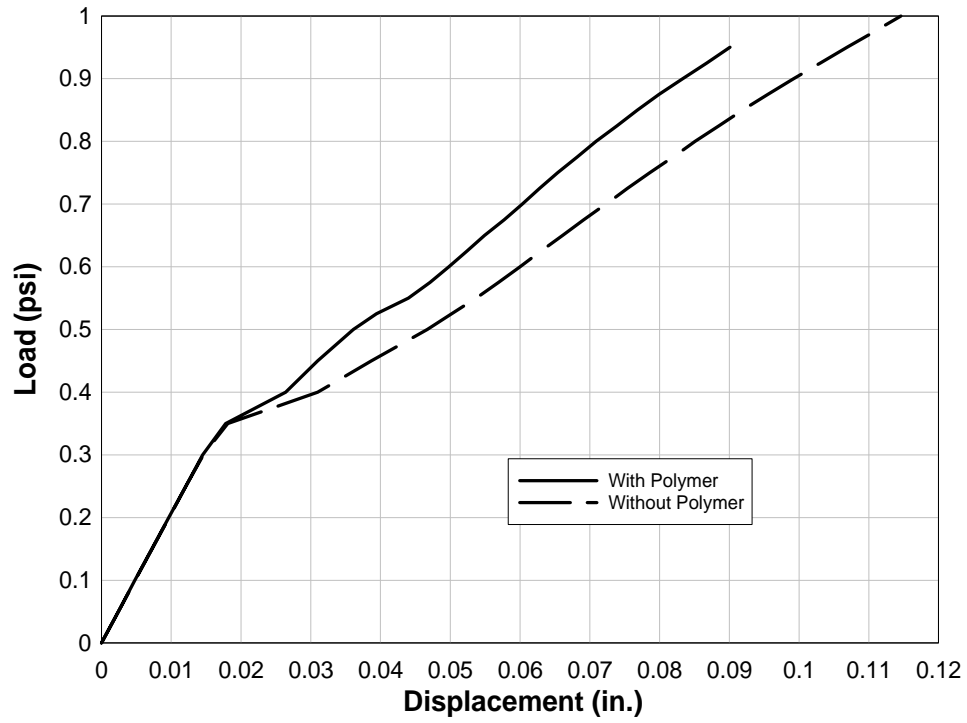


**FIG. 137. Load-Displacement Curve for Model 2**

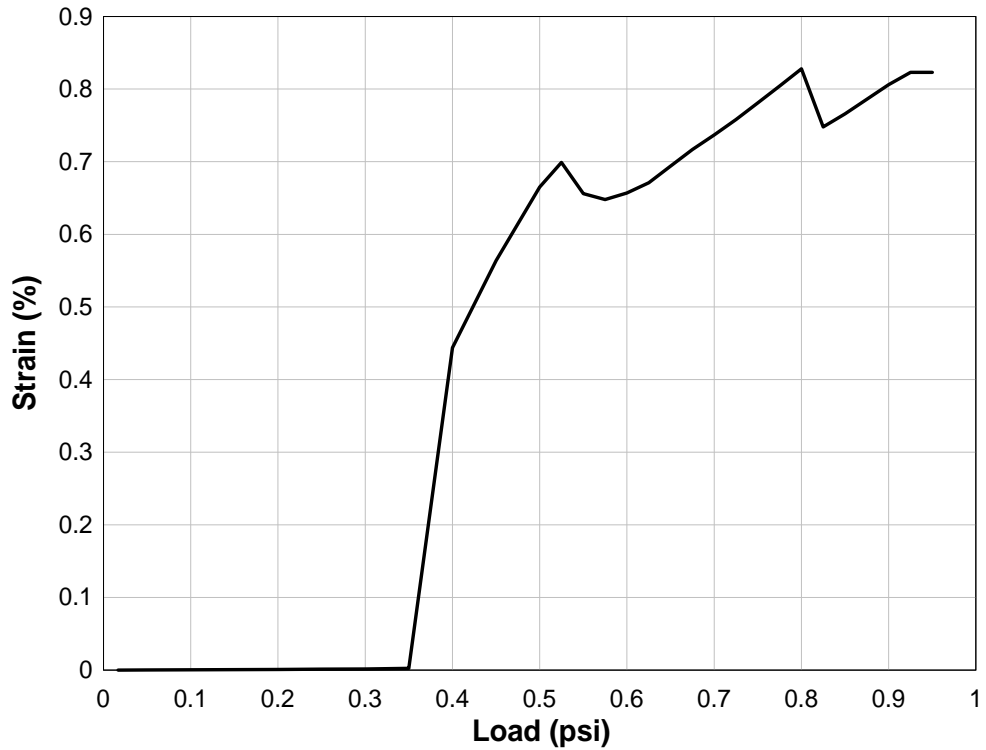


**FIG. 138. Mortar Joint Strain near Mid-Height**

### 6.1.3 Model 3 Setup

The translational restraints were applied to the front edges of the wall at the top and bottom to study the behavior of the model without arching effects. The polymer nodes were merged with block nodes. A maximum load of 0.15 psi was applied (Fig. 139).

Fig. 140 shows the resistance curve. Failure occurred at the mortar joints at 0.075 psi load. Fig. 141 shows the stiffening in polymer after mortar joint failure. The model became unstable at 0.13 psi load.

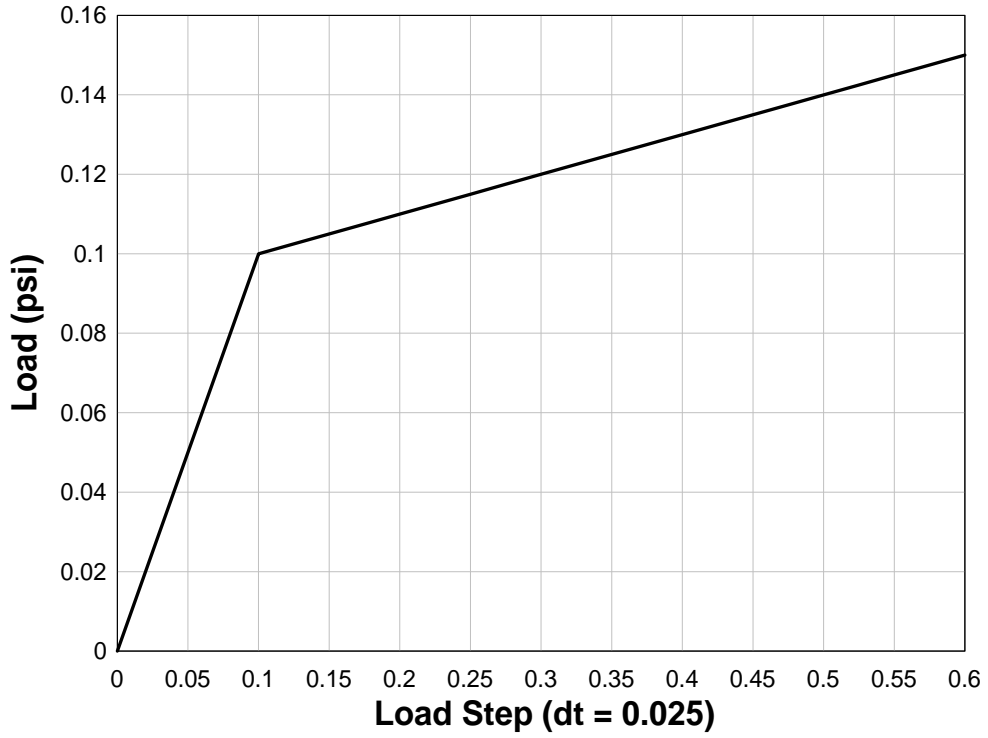


**FIG. 139. Load-Load Step Curve for Model 3**

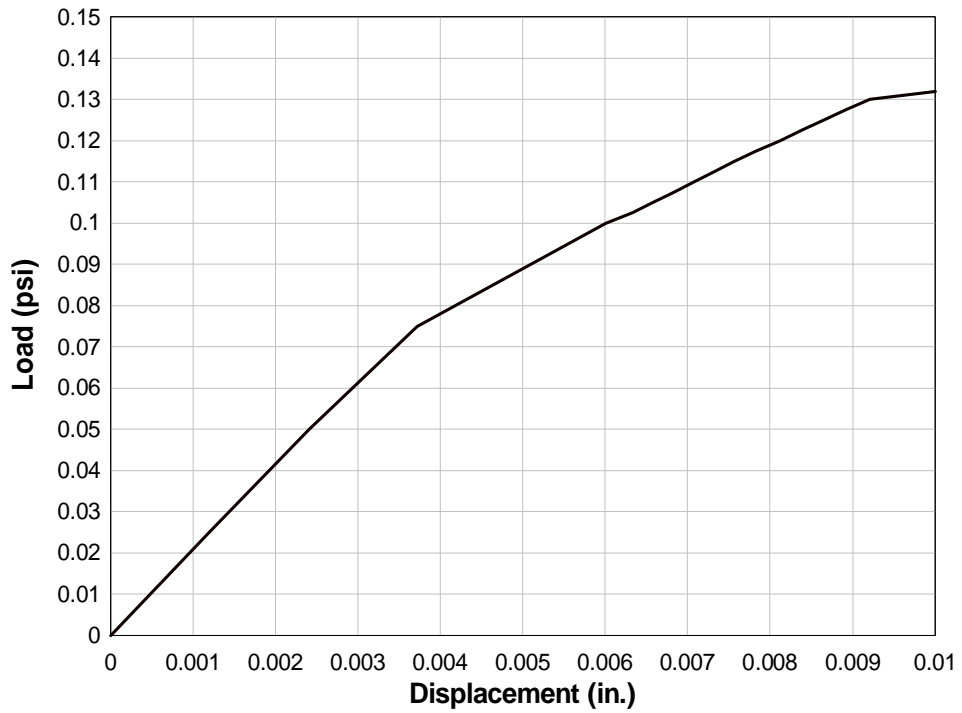


**FIG. 140. Load-Displacement Curve for Model 3**

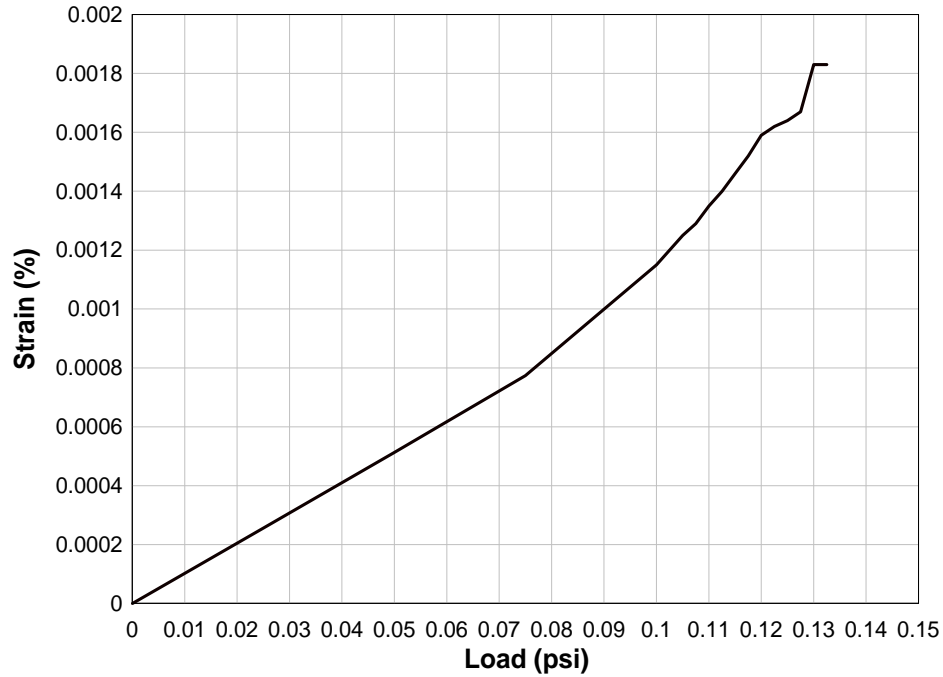


**FIG. 141. Strain in Polymer at Mid-Height**

## 6.2 Static Resistance of Membrane

### 6.2.1 Need

One approach for developing a resistance function of the polymer-reinforced wall is to add the resistance provided by the polymer reinforcement to the resistance provided by the masonry. The thickness of the polymer reinforcement used in AFRL tests was approximately 1/8 in. The total static resistance of the wall can be approximated as the sum of resistances of the components that make up the wall (Knox et al. 2000). Also, the deflection in the polymer and other components is assumed to be equal to that of the wall. The polymer is subjected to the static uniform pressure acting normal to the membrane. Therefore, to study the behavior of the membrane, static analyses of the membrane were conducted. Translations are restrained for nodes along shorter edges for one-way action. The elastomer reinforcement can be idealized as a simply supported thin membrane using classical membrane theory (Knox et al. 2000).

### 6.2.2 Equation

Let  $\nu$  = Poisson's ratio,  $E$  = modulus of elasticity,  $t$  = thickness of membrane,  $a$  = unsupported length of membrane, and  $k$  = constant for Poisson ratio:

$$k = \sqrt[3]{3 \cdot (1 - \nu^2)} \quad (20)$$

At the center of the membrane subjected to uniform pressure,

Deflection

$$\Delta = \frac{k}{4} \cdot t \cdot \sqrt[3]{\frac{p \cdot a^4}{E \cdot t^4}} \quad (21)$$

Strain

$$\varepsilon = \frac{t}{2 \cdot k} \left( \frac{p \cdot a}{E \cdot t} \right)^{\frac{2}{3}} \quad (22)$$

The strain can be calculated from the displaced membrane as follows:

$$\varepsilon = \frac{8 \cdot t \cdot \Delta^2}{3 \cdot (1 - \nu^2) \cdot a^3} \quad (23)$$

The AFRL tests involved 88 in. X 144 in. wall panels. The membrane of similar dimensions was modeled with 44 X 72 elements. CQUAD4 shell elements were used to define nonlinear hyperelastic membrane bending behavior. The top and bottom edges were restrained against translation for one-way action. The model was developed using MSC-PATRAN, and MSC-NASTRAN solver was used for analysis. Geometric nonlinear static analysis was carried out.

### 6.2.3 Results

Four models were analyzed by varying the thickness, pressure applied, and number of iterations used by the solver. Nodal deflection at the center of the membrane was plotted.

#### 6.2.3.1 Analysis I

In this analysis, 10 psi pressure was applied on 1 in. thick polymer. PATRAN analysis resulted in 18.1 in. deflection after 25 iterations, whereas the equation resulted in 17.1 in. displacement. Hence 4.8% error was noted. Fig. 142 shows the displacement variation at the center of the membrane with increase in load.

#### 6.2.3.2 Analysis II

In this analysis 5 psi pressure was applied on 0.5 in. thick polymer. PATRAN analysis resulted in 18.7 in. deflection after 50 iterations, whereas the equation resulted in 17.1 in. displacement. Hence 8.7% error was noted. Fig. 143 shows the displacement variation at the center of the membrane with increase in load.

#### 6.2.3.3 Analysis III

In this analysis 5 psi pressure was applied on 0.25 in. thick polymer. PATRAN analysis resulted in 23.1 in. deflection after 250 iterations, whereas the equation resulted in 21.5 in. displacement. Hence 6.11% error was noted. Fig. 144 shows the displacement variation at the center of the membrane with increase in load.

#### **6.2.3.4 Analysis IV**

In this analysis 1 psi pressure was applied on 0.125 in. thick polymer. PATRAN analysis resulted in 16.8 in. deflection after 50 iterations, whereas the equation resulted in 15.8 in. displacement. Hence 5.02% error was noted. Fig. 145 shows the displacement variation at the center of the membrane with increase in load.

#### **6.3 Summary and Conclusions**

The equation presented by Seide et al. (1977) can be used to define the resistance of the membrane. Finite element analyses demonstrated the accuracy of the equations to predict the maximum deflection and in-plane stresses in the membrane. Finite element results deviated from the postulated equations by 5% to 10%. The difference could be reduced by refining the mesh, but at the expense of computation time and storage space. An equation that is independent of applied load and modulus of elasticity is postulated to calculate the strain from displacement. Resistance function of polymer reinforced single unit width wall model was investigated using an implicit static LS-DYNA analysis. A brittle failure of mid-height mortar joint was observed at 0.42 psi uniformly applied pressure due to arching in wall when the tensile limit for concrete was set to 50 psi. When the arching effect was eliminated, the concrete failed at 0.08 psi, and stiffness was provided by the polymer. However, computational instabilities were observed for most of the analyses. Further work is required to eliminate these problems and obtain a complete resistance function of the system.

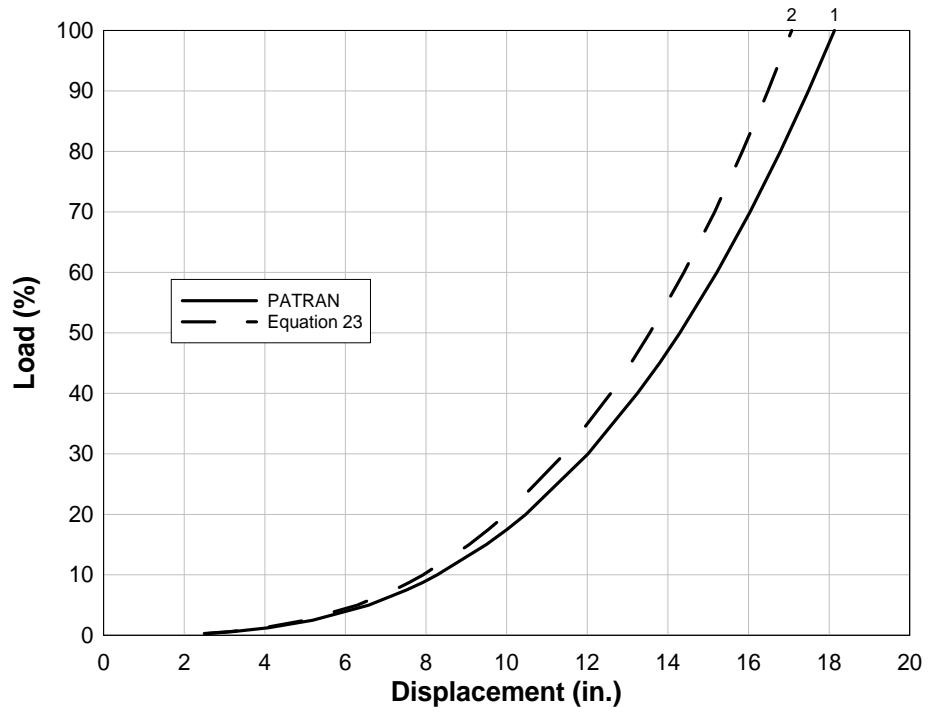


FIG. 142. Membrane Static Analysis I

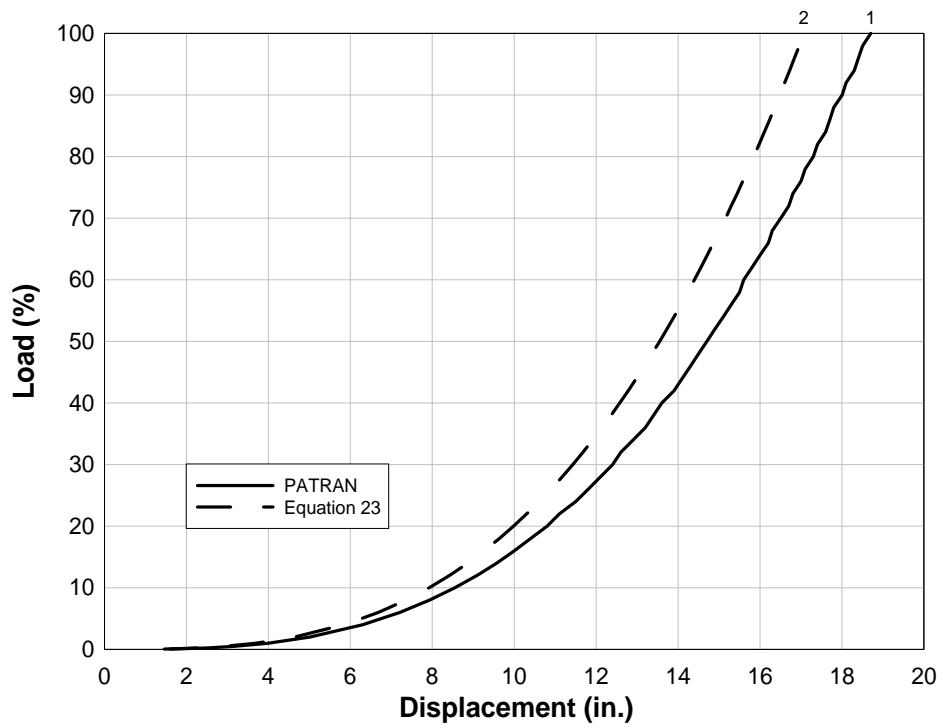
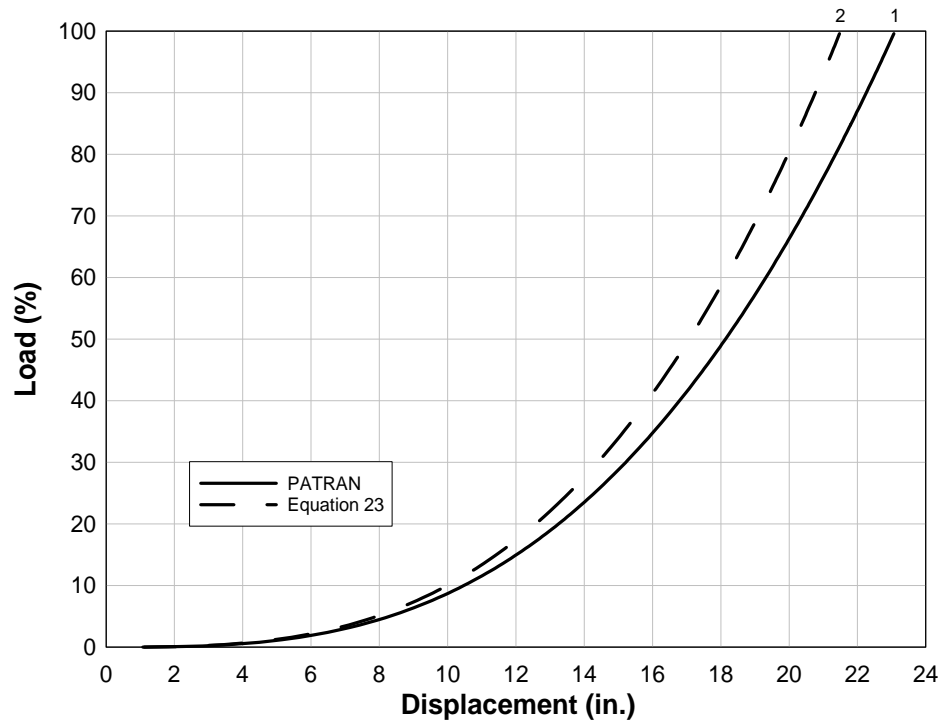
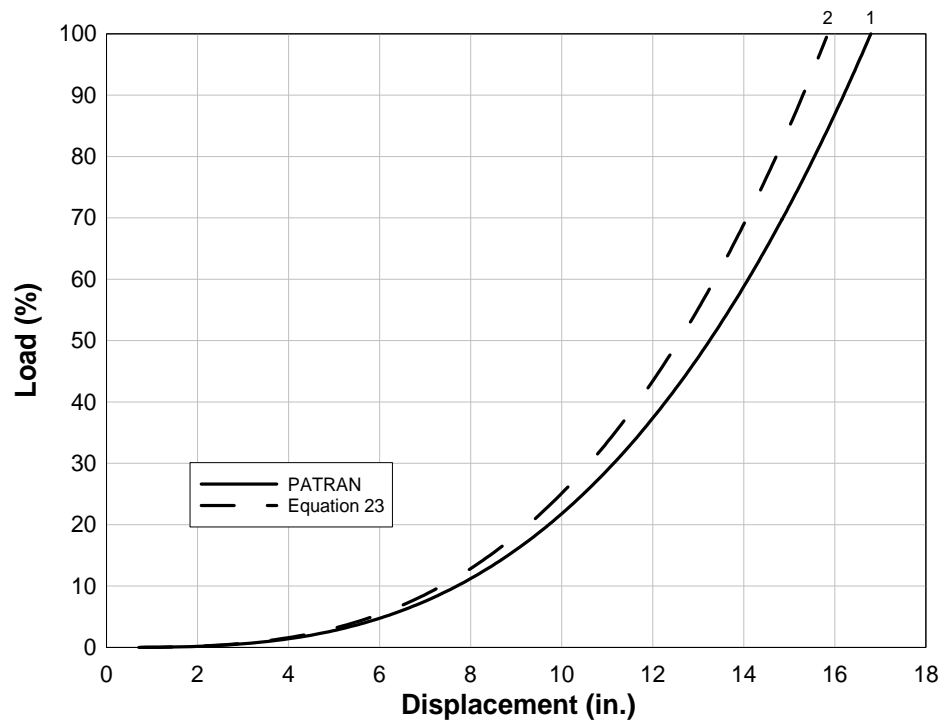


FIG. 143. Membrane Static Analysis II



**FIG. 144. Membrane Static Analysis III**



**FIG. 145. Membrane Static Analysis IV**

## CHAPTER 7. CONCLUSIONS

### 7.1 Summary and Conclusions

Finite element models were developed to evaluate the behavior of polymer reinforced masonry walls subjected to blast loads. Several modeling and meshing approaches were used, varying from a single concrete masonry unit with high fidelity meshing to entire walls with door and window openings. LS-DYNA, a nonlinear finite element solver, was used to conduct transient dynamic analyses. The various constitutive material models available in LS-DYNA were evaluated, and the most suitable model was chosen for simulating the concrete and polymeric components. Contact interfaces required to simulate the relative displacement between components were included with the resistance defined with normal stress limits, shear stress limits, and friction resistance. Good correlation to test data was achieved.

Modal analyses required to calculate damping input parameters were conducted, and the natural frequencies and modes of vibration of the wall were extracted. A 5% global damping was adopted for the analyses. Gravity preload was induced using dynamic relaxation methods and was verified from interface forces. However, it was demonstrated that gravity load had little influence on the transverse displacement of the wall. Blast load was applied using an imbedded blast function that requires only the TNT equivalent and the coordinates of the explosive charge origin. Three loading functions were used for the analyses: Load I, peak pressure = 66.3 psi and impulse = 214.8 psi-msec; Load II, peak pressure = 44.5 psi and impulse = 220.6 psi-msec; and Load III, peak pressure = 129.9 psi and impulse = 356.8 psi-msec.

A "baseline" model of a one-way flexure single CMU width of the masonry wall was constructed. The overall dimensions and support conditions reflected tests conducted by AFRL at Tyndall Air Force Base. The unit width approach was necessary so that high fidelity models could be developed without exceeding the capacity of computation resources. The baseline model included two elements through the block face shells and webs. The analyses were run on a parallel processing supercomputer using up to 128 processors and produced 3.5 GB of output per analysis. The lateral displacement results of the baseline model compared well with field test data available from AFRL explosive tests.

Displacements, effective stresses, interface forces, vertical strain at various locations in the polymer, and energy distribution in the system were studied for the Load I and Load III loading conditions using the baseline model. The maximum displacement and velocity were 7.5 in. and 280 in./sec, respectively, for Load I, and 12.5 in. and 480 in./sec, respectively, for Load III. Fracture of the front face occurred under Load III, and the excessive displacement would have resulted in collapse of the system. However, complete fracture of the concrete masonry face shells was not evident under Load I. The maximum effective stresses in the polymer for Load I and Load III were 1600 psi and

2150 psi, respectively. Maximum strains in the polymer occurred near the bottom mortar joint and were 2.4% and 3.5% for Load I and Load III, respectively.

An input sensitivity study was conducted by systematically altering input parameters of the baseline model and studying the effects on the global response of the structure. Parameters varied included initial modulus, yield strength, rupture strain, polymer thickness, bond strength between mortar joints, and bond strength between polymer and CMUs.

The rupture strain input parameter was varied as 2%, 5%, and 10% elongation. Failure in the polymer occurred for the 2% rupture strain, and significant changes to the wall behavior resulted. The internal energy in the polymer reduced by 18% for Load I and 9% for Load III when the rupture strain input parameter was decreased from 10% to 2%. No effect on displacements and velocities occurred for the 5% and 10% rupture strain models.

The polymer thickness was varied as 1/16th in., 2/16th in., 3/16th in., and 4/16th in. No significant change in displacement and velocity was noted with this variation. However, strain energy in the polymer increased by 50%, 35%, and 20%, and kinetic energy in polymer increased by 85%, 45%, and 30% with 1/16th in. polymer thickness increases.

When the initial modulus of the polymer was increased by multiples of 10, no significant change in wall displacement and velocity occurred. The internal strain energy absorbed by the polymer increased in multiples of 2.5 to 3, and vertical strains in the polymer decreased by 25% to 30%. It was concluded that an increase in elastic modulus of polymer decreases peak strains in the polymer and increases internal energy absorbed by the polymer.

The effect of polymer yield stress on wall behavior was studied. Polymer input parameters representing 800 psi, 1000 psi, and 1400 psi yield stress were used. Polymer with 800 psi and 1000 psi yield stress demonstrated 3% to 7% effective plastic strains near the bottom mortar joint. It was noted that the lower values of yield stress resulted in more strain energy absorption by the polymer.

Arching did not occur in the models. Fracture of some of the front face shell elements at early stages of the response, along with large shearing displacement at the top and bottom mortar joints, resulted in only slight upward movement of the topmost block.

The mortar joint bond strength affects the failure mode of the wall. The energy transferred to the polymer depends on the mortar failure limits. Strains in the polymer near the interfaces increased by multiples of approximately 3.5 for Load I and 4.5 for Load III when the mortar joint resistance parameters were very low.

The effect of polymer-CMU bond strength was studied. Maximum strains in the polymer decreased by more than 50% when the interface strength input parameter was very low, and stresses were uniformly distributed over the polymer. The strain energy absorbed by the polymer decreased by 10% when polymer was not bonded to the wall. However, stresses at connections to the roof and floor boundaries increased substantially, indicating the need for careful connection design if a “catcher system” approach is used.

Walls with openings of various sizes were studied using less-refined meshes. The openings sizes were the same as used in field tests conducted by AFRL. Wall openings increased the overall displacements in the wall by 10% to 15%. Hence, the resistance description for walls with windows and doors is different than one without openings. It

was noted that increasing the polymer thickness around openings decreased displacement. Stress concentrations propagated from corners of openings. However, because a smeared-mass meshing approach was used and the windows/doors and frames were not included in the models, additional modeling work is needed to firmly understand the influence of window and door openings on polymer reinforced walls.

An in-depth study was conducted to determine the rate of strain incurred by the polymer. The strain rate can be attributed to two phenomena. The first is the shock wave propagation through the material in which the strains in the polymer are low but the strain rate can be very high. The strain rate response studied in this effort, however, is the rate due to the flexural response of the system and is highest after the loading and stress wave propagation has subsided.

Four heuristic finite element models were developed to analyze the strain rate in the polymer reinforcement. These included a membrane under impulse load, membrane subjected to tension at rates similar to those observed in explosive tests, membrane subjected to shear, and polymer applied to a high fidelity single CMU width model. Theoretical analogies were also developed to derive closed form solutions. The polymer membrane resulted in strain rates up to  $1000 \text{ sec}^{-1}$ . The tension and shear models resulted in strain rates less than  $100 \text{ sec}^{-1}$ . The single unit width model resulted in a strain rate of less than  $10 \text{ sec}^{-1}$ . The conclusion from the strain rate study was that the maximum rate of strain incurred from the flexural response of the system under loading that would be withstood by the polymer reinforced CMU wall is moderate, less than  $100 \text{ sec}^{-1}$ .

Finally, the ability to develop nonlinear resistance functions using the static analyses capabilities of LS-DYNA was explored. The static resistance using the single unit width model with simply supported boundaries was defined. Difficulties arose with the contact interfaces. Arching stiffening was observed and significantly changed the behavior of the system after mortar joint failure at mid-height. Also, an equation for membrane displacement under static pressure was reviewed, and its validity was confirmed by geometric nonlinear finite element analyses.

## **7.2 Recommendations and Suggested Research**

Since this concept of improving the blast resistance of structures using polymer reinforcement is still in a state of development, further research holds tremendous potential. Additional parametric studies can provide better insight into the influence of dominant parameters. This study involved only one wall height and two loading conditions. Therefore, charge size and the standoff distances can be varied and the effects of global geometric parameters such as height of the wall and boundary conditions can be varied to study their effects on behavior. Furthermore, there is a tendency to focus on the displacement of the wall at the height-wise center, whereas this parameter is mass dominated and only slightly sensitive to major changes in material stiffness attributes of the thin elastomer coating. A better approach to studying the effectiveness of the polymer reinforcement is to look carefully at strain energy absorbed by the polymer with changes in input parameters and at the redistribution of maximum stresses and strains.

Future research may involve higher fidelity models for walls with openings that include integration with windows and doors and the rigidity of their frames. A parametric study can be conducted by varying opening size and polymer thickness to study strains in

the polymer, energy absorption effectiveness, and overall wall displacement. Static and dynamic analyses can be conducted.

The destructive nature of field tests makes it difficult to collect data that can be used to verify finite element models of structures subjected to blast. There is a need for additional field test data to verify the accuracy of finite element models. Furthermore, verification of some aspects of modeling approach can be done through laboratory tests. LS-DYNA offers many material models for concrete and polymeric materials. Laboratory tests can be conducted to understand the behavior of CMU and polymer under shock and impact loads and to verify that appropriate material models have been implemented in full-scale models subjected to blast loading.

The development of a static resistance function is critical for defining engineering approach for external reinforcement mechanisms. This effort explored the ability of the LS-DYNA models developed for nonlinear transient analysis to be used to define the static resistance of the wall. Additional work is required to use this approach for defining the static resistance of the system and for understanding the differences between the static resistance and dynamic resistance mechanisms.

Contrast between the “catcher” system approach and a well-bonded reinforcement has not been thoroughly examined. This effort demonstrated that the maximum strains that occur at mortar joints can be reduced with less bonding, but forces at connections increase. Stiffer, stronger, and more cost efficient materials may be a more suitable reinforcement if a strong bond is not required.

Finally, studies focused on connections and involving walls integrated with structural frames are needed. This study was limited to isolated reinforced walls. However, as effective reinforcement techniques are developed, additional loads will be transferred to the structural frames, which could lead to catastrophic progressive collapse of the entire building.

## LIST OF REFERENCES

- Avallone, E.A. and Baumeister, T. (1987). *Mark's standard handbook for mechanical engineers*, McGraw-Hill, New York, N.Y.
- Bala, S. (2001). "Contact modeling in LS-DYNA Part 2 of 4." *FEA Information International News*, September 2001, 6-11.
- Beshara, F.B.A. (March 1994). "Modelling of blast loading on aboveground structures-I. General phenomenology and external blast." Technical Paper, *Computers & Structures* Vol.51, No. 5, 585-596.
- Britt, J.R. and Lumsden, M.G. (1994). *Internal blast and thermal environment from internal and external explosions: A User's guide for BLASTX Code, Version 3.0*, Science Applications International Corporation, St. Joseph, Louisiana, Report No. SAIC 405-94-2.
- Broadhouse, B.J. (February 1995). *The Winfrith Concrete Model in LS-DYNA*, Structural Performance Department, AEA Technology, Winfrith Technology Centre.
- Connell, J.D. (2002). *Evaluation of elastomeric polymers for retrofit of unreinforced masonry walls subjected to blast*, Masters Thesis, University of Alabama at Birmingham, Alabama.
- Crawford, J.E., Bogosian, D.D., and Wesevich, J.W. (1997a). "Evaluation of the effects of explosive loads on masonry walls and an assessment of retrofit techniques for increasing their strength." *Proc., 8<sup>th</sup> International Symposium on Interaction of the Effects of Munitions with Structures*, McLean, Virginia.
- Crawford, J.E., Malvar, L.J., Wesevich, J.W., Valancius, J., and Reynolds, A.D. (1997b). "Retrofit of reinforced concrete structures to resist blast effects." Title No. 94-S34, *ACI Structural Journal*, 94(4), 371-377.
- Davidson, J.S., Porter, J.R., Dinan, R.J., Hammons, M.I., Connell, J.D. (2004). "Explosive testing of polymer retrofit masonry walls." *Journal of Performance of Constructed Facilities*, Vol. 18, No. 2, 100-106.
- Dennis, S.T. (1999). *Masonry walls subjected to blast loading-DYNA3D analysis*, U.S. Army Engineer Waterways Experiment Station, Vicksburg, Mississippi.

- Dharaneepathy, M.V., Keshava Rao, M.N., Santhakumar, A.R. (October 1995). "Critical distance for blast-resistant design." *Computers & Structures* Vol. 54, No. 4. pp. 587-595.
- Dinan, R.J., Fisher, J.W., Hammons, M.I., Porter, J.R. (2003). "Failure mechanisms in unreinforced concrete masonry walls retrofitted with polymer coatings," *Proceedings of the 11<sup>th</sup> international Symposium on Interaction of the Effects of Munitions with Structures*, May 5-9, 2003.
- Drysdale, R.G., Hamid, A.A., Baker, L.R. (1994). *Masonry and Structures: Behavior and Design*, Prentice Hall, Englewood Cliffs, New Jersey 07632.
- Du Bois, P.A. (2004). *Crashworthiness engineering course notes*, Livermore Software Technology Corporation, California.
- Govindjee, S., Kay, G. J., Simo, J.C. (1995). "Anisotropic modelling and numerical simulation of brittle damage in concrete." *International Journal for Numerical Methods in Engineering*, Vol. 38, 3611-3633 (1995).
- Hamid, A.A. and Drysdale, R.G. (January 1988). "Flexural tensile strength of concrete block masonry." *Technical Paper, Journal of Structural Engineering*, Vol. 114, No.1. pp. 50-66.
- Hill S.I. (2003). *High rate tensile tests of 2003HSD001 polyurea*, Evaluation Report UDR-TR-2003-00130, Report Submitted to Air Force Research Laboratory, Tyndall, Florida by Structural Test Group, University of Dayton Research Institute.
- Knox, K. J., Hammons, M. I., Lewis, T. T., and Porter, J. R. (2000). *Polymer materials for structural retrofit*, Force Protection Branch, Air Expeditionary Forces Technology Division, Air Force Research Laboratory, Tyndall AFB, Florida.
- Krauthammer, T. and Otani, R.K. (1997). "Mesh, gravity and load effects on finite element simulations of blast loaded reinforced concrete structures." Technical Paper, *Computers & Structures* Vol.63, No.6, pp. 1113-1120
- Krieg, R.D. (1972). *A Simple Constitutive Description for Cellular Concrete*, Sandia National Laboratory.
- Livermore Software Technology Corporation (2003) <[ftp://ftp.lstc.com/outgoing/faq/energy\\_balance](ftp://ftp.lstc.com/outgoing/faq/energy_balance)> (September 10, 2004).
- LS-DYNA keyword user's manual: nonlinear dynamic analysis of structures* (2003 version 970). Livermore Software Technology Corporation, Livermore, California.
- LS-DYNA theoretical user's manual: nonlinear dynamic analysis of structures*. (May 1998). Livermore Software Technology Corporation, Livermore, California.

- Martini, K. (1996a). *Finite element studies in the out-of-plane behavior of unreinforced masonry*, Ancient Reconstruction of the Pompeii Forum, School of Architecture, University of Virginia.
- Martini, K. (1996b). *Finite element studies in the two-way out-of-plane behavior of unreinforced masonry*, Ancient Reconstruction of the Pompeii Forum, School of Architecture, University of Virginia.
- Melis, G. (2002). *Displacement-based seismic analysis for out of plane bending of unreinforced masonry walls*, Masters Dissertation, European School Of Advanced Studies in Reduction Of Seismic Risk, Rose School.
- Moradi, L. (2003). *Constitutive properties of a single concrete masonry unit (CMU) subjected to blast*, Masters Project Report, University of Alabama at Birmingham.
- Randers-Pehrson, G. and Bannister, K.A. (March 1997). *Airblast loading model for DYNA2D and DYNA3D*, Army Research Laboratory, ARL-TR-1310.
- Schwer, L. (2001), *Laboratory tests for characterizing geomaterials*, Livermore Software Technology Corporation, Livermore, California.
- Seide, P. (1977). "Large deflection of rectangular membranes under uniform pressure." Technical paper, *International Journal of Nonlinear Mechanics*, Vol.12, pp397-406.
- Thornburg, D. (2004). *Evaluation of elastomeric polymers used for external reinforcement of masonry walls subjected to blast*, Masters Thesis, University of Alabama at Birmingham, Alabama.

## **APPENDIX**

### **LS-DYNA INPUT DECK FOR BASELINE MODEL**

```

$-----1-----2-----3-----4-----5-----6-----7-----8
$ LS-DYNA(960) DECK WRITTEN BY : eta/FEMB-PC version 28.0
$ ENGINEER :
$ PROJECT :
$ UNITS : IN, LB*SEC^2/IN, SEC, LB
$ TIME : 02:24:41 PM
$ DATE : Monday, November 24, 2003
$-----1-----2-----3-----4-----5-----6-----7-----8
*KEYWORD
$-----1-----2-----3-----4-----5-----6-----7-----8
*TITLE
Baseline Model
$-----1-----2-----3-----4-----5-----6-----7-----8
$
$ CONTROL CARD
$
$-----1-----2-----3-----4-----5-----6-----7-----8
*CONTROL_PARALLEL
$ NCFU NUMRHS CONST PARA
$ 16 0 2 0
*CONTROL_TERMINATION
$ ENDTIM ENDCYC DTMIN ENDENG ENDMAS
$ 0.150 0 0.0 0.0 0.0
*CONTROL_CONTACT
$ SLSFAC RWPNAL ISLCHK SHLTHK PENOPT THKCHG ORIEN ENMASS
$ 0.10 0.0 2 0 1 1 1
$ USRSTR USRFRCS NSBCS INTERM XPENE SSTHK ECDT TIEDPRJ
$ 0 0 10 0 4.0 0 0 0
$ SFRIC DFRIC EDC VFC TH TH_SF PEN_SF 0.0
0.0 0.0 0.0 0.0 0.0 0.0
$ IGNORE FRCENG
$ 0 0
*CONTROL_TIMESTEP
$ DTINIT TSSFAC ISDO TSLIMIT DT2MS LCTM ERODE MS1ST
$ 0.0 1.0 0 0.0 0.0 0 1 0
$ DT2MSF
*CONTROL_BULK_VISCOSITY
$ Q2 Q1 TYPE
$ 1.5 0.060 1
*CONTROL_SHELL
$ WRPANG ESPORT IRNXX ISTUPD THEORY BWC MITER PROJ
$ 20.0 2 -1 0 2 2 1 0
$ ROTASCL INTGRD LAMSHT
$ 1.0 0 0
*CONTROL_ENERGY
$ HGEN RWEN SLNTEN RYLEN
$ 2 2 2 2
*CONTROL_OUTPUT
$ NPOPT NEECHO NREFUP IACCOP OPIFS IPNINT IKEDIT IFLUSH
$ 0 0 0 0 0.0 0 100 5000
$ IPRTF
$ 0
$-----1-----2-----3-----4-----5-----6-----7-----8
$
$ Dynamic Relaxation Section
$
$-----1-----2-----3-----4-----5-----6-----7-----8
*CONTROL_DYNAMIC_RELAXATION
$ NRCYCK DRTOL DRFCTR DRTERM TSSFDR IRELAL EDTTL IDRFLG
$ 250 0.0001 0.1000 0.0 0.0 0 0.040 -1
*DEFINE_CURVE
$ ^GRAVITY
$ LCID SIDR SFA SFO OFFA OFFO DATTYP
$ 100 0 1.0 1.0 0.0 0.0 0
$ A1 O1
$ 0.0 386.4
0.150 386.4
*DEFINE_CURVE
$ ^DYNAMIC_RELAXATION
$ LCID SIDR SFA SFO OFFA OFFO DATTYP
$ 200 1 1.0 1.0 0.0 0.0 0
$ A1 O1
$ 0.0 0.0
0.008 386.4
0.150 386.4
*DATABASE_BINARY_D3DRLF
$ DT/CYCL
$ 20
*LOAD_BODY_Z
$ ^BODY

```

```

$      LCID      SF      LCIDDR      XC      YC      ZC
$      100      1.0      200      0.0      0.0      0.0
$-----1-----2-----3-----4-----5-----6-----7-----8
$
$                                     DATABASE CONTROL FOR ASCII
$
$-----1-----2-----3-----4-----5-----6-----7-----8
$*DATABASE_NODOUT
$      DT
$      0.00050
$*DATABASE_ELOUT
$      DT
$      0.00050
$*DATABASE_RCFORC
$      DT
$      0.00050
$*DATABASE_GLSTAT
$      DT
$      0.00050
$*DATABASE_MATSUM
$      DT
$      0.00050
$*DATABASE_SLEOUT
$      DT
$      0.00050
$-----1-----2-----3-----4-----5-----6-----7-----8
$
$                                     DATABASE CONTROL FOR BINARY
$
$-----1-----2-----3-----4-----5-----6-----7-----8
$*DATABASE_BINARY_D3PLOT
$      DT/CYCL      LCDT      BEAM      NPLTC
$      0.00050      0      0
$*DATABASE_BINARY_D3THDT
$      DT/CYCL      LCDT
$      0.00050
$-----1-----2-----3-----4-----5-----6-----7-----8
$
$                                     DATABASE EXTENT CARDS
$
$-----1-----2-----3-----4-----5-----6-----7-----8
$*DATABASE_EXTENT_BINARY
$^
$      NEIPH      NEIPS      MAXINT      STRFLG      SIGFLG      EPSFLG      RLTF LG      ENGFLG
$      0      0      3      1      1      1      1      1
$      CMPFLG      IEVERP      BEAMIP      DCOMP      SHGE      STSSZ      N3THDT
$      0      0      0      0      0      0      2
$-----1-----2-----3-----4-----5-----6-----7-----8
$
$                                     PART CARDS
$
$-----1-----2-----3-----4-----5-----6-----7-----8
$*PART
$HEADING
BLOCK1
$      PID      SECID      MID      EOSID      HGID      GRAV      ADPOPT      TMID
$      1      1      1      0      2      0      0      0
$*PART
$HEADING
BLOCK2
$      PID      SECID      MID      EOSID      HGID      GRAV      ADPOPT      TMID
$      2      1      1      0      2      0      0      0
$*PART
$HEADING
BLOCK3
$      PID      SECID      MID      EOSID      HGID      GRAV      ADPOPT      TMID
$      3      1      1      0      2      0      0      0
$*PART
$HEADING
BLOCK4
$      PID      SECID      MID      EOSID      HGID      GRAV      ADPOPT      TMID
$      4      1      1      0      2      0      0      0
.
.
.
.
.
.
.
.
.
.

```















59542	42	94128	94166	94168	94130	94129	94167	94169	94131
59543	42	94130	94168	94170	94132	94131	94169	94171	94133
59544	42	94132	94170	94172	94134	94133	94171	94173	94135
59545	42	94134	94172	94174	94136	94135	94173	94175	94137
59546	42	94136	94174	94176	94138	94137	94175	94177	94139
59547	42	94138	94176	94178	94140	94139	94177	94179	94141
59548	42	94140	94178	94180	94142	94141	94179	94181	94143
59549	42	94142	94180	94182	94144	94143	94181	94183	94145
59550	42	94144	94182	94184	94146	94145	94183	94185	94147

\$---+---1---+---2---+---3---+---4---+---5---+---6---+---7---+---8  
 \*END